

Experimental and numerical investigations on  
grouted connections for monopile offshore  
wind turbines

by

**Nikolaos Tziavos**

A thesis submitted to the University of Birmingham

for the degree of DOCTOR OF PHILOSOPHY

Department of Civil Engineering,

School of Engineering

University of Birmingham

February 2019

UNIVERSITY OF  
BIRMINGHAM

**University of Birmingham Research Archive**

**e-theses repository**

This unpublished thesis/dissertation is copyright of the author and/or third parties. The intellectual property rights of the author or third parties in respect of this work are as defined by The Copyright Designs and Patents Act 1988 or as modified by any successor legislation.

Any use made of information contained in this thesis/dissertation must be in accordance with that legislation and must be properly acknowledged. Further distribution or reproduction in any format is prohibited without the permission of the copyright holder.

*In loving memory of my beloved sister Olympia*

*You will forever live in our hearts*

## ABSTRACT

The future growth of the offshore wind (OW) energy sector greatly depends on the development of reliable substructures which will enable the utilisation of generators with larger capacity at greater water depths. Current substructures are solely relying on grouted connections (GC) to withstand the harsh offshore environmental conditions. The structural performance of the connections is vital, however during early days their design was mainly based on experience drawn from oil and gas (O&G) structures, limited experimental data and simplified analytical models. This led to unexpected settlements of monopile GCs owing to insufficient assumptions, lack of dedicated tests and absence of monitoring tools. Within this context the current research project aims to offer an improved understanding and a comprehensive insight on the structural behaviour of GCs with shear keys. Moreover, real-time monitoring of the joint's condition has been carried out using acoustic emission (AE) monitoring.

On modern offshore GCs the loading regime is better described by reversed loading conditions. As such, in order to assess the influence of load reversal, a new set of experiments was conducted on tubular GCs. It was revealed that for the designed configuration the ultimate bending capacity of the tested GC was not reduced by the preceding reversed bending loads and the specimens survived the cyclic protocol. However, crushing at the tip of the shear keys was reported following the visual inspections owing to the large shear key ratio. The experimental campaign was complemented by detailed numerical studies employing finite element analysis (FEA). Several numerical models of varying geometries were validated with very good agreement against the author's tests and experiments from the literature. For stockier cross-sections a cohesive-based modelling approach was suggested to model the grout confinement with accuracy. Furthermore, principal geometrical features related to shear key height and spacing were also evaluated and the robustness of the numerical model was

proven for varying configurations. It is suggested that the presented numerical scheme and FE models could accurately supplement the design of GCs.

Ultimately, monitoring of the grout integrity during destructive testing by means of AE was benchmarked. The results are presented in the form of a pilot case-study which establishes the use of AE as an excellent alternative for assessing the condition of the grout. Damage patterns were traced by means of b-value analysis which was shown to be an excellent tool for crack detection. A parametric analysis revealed several key performance indicators (KPIs), which can be used for detection, assessment and evaluation of the GC condition.

**Keywords:** Grouted connections, Offshore Wind Turbines, Experimental testing, Finite Element Analysis, Inspection and Monitoring, Acoustic Emission

## LIST OF PUBLICATIONS

The results of this research project have been published or submitted for publication in scientific journals and conferences relevant to the research field and are the author's own work. Where necessary explicit reference is made in text.

**Tziavos, N.I.**, Hemida, H., Metje N. and Baniotopoulos, C. (2019). Non-linear finite element analysis of grouted connections on monopile wind turbines, *Ocean Engineering*, 171, pp. 633-645.

**Tziavos, N.I.**, Hemida, H., Metje N. and Baniotopoulos, C. (2018). Grouted Connections for offshore wind turbines: A numerical study. *In Energy and Geotechnics, vol 18, The first Vietnam Symposium on advances in offshore engineering.*

**Tziavos, N.I.**, Hemida, H., Dirar, S., Papaelias, M., Metje, N. and Baniotopoulos, C. (2019). Structural health monitoring of grouted connections for offshore wind turbines by means of acoustic emission (*In preparation*).

**Tziavos, N.I.**, Hemida, H., Dirar, S., Metje N. and Baniotopoulos, C. An experimental and numerical study on grouted connections for offshore wind turbines under bending loads. (*In preparation*).

**Tziavos, N.I.**, Hemida, H., Metje N. and Baniotopoulos, C. (2016). Grouted connections on offshore wind turbines: A review. *Engineering and Computational Mechanics (ICE)*, Themed issue on offshore wind, 169(4), pp. 183-195. <https://doi.org/10.1680/jencm.16.00004>

**Tziavos, N.I.** (2015). Grouted connections on offshore wind turbines. WINERCOST action TU1304, STSM Report.

## ACKNOWLEDGEMENTS

First and foremost, I would like to express my sincere gratitude to my supervisors, Dr Hassan Hemida, Professor Charalampos Baniotopoulos and Professor Nicole Metje, for their generous guidance, advice and constructive suggestions throughout this project. Their continuous encouragement and support they offered is greatly acknowledged. To my principal supervisor Dr Hassan Hemida I am particularly thankful, for giving me the opportunity to work on an external project during my PhD, from which I gained valuable relevant experience within my field of research. Moreover, I wish to thank Dr Samir Dirar for the in-depth insight offered on experimental testing and for acting as my reviewer for all those years with valuable suggestions and recommendations. I would also like to thank Dr Mayorkinos Papaelias from the School of Metallurgy and Materials, for introducing me to the field of non-destructive testing and Acoustic Emission. I have greatly benefited from our discussions throughout. I am grateful to have been supervised by such a team of academics at the School of Engineering.

The School of Engineering is gratefully acknowledged for funding my PhD along with the WINERCOST COST Action TU1304 for funding a Short-Term Scientific Mission (STSM) at Leibniz Universität Hannover. I would like to acknowledge DENSIT<sup>®</sup> for generously providing the grout material that was needed for the experimental campaign. Thanks goes to the Civil Engineering laboratory technical staff, Dave Cope, David Allsop, Mike Vanderstam and Mark Carter for their assistance during the experiments and also David Price from the School of Metallurgy and Materials who assisted with material testing.

Also, thanks to all my PhD colleagues that have been a part of the everyday office life and created an ideal working environment. Special thanks to my cousin Sokratis for his continuous help and our endless discussions about work and life

in general throughout our doctorates.

To my parents I do not have enough words to express my gratitude for their continuous support, encouragement and for patiently helping me throughout; without them this work would not have been possible. Finally, Georgia, my better half, for all those days that were not easy to cope with and for always being there during this challenging journey no matter what, I am forever grateful.

# TABLE OF CONTENTS

<b>1 INTRODUCTION.....</b>	<b>1</b>
1.1 Background .....	1
1.2 Research Motivation .....	4
1.3 Aim and objectives.....	5
1.4 Outline of materials and methods .....	5
1.5 Thesis structure.....	6
<b>2 STATE-OF-THE-ART LITERATURE REVIEW .....</b>	<b>9</b>
2.1 Overview .....	9
2.2 Grouted connections in marine structures .....	11
2.3 Experimental testing – The Oil and Gas era.....	15
2.4 Development of offshore wind turbines.....	19
2.5 Offshore wind turbine substructures .....	20
2.6 Materials and construction .....	23
2.6.1 Ultra-High-Performance-Grout (UHPG).....	25
2.7 Tubular grouted connections .....	26
2.8 Settlements and failure modes .....	29
2.9 Experimental testing – The Offshore Wind era .....	31
2.10 Numerical computations.....	36
2.11 Numerical modelling of grouted connections .....	37
2.12 Standard codes.....	40

2.12.1 Offshore load regime .....	44
2.12.2 Ultimate Limit State (ULS) analytical model .....	44
2.12.3 Fatigue Limit State (FLS) considerations .....	46
2.13 Monitoring and maintenance approaches .....	48
2.14 Structural Health Monitoring (SHM) methods.....	50
2.15 Monitoring techniques for grouted connections .....	53
2.16 Research gap and motivation .....	54
<b>3 EXPERIMENTAL CAMPAIGN .....</b>	<b>56</b>
3.1 Overview .....	56
3.2 Test programme description and rationale .....	57
3.3 Test specimens .....	59
3.4 Ultra-High-Performance-Cementitious (UHPC) material .....	61
3.4.1 Mixing and curing.....	62
3.5 Material testing.....	66
3.5.1 Steel coupon tensile tests.....	66
3.5.2 Grout mechanical testing .....	67
3.6 Grouting procedure .....	69
3.6.1 Trial grouting tests .....	70
3.6.2 Pressure grouting of specimens .....	75
3.7 Ultimate strength-test layout.....	76
3.7.1 Fatigue test rig .....	78
3.8 Instrumentation .....	81

3.9 Test protocols.....	83
3.9.1 Fatigue programme .....	83
3.10 Ultimate bending results .....	85
3.11 Fatigue bending results .....	88
3.12 Residual bending capacity .....	93
<b>4 ACOUSTIC EMISSION MONITORING .....</b>	<b>98</b>
4.1 Overview .....	98
4.2 Acoustic Emission principles.....	99
4.3 Acoustic emission notation.....	101
4.4 Sensors and instrumentation system.....	102
4.5 Key Performance Indicators (KPIs) .....	104
4.5.1 Acoustic Emission events and energy.....	105
4.5.2 Root Mean Square (RMS) analysis.....	109
4.6 b-value analysis .....	112
4.7 Ib-value analysis .....	113
4.8 b and Ib-value results .....	113
<b>5 NUMERICAL MODELLING.....</b>	<b>119</b>
5.1 Overview .....	119
5.2 Numerical schemes and computations .....	121
5.3 Element selection.....	124
5.4 Contact considerations .....	125
5.4.1 Cohesive modelling .....	127

5.4.2 Surface-based cohesive behaviour.....	128
5.5 Material modelling.....	130
5.5.1 Steel modelling .....	130
5.5.2 Grout modelling .....	131
5.6 Finite Element model validation.....	135
5.7 Axially-loaded connections.....	135
5.7.1 Boundary conditions .....	137
5.7.2 Model validation .....	137
5.7.3 Dilation angle and friction coefficient.....	140
5.8 Grouted connections in bending.....	140
5.8.1 Experiments at Leibniz University of Hannover.....	142
5.8.2 Global behaviour and failure modes.....	145
5.8.3 Experiments at University of Birmingham .....	149
5.8.4 Global behaviour and failure modes.....	150
5.8.5 Grout confinement and composite action .....	152
<b>6 PARAMETRIC ANALYSIS.....</b>	<b>156</b>
6.1 Overview .....	156
6.2 Parametric study notation.....	158
6.3 Local behaviour of grout.....	159
6.4 Influence of shear key number and overlap length .....	162
6.5 Effect of shear key spacing.....	167
6.6 Cross-section effect on bending strength.....	172

6.7 Influence of grout thickness.....	176
6.8 Installation tolerances.....	178
6.8.1 Influence of horizontal tolerance.....	178
6.8.2 Influence of vertical tolerance.....	179
6.9 Summary.....	180
<b>7 CONCLUSIONS AND RECOMMENDATIONS.....</b>	<b>181</b>
7.1 Overview.....	181
7.2 Summary.....	181
7.3 Conclusions.....	182
7.4 Research Impact.....	189
7.5 Recommendations for future work.....	190
<b>REFERENCES.....</b>	<b>193</b>
<b>APPENDICES.....</b>	<b>213</b>
<b>A.1 EXPERIMENTAL DRAWINGS.....</b>	<b>214</b>
<b>A.2 TENSILE COUPON TESTING.....</b>	<b>227</b>

## LIST OF TABLES

Table 2.1: Summary of experimental tests on GCs for OWTs .....	35
Table 2.2: Recommendations for geometrical limits for offshore GCs .....	40
Table 2.3: Evolution of standard codes focusing on GCs (Tziavos et al., 2016) ..	43
Table 2.4: Capabilities and limitations of SHM methods for OWTs.....	52
Table 3.1: Geometrical features of steel pile and sleeve .....	61
Table 3.2: Material properties of steel parts (Average values) .....	66
Table 3.3: Ducorit® S5R mechanical properties.....	68
Table 3.4: Fatigue bending load range during the final load stage.....	84
Table 3.5: Fatigue test load stages.....	84
Table 3.6: Ultimate load and moment corresponding midspan deflection for each GC.....	94
Table 4.1: Acquisition parameters.....	104
Table 4.2: RMS values for GCs during bending tests.....	110
Table 5.1 HSG and CDP parameter identification.....	135
Table 5.2: Geometrical parameters of GC model in compression .....	136
Table 5.3: FEM vs experiment of axially-loaded GC.....	139
Table 5.4: Summary of GC tests in bending used within the validation study	141
Table 5.5: FE model geometry based on Wilke, 2013 and Lochte-Holtgreven, 2014 .....	143
Table 5.6: Summary of FE model results against test results.....	155
Table 6.1: Geometrical characteristics of FE models for parametric analysis....	170
Table 6.2: FE parametric models for $D/t$ effect.....	175

# LIST OF FIGURES

Figure 1.1: Monopile and jacket substructures (photo source: Handelsblatt, 2016) .....	2
Figure 1.2: a) Schematic layout of monopile and GC (Tziavos et al., 2016), b) Design of GC employed Horns Rev wind farm illustrating boat landing and platform appurtenances (source: Densit, 2002) .....	3
Figure 1.3: Schematic layout of research approach .....	6
Figure 2.1: Geometrical parameters of a GC shown in different cross sections. $R$ is the radius, $t$ is the thickness, $L_g$ the length of grout, $h$ is the height and $s$ the distance between shear keys. The subscripts $s$ , $p$ , $g$ refer to the sleeve, pile and grout, respectively.....	11
Figure 2.2: Shear key types for use in GCs: a) semi-circular weld beads, b) fillet- welded bars, c) fillet-welded round bars (Concept after BSI 19902, 2007) .....	12
Figure 2.3: Schematic layout of O&G offshore jacket platform with grouted cluster piles (left) and grouted jacket leg to pre-driven pile (right) .....	13
Figure 2.4: North Rankin B offshore platform (FoundOcean, 2015).....	14
Figure 2.5: Effect of grout compressive strength to bond strength of axially- loaded GC with shear keys .....	18
Figure 2.6: Annual and cumulative installed capacity from OWTs (WindEurope, 2017) .....	19
Figure 2.7: Breakdown of a) installed capacity of OWTs, b) installed substructures in Europe (Redrawn from WindEurope, 2017).....	21
Figure 2.8: Most common types of substructures used to-date within the OW sector and notation (After DNV ST-0126, 2016).....	21
Figure 2.9: Diameter and thickness data from offshore monopile across Europe (Bocher et al., 2018). [Reprinted from Ocean Engineering, Vol 160, Bocher et al.,	

2018, New shape function solutions for fracture mechanics analysis of offshore wind turbine monopile foundations. Pages No. 264-275, Copyright (2018), with permission from Elsevier] .....	22
Figure 2.10: Installation of monopile transition piece with platform and appurtenances in Anholt, Denmark (Photo source: Ramboll, 2017).....	23
Figure 2.11: Microstructural viewpoint of cement (left) and cement with fine particles (right) (Dorph and Sipavicious, 2010, Original figure from Bache, 1995) .....	25
Figure 2.12: Cracking within a) UHSG and b) normal concrete matrix .....	26
Figure 2.13: Force transfer mechanism in a GC under bending moment (Lotsberg, 2013). Top figure illustrates the contact pair of opposing contact forces on the sides of the GC and bottom figure the gaps and cracks on a GC. [Reprinted from Marine Structures, Vol 32, Lotsberg, I., Structural mechanics of grouted connections Pages No. 113-135, Copyright (2018), with permission from Elsevier] .....	28
Figure 2.14: Monopile GC with centrally-located shear keys.....	32
Figure 2.15: Bond strength comparison of GC specimens for different applications .....	34
Figure 2.16: Diameter to thickness ratio of monopiles for UK wind farm [Data extracted from Arany et al. (2017)] .....	42
Figure 2.17: Cyclic load notation.....	46
Figure 2.18: Classification of maintenance approaches for different parts of OWTs .....	49
Figure 3.1: CHS geometry and GC layout .....	60
Figure 3.2: The process for compressive strength determination of grout cubes: a) Weighing Ducorit® S5R prior to mixing, b) Grout casted in cubic moulds, c) Curing of grout cubes in water-filled tank .....	65

Figure 3.3: Cylindrical S5R sections.....	65
Figure 3.4: Example of stress strain curve from steel coupon test .....	67
Figure 3.5: Strength-development curve of S5R UHSG after 28 days .....	68
Figure 3.6: (a, b) Test frames for compression and flexural tests along with (c) cylinder (d-f) and grout cube failure modes after 1, 7 and 28 days.....	69
Figure 3.7: Pile and sleeve geometry of GC mock-up used in trial tests (dimensions in <i>mm</i> ).....	70
Figure 3.8: Fabrication process of steel parts for trial grouting.....	72
Figure 3.9: Mock-up grouting layout and investigations.....	73
Figure 3.10: Putzmeister SP11 LMR.....	73
Figure 3.11: Set-up for laboratory bottom-to-top grouting.....	76
Figure 3.12: Schematic layout (top) and set-up of the ultimate bending test (bottom) (dimensions in <i>mm</i> ).....	77
Figure 3.13: Details of the specimen set-up for the four-point ultimate strength bending tests .....	78
Figure 3.14: Support system during the fatigue test (dimensions in <i>mm</i> ) .....	79
Figure 3.15: Fatigue test set-up.....	80
Figure 3.16: Instrumentation plan on the GC specimen.....	81
Figure 3.17: Strain gauges LVDTs and AE sensors on GC.....	82
Figure 3.18: GC notation and orientation used for the experiments .....	82
Figure 3.19: GC-1 load-deflection curve .....	85
Figure 3.20: (left) Pile local buckling at GC bottom (location: 0°) and (right) interface opening (location: 180°) .....	86
Figure 3.21: Longitudinal strains for GC-1 at sleeve top (top) and bottom (bottom) .....	87

Figure 3.22: Grout cracking patterns following inspection of GC-1 .....	88
Figure 3.23: Load versus displacement curve during stages 1 and 2 .....	89
Figure 3.24: Load versus displacement curve during stages 2 and 3 .....	90
Figure 3.25: Load versus displacement curve during stages 3 and 4 .....	90
Figure 3.26: Initial and final cycles of stage 5 and comparison with stage 3 .....	91
Figure 3.27: Specimen stiffness for Levels 1 and 2 .....	92
Figure 3.28: Specimen stiffness at different load levels .....	92
Figure 3.29: GC stiffness during load level 5 .....	93
Figure 3.30: Load-midspan deflection curves for GC specimens.....	94
Figure 3.31: Shear key misalignment following visual inspection for GC-2 .....	95
Figure 3.32: Hairline cracks on the outer grout surface of GC-1 (left) and GC-2 (right) .....	96
Figure 3.33: Interface opening along the length of the connection in cut view (top) and side view (bottom-left) and pile buckling (bottom-right) .....	96
Figure 3.34: Visual inspection of GC-2 core. a) Evenly distributed aggregates at the middle of the grouted length, b-d) Grout crack patterns and failure surfaces between two opposing shear keys at bottom and top locations .....	97
Figure 3.35: Crushed grout in front of shear key tip (GC-2).....	97
Figure 4.1: Schematic layout of AE instrumentation and acquisition system .....	99
Figure 4.2: AE signal parameters .....	101
Figure 4.3: AE sensor location along the grouted length (top) and pre-amplifier used to set signal gain along with R50a sensors (bottom) .....	103
Figure 4.4: Amplitude against absolute energy - AE4 sensor specimen GC1 ...	105
Figure 4.5: AE events per unit time (GC-1) .....	106
Figure 4.6: Duration of AE signals against time for GC-2 (left), Cross plot of	

amplitude against counts (right).....	107
Figure 4.7: Cumulative energy from GC-1 at the tensile (AE3) and compressive side (AE2) .....	108
Figure 4.8: Load against cumulative energy (AE3) for GC2.....	108
Figure 4.9: Phases used for RMS analysis.....	110
Figure 4.10: RMS for GC-1 (top) and GC-2 (bottom) at different stages during test .....	111
Figure 4.11: Correlation of AE RMS with load .....	111
Figure 4.12: Effect of event number on $b$ (left) and $Ib$ -value (right).....	114
Figure 4.13: Comparison between $b$ and $Ib$ -value .....	115
Figure 4.14: Peaks and drops of $Ib$ -value for GC-1.....	116
Figure 4.15: Cumulative signal strength against applied load for GC-1.....	117
Figure 4.16: CSS and $Ib$ -value correlation.....	118
Figure 4.17: Correlation of $Ib$ -value and RA .....	118
Figure 5.1: Example of energy output from quasi-static simulation for a GC model solved with Abaqus/Explicit .....	123
Figure 5.2: Zero energy mode on an element with reduced integration in bending .....	125
Figure 5.3: Hourglassing mode example on a GC model. The pile has been removed for illustration purposes .....	125
Figure 5.4: Traction separation constitutive model and damage evolution.....	129
Figure 5.5: Typical $\sigma$ - $\varepsilon$ curve of UHPG in compression (Concept adopted by Fehling et al., 2014).....	131
Figure 5.6: Grout engineering and true $\sigma$ - $\varepsilon$ curve .....	133
Figure 5.7 Exponential tensile softening (left) and damage (right) .....	134

Figure 5.8: Small scale FE model (left) and component identification (right)...	136
Figure 5.9: Comparison between numerical simulation and experimental results (Tziavos et al., 2018).....	138
Figure 5.10: Cracking within the grout core by means of plastic strains from initiation to fully-developed compression struts. Crack patterns (right) from experimental test (Photo property of GROWup research project) .....	139
Figure 5.11: Effect of Dilation angle (left) and friction coefficient (right) (Tziavos et al., 2018).....	140
Figure 5.12: GC notation for FE models.....	141
Figure 5.13 Model geometry and close up on (top left) PGC and (top right) SKGC1 .....	142
Figure 5.14 Meshed GC and zoomed shear key detail .....	144
Figure 5.15 Boundary conditions and constraints applied in the FE model ....	145
Figure 5.16: Force-displacement and force-gap between FE models and experiments.....	146
Figure 5.17: a) Gap formation owing to force-transfer mechanism and b) stresses on GC under bending .....	146
Figure 5.18: Longitudinal stresses at load level $F=435\text{ kN}$ for SKGC.....	147
Figure 5.19: Longitudinal stresses at $F=435\text{ kN}$ for PGC.....	147
Figure 5.20: Force-displacement for GC with $F_0=1$ .....	148
Figure 5.21: Tresca stresses on the pile-grout interface .....	148
Figure 5.22: Four-point test configuration and boundary conditions .....	149
Figure 5.23: FE results against UoB tests .....	150
Figure 5.24: FE model failure modes .....	151
Figure 5.25: Strut cracking in the grout core and corresponding plastic strains	

from FE model .....	151
Figure 5.26: Longitudinal stresses at different load levels .....	152
Figure 5.27: Comparison between Coulomb-friction model and Cohesive behaviour.....	154
Figure 6.1: Iso-surface and contour plots depicting grout plastic strains on a GC with a spacing of $s=60\text{ mm}$ .....	160
Figure 6.2: Iso-surface contour plots depicting grout plastic strains on a GC with a spacing of $s=30\text{ mm}$ .....	161
Figure 6.3: Iso-surface contour plots depicting grout plastic strains on a GC with a spacing of $s=120\text{ mm}$ .....	162
Figure 6.4: Grout failure modes for varying shear key spacing. a) $s=60\text{ mm}$ , b) $s=30$ $\text{mm}$ , c) $s=120\text{ mm}$ .....	162
Figure 6.5: Force–displacement curve illustrating the effect of $F_o$ .....	163
Figure 6.6: Maximum interface opening at the bottom of the GC .....	163
Figure 6.7: Force-deflection curves for: a) $F_o=1$ , b) $F_o=1.3$ .....	164
Figure 6.8: Maximum developed gap at the top of GC at $M_{\max}$ for a) $F_o=1$ , b) $F_o=1.3$ , c) $F_o=1.5$ .....	165
Figure 6.9: Contact pressure at maximum opening around the sleeve circumference for a) $F_o=1$ , and b) $F_o=1.3$ .....	166
Figure 6.10: Grout plastic stain vectors at maximum load level .....	167
Figure 6.11: Displacement growth over normalised length for: a) $F_o=1.3$ , b) $F_o=1.5$ .....	168
Figure 6.12: Force – Relative displacement for a) $F_o=1$ , b) $F_o=1.3$ , c) $F_o=1.5$ .....	169
Figure 6.13: Maximum gap opening against shear key span from parametric models.....	170

Figure 6.14: Effect of pile  $D/t$  to the overall response ..... 172

Figure 6.15: Effect of sleeve  $D/t$  to the overall response ..... 173

Figure 6.16: Sleeve contribution to ultimate load ..... 174

Figure 6.17: Pile contribution to ultimate load..... 174

Figure 6.18: Influence of radial stiffness ..... 175

Figure 6.19: Load-displacement curves for varying grout cores (effect of pile - constant sleeve)..... 177

Figure 6.20: Load-displacement curves for varying grout cores (constant pile) ..... 177

Figure 6.21: Horizontal and vertical tolerances during GC installation (DNV ST-0126, 2016) ..... 178

Figure 6.22: Influence of uneven thickness on ultimate load ..... 179

Figure 6.23: Iso-surface plot on GC model with misaligned pile and sleeve shear keys..... 180

## LIST OF ABBREVIATIONS AND ACRONYMS

<b>AE</b>	<b>Acoustic Emission</b>
<b>AF</b>	<b>Average Frequency</b>
<b>ALS</b>	<b>Accidental Limit State</b>
<b>API</b>	<b>American Petroleum Institute</b>
<b>ASTM</b>	<b>American Society for Testing and Materials</b>
<b>BlueBEAR</b>	<b>Birmingham Environment for Academic Research</b>
<b>BSI</b>	<b>British Standards Institution</b>
<b>CAE</b>	<b>Computer Aided Engineering</b>
<b>CAPEX</b>	<b>Capital Expenditure</b>
<b>CDP</b>	<b>Concrete Damage Plasticity</b>
<b>CM</b>	<b>Condition Monitoring</b>
<b>CSS</b>	<b>Cumulative Signal Strength</b>
<b>DAQ</b>	<b>Data Acquisition System</b>
<b>DEn</b>	<b>Department of Energy</b>
<b>DP</b>	<b>Drucker Prager</b>
<b>DUR</b>	<b>Duration</b>
<b>FE</b>	<b>Finite Element</b>
<b>FEA</b>	<b>Finite Element Analysis</b>
<b>FLS</b>	<b>Fatigue Limit State</b>

<b>GCs</b>	<b>Grouted Connections</b>
<b>HSG</b>	<b>High Strength Grout</b>
<b>JIP</b>	<b>Joint Industrial Project</b>
<b>KPIs</b>	<b>Key Performance Indicators</b>
<b>LcoE</b>	<b>Levelised Cost of Energy</b>
<b>LVDT</b>	<b>Linear Variable Displacement Transducer</b>
<b>NDT</b>	<b>Non-Destructive Techniques</b>
<b>O&amp;G</b>	<b>Oil and Gas</b>
<b>O&amp;M</b>	<b>Operation and Maintenance</b>
<b>OW</b>	<b>Offshore Wind</b>
<b>OWT</b>	<b>Offshore Wind Turbine</b>
<b>PAC</b>	<b>Physical Acoustics Corporation</b>
<b>PFC</b>	<b>Parallel Flange Sections</b>
<b>RA</b>	<b>Rise Time to Amplitude ratio</b>
<b>RMS</b>	<b>Root Mean Square</b>
<b>RT</b>	<b>Rise Time</b>
<b>SHM</b>	<b>Structural Health Monitoring</b>
<b>SLS</b>	<b>Serviceability Limit State</b>
<b>TP</b>	<b>Transition Piece</b>
<b>UHPC</b>	<b>Ultra High Performance Cementitious</b>

<b>UHPG</b>	<b>Ultra-High-Performance Grout</b>
<b>UHSG</b>	<b>Ultra High Strength Grout</b>
<b>ULS</b>	<b>Ultimate Limit State</b>
<b>UPV</b>	<b>Ultrasonic Pulse Velocity</b>

## NOMENCLATURE

$A$	AE emission signal Peak amplitude
$A$	Area of the cross-section
$a, b$	Constants
$a_1, a_2$	User-defined constants for Ib-value analysis
$A_{dB}$	AE emission signal Peak amplitude in $Db$
$b$	b-value
$c_d$	Dilational wave speed
$D$	Damage initiation
$d_a$	Diameter of aggregate
$d_c$	Damage of concrete in compression
$D_g$	Diameter of the grout core
$D_p$	Diameter of the pile
$D_s$	Diameter of the sleeve
$E$	Young's modulus
$E_g$	Young's modulus for grout
$E_s$	Young's modulus for steel
$\varepsilon_y$	Yield strain
$\varepsilon_u$	Yield at fracture
$f_{bk}$	Interface shear capacity

$f_{bu}$	Bond strength
$F_{bu}$	GC bond strength
$f_{ck}$	Characteristic compressive strength from 75 mm cubes
$f_{cm}$	Compressive strength
$f_{cm0}$	Compressive strength base value (10 MPa)
$f_{cu}$	Compressive strength of cubic grout sample at 28 days
$F_o$	Overlap length of grouted connection
$F_{su}$	GC slip strength
$f_t$	Tensile strength of grout at 28 days
$F_u$	Ultimate load
$F_{u,FE}$	Computed ultimate load from finite element analysis
$f_y$	Yield strength of steel
$G_c$	Fracture energy
$G_{F0}$	Fracture Energy base value
$h$	Height of shear key
$Ib$	Improved b-value
$k$	Radial Stiffness
$\mathbf{K}$	Stiffness matrix
$k_{eff}$	Effective stiffness
$K_{gc}$	Specimen equivalent stiffness

$K_{nn}$	Normal direction stiffness matrix
$K_{ss}$	Tangential direction stiffness matrix
$K_{tt}$	Tangential direction stiffness matrix
$l$	Length between loading points
$L$	Total span of specimen
$L^e$	Element length
$L_g$	Grouted length
$L_{ge}$	Effective Grouted length
$M$	Bending moment
$M_L$	Magnitude of earthquake
$M_d$	Design bending moment
$M_u$	Ultimate bending moment
$N$	Frequency of AE events
$n$	Number of shear keys
$n_{eff}$	Effective number of shear keys
$P_{nom,d}$	Nominal, design contact pressure
$R$	Stress ratio
$R_g$	Radius of the grout core
$R_p$	Radius of the pile
$R_s$	Radius of the sleeve

$RS$	Ratio of slenderness
$s$	Spacing between two adjacent shear keys
$s_{eff}$	Distance between two consecutive shear keys minus the width
$T$	Cycle period
$t$	Thickness of a cross-section
$t_g$	Thickness of the grout cross-section
$t_{n, s, t}^o$	Maximum stress in normal and tangential directions
$t_p$	Thickness of the pile cross-section
$t_s$	Thickness of the sleeve cross-section
$u$	Vertical deflection
$w$	Width of shear key
$w/c$	water to cement ratio
$\Delta F$	Maximum-minimum load
$\delta_{o, f}^{m, f}$	Separation at damage initiation and failure
$\delta_{n, s, t}^o$	Maximum displacement in normal and tangential directions
$\Delta t$	Time increment
$\Delta t_{min}$	Minimum time increment
$\Delta u$	Maximum-minimum displacement
$\varepsilon$	Strain
$\varepsilon_{c1}$	Peak strain

$\varepsilon_{\text{eng}}$	Engineering strain
$\varepsilon_{\text{true}}$	True strain
$\theta$	Dilation angle
$\kappa$	Curvature
$\lambda, \mu$	Constant values
$\mu$	Friction coefficient
$\nu$	Poisson's ratio
$\sigma$	Standard deviation
$\sigma$	Stress
$\sigma_a$	Load cycle stress amplitude
$\sigma_c$	Concrete stress corresponding to inelastic strain
$\sigma_{\text{eng}}$	Engineering stress
$\sigma_{\text{max}}$	Maximum stress
$\sigma_{\text{min}}$	Minimum stress
$\sigma_{\text{true}}$	True stress
$\Psi$	Design coefficient factor

## LIST OF APPENDICES

A.1 Experimental drawings .....	214
A.2 Tensile coupon testing.....	227

# 1 INTRODUCTION

## 1.1 Background

Since the seventies, Grouted Connections (GCs) have been integral structural elements of fixed-bottom offshore structures. Their application is widely adopted within the Oil and Gas (O&G) and offshore wind (OW) energy sectors. GCs are typically constructed by attaching concentric tubular steel members with a cementitious-based grout of high compressive strength (Dallyn et al., 2015; Tziavos et al., 2016). The main benefit of GCs is the composite action induced by the interaction of the grout core with the steel piles, which offers increased stiffness and greatly enhances the capability of the structure to withstand external environmental and operating loads. Offshore Wind Turbine (OWT) substructures employ GCs since the early 2000s, when seven fixed bottom OWTs were installed in shallow water depths at the Baltic sea employing connections formed by an ultra-high-strength-grout (UHPG) (Andersen, 2002; Bechtel, 2017).

Prior to their application on OWTs, GCs have already been common practice in marine structures and their robust performance has been documented within

O&G jacket platforms for decades (Lotsberg, 2013). Their principal use was to connect steel piles with clusters of jacket legs or to strengthen various parts of the structure (Dallyn et al., 2015; Tziavos et al., 2016). The satisfactory structural record of this structural component was the main motive within the industry, to transfer the concept of GCs on OWTs. Nowadays, the connections are employed on different types of fixed-bottom substructures, which are installed in varying water depths that can reach up to 60 m. Monopiles, jackets or tripods are the most commonly installed substructures globally, with monopiles offering the most straightforward and favourable design. Typical modern jacket and monopile substructures for OWTs are shown in Figure 1.1.



Figure 1.1: Monopile and jacket substructures (photo source: Handelsblatt, 2016)

On monopiles, GCs are in-situ achieved, by filling the annuli of two overlapping hollow tubular steel tubes – the Transition Piece (TP) and the monopile, with an UHPG as depicted in the illustration of Figure 1.2a. The TP is commonly of a larger diameter and owing to this arrangement, they are otherwise referred to as

pile-to-sleeve connections in the literature (see e.g., Klose et al. 2008; Jiang et al., 2011). This unconventional arrangement with the TPs being larger, is chosen to allow the installation of a platform, which subsequently enables boat landing for operation and maintenance (O&M) tasks to be carried out (Figure 1.2b).

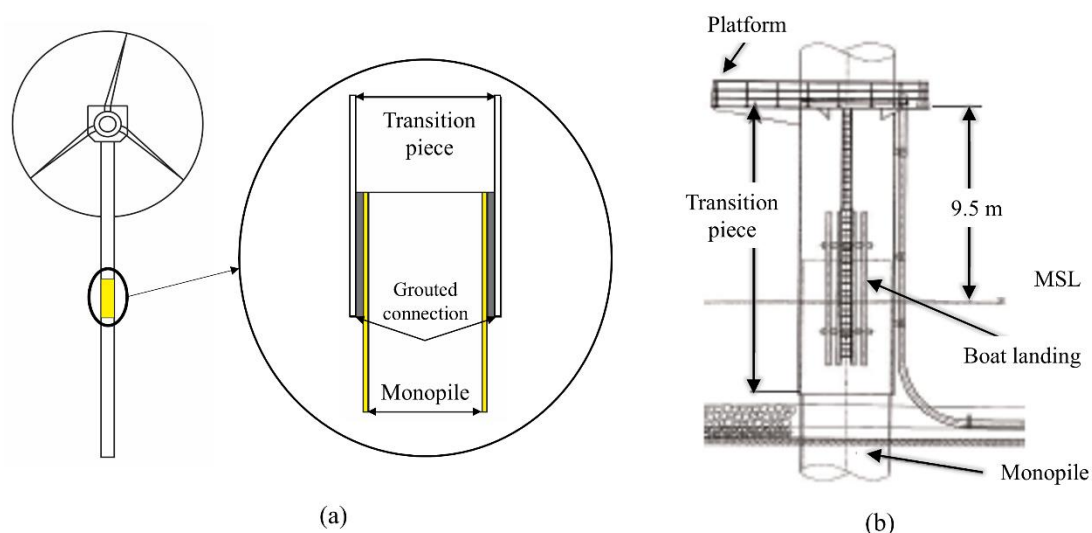


Figure 1.2: a) Schematic layout of monopile and GC (Tziavos et al., 2016), b) Design of GC employed Horns Rev wind farm illustrating boat landing and platform appurtenances (source: Densit, 2002)

Once the GC is established, the tower and the nacelle-rotor assembly are installed on top. GCs are a simple, efficient and cost-effective technique to assemble an OWT substructure in offshore environments. In addition, it benefits the installation process compensating for pile inclinations induced by driving the foundation pile into the seabed, ensuring verticality of the tower (Andersen, 2002). The current practice on OWTs is to employ tubular connections with shear keys (Lotsberg et al., 2013) or plain conical GCs (Lotsberg et al., 2012). For the remaining of this thesis by shear keys we refer to welded beads on the internal and external surfaces of the monopile and TP, aiming to provide enhanced mechanical interlock.

Owing to the development of the OW sector, monopiles constantly become larger in size. Monopile diameters today range from 5 to 7.5 *m* and the depth of installation can reach up to 30-35 *m*. Nevertheless, the current trends in the OW community dictate moving towards even larger piles with diameters in excess of 8 *m* weighing up to 1,500 *tonnes*, which are known as XL-monopiles. It is evident that while the OW sector further expands, the size of the substructures will require a significant upscale to accommodate this development. Subsequently, by that time the already notable cost of the structure becomes crucial when compared to the total investment required for an OWT.

## 1.2 Research Motivation

The motivation for this work originates back to 2010, when routine inspections on monopiles around Europe revealed issues with the performance of GCs. Notably, TPs on monopiles have slid downwards, putting the integrity of the substructure under investigation. Amongst other, TPs located in the coast of Kent, England, as part of the Kentish flats wind farm, have demonstrated some questionable structural performance (Dallyn et al., 2015). Following the inspections, concerns were raised on the design process and ultimately the performance of the structural joint (see e.g., Klose et al., 2012; Lotsberg, 2013a; Tziavos et al., 2016).

Taking into consideration the rapid growth and need for further development of OWTs, this thesis deals with an emerging and critical aspect of the design of OWT substructures aiming initially to further investigate the structural performance of GCs and secondly to examine a real-time monitoring approach using non-destructive testing (NDT).

### 1.3 Aim and objectives

The aim of this research project is devoted in providing an in-depth insight on the performance and integrity of GCs. Within the scope of this work and to achieve this aim the following key objectives have been set:

- To investigate the performance of GCs by conducting physical tests on laboratory-scaled specimens under static and cyclic loads.
- To develop robust, comprehensive and validated Finite Element (FE) models of GCs that prevail over the challenges induced by the nonlinear material behaviour and the computational cost.
- To carry out an extensive parametric analysis using the validated FE models and investigate a series of principal design parameters on the behaviour of GCs.
- To monitor the integrity of the GC in real-time, employing a Structural Health Monitoring (SHM) approach, namely Acoustic Emission (AE).
- To present a framework for monitoring the degradation of the grout through Key Performance Indicators (KPIs).

### 1.4 Outline of materials and methods

To fulfil the aforementioned aim and objectives of this research project, experimental approaches along with numerical techniques have been utilised. The experiments as well as the numerical computations using Finite Element Analysis (FEA) were carried out at the University of Birmingham, UK. An overview of the approach and methods which were used to accommodate the presented research project is illustrated in the schematic flowchart in Figure 1.3.

Physical testing on GCs were performed to generate new data sets and enhance

the existing literature on the performance of GCs as well as supplement the validity of numerical models. The FE models were used to carry out an extensive parametric study on critical geometric parameters that contribute significantly in the structural behaviour of GCs, to assess the significance of unknown geometrical attributes. Additionally, the tests enabled real-time monitoring of the integrity of the connection by means of AE. The grout damage and overall condition of the GCs was monitored using acoustic sensors and statistical approaches were applied to correlate AE KPIs with damage in GCs.

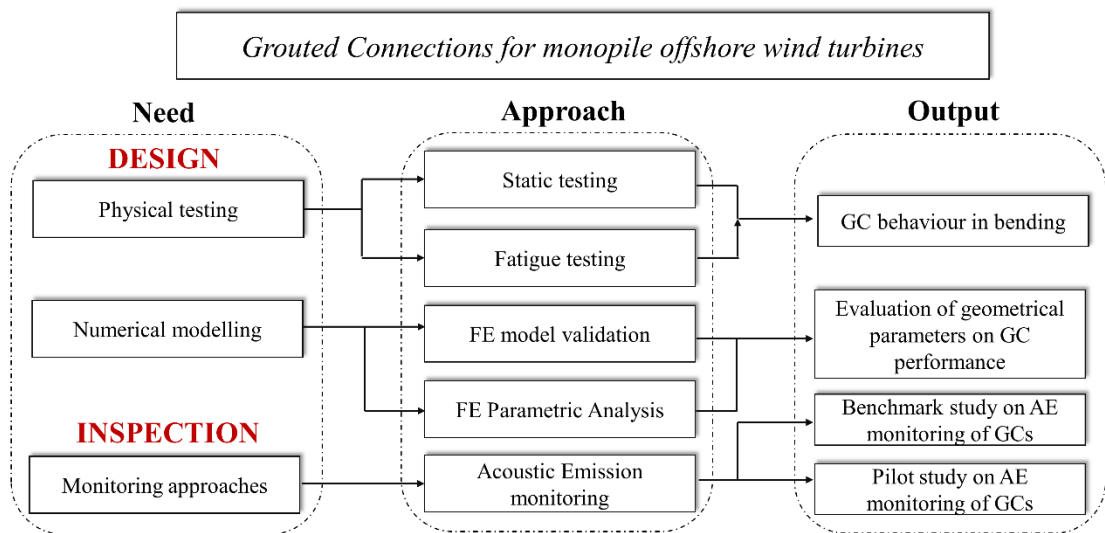


Figure 1.3: Schematic layout of research approach

## 1.5 Thesis structure

This introductory chapter provided a brief background on the concept and application of GCs in fixed-bottom offshore structures and particularly OWTs during the past decades. The rationale behind this research thesis was presented and subsequently, the aim and objectives were highlighted along with the methodological framework to achieve them.

Chapter 2, thoroughly reviews the published literature, focusing on previous

experimental and numerical work, while presenting crucial research findings and evolution of engineering practice. The chapter also addresses relevant monitoring and SHM approaches which are of interest for OWTs and their substructures. Each corresponding chapter will also present and discuss specialised topics which are directly related to the methods employed by the author.

In Chapter 3, the experimental campaign is thoroughly presented. Experimental details of the campaign such as specimen preparation, grouting methods and investigations along with testing for mechanical properties are covered. Ultimately, the results from the static and cyclic tests are given and discussed, while considering findings from previous studies.

The SHM aspect of the experimental work is the central point of Chapter 4, which is presented in the form of a case study. The set-up, post-filtering and post-processing approach that was followed is introduced along with a review of specialised literature. The analysed results are finally presented and discussed and a correlation with the destructive test data is given.

Chapter 5 deals with the numerical aspect of this project. GCs are examined under bending and axial load configurations. For this purpose, advanced FE models are developed and validated against various experimental tests. An in-depth analysis follows, along with a comprehensive discussion on the selected numerical scheme.

Chapter 6 presents the parametric analysis which was carried out by means of FE modelling. The validated models are taken forward and an extensive investigation is conducted, emphasising on shear key parameters and their influence on GC performance. Dedicated sections discuss design of GC by means of FE and how the presented work contributes in improving engineering practice.

Finally, Chapter 7 presents the conclusions and a thorough discussion on the principal findings deriving from this research work. Based on the knowledge base created, recommendations for future research are given.

# 2 STATE-OF-THE-ART LITERATURE REVIEW

## 2.1 Overview

Chapter 2 entails a comprehensive review and discussion of the literature which deals with research studies on GCs. The chapter is structured upon three main aspects: *i)* experimental testing, *ii)* FE modelling and *iii)* SHM methods for OWTs and substructures. To begin with, a historic background dating back to the early days of pile-to-sleeve connections (see Section 2.2) within the main sectors of application is given. Subsequently, experimental studies on GCs for O&G structures are presented in a chronological sequence in Section 2.3, to highlight events that contributed to the developments that took place in the design process and led to the current state. Moreover, the transition to OWTs and the main substructures employing GCs today are presented along with the working principles of tubular connections (Section 2.5 and 2.7). In Section 2.6 the specialised materials that are used in the construction of the joints are discussed and the differences found between O&G and OWT GCs are presented.

The main reasons behind the questionable performance of monopile GCs and the failures that occurred in the onset of the current decade are discussed in section 2.8. In Section 2.9 relevant experimental work is discussed, aiming to further comprehend the performance of the connections under the complex stress-state they are subjected to. Subsequently, advances in the field of numerical modelling and findings from computational studies are introduced in section 2.10. Within this context, as a considerable amount of numerical work will be presented in the following chapters, some fundamental concepts on FE analysis are introduced. The chapter also brings together the evolution of the codification followed by researchers and engineers for the design of GCs in Sections 2.12 and 2.4. Finally, in sections 2.13-2.15, the chapter introduces monitoring tools involving SHM methods focusing on their applicability for maintenance purposes on OWTs. Focus is on GCs as such tools aim to assist with damage prevention and subsequently reduce O&M costs.

A review paper related to this chapter's scope has been published by the author and is explicitly referenced in text where applicable:

**Tziavos, N.I.,** Hemida, H., Metje N. and Baniotopoulos, C. (2016). Grouted connections on offshore wind turbines: A review. *Engineering and Computational Mechanics (ICE)*, Themed issue on offshore wind, 169(4), pp. 183-195. <https://doi.org/10.1680/jencm.16.00004>

## 2.2 Grouted connections in marine structures

The primary role of a GC is to accommodate the load transfer mechanism between the piles, hence providing sufficient resistance to withstand the deadload, operational and severe environmental loads the structure is experiencing (Lee et al., 2014). Therefore, it is appreciated that their performance is vital and the joint is most certainly a critical structural element in the design process. The main geometrical characteristics of such a joint are illustrated in Figure 2.1.

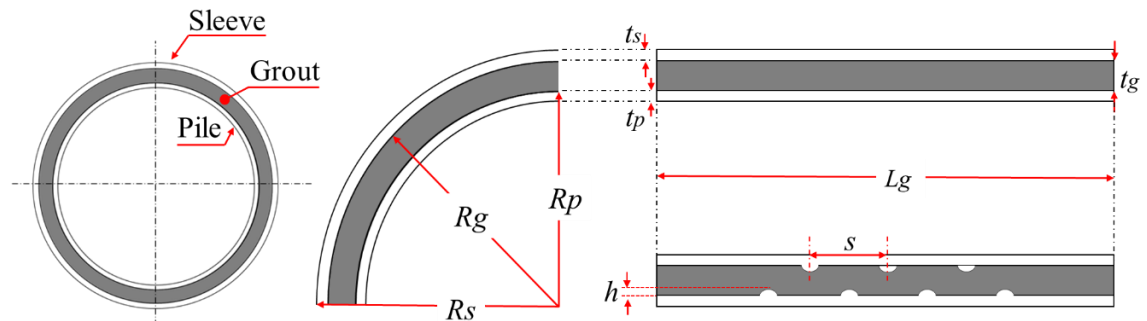


Figure 2.1: Geometrical parameters of a GC shown in different cross sections.  $R$  is the radius,  $t$  is the thickness,  $L_g$  the length of grout,  $h$  is the height and  $s$  the distance between shear keys. The subscripts  $s$ ,  $p$ ,  $g$  refer to the sleeve, pile and grout, respectively.

Historically, GCs have been constructed in different scales depending on the platform's requirements or the location, either using plain pipes or shear keys. In fixed offshore marine structures, circumferentially-welded circular beads or fillet-welded bars are called shear keys or sometimes shear connectors. Their purpose is to provide enhanced mechanical interlock, thus improving the axial capacity of the connection. Typical idealised shear key shapes which can be used according to BSI 19902 (2007) are shown in the schematic of Figure 2.2.

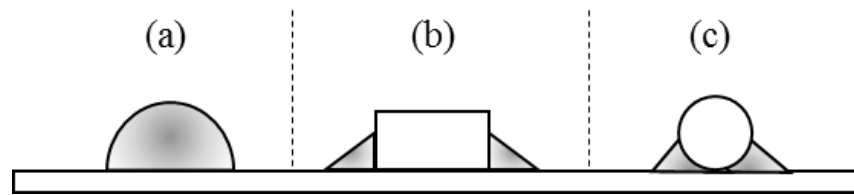


Figure 2.2: Shear key types for use in GCs: a) semi-circular weld beads, b) fillet-welded bars, c) fillet-welded round bars (Concept after BSI 19902, 2007)

Dating back to 1970, although some advances were made towards buoyant structures, the most favourable solution for offshore platforms within the O&G sector was the pile-jacket fixed-bottom structure (Billington, 1980). Jackets further established their popularity in the sector once their applicability to larger water depths was enabled by expanding the use of GCs on the foundation installation. The connection was typically formed and located underwater, especially in deep water and was utilised in different ways. For example, in greater water depths cluster piles were attached to the jacket legs or positioned between the jacket legs at evenly spaced locations. On the contrary, for shallow foundations the jacket legs were mostly connected to pre-driven piles by filling the annulus with cement-based grouts (Billington and Lewis, 1978). Typical applications of grouted joints as the ones mentioned above are illustrated in the schematic of Figure 2.3. Regardless of the installation type, the greatest benefit of a GC is the enhanced performance induced by the grout containment within the steel tubulars which leads to higher strengths and enhanced ductility (Billington, 1980).

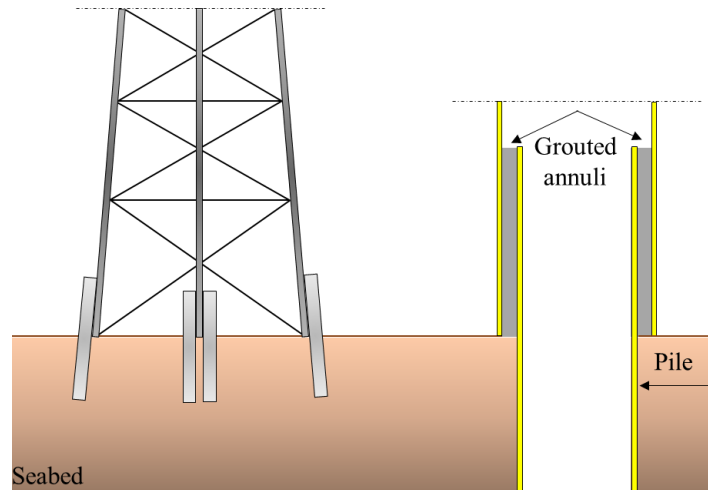


Figure 2.3: Schematic layout of O&G offshore jacket platform with grouted cluster piles (left) and grouted jacket leg to pre-driven pile (right)

By the end of the 70s the O&G industry reached a deadlock, when the need for the exploitation of remote sites with greater potential surfaced. The need to explore remote offshore environments caused an increasing demand for larger jacket structures with enlarged piles (Billington and Lewis, 1978). This urge for offshore expansion, was also highlighted within the European Commission (1979), where the necessity for new concepts that would allow for larger platforms that can be installed in greater depths was underlined. Considering the above, the use of GCs with lower radial stiffness ( $k$ ) was considered to be a possible solution and their implementation received increasing popularity. Billington (1980) suggested that GCs could also provide an excellent solution for strengthening the existing joints and a promising alternative for the construction of nodal joints.

Nodal joints in steel platforms were typically formed from welded tubular piles. To broaden the range of application and enable even greater depths, larger piles were required. However, that translates to significant welding operations which could prove to be impractical and not feasible in terms of cost. Instead, employing GCs would also alleviate construction difficulties and significantly reduce

welding requirements.

Design of GCs with shear keys was allowed by standard codes at the time even for slender cross sections, but knowledge on their performance and influence was very limited. For that reason, studies focused primarily on the use of shear keys (Billington and Lewis, 1978; Krahl and Karsan, 1985). The main aim was to provide a verified and documented approach on the determination of the connection's strength and the alterations the welded beads cause in the structural behaviour. However, it was further noted that the influence of several parameters on the performance of GCs was not fully-comprehended (Billington and Lewis, 1978; Billington, 1980). Such parameters ranged from geometrical properties to loading conditions or early age performance.

A common measure that is used for the assessment of GCs is bond strength,  $f_{bu}$ . The parameter is defined as the ratio of the ultimate load ( $F_u$ ) that was sustained by the connection over the surface area of the interface between the steel tube and grout infill. Grouting of steel piles is extensively used to date in offshore platforms with a positive structural performance record (Lotsberg, 2013b). An example of a modern O&G platform is the North Rankin B platform shown in Figure 2.4.



Figure 2.4: North Rankin B offshore platform (FoundOcean, 2015)

## 2.3 Experimental testing – The Oil and Gas era

Once the tendency to employ different concepts and scales on GCs was fully adopted in marine structures, several experimental campaigns have been carried out the past decades to bridge the gap of knowledge. The planned installation of several platforms in the North Sea also pointed towards this direction. The objective was to isolate known factors that influence the performance of GCs the most and provide sufficient design guidance for plain pipe and shear-keyed GCs.

The first major test campaign received funding from the UK Department of Energy (DEn) and the findings were presented in a series of research papers (see, e.g., Billington and Lewis, 1978; Billington, 1980; Billington and Tebbet, 1982). At Wimpey laboratories a significant total of approximately 400 downscaled specimens – with varying geometrical characteristics, were tested under axial static loads. At the time, very limited experimental data were available on the design of GCs, thus several parameters required investigation. Some of the parameters that were studied within the tests, were the radial stiffness ( $D/t$ ) of pile and sleeve, the grout compressive strength ( $f_{cu}$ ), the overlap length ( $L_g/D_p$ ) and finally the steel surface roughness ( $C_s$ ). The overlap length is a non-dimensional parameter which was introduced to allow for comparison between specimens and is widely used to date to describe a GC.

To analyse the data and extract conclusions from these tests, the bond strength each GC exhibited was employed as an assessment measure. From the Wimpey laboratory tests, Billington (1980) proposed a linear analogy between the bond strength of plain pipe GCs and the compressive strength of the grout as per equation 2.1. This was further expanded in Billington and Lewis (1978), by suggesting a linear relationship between radial stiffness, shear key parameters and bond strength. It was also noted that a significant variation of the bond

strength is to be expected with piles of varying surface roughness. When piles with typical offshore surface-finish were used, the scatter on the test results was even more pronounced (Billington and Lewis, 1978).

$$f_{bu} \propto f_{cu}^{0.5} \quad 2.1$$

Nevertheless, following this pioneering experimental campaign the use of shear keys was highly recommended as the first questions and concerns on the performance of large-diameter connections were raised. The abovementioned tests were supplemented by fatigue tests on small scale axially-loaded GCs and the findings were presented in Billington and Tebbett (1982). Weld-beaded and plain pipe connections of 1:5 scale were examined, focusing on early and long-term fatigue life. This work was the first to investigate early age effects and the authors attempted to represent realistic offshore conditions. Those included grouting in upright position, depicting offshore conditions and loading at a frequency of 0.1 Hz, which represents wave actions. The test results indicated that plain pipe joints are less susceptible to fatigue when compared to joints with shear keys.

The rationale behind this finding was that the shear keys although contributing to bond strength, hinder the fatigue capacity due to grout crushing on the tip of the welded keys. Despite the significance of this study, these findings were based only on a few tested specimens, resulting in a very limited data pool. Additionally, the grouted length of plain and shear key connections was not identical, to accommodate limitations of the testing frame, thus the results between the two types were not directly comparable.

Following the detailed investigations led by the DEn, Karsan and Krahl (1984) and Krahl and Karsan (1985) also focused on the axial strength of GCs with shear keys. Based on their experiments and the Wimpey test data set they proposed a

new set of equations for the prediction of GC bond strength. Their hypothesis was that the connection's strength is driven by two components: a) the bond strength between grout and pile and b) the contribution of shear keys. The authors suggested that a high shear key ratio ( $h/s$ ) up to 0.1 can be beneficial to the resulting axial capacity. However, the authors did not support this argument by further physical testing. Their recommendations were subsequently included in the American Petroleum Institute (API) guidelines (API RP2A, 1984). At this point it is worth noting that the corresponding guidelines by DEn (1984) – based on the Wimpey laboratory tests – suggested limiting the ratio to  $h/s < 0.4$ . This particularly highlights the uncertainties that existed on the influence of shear keys.

In Forsyth and Tebbet (1988) shear key ratios were also the central focus. A series of GCs with  $h/s$  up to  $\sim 0.15$  were tested, aiming to examine the effect of closely spaced weld beads. The authors concluded that a limiting ratio for the connection exists, after which the ultimate strength does not increase anymore. However, it was suggested that this ratio is closely related with the radial stiffness of the GC geometry. For the examined configurations the highest strengths were reported for  $h/s = 0.075$ . The authors compared the experimental results with the API and DEn guidelines suggesting an increase in the DEn limit value for shear key ratios.

To further comprehend the effect of shear keys in GCs, Lamport (1988) focused on installation defects or tolerances that can occur in an offshore environment. Those included connections with misaligned pile and sleeve and shear keys, however the author states that no bond strength reduction was reported. Lamport and his co-workers (Lamport et al., 1991) also confirmed the findings by Aritenang et al. (1992) that the DEn formulation yields the best agreement with their experimental data.

Ingebritsen et al. (1991) developed an improved set of design equations for static limit states. The new design recommendations was the outcome of 202 tests on plain and weld-beaded specimens in scales of 1:3 and 1:5. The authors also performed some fatigue testing, however fatigue S-N curves were not developed, as the number of tests was not sufficient especially for fully-reversed loading conditions. To that extent the authors provided only some recommendations for the GCs under purely compressive cyclic loads. The ISO guidelines included the design recommendations which were based on the work carried out by Harwood et al. (1996). The equations were suggested following a review of 30 tests from the literature.

A synopsis of the effect of compressive strength on the bond strength of GCs is shown in Figure 2.5. Each data point represents a test and considering the scatter of results it is shown that the linear relationship between grout strength and bond strength is true only for lower strength materials up to 40 MPa.

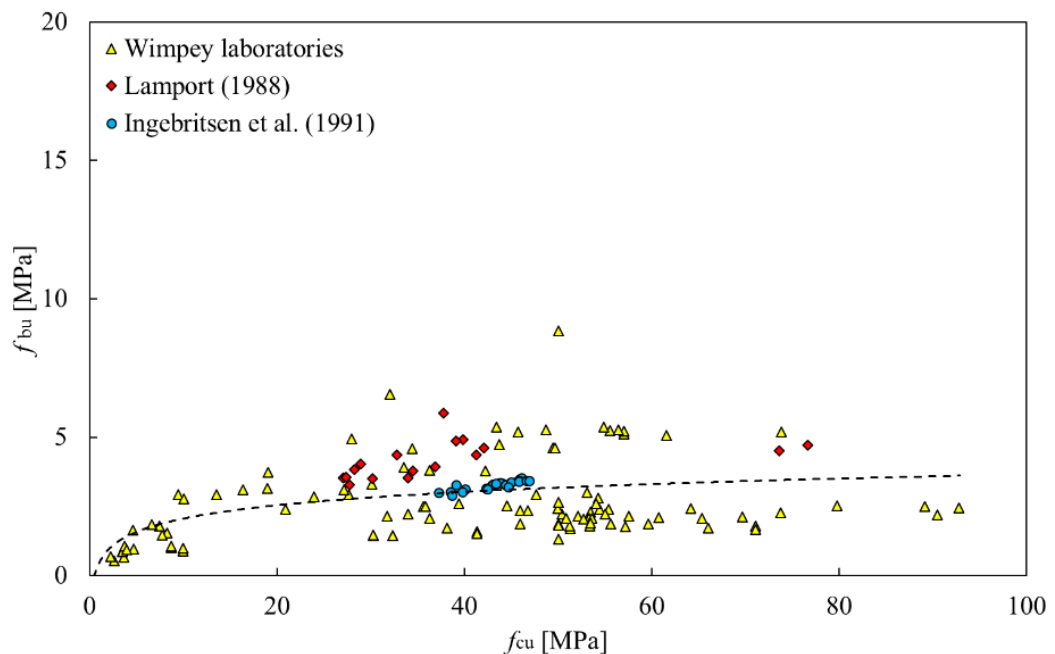


Figure 2.5: Effect of grout compressive strength to bond strength of axially-loaded GC with shear keys

## 2.4 Development of offshore wind turbines

The past two decades the field of OW has grown significantly and this is indicated by the installed capacity of OWTs in Figure 2.6. In the UK, the extent of this growth is estimated to result in 10% of the annual electricity consumption being produced from OW by 2020. One of the aspects that enable this development, is the significant reductions which are being achieved in capital costs. To quantify the cost of the required expenditure, the Levelised cost of Energy (LcoE) is commonly used as an indicator. LcoE is a normalised measure of expenditure so as to allow comparison between different energy sources. The goals that were set for OWTs in terms of LcoE have already been exceeded. This is noted in a report published by the Global Wind Energy Council (2016) stating that the LcoE has been reduced to a low point of £50/MWh, establishing OW as the most competitive energy source. To achieve such ambitious goals there has been significant developments in the manufacturing and installation processes which allowed for cost reduction. Moreover, considering that the potential of the sector is not yet fully exploited the future for OW is bright.

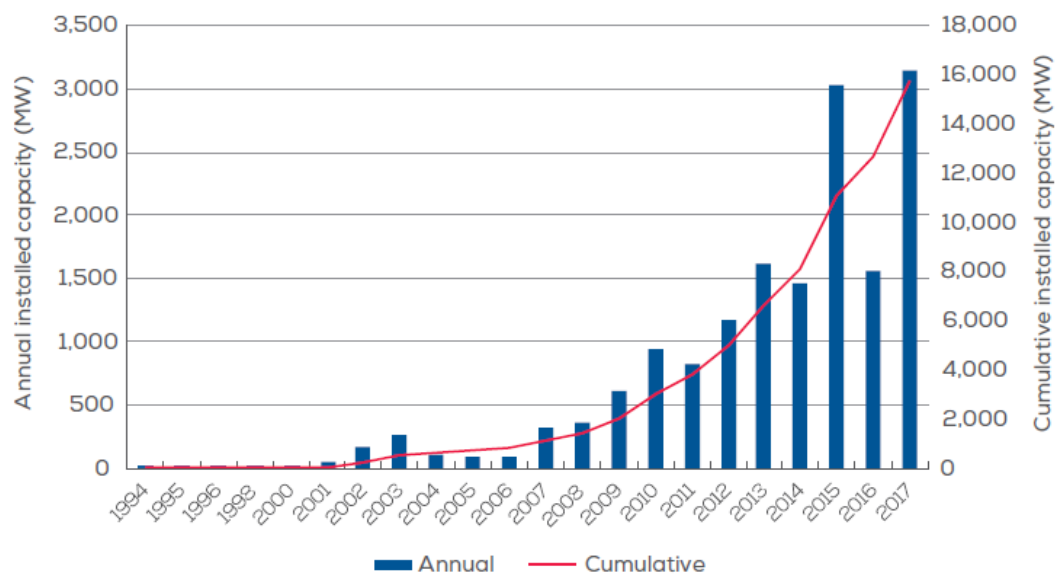


Figure 2.6: Annual and cumulative installed capacity from OWTs (WindEurope, 2017)

To enable further development and expansions an aspect that needs to be further improved is the structural performance and integrity of OWT substructures (Bocher et al. 2018). There are several aspects on OWT structures that require attention, and some may still be unknown. This is due to the majority of OWTs being in the early or middle stages of their lifetime (Martinez-Luengo et al., 2016).

Corrosion on the internal surfaces of monopiles, slippages occurring on GCs and weld integrity are some of the main issues related to the substructure performance (Offshore Renewable Energy, 2017). Thus, the reliability of OWTs can be significantly strengthened by reducing the uncertainty introduced by such issues. Future failures could be avoided with the realisation of maintenance and monitoring tools. On offshore structures, monitoring tools require some special consideration due to the remote location and environmental factors inducing further challenges when it comes to the development of such tools.

## 2.5 Offshore wind turbine substructures

The UK has established itself as the world leader in the installed capacity of OW generators (see Figure 2.7a), with approximately 1900 turbines operating in 37 wind farms (RenewableUK, 2018). Across Europe a variety of fixed and recently floating support structures are used to support the rotor-nacelle assembly (Higgins and Foley, 2014). The main OWT types which are installed in Europe are identified in Figure 2.7b. The breakdown of the installed substructures shown in Figure 2.7b, reveals that the majority of OWTs are installed on top of monopile substructures, although recently there has been an attempt to increase jackets and tripods. Tripods and jacket substructures differ slightly in terms of installation from monopiles. The distinction is that the joint can be either post-piled or pre-piled. Hence, piles are driven in the seabed prior to installation of the substructure or afterwards (DNV ST-0126, 2016; Bechtel, 2017). For consistency

purposes, throughout this thesis the notation shown in Figure 2.8 will be followed.

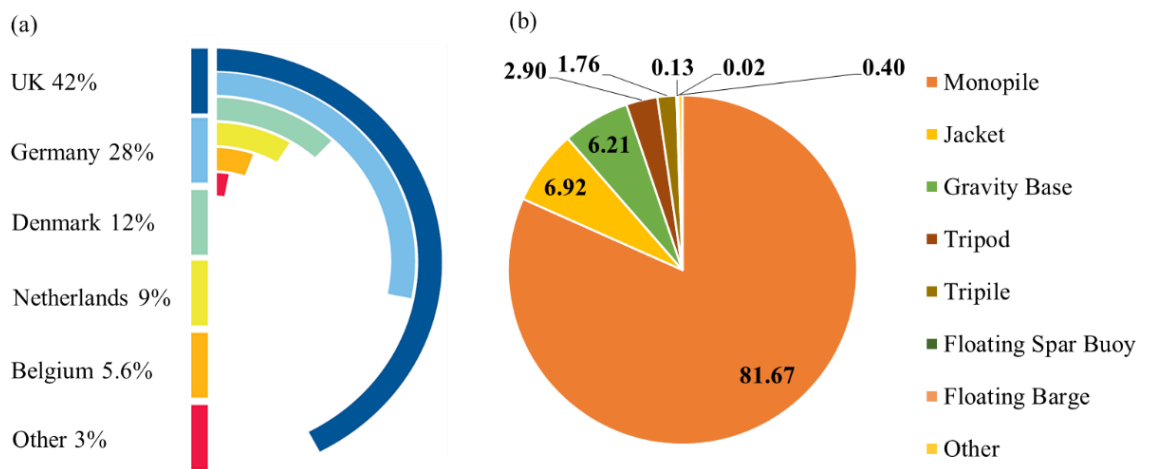


Figure 2.7: Breakdown of a) installed capacity of OWTs, b) installed substructures in Europe (Redrawn from WindEurope, 2017)

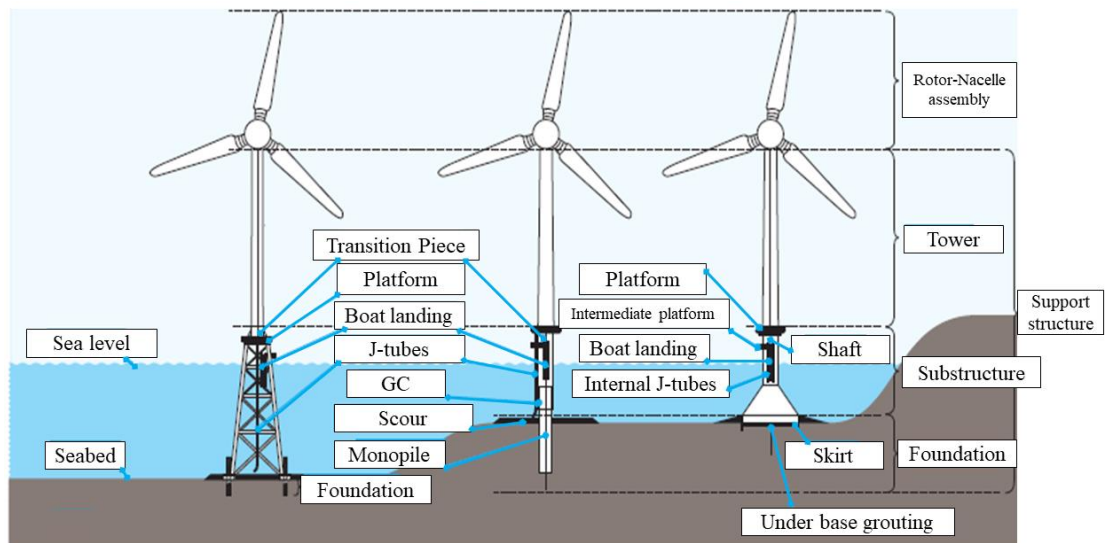


Figure 2.8: Most common types of substructures used to-date within the OW sector and notation (After DNV ST-0126, 2016)

The monopile is often selected due to design simplicity and its water depth applicability. The nominal depth of a monopile installation can reach up to 40 m, where their installation is favourable due to economic feasibility (WindEurope, 2017). Their popularity can be easily appreciated if one considers that the average

water depth of the currently installed structures for 2017 was 27.5 m, which is an ideal condition for monopiles (WindEurope, 2017). Additionally, there is an enhanced manufacturing capacity for single large diameter piles when compared to jackets. The piles can be fabricated using a rolling process for flat steel sheets and longitudinal welds are applied to form the tubular by attaching two halves together (Bocher et al., 2018). The end-products are designed and manufactured with varying diameter to thickness ratios based on soil and seabed characteristics. Some typical dimensions are shown in Figure 2.9.

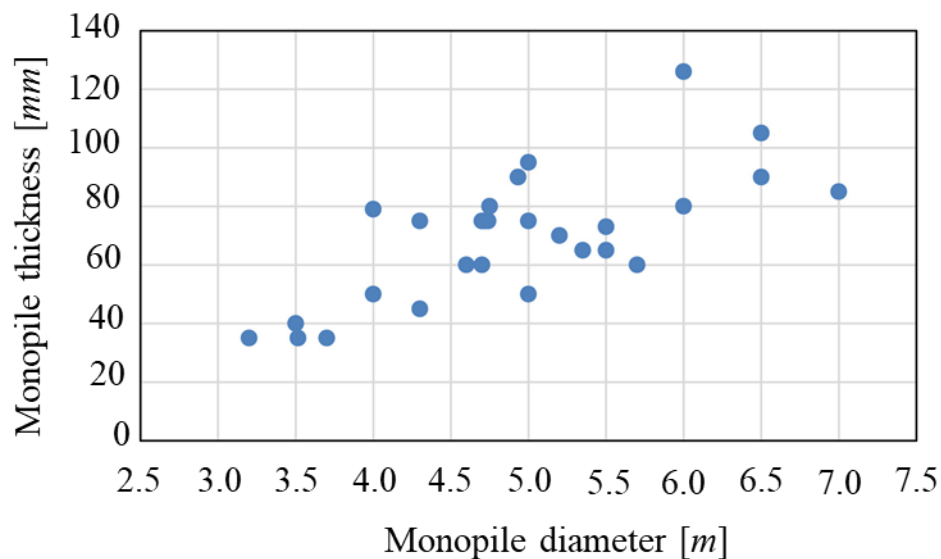


Figure 2.9: Diameter and thickness data from offshore monopile across Europe (Bocher et al., 2018). [Reprinted from Ocean Engineering, Vol 160, Bocher et al., 2018, New shape function solutions for fracture mechanics analysis of offshore wind turbine monopile foundations. Pages No. 264-275, Copyright (2018), with permission from Elsevier]

GCs on OWT substructures have been employed since the installation of the first wind farms at the onset of the current century. Initially bolted-flange joints were considered for the substructures in Blyth and Scroby sands (Golightly, 2016), however the cost of those was significantly higher compared to grouted solutions and the installation was more demanding and time consuming. The first grouted monopiles which were installed, are located in Sweden for the Utgrunden I wind

farm and had an external diameter of three meters (4Coffshore, 2018). Taking into account that monopiles of 7 m in diameter are installed the rapid upscaling and development can be easily appreciated. The installation of a typical TP for a monopile substructure is shown in Figure 2.10.



Figure 2.10: Installation of monopile transition piece with platform and appurtenances in Anholt, Denmark (Photo source: Ramboll, 2017)

Nowadays, as the capacity of generators increases, remote sites are investigated and water depth can impose limitations for conventional monopiles. Thus, the application of XL-monopiles increases in popularity compared to jackets. The preference for those large-diameter monopiles is justified by the manufacturing capabilities and economic advantage gained during the wind farm design. This was the case for two wind farms, namely Nordsee I and Gennaker, for which the initial plan included jacket substructures which were subsequently replaced by large diameter monopiles.

## 2.6 Materials and construction

The construction of the grouted joints in the O&G and OW industries is based on the same structural concept and the use of cementitious-based grouts is

customary. The experimental work that was carried out for O&G structures established a solid foundation for the design of GCs. However, the existing knowledge basis reflects on the characteristics of the O&G structures rather than the unique monopile features. In the early days of OWTs these differences have not been considered. Some of the main differences are radial stiffness and grout compressive strength.

For example, since the onset of the OW industry, the annuli between the monopile and TP is by default filled with cement-based grouts of ultra high compressive strength. In the Horns Rev I wind farm, which is one of the first large OW sites, TPs were grouted with the UHPG Ducorit® D4, which has a strength of  $f_{cu} \sim 205 \text{ MPa}$  (Densit, 2002).

The first OW TPs were mounted on plain pipe steel tubes. It was considered that a material with an excessively high-strength could alleviate any concerns for degradation during the life time of the substructure (Nielsen, 2007). Moreover, shear keys were not employed, as initial experimental work in Aalborg, Denmark, revealed that plain pipe connections can offer sufficient performance (Andersen and Petersen, 2004). However, it should be noted that shear keys entail an additional fabrication cost which increase the initial capital expenditure (CAPEX) significantly.

In the relevant literature cementitious materials which are primarily used in the construction of joints for OWTs are referred to as UHPGs, High-Strength Grouts (HSGs), Ultra-High-Strength Grouts (UHSGs) and Ultra-High-Performance-Cementitious (UHPC) material. In this work these terms will be used interchangeably and will always refer to cementitious-based material employed in OWTs nowadays with a nominal compressive strength of at least  $90 \text{ MPa}$ .

## 2.6.1 Ultra-High-Performance-Grout (UHPG)

Compared to conventional concrete, UHPGs are of much higher compressive strength which typically ranges from 90 to 200 *MPa*. Some of the main characteristics of those materials, which are specifically designed and certified for offshore use, are the rapid gain of strength and also the higher tensile strength. A typical tensile strength of an offshore UHPGs is around 8 *MPa*.

If one examines these materials from a microscopic point of view, their microstructure is much more compact than typical concrete (Fehling et al., 2014). This dense formation is a result of the use of superplasticizers, which allow for a congestion of fine particles within the matrix. Consequently, a water to cement ratio ( $w/c$ ) as low as 0.2 can be achieved (Fehling et al., 2014). This microstructural content difference is illustrated in the schematic of Figure 2.11.

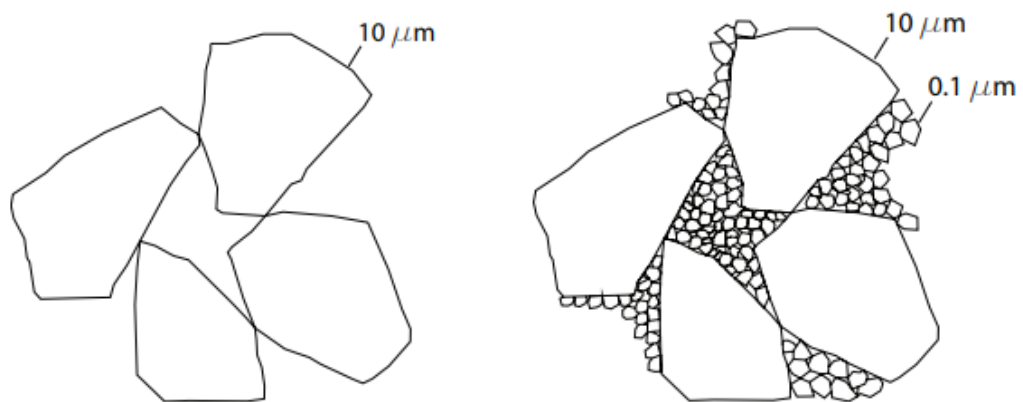


Figure 2.11: Microstructural viewpoint of cement (left) and cement with fine particles (right) (Dorph and Sipavicious, 2010, Original figure from Bache, 1995)

Different types of particles are mixed together such as sand, quartz powder or silica fume to achieve the optimum synthesis (Wilke, 2013; Fehling et al., 2014; Bechtel, 2017). This concept leads to an end-material with excellent flowability, while the compressive strength is magnified. The flowability is without doubt one of the most critical attributes of such material, as visibility of the grouting

process is very limited and installation relies on experience and pre-calculated volumes of material (Jefferis, 2003). Furthermore, it can affect the grout overflow when the GC is located underwater and mixing with water is inevitable. This alteration in the “anatomy” of the material’s matrix has an effect on the cracking behaviour. In UHSGs the cracks initiate and develop through the matrix without being affected by the presence of aggregates as illustrated in Figure 2.12. This is mainly due to their fine size and the materials homogeneity. Nevertheless, considering the behaviour of the material macroscopically again, it explains the abrupt brittle nature when compared to conventional concrete.

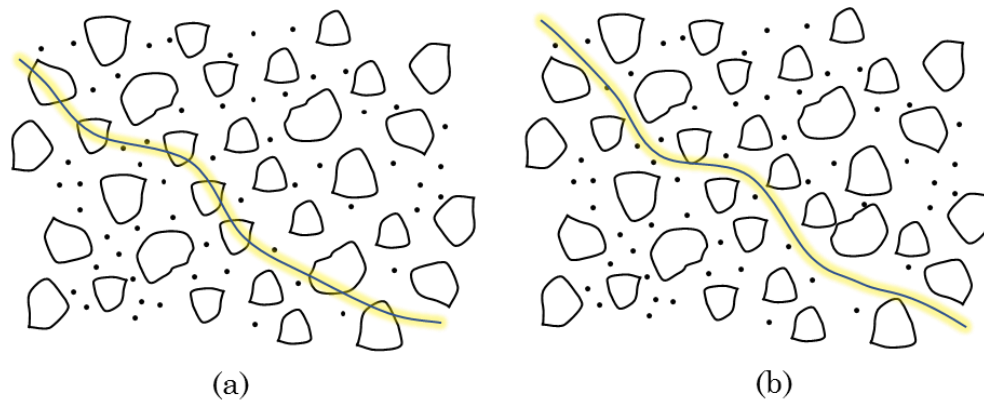


Figure 2.12: Cracking within a) UHSG and b) normal concrete matrix

In O&G platforms the use of HSGs or even UHSGs was not as common. Typically, the compressive strength up of such grouts could reach 80 MPa. Billington and Lewis (1980) discussed the use of cementitious-based grouts with additives or high-alumina cement, but both choices were questioned as concerns for long-term corrosion were raised. Nowadays, the internal microstructure addresses effectively corrosion issues in a way that such issues are no longer a concern in the long-term performance of the infill material (Fehling et al., 2014).

## 2.7 Tubular grouted connections

GCs on monopiles experience a complex regime which are the result of the

combined environmental loads resulting from the action of winds, waves and currents, operational loads from the rotor and blades along with deadloads (Jensen et al., 2011; Tziavos et al., 2016). The environmental loads cause overturning bending moments of different directions which are of greater magnitudes than axial loads (Schaumman et al., 2010; Lotsberg, 2013; Tziavos et al., 2018). In Dallyn et al. (2016) it is mentioned that the ratio of moment to axial force is four times higher than the one O&G joints are experiencing. These alternating moments cause wear and ovalisation-induced cracks which lead to slippages (Lee et al., 2014; Dallyn et al., 2017).

In Figure 2.13 the load-transfer mechanisms that take place in a typical cylindrical-shaped joint are illustrated. GCs are responsible to withstand the aforementioned conditions and provide sufficient capacity (Lotsberg, 2013). The connection acts as a moment-transfer mechanism between the steel piles (DNV-ST-0126, 2016). Bending on the GC translates to contact forces across the TP in the opposing top and bottom ends of the joint and shear forces in the interfaces. Several components contribute to the load transfer mechanism and can be classified to contact pressure, frictional resistance either horizontally or vertically and finally the shear key load contribution. It is the contact pressure that induces high tensile stresses on the grout when large moments occur, which leads to radial cracks of the grout infill (Lotsberg, 2013).

The joint's role in the structure is deployed once relatively small displacements take place (Dallyn et al., 2016). Such small movements are expected in offshore conditions and trigger the transfer mechanism. For those movements to take place the shear resistance due to fabrication tolerances and the adhesion between grout and steel needs to be exceeded. Although, this initiation mechanism is expected, it may potentially cause grout crushing in front of shear keys and could potentially lead to wear at the interface. This is one of the reasons why shear keys

have been questioned initially from a fatigue point of view in previous studies and whether their size should be kept to a minimum (see, e.g., Billington and Tebbet, 1982, Andersen and Petersen, 2004).

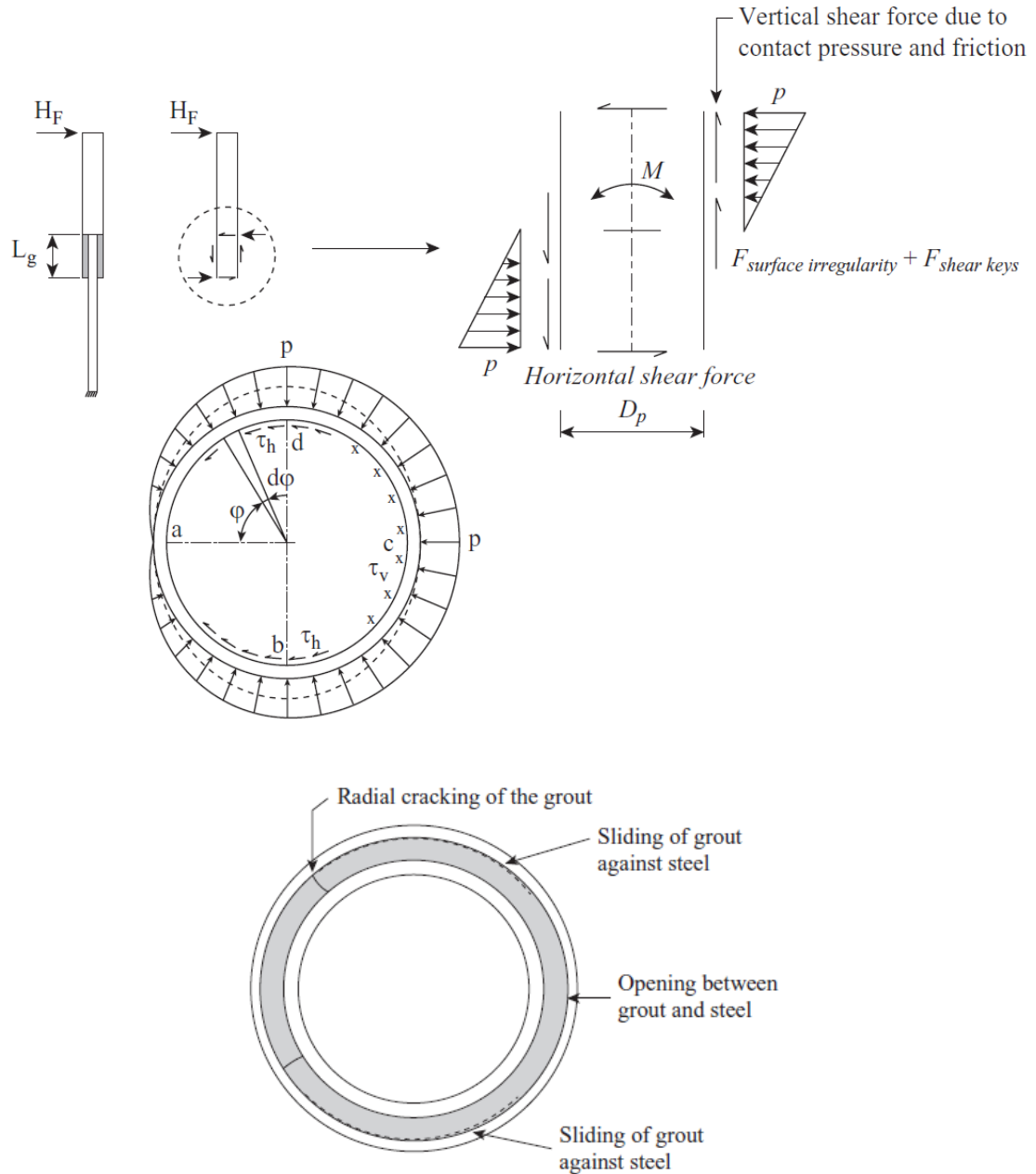


Figure 2.13: Force transfer mechanism in a GC under bending moment (Lotsberg, 2013). Top figure illustrates the contact pair of opposing contact forces on the sides of the GC and bottom figure the gaps and cracks on a GC. [Reprinted from Marine Structures, Vol 32, Lotsberg, I., Structural mechanics of grouted connections Pages No. 113-135, Copyright (2018), with permission from Elsevier]

Eventually, the large bending moments in combination with the high ratios of diameter to thickness one finds in monopiles, lead to gaps at the interface once the slip strength is exceeded. These gaps can grow significantly along the length, which subsequently results in a shear key pair being inactive. (Figure 2.13). Hence, on newer monopiles shear keys are installed in the middle region of the  $L_g$  to avoid the developed gap.

## 2.8 Settlements and failure modes

As of September 2009, the routine inspections that took place on monopile substructures revealed several TPs sliding of up to 90 *mm* against the foundation pile (see, e.g., Lotsberg, 2013; Dallyn et al., 2015; Dallyn et al., 2016; Tziavos et al., 2016). Following the examination of almost 1000 monopiles in various European wind farms (see, e.g., Kentish Flats and Horns Rev I wind farms), approximately 700 were found to have experienced significant slippages. Moreover, significant gaps between the grout and steel were found at the top of the joint and on some monopiles water ingress was obvious (Dallyn et al., 2016; Brett et al., 2018). Thereinafter, reports urgently requested the re-assessment of the design practice for GCs on monopile OWTs, raising concerns on their axial and bending capacity. Estimates of the retrofitting work that followed and involved additional steel brackets or bearings, suggest that the cost for each turbine was in excess of £100,000 (Muller, 2017) inflating the CAPEX of the substructures. Nevertheless, such retrofitting measures are meant to be temporary measures and do not replace the role of the joint.

It was soon appreciated that the design practice calls for reconsideration of several factors, amongst which, the scale effects that are introduced in typical monopiles. Additionally, due to the basis of GC design being out-dated and the groundwork was undertaken for O&Gs structures that experienced different

conditions, geometric limits required revision as the existing were intended for different purposes. More specifically, the load-transfer mechanism differs from a typical subsea structure which is designed for axial loads. Here, it is worth mentioning that in Germany, which has the second largest installed capacity of OW generators, a case by case certification specifically for GCs is necessary until today (Schaumann et al., 2013). This is due to the lack of codified design approaches and absence of extensive knowledge on the UHPG behaviour.

Prior to these failures ISO 19902 (2007) was the industry standard that was mostly followed for the design of monopiles, which was developed in the 90s. Of interest is the fact that the design recommendations suggested that cyclic bending moments on the structure due to the environmental loading do not imply that a fatigue assessment of the connection is required. Hence, abrasive wear and cyclic degradation of the grout were not considered in early designs (Nielsen, 2007). As already mentioned, the consensus was that the high compressive strength of an UHPG will compensate for all the concerns. Therefore, this justifies why the use of high and ultra-high-strength grouts became a common convention since the onset of OWTs.

Summarising, understanding the behaviour of GCs is of great importance in order to address the issues related to their performance. The complexity of the factors affecting the connection is the reason why further research towards this direction is required in order to achieve deeper understanding on the behaviour of the pile to sleeve GCs. Hence, this work intends to investigate the mechanisms occurring in GCs under bending loads and offer further insight, to improve the current engineering practice and monitoring methods used for such connections.

## 2.9 Experimental testing – The Offshore Wind era

The first experimental campaign on GCs for OWTs dates back to 2004 and took place in Aalborg, Denmark. The tests were used as a verification study for the design of the Horns Rev 1 monopiles Andersen and Petersen (2004) provide some details on the specimens and loading protocols that were used in this experimental campaign. The authors noted that following the tests plain pipe connections can suffice the offshore load regime.

Once the settlements were reported in 2009 and owing to the urgency of the events, a Joint Industrial Project (JIP) (DNV 1053, 2010) was launched to investigate the causes and propose alternative solutions. The outcome of this work was the conical TPs to replace the tubular plain-pipe GCs. A small inclination of the TP (up to 3°) could minimise slippages in future monopile installations. This method was included in the offshore standard published by DNV (DNV OS-J101, 2011) where the use of cylindrical plain GCs has been discouraged. It should be noted that the use of shear keys is not allowed for conical GCs. Following the first research initiative, JIP II was put in order to investigate the use of shear keys as an alternative (DNV 0371, 2012). A typical arrangement of a monopile GC with square-shaped shear keys arranged across the middle third of the grouted length is shown in Figure 2.14.

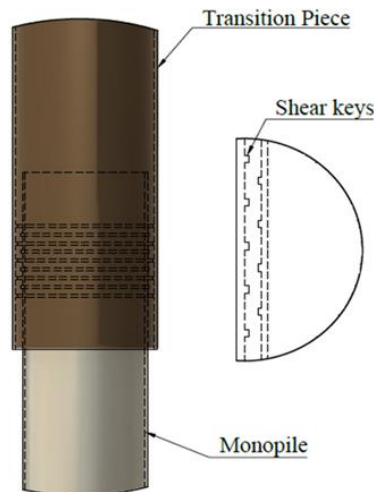


Figure 2.14: Monopile GC with centrally-located shear keys

JIP II results derived from tests on box-shaped joints and those were used as a basis for a new design guidance for tubular connections with shear keys. The methodology was implemented in DNV OS-J101 (2014) superseding the design of plain pipes. This test campaign was the first one to employ an alternative design concept. The box-shaped connections were designed to represent the equivalent radial stiffness of a cylindrical one and aimed at alleviating scale effects induced by laboratory requirements. However, box GCs were found to withstand higher loads and different failure mechanisms within the core were reported. This is also noted by Chen et al. (2018) that testing of GCs should ideally be carried out on cylindrical specimens.

At the same time, research studies carried out by Schaumann and his co-workers (Schaumann and Wilke, 2007; Schaumann et al., 2010) revealed that significant gain is achieved by using shear keys in the middle third of the grouting length. This was originally suggested in the early days of GCs by Billington and Lewis (1978) pronouncing the systemic error to not include shear keys originally in the design of OWT joints. In another study, Anders and Lohaus (2008) investigated grout fillings with steel fibres which had a positive impact on the axial capacity

of small-scale GCs. However, reinforced cementitious UHPG have not grown in popularity over the years due to the uncertainties introduced in the mixing and grouting procedures.

Driven by the lack of knowledge on the effect of bending on the axial capacity of GC, Wilke (2013) carried out four-point bending tests on cylindrical joints. The use of shear keys was primarily investigated in small scale axially-loaded specimens proving advantageous. Consequently, a plain-pipe and a shear-keyed GC of larger scale were tested and compared to consolidate the argument that shear keys are beneficial to the performance of GCs.

The axial capacity of five cylindrical specimens was investigated by Lee et al. (2017) with respect to eccentric application of the load. When compared to concentric loading conditions no influence on the bond strength has been found for the presented axial configuration. To reduce the cost of fully cylindrical specimens Wang et al. (2017) performed axial strength tests on GC segments following the same approach as used during JIP I and JIP II where box GCs were employed. The argument in favour of the box specimens was that the radial stiffness of scaled cylindrical GC is too high when compared to the segmented-type of joint due to scale effects. However, when fatigue behaviour is of interest the radial stiffness and confinement levels of the grout still remain questionable.

In order to summarise the existing test data to date, in Figure 2.15 the resulting bond strength from recent axially-loaded static tests are summarised along with experimental results from older O&G joints. Each data point represents a test aiming to highlight the difference in material strength. The data include only GCs with shear keys. The interpretation of these data requires diligence and the increased bond strength should not necessarily be attributed only to material enhancements. This is because the radial stiffness of each specimen was not considered in the figure in order for the results to be directly comparable.

However, considering the tests on OWT connections the scatter is considerably higher for joints formed by higher compressive strength material.

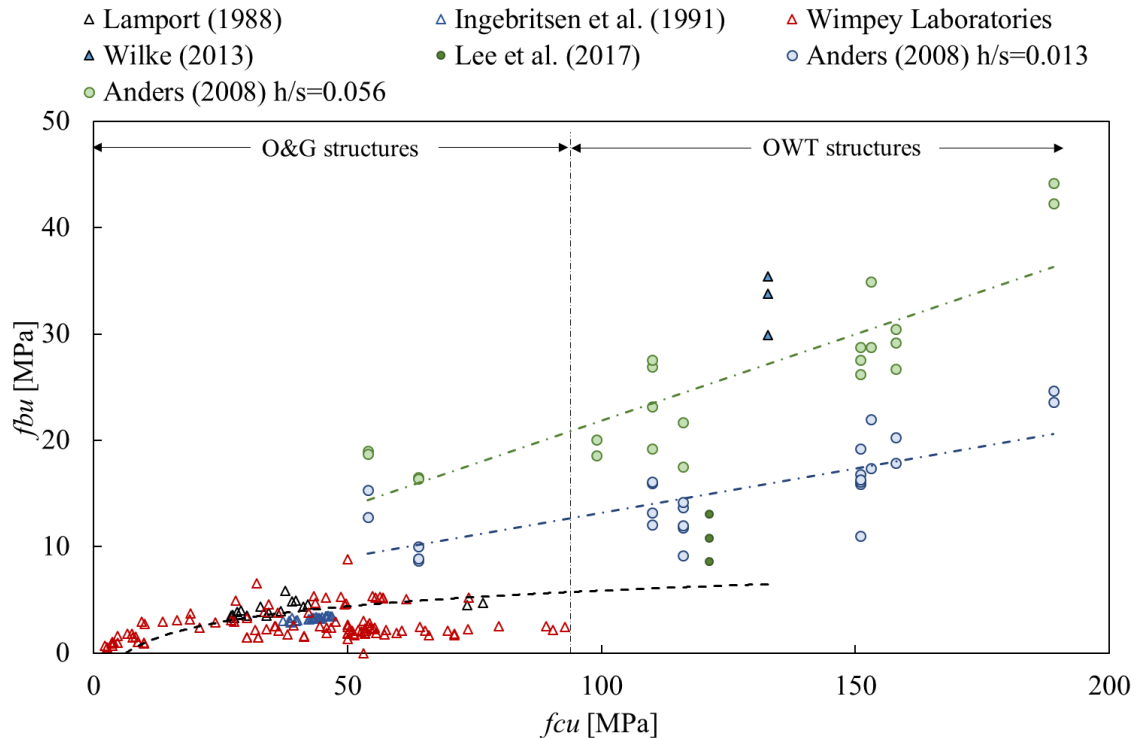


Figure 2.15: Bond strength comparison of GC specimens for different applications

The axial performance under fatigue loads is discussed in Johansen et al. (2018) on GCs formed by lower strength material. The authors noted that there are no evidence to justify the use of UHPGs to date and the benefits of such a solution are questionable. The use of materials of high-strength has also been questioned by researchers in the past (e.g., Wilke, 2013), however there are not enough data yet to support that normal strength media can be used to replace UHPGs. On the contrary the drawbacks of using conventional material such as ordinary Portland cement is the early age cracking that takes place during hardening at higher temperatures and the hydration levels. It is the author's opinion that cracking would be even more pronounced for a GC owing to the high temperature gradients induced by the annulus length or thickness, particularly if a jacket joint is casted. Also, the flowability and hydration levels that UHPG exhibits are far

more superior than ordinary concrete.

Chen et al. (2018) carried out fatigue bending tests on cylindrical GCs. The specimens survived 2 million cycles without any notable degradation of the grout. The only notable defect on the test specimens was interface gaps. In Table 2.1 a summary of the key test parameters of the experimental tests that have been performed to date is given.

Table 2.1: Summary of experimental tests on GCs for OWTs

Source	Loading	Geometry	GCs	F <sub>o</sub>	f <sub>cm</sub> [MPa]
Schaumann et al. (2010)	Bending-F, S	Cylindrical	5	1-1.3	<130
Wilke (2013)	Bending-F, S	Cylindrical	2	1.3	130
Wang et al. (2017)	Axial-S	Segmental	9	n/a	90
Lee et al. (2017)	Axial-S	Cylindrical	5	1-2	~120
Johansen et al. (2018)	Axial-F	Segmental	4	n/a	~60
Chen et al. (2018)	Bending-F	Cylindrical	5	1.4-1.8	~110
Marion et al. (2018)	Bending-F	Segmental	12	n/a	74.5

\*F: Fatigue, S: Static

Considering the installed GCs nowadays, the expected growth and the cost of the sector it is apparent that the amount of research data that are available in the literature are scarce. This is even more pronounced if the number of parameters that affect the performance of a joint is considered.

In recent research studies other aspects relevant with GC conditions and failures have been tested. Dallyn and his co-workers aimed at quantifying the long-term wear rates under different ambient conditions. Water influence was found to be detrimental as wear rates are accelerated with its presence. A numerical model

was also developed to predict wear rates (Dallyn et al., 2017). The model was developed as a case study based on wind data from a wind farm. Water ingress was the core of the study by Schaumann et al. (2016). The specimens were mainly subjected in compression-only cyclic load, however a significantly reduced capacity of the specimens that the grout core was exposed to water was reported. The latter was primarily observed by Sørensen (2011) who compared the fatigue performance of cylindrical UHPG samples in wet and dry ambient conditions but back then water was not considered critical in the design process.

## 2.10 Numerical computations

A promising alternative to physical modelling is the use of numerical methods such as the FE method. The past decades significant progress has been made in commercial FE software and computational capabilities, making numerical modelling a feasible and approachable alternative. A principal advantage of numerical techniques is the ability to extensively investigate a large number of parameters and thus alleviate the expenses of physical testing. Particularly for GCs this is of great significance, if one considers the size of real-scale specimens and the series of tasks that ought to be carried out for specimen preparation prior to conducting a comprehensive test campaign. Moreover, it offers enhanced post-processing and visualisation capabilities, which are not possible using conventional laboratory equipment and visual inspections.

A variety of commercial FE software have been employed during the past decades as a medium to enhance and expand the results of experimental studies. Numerical models have proven to be very robust and accurate when compared to experimental results in a series of applications. In the following section the research advances made in the field of GCs are presented chronologically. Theoretical aspects along with specialised topics on FE models which were

employed in the context of this thesis will be presented in more detail in Chapter 4.

## 2.11 Numerical modelling of grouted connections

In the early 80s, Chilvers (1984) undertook numerical work to analyse the parameters involved in the design of GCs. When it comes to offshore joints this study was one of the first to appreciate the scale effects between laboratory downscaled specimens and real structures. The authors focused on the grout-steel interface and introduced a friction element with springs to model the bond slip. Finally, it was claimed that square shear keys might be beneficial compared to the semi-circular weld-beads, but this was not supported by experiments.

Numerical studies were also conducted by Elnashai and Aritenang (1991) concluding that height and spacing of shear keys should not be one parameter as they yield different results. A similar conclusion was extracted by Chilvers (1984), suggesting the reduction of spacing might have a larger impact on bond strength than shear key height. Finally, it was concluded that radial stiffness should be included in API guidelines and that the DEn should also include a parameter that accounts for shear key height in its recommendations. The analytical work by Elnashai and Dowling (1991) also acknowledged the importance of the radial stress states experienced by the grout and stressed that many of the GCs are designed outside the proposed limits and without adhering to the recommendations. Aritenang et al. (1992) supplemented the numerical work presented in Elnashai and Aritenang (1991) by developing an analytical model to predict the bond strength of GCs. An interesting finding was that the pile thickness had minimal effect on the ultimate strength of the connections.

Once the application of GCs received increased popularity on OWTs, the first attempt to provide guidance on FE modelling of GCs is presented in a short

review by Nielsen (2007). The author reviewed the different material models for cementitious material and contact schemes available in the most commonly used commercial FE software for the analysis of GCs, Ansys (Ansys, 2013) and Abaqus (Abaqus, 2013). An important aspect is that the grout integrity due to cyclic loading was not considered to be of major concern and that using HSGs would compensate for those actions. This explains why for OWTs the use of higher compressive strength material was adopted since 2000s. The inclusion of shear keys was not of concern in this review paper as the installation of plain pipe GCs was the standard engineering practice in the early days. In a similar review, Prakhya et al. (2012) discussed the design equations provided by DNV for plain joints and proposed a simplified analytical model for the moment transfer mechanism.

The bending tests for Horns Rev wind farm were modelled using the Drucker-Prager (DP) model in Andersen and Petersen (2004). In this study a friction coefficient of 0.4 was used to model the steel-grout interfaces. The use of DP model was later questioned by Schaumann and Wilke (2006) due to not being able to represent the grout behaviour sufficiently. However, it was acknowledged that when the global behaviour is of interest DP can yield sufficient accuracy. Gjersoe et al. (2011) focused on the interfacial behaviour and how this contributes to damage in the grout core. To avoid cracking or crushing of grout packers were proposed to increase the confining pressure on the grout. As in earlier studies only plain pipes were considered as the use of shear keys has not been implemented yet.

Following the discontinuation of tubular plain-pipe connections, studies by Löhning and Muurholm (2013) and Fehling et al. (2013) discussed the concept of shear keys on GCs and how their numerical representation could be achieved. The focal point of these studies was the computational cost induced by the

increased element numbers. Additional elements are inevitable when shear keys are included in a GC model due to their relatively small size when compared to the model's dimensions. In typical laboratory-scaled specimens shear keys are usually of few millimetres in size. Particularly, when solid elements are used this results in a significantly denser mesh to achieve the required curvature in the geometries. Löhning and Muurholm (2013) suggested that springs elements can be used diagonally or vertically to represent the shear key role.

Springs were also employed by Wilke (2013) instead of shear keys. The approach was compared to solid-elements and the reduction in computational cost was considered of benefit. However, spring elements entail uncertainty levels due to unknown properties and also the local stresses around shear keys are not modelled. This translates that the calibration of the spring stiffness with experimental data is a necessity. The author believes that sound engineering practice is needed when the approach is elected. Wilke (2013) also suggested careful implementation due to interface openings occurring. This is because of the extent of gaps formed in bending on monopiles. Inspections, experiments and numerical models have shown that opening at the interface can occur significantly across the length of the GC.

Löhning et al. (2013) employed the Concrete Damage Plasticity (CDP) model to simulate the grout behaviour of a plain GC. The CDP model is primarily used to model brittle cementitious material and is included in the commercial FE suite Abaqus (Abaqus, 2013). The FE study focused on the interaction of bending and axial loads, however the model was only calibrated against an axially-loaded small scale GC without considering scale effects and differences between the experimental and numerical set-up.

The computational requirements along with the degree of accuracy of the results are affected from the constitutive material models. For HSGs effective modelling

requires the inclusion of cracking and crushing behaviour. For example, earlier approaches (Wilke, 2013) slightly overestimated owing to the softening behaviour of the grout being suppressed.

Considering the research work to date, it is easily comprehended that the drivers for an accurate numerical representation of a GC, are the material behaviour of the grout along with the interface modelling, particularly focusing on the shear keys. The combination of the aforementioned requirements makes modelling of GCs a complex process taking into consideration the significant computational effort that is required. Nowadays, there is a lack of comprehensive numerical studies, which investigate validated models against a range of experimental data focusing on the behaviour of GCs with shear keys. FE modelling of GCs can be of remarkable benefit in the design process. It can provide visualisation insights on the grout condition as well as the load transfer mechanisms taking place in the connection. Furthermore, it allows for extensive parametric investigations which are prohibited in laboratories due to cost requirements.

## 2.12 Standard codes

From the reviewed literature it can be noted that geometrical parameters influence the capacity of the joint significantly. For monopiles this can be even more pronounced due to large slenderness ratios. Reference to the current limits of validity for GCs on OWTs as those are dictated from various standard codes is made in Table 2.2.

Table 2.2: Recommendations for geometrical limits for offshore GCs

Parameter	DNV <sup>1</sup>	Norsok <sup>2</sup>	ISO <sup>3</sup>
$D_p/t_p$	20-60	20-40	20-40

$D_s/t_s$	18-140	30-140	30-140
$D_g/t_g$	n/a	10-45	10-45
$f_{cu}$ [MPa]	n/a	20-80	20-80
$h/s$	$\leq 0.1$	$\leq 0.1$	$< 0.1$
$F_o$	1.5-2.5	n/a	1.5-3.0
$w/h$	1.5-3.0	n/a	n/a
$k$	$\leq 0.02$	0.02	n/a
$s$	$\geq \min \left( \frac{0.8 \sqrt{R_p t_p}}{0.8 \sqrt{R_s t_s}} \right)$	n/a	n/a
$h/D_p$	n/a	$\leq 0.012$	n/a
$D_p/s$	n/a	$\leq 16$	n/a

<sup>1</sup>DNV-ST-0126 (2016), <sup>2</sup>Norsok N-004 (2013), <sup>3</sup>ISO 19902 (2014)

Arany et al. (2017) collected diameter to thickness ratios from installed offshore monopiles in European wind farms. Maximum and minimum ratios which are met in those installed in the UK (Arany et al., 2017) are illustrated in Figure 2.16. Considering the recommendations provided by standard codes, it is easily admitted that many of those substructures lie outside their limits of validity. Along with the current trends to increase the size of the monopile diameters to accommodate larger turbines, it is apparent that the codified limits are not covering the engineering practice within the OW sector. Within an offshore wind farm variable ratio can be found due to varying depths or soil conditions.

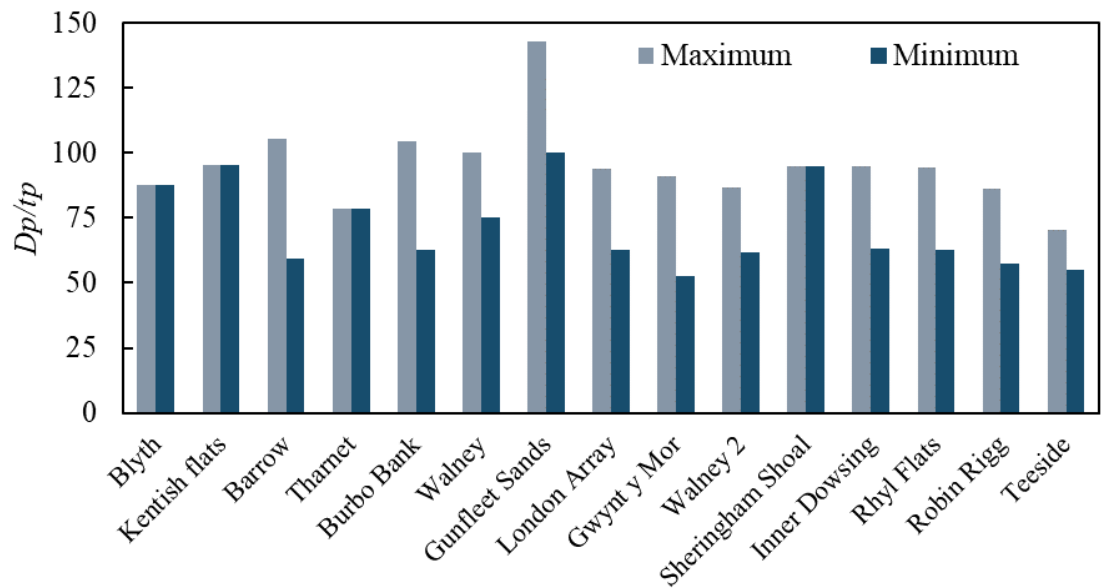


Figure 2.16: Diameter to thickness ratio of monopiles for UK wind farm [Data extracted from Arany et al. (2017)]

The limits of application for GCs which are given in present guidelines are the result of the ongoing research on GCs that originates back to the O&G years. From the beginning of OW, very little changes have been implemented in geometrical attributes even though there have been several re-considerations of the design approaches. The chronological development of each standard code is depicted in Table 2.3 with the focus being on GCs for offshore structures. Re-evaluation of design methods usually occurred once an alarming event took place or the need for further development emerged. These events and research findings that triggered changes are presented in the motivation tab.

Table 2.3: Evolution of standard codes focusing on GCs (Tziavos et al., 2016)

	1970s	1980s	1990s	2000s	2010s
<i>Design Basis</i>	Design for GCs is based on <sup>1</sup> API	Oil & Gas <sup>4</sup> DEn	<sup>4</sup> DEn, <sup>10</sup> API, <sup>11</sup> DNV	OWTs	<sup>23</sup> ISO, <sup>24</sup> DNV, <sup>15</sup> API
<i>Motivation</i>	<p><sup>1</sup>Unsatisfactory design recommendations for GCs with Shear Keys</p> <p><sup>1</sup>Based on small-diameter GCs</p> <p><sup>1</sup>Lack of guidance on the capacity of GCs with Shear Keys</p>	<p>Reconsideration of <sup>1</sup>API</p> <p><sup>5,6</sup>New Design process for API code on GCs</p> <p><sup>8</sup>Development of DNV code for fixed offshore structures</p>	<p><sup>12</sup>Assessment of the existing design equations</p> <p>Development of <sup>14</sup>ISO standard code for offshore structures</p>	<p>2000: Design phase of Horns Rev I Wind Farm</p> <p>2009: Slippage of TP in several OWTs</p> <p>Lack of large scale testing and effect of bending moments remain unknown</p>	<p><sup>29, 31</sup>Effect of wet conditions is unclear</p> <p><sup>17, 20</sup>Bending moments are of significance and are introduced in the testing procedure</p>
<i>Action</i>	<p><sup>2, 3</sup>Experimental testing on axial capacity of GCs at Wimpey Laboratory, UK</p>	<p><sup>7</sup>Analytical model for GCs with Shear Keys under axial loading</p> <p><sup>8</sup>Axial capacity tests for DNV draft offshore standard code</p>	<p><sup>13</sup>Review of 30 model test for ISO design equations</p> <p><sup>12</sup>Experimental testing for a new analytical model</p>	<p><sup>15</sup>Aalborg University model tests</p> <p><sup>16, 19</sup>Research project GROW, Hannover</p> <p><sup>16, 19</sup>Small and large scale testing of GCs</p> <p><sup>20, 21, 24</sup>JIP I</p>	<p><sup>23</sup>New recommendations for GCs with shear keys.</p> <p><sup>27</sup>Guidelines for GCs with shear keys</p> <p><sup>23</sup>JIP II: fatigue testing, new design methodology for cylindrical shear-keyed GCs</p>
<i>Outcome &amp; Code Development</i>	<p><sup>2, 3</sup>Significant amount of test data, new design equations on the strength of axially loaded GCs →</p> <p>Revised <sup>4</sup>DEn</p>	<p>Revised:</p> <p><sup>10</sup>API, <sup>11</sup>DNV</p>	<p><sup>12</sup>Combined loading does not have a detrimental effect on the axial capacity of GCs</p> <p><sup>14</sup>API</p>	<p>Design equations do not represent actual capacity → Amendment of GCs section in <sup>22</sup>DNV</p> <p><sup>21</sup>Design methodology for conical GCs</p>	<p><sup>27</sup>DNV</p> <p><sup>27</sup>Technical note on GCs</p> <p><sup>29, 31</sup>Large scale cyclic tests under wet and dry conditions</p>

<sup>1</sup>API RP2A (1977), <sup>2</sup>Billington and Lewis (1978), <sup>3</sup>Billington and Tebbett (1980), <sup>4</sup>DEn (1980), <sup>5</sup>Karsan and Krahl (1984), <sup>6</sup>Krahl and Karsan (1985), <sup>7</sup>Lampert et al. (1987), <sup>8</sup>Sele and Kjeoy (1989), <sup>10</sup>API RP2A (1984), <sup>11</sup>DNV C101-1989 (1989), <sup>12</sup>Lampert et al. (1991), <sup>13</sup>Harwood et al. (1996), <sup>14</sup>API RP2A (2000), <sup>15</sup>Andersen and Petersen (2004), <sup>16</sup>Schaumann and Wilke (2006), <sup>17</sup>Schaumann and Wilke (2007), <sup>18</sup>Schaumann et al. (2010), <sup>19</sup>Wilke (2013), <sup>20</sup>Lotsberg et al. (2012), <sup>21</sup>Lotsberg et al. (2013a), <sup>22</sup>Lotsberg et al. (2013b), <sup>23</sup>BSI (2007), <sup>24</sup>DNV (2011), <sup>25</sup>DNV (2007), <sup>26</sup>DNV (2014), <sup>27</sup>Lloyd (2013), <sup>28</sup>Schaumann et al. (2014a), <sup>29</sup>Schaumann et al. (2014b), <sup>30</sup>Schaumann and Raba (2015).

### 2.12.1 Offshore load regime

Loading on OWTs can be classified based on the source of action. A typical example are loads originating from environmental sources like wind, waves and currents. Loading also originates from the operating turbine, accidental loads and dead loads. Codified approaches follow a limit state approach in order to design for these desired load conditions. The limit states concerning OWTs are Ultimate Limit State (ULS), Fatigue Limit State (FLS), Accidental Limit State (ALS) and Serviceability Limit State (SLS). For the design of GCs, the limit states of interest are ULS and FLS and some of the approaches entailed in DNV ST-0126 (2016) are presented and discussed hereinafter.

### 2.12.2 Ultimate Limit State (ULS) analytical model

Based on the experimental work conducted within JIP I, II, guidelines have been developed for the design of GCs based on the selected geometry (DNV ST-0126, 2016). When detailed FE calculations or experimental data are not available, then the following analytical model can be employed as long the geometry of the connection adheres to the limits of validity as per Table 2.2.. The analytical model can be used for different types of GCs ranging from plain tubular, tubular GCs with shear keys to conical without shear keys. Due to vertical movements on plain GCs, those are allowed for use only if they are not intended to offer resistance in the axial direction (DNV-ST-0126, 2016). It also distinguishes between jacket and monopile substructures. For tubular GCs with shear keys the nominal contact pressure caused by a design moment ( $M_d$ ) as per DNV-ST-0126 (2016) reads:

$$P_{nom,d} = \frac{3 \pi M_d E L_g}{EL_g [R_p L_{ge}^2 (\pi + 3\mu) + 3\pi\mu R_g^2 L_{ge}] + 18\pi^2 k_{eff} R_p^3 \left[ \frac{R_p^2}{t_p} + \frac{R_s^2}{t_s} \right]} \quad 2.2$$

where  $\mu$  is the friction coefficient, assumed to be equal to 0.7 in the absence of experimental data,  $L_{ge}$  the effective length of grout reduced by the thickness of the grout twice to represent the length of the GC in real conditions and  $k_{eff}$  the effective stiffness of each shear key calculated by equation 2.3. The reduction to the grouted length is adopted to include the material properties variability due to offshore grouting.

$$k_{eff} = \frac{2 t_s s_{eff}^2 n E \Psi}{4^4 \sqrt{3(1-\nu^2)} t_g^2 \left[ \left( \frac{R_p}{t_p} \right)^{\frac{3}{2}} + \left( \frac{R_s}{t_s} \right)^{3/2} \right] t_s + n s_{eff}^2 L_g} \quad 2.3$$

where  $s_{eff}$  is the distance between shear keys minus the width of a shear key and  $\Psi$  is the design coefficient equal to 0.5. The interface shear capacity ( $f_{bk}$ ) is as written in 2.4:

$$f_{bk} = \left[ \frac{800}{D_p} + 140 \left( \frac{h}{s} \right)^{0.8} \right] k^{0.6} f_{ck}^{0.3} \quad 2.4$$

where  $f_{ck}$  is the characteristic compressive strength and  $k$  is the radial stiffness of the connection calculated as follows:

$$k = \left[ \left( \frac{2R_p}{t_p} \right) + \left( \frac{2R_s}{t_s} \right) \right]^{-1} + \left( \frac{E_g}{E} \right) \left[ \frac{2R_s - 2t_s}{t_g} \right]^{-1} \quad 2.5$$

The grout matrix failure is dictated as per 2.6 and  $f_{bk}$  shall comply accordingly:

$$f_{bk} = \left[ 0.75 - 1.40 \left( \frac{h}{s} \right) \right] f_{ck}^{0.5} \quad 2.6$$

### 2.12.3 Fatigue Limit State (FLS) considerations

One unique characteristic of OWTs is the number of cycles the substructure experiences over its lifetime. A typical OWT will be subjected to a total of  $10^9$  load cycles which is larger by at least one order when compared to other structures or components which are heavily loaded during their lifetime, such as aerospace structural elements or rail tracks (Bechtel, 2017). Thus, investigating the fatigue performance is of great importance.

In order to produce reliable data, experimental fatigue campaigns ought to depict realistic offshore conditions as much as possible. One parameter requiring careful consideration, is the stress ratio. Stress ratio defines the loading pattern; for example, if the structure or component under investigation is loaded in tension, compression or a combination of both (Vasilopoulos, 2010). It is defined as the minimum to maximum stress ( $R = \sigma_{\min} / \sigma_{\max}$ ). The main features which are critical for fatigue tests are illustrated in Figure 2.17.

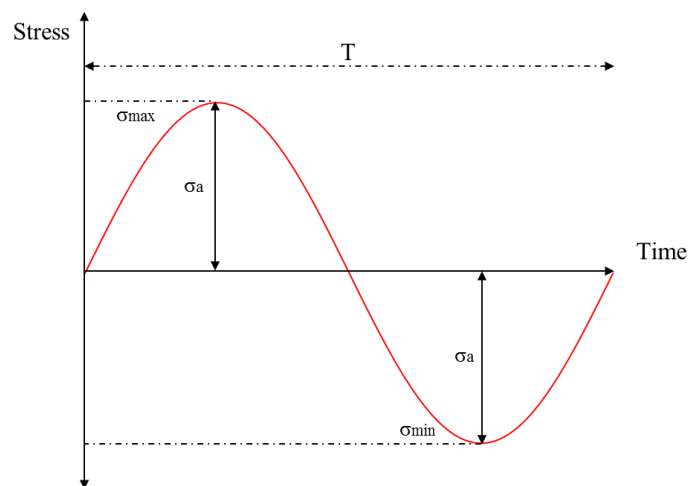


Figure 2.17: Cyclic load notation

Apart from total cycles, civil or mechanical structures when compared to OWTs, also experience different stress ratios. Due to the complexity of the stress state caused by environmental conditions in offshore locations, load ratios for OWT

substructures are better described as fully-reversed ( $R=-1$ ). Fully reversed loads correspond to equivalent tensile and compressive loads. DNV-ST-0126 (2016) suggests that a fully-reversed cycle reduced by a percentage in order to account for the rotor-nacelle dead load should be employed when evaluating the fatigue performance. Not many structures are subjected to such conditions. For example, a typical stress ratio for an aerospace component is  $R=0.1$ , as the load regime is better described as tension-tension.

Despite some experimental campaigns having focused to the fatigue behaviour of GCs there is a lack of reliable S-N curves. Some suggestions for S-N curves were given by Harwood et al. (1996) and also some recommendations are presented in DNV-ST-0126 (2016). Marion et al. (2018) highlight the unknown factors that cause the lack of representative guidelines for fatigue design. The main reasons are the confinement levels of the grout and the alternating stresses at the GC level.

Following recent studies by Lotsberg et al. (2013) and Sølund and Johansen (2018) it is acknowledged that events that are most likely to damage the connection and hinder the integrity of the grout are extreme events. Such occurrences can be storms that take place offshore and their duration can range from a few thousand cycles up to one hundred thousand cycles. Early experiments were conducted under compression only cycles which are however not close to the actual offshore regime (Wilke, 2013; Lochte-Holtgreven, 2014; Chen et al. 2018).

Another level of ambiguity which is often introduced during laboratory modelling is the selection of stress ranges. Typically fatigue load levels can be defined using experimental or analytical methods. Experimental methods require testing for the determination of the ultimate capacity. Analytical methods involve aero-elastic computer aided engineering (CAE) tools or design equations from standards such as DNV ST-0126 (2016). Analytical methods are often

favoured from experiments due to cost. Alternatively, the response of OWTs is often simulated using CAE tools such as FAST (Jonkman and Buhl, 2005) in combination with counting methods such as rain-flow. Subsequently, the fatigue data are used for the determination of relevant stress ranges.

## 2.13 Monitoring and maintenance approaches

Following the design aspect of the joints one of the challenges that OW sector faces nowadays is the need to confront and minimise maintenance costs for each turbine and subsequently each wind farm. Demand has been growing within industry and researchers to develop monitoring methods and tools that could potentially prevent unexpected failures and events. There is an urge to explore the potential of Non-Destructive Techniques (NDT) and develop tools to monitor the integrity of the offshore assets.

Monitoring on OWTs is often distinguished in various categories based on the intended application. Those include, Condition Monitoring (CM), SHM, Statistical Process Control and Damage identification through non-destructive evaluation as distinguished in the review study by Martinez-Luengo et al. (2016). As many types of classification exist between CM, SHM and NDT within this work reference to SHM is made as the field of application of NDT or other type of methods for monitoring of structures and particularly composite joints such as GCs. According to Wymore et al. (2015), SHM can be useful for detection, localisation of damage, assessment and remaining life evaluation. Nevertheless, each monitoring field or method aims to enable favourable maintenance techniques for OWTs. The ultimate goal for future substructures is to employ preventive instead of corrective maintenance allowing for a significant reduction of the O&M costs.

An example of corrective maintenance on OWTs are the reported failures on

monopile GCs where the component in question has already failed and mitigation solutions were necessary. Such failures require the so-called corrective maintenance tasks. Within the OW industry the transition to condition-based rather than corrective maintenance is one of the greatest challenges (Figure 2.18). Condition-based maintenance refers to the early detection of damage which accommodates the limitations imposed by environmental conditions and reduces the O&M cost for OWTs (Rolfes et al., 2014).

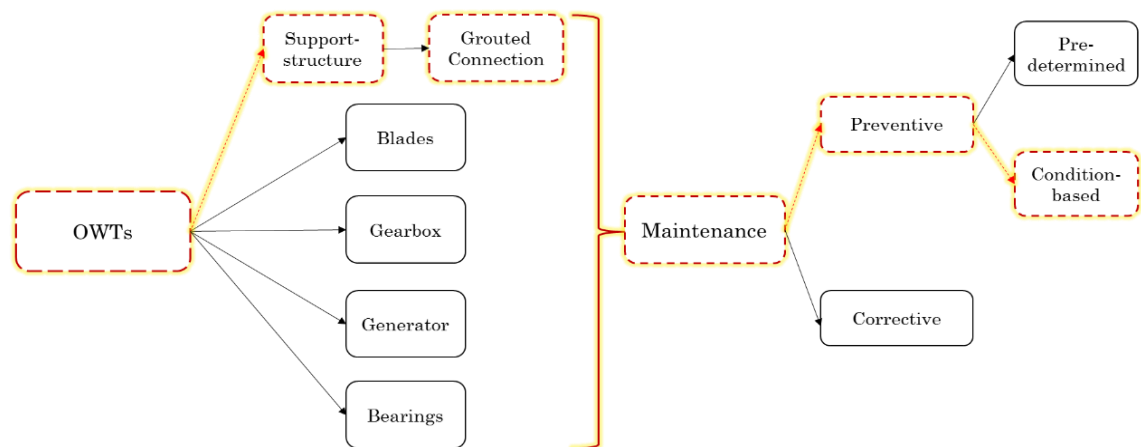


Figure 2.18: Classification of maintenance approaches for different parts of OWTs

SHM approaches are in the forefront for the development of reliable monitoring systems for OWTs. They can greatly improve reliability acting as prolepsis against a plethora of damage types often occurring offshore (Martinez-Luengo et al., 2016). To date there has been very limited research focusing on monitoring methods for OWT substructures and particularly the integrity of the grout within a connection.

The interest in monitoring the individual components is significant recently, owing to the O&M expenditures approaching the initial CAPEX (Shafiee et al., 2016). It is worth noting that the cost of the foundation and substructure in general is about 35% of the total investment. Taking into account the costs of performing offshore tasks it cannot be argued how important a well-designed

structure is. Cost of maintenance is attributed to the remote offshore locations and the fact that repairing failures or applying mitigation measures greatly depends on accessibility due to environmental conditions. Additionally, a complete shutdown of the generator is usually required to perform the required engineering work (Marquez et al., 2012; Shafiee and Sørensen, 2018).

## 2.14 Structural Health Monitoring (SHM) methods

Several methods for SHM exist, which can be modified and adapted on a case by case basis. Those come with positive and negative aspects with regards to their effectiveness and ease of application. Recent review papers focusing on the application of SHM on OWTs have attempted to put together the most recent advances in the field (see, e.g., Marquez et al., 2012; Martinez-Luengo et al., 2016). In their review, Martinez-Luengo et al. (2016) highlight the benefits of applying SHM in the aerospace and civil engineering sectors during the past decades, emphasizing on how such methods have largely increased the reliability and profit. For example, monitoring of concrete bridges or railways for crack detection and to evaluate their condition, has been particularly effective and beneficial. Some of the commonly used techniques are: thermal imaging, strain monitoring, ultrasonic methods, AE and vibration-based methods. Detailed reviews on the capabilities of these methods can be found in the literature (see, e.g., Martinez-Luengo et al., 2016). Herein, a brief summary on the main aspects of some methods is presented to introduce the reader. The main advantages and limitations of SHM techniques used to date, are tabulated in Table 2.4.

All SHM approaches are distinguished as passive or active; where active are the ones that require external stimuli. Ultrasounds are a typical example of an active method. The emitted ultrasonic waves are used to identify the condition of the interior of an element or structure. For instance, in concrete cracks can be detected

with high accuracy. One of the methods that can be categorised as hybrid (passive or active) is thermal imaging. In principal thermal imaging is passively applied, however for blades the use of external light sources is common, thus making it an active method for such cases. Wind turbine blades is the main field of application for thermal imaging, where damage of the component is detected based on temperature gradients of the examined surfaces. Many studies can be found in the literature, noting the promising potential of this method for OWT blades (see e.g., Hahn et al., 2002; Martinez-Luengo et al., 2016).

On the contrary, AE is a purely passive method due to the excitation which is required for energy to be released (Grosse and Ohtsu, 2008). AE is one of the techniques of the larger family of SHM which can be applied for monitoring OWT foundations and notably connections. The main principle is the detection of the elastic energy changes caused by external motives (Grosse and Ohtsu, 2008).

Events such as cracking or debonding release energy waves (Martinez-Luengo et al., 2016) making AE a potential candidate for monitoring purposes. Some of the advantages of AE include high-resolution for cracking events along with real time monitoring capabilities. Nonetheless, post-processing can be a tedious task due to lack of a unified approach and data analysis being dependent on the acquisition system. The use of AE for damage detection has already been adopted for monitoring OWT blades (Jungert, 2008). Additionally, it has also been successfully employed in a variety of civil engineering structures to capture crack growth or degradation of brittle material. Specifically, for structures where cement-based material is present, AE focuses on damage quantification, source localisation and identification. Examples of such research works can be found in the literature (Farhidzadeh et al., 2013; Sagar and Rao, 2014; Abdelrahman et al., 2014, Li et al., 2017; Shi et al., 2018).

Table 2.4: Capabilities and limitations of SHM methods for OWTs

Method	Monitoring capabilities	Limitations	Applications
Visual Inspection	Requires visible parts/ components  No equipment is required  Used in conjunction with other methods	Accuracy  Limited information  Defects beneath the surface are not detected	All types of structures and components
AE	Real-time monitoring of blades or structures  Subsurface cracking/ delamination of interfaces  Classification of cracks  Damage assessment	Tedious post-processing  Sensitivity to background noise  Locating cracks	OWT blades  Substructures/ GCs
Ultrasonic	No preparation is required  Can be used with thick layers  Instant results	Coupling on grained-surface materials  Defects of small size can go undetected  Requires access to surfaces	Substructures – Composite structures
Thermal imaging	Subsurface crack detection by monitoring the temperature gradient  Enables monitoring of large regions/ components  Quick application	Resolution of images - Image processing  Automated post-process tedious  Deep defects can go undetected	UAV applications  Blades

Vibration based monitoring	Ease of installation Resonance frequency – Damping Coefficient Damage indicators	Post-processing tedious Uncertainty due to random loading Limiting real-time monitoring Misalignments of equipment	Rotating machinery Composite structures Scour monitoring
Strain monitoring	Microscopic level Passive method does not require external excitation Ease of installation	Not very robust Knowledge of critical regions Noise sensitivity	Component level/ GCs

## 2.15 Monitoring techniques for grouted connections

GCs fall within the SHM field and following the events that took place at 2009 (see detailed discussion in section 2.7) there has been some motivation within OWT owners to develop tools and install monitoring equipment on monopiles to assess the performance of the connections. Dallyn (2017) refers to a strain monitoring system installed at the Robin Rig wind farm. The system was installed after 2010 to monitor the loads at a TP. Some of the recovered data focused on measuring the loads that were experienced on the external pile. What is of interest is that they were found to be lower than the expected design loads. Even so, GCs have been showing signs of insufficient performance and slippages. This explains that slippages occurred due to grout degradation and the importance of monitoring the grout condition is reiterated.

Iliopoulos et al. (2016) presented the first application of NDT on grout cores extracted from in-service offshore monopile GCs. Ultrasonic Pulse Velocity

(UPV) and X-rays were used to evaluate the condition of the samples which were drilled from different locations across the length of the GCs. A global approach using vibration-based monitoring of a GC was carried out by Häckell et al. (2017), while, Moll (2018) presented a case study of the application of Electromechanical Impedance Spectroscopy on a small-scale GC. Brett et al. (2018) developed a mathematical model based on ultrasonic testing which was validated against small-scale steel-grout-steel samples and field trials. The results of these studies have been promising, encouraging such approaches for the development of monitoring tools to prevent future failures and reduce unnecessary O&M costs.

AE can be effectively employed to capture events such as crack growth and crack development in brittle material. Examples of such research works can be found in the literature. Rao and Lakshmi (2005) investigated rock fracture using AE signals in rocks focusing on micro-cracking development and data analysis of AE wave features. Fundamental investigations on concrete behaviour and the identification of cracking mechanisms were conducted by Aggelis (2011) and Aggelis et al. (2012). Sagar and Rao (2014) also attempted to correlate AE activity with fracture characteristics in concrete. Most of the research projects using cementitious material along with AE involve concrete and reinforced concrete beams rather than grout-filled steel tubes or connections.

## 2.16 Research gap and motivation

The presented state-of-the-art was classified in three principal categories: Experimental testing, numerical modelling and SHM methods. Taking into consideration the comprehensive review of the literature the following research gaps were identified:

- The current data pool resulting from experimental campaigns on GCs is still limited and several parameters have not been investigated.

- FE modelling approaches are scarce, lack accuracy and consistency. There are very limited research papers with validated models and in-depth parametric studies to fully exploit the potential of numerical modelling.
- There is a significant lack of knowledge on the application of SHM on OWTs and particularly for substructures and composite joints.

The aim of this work is to tackle all three pillars of interest and provide further scientific insights and understanding on the performance of GCs for OWTs. To that extent physical testing of cylindrical connections is undertaken which is supplemented by detailed, validated and robust FE models. Finally, a novel pilot study investigating the potential use of AE for monitoring GC on OWTs is carried out. The presented research aims to contribute to the development of the OW sector by being of benefit to the design and monitoring aspects of a substructure.

# 3 EXPERIMENTAL CAMPAIGN

## 3.1 Overview

Within this chapter the experimental tests which were undertaken at the structural testing facilities of the University of Birmingham, UK are comprehensively presented along with the adopted methods. The campaign comprised static and fatigue testing of GCs under bending loads, mechanical characterisation of material and AE monitoring.

Section 3.2 introduces the reader to testing protocols whereas the two downscaled cylindrical GCs which were designed are presented in Section 3.3. The cementitious grout used is presented in section 3.4 along with mixing and curing considerations. In section 3.5, material testing for steel and grout is given. Section 3.6 introduces the procedure that was adopted for the annular grouting of the specimens, the initial trial grouting tests that were performed and provides general considerations for grouting of laboratory-scaled GCs. The test frames that were used to accommodate the experiments along with the employed instrumentation are presented in sections 3.7, 3.8 respectively. Finally, the test results are given in sections 3.10 and 3.11.

### 3.2 Test programme description and rationale

The experiments were designed taking into consideration the comprehensive literature review that was presented in Chapter 2. Thus, bending tests under static and cyclic loads were selected for this campaign and the reasoning is presented thereafter.

At the time when these tests were designed and eventually carried out, the only campaign focusing on downscaled cylindrical GCs under bending loads following the events of 2009 is presented in Schaumann and Wilke (2010). It is worth mentioning that some tests have been performed in research institutes or by industrial parties, however those are not publicly available due to confidentiality restrictions. Moreover, interest on bending loads has increased over the past years progressively even for lattice substructures (Marion et al., 2018). As the OW sector is exploiting greater depths, jackets and tripods employ far more vertical than inclined piles, which in principle are subjected predominantly to bending, similarly to monopiles. Also, the limited data on GCs in bending has been highlighted in several research and review papers (see e.g., Lotsberg and Solland, 2013; Dallyn et al., 2016; Tziavos et al., 2019; Marion et al., 2018).

During the inspections of 2010, apart from slippages, the failures that were reported involved interface opening, cracking of the grout and water ingress as noted by Brett et al. (2018). Although water ingress was reported on several substructures, the sites are not publicly revealed by operators (Dallyn et al., 2016). Considering the above, the designed GCs were tested in a four-point configuration depicting simply supported beams. This configuration allowed for reversed fatigue loads to be applied. Also, initial FE simulations that were performed, revealed that bending provokes failure modes or events that suggest

insufficient performance. The resulting failure modes were of importance so as to benchmark the monitoring approach simultaneously. Additionally, the test configuration allowed for a direct comparison with the tests conducted by Schaumann et al. (2010).

Initially, a static strength test of a GC in pure bending was performed aiming to determine the global behaviour, ultimate load and corresponding failure modes. The ultimate load recorded was subsequently used to define the fatigue load ratios. In the available literature there are few tests available for ultimate loads in bending; this is due to interest in fatigue behaviour. However, such tests are critical for GCs as the design is often based on simplified ULS approaches. A static test enhances the existing data in the literature and allows the validation of detailed FE models.

The second test took place in two stages. Initially, a high-cycle protocol with reversed bending loads followed by an ultimate test, to evaluate the influence of cyclic loads on the GC capacity. It has been documented that reversed bending loads are detrimental to the performance of GCs and also represent a realistic stress state. Solland and Johansen (2018) noted that reversed cyclic loads which are short in duration represent storm condition and are critical for the performance of GCs. Experimental work on GCs in reversed loading conditions is scarce nowadays and the effects are not known.

Ultimately, the designed tests accommodated the objectives that have been set in section 1.3. Those are summarised as follows:

- To investigate the bending behaviour of tubular GCs with a high shear key ratio ( $h/s$ )
- To examine the effect of short-duration reversed bending loads on the ultimate moment capacity,  $M_u$  of a GC

- To supplement and enhance the limiting pool of static bending tests
- To investigate and benchmark the application of AE as a SHM tool for grout monitoring
- Identify the differences between static and fatigue AE monitoring

### 3.3 Test specimens

Contrary to JIP I and II (DNV 2010-1053, 2011; DNV 2012-0371, 2013), for which box specimens were designed to imitate radial stiffness of large scale GCs, the geometry of the specimens was chosen to be tubular, thus representing actual GC designs. As discussed in section 2.9, it is believed that box specimens introduce further uncertainty in the interpretation of the results.

Tubular steel sections of the same S275 JR2 equivalent steel grade were chosen for the piles and sleeves. A typical steel grade for monopiles is the S355, however the tests aim was to test until failure, thus considering the capacity of the loading jacks this steel grade was not suitable. The cross-sectional dimensions were based on initial FE models taking into consideration existing tests and also the validation study of the numerical models.

The fabrication process of the specimen is illustrated in Figure 3.1. Shear keys were welded around the circumference of the external and internal faces of the piles and sleeves. To do so the surfaces were mechanically cleaned as shown in Figure 3.1a. In both tests the shear keys were formed by fillet-welded flat bars (Figure 3.1b). Previous researchers have employed irregular hand-welded protrusions aiming to achieve semi-circular keys. The square profile was selected so as to examine if any cracking is amplified by the corner edges when compared to a circular one. Ultimately, four shear key pairs were welded along the length of the GC.

Considering the circular geometry of the steel piles, circular rings with flat faces were externally-welded on each tube to assist with the test's boundary conditions. The simply supported boundary conditions were achieved by using steel rollers. Each pile was equipped with two 25 mm-thick rings as depicted in Figure 3.1c. In the exact same locations, circular steel circular disks were welded on the internal side of each pile, to act as stiffeners at load bearing locations in order to prevent local failure during the test.

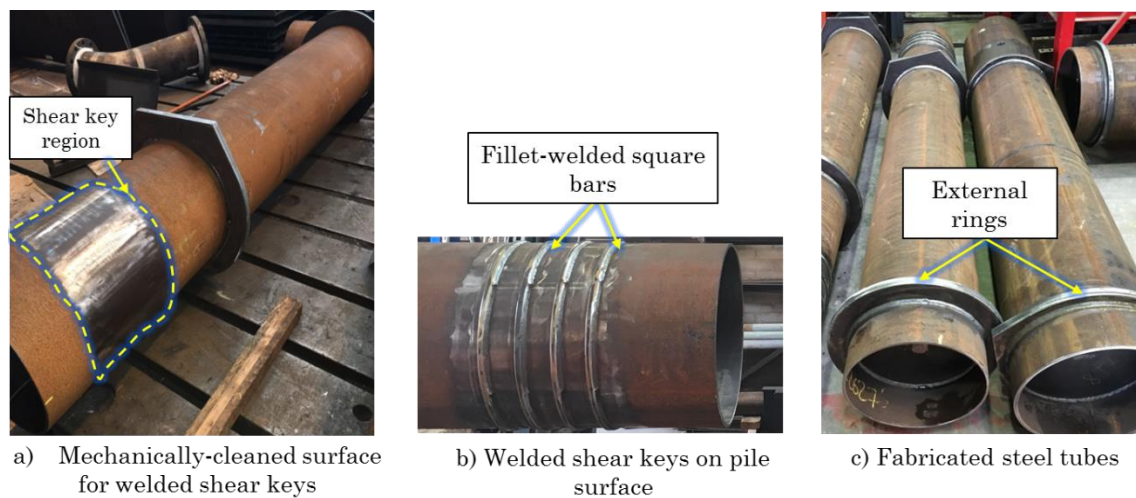


Figure 3.1: CHS geometry and GC layout

Once the fabrication process was complete, thorough measurements of the geometrical characteristics of each steel section were taken, including the fillet-welded shear keys. Multiple values were recorded on different locations along the circumference of each steel pile. The design values are tabulated in Table 3.1.

Table 3.1: Geometrical features of steel pile and sleeve

	Sleeve	Pile	Grout
Length ( <i>mm</i> )	2500	2500	610
Diameter ( <i>mm</i> )	473	406	450.8
Thickness ( <i>mm</i> )	11.1	8	22.4
Grouted length ( <i>mm</i> )			610
Shear key height ( <i>mm</i> )	5	5	n/a
Shear key width ( <i>mm</i> )	10	10	n/a
Shear key spacing ( <i>mm</i> )	60	60	n/a
Shear key number	5	4	n/a

### 3.4 Ultra-High-Performance-Cementitious (UHPC) material

The grout material that was used to attach the steel tubes is the pumpable UHPC material – Ducorit<sup>®</sup> S5R (Densit, 2018), with a nominal compressive strength of 130 *MPa*. The Ducorit<sup>®</sup> S5R is a cementitious-based material comprising very fine aggregates of up to 5 *mm* in diameter. It has been used extensively offshore in multiple wind farms and this was one of the main reasons that it was employed. Considering the multidisciplinary nature and purpose of the test campaign, the use of an offshore grout was considered appropriate, rather than using a conventional grout so as to imitate realistic results. Furthermore, the S5R is an appropriate solution for the specimen’s targeted annuli following discussions with the manufacturer. For such an aggregate-based grout a gap of at least four times the maximum aggregate size is required. No scaling was performed on the material’s composition as often performed when scaling-down concrete-based specimens. Material-wise the main characteristics it exhibits, are early age strength, minimum shrinkage and an exceptionally ultra-high strength. The

strong coherence of the S5R permits grouting water filled annuli without any admixture with water. Hence, very small variations were expected throughout the length of the connection and a homogeneous content was to be expected for the grout core.

### 3.4.1 Mixing and curing

Preparing, mixing and mechanical testing UHSGs that are meant for offshore applications or in laboratories, is usually performed by following the material's specifications and guidelines or technical standards dedicated to concrete such as those published from the American Standard for Testing Material (ASTM) or the British Standards Institution (BSI).

Due to the unique characteristics, behaviour and the S5R being a pumpable material, trial tests were performed aiming to establish the optimum procedure for mixing and curing the UHSG. Moreover, the trials targeted achieving optimum mix composition for the specimens with properties similar with the manufacturer's datasheet and specifications (Densit, 2018). UHSGs usually require a mixing procedure that is unique and slightly different to concrete. The process is often dictated by the contents of the material, the workability of the mix and ultimately the equipment which is used for mixing. The need for an established mixing approach is attributed to the very low water content that is typical to material of this nature and the laboratory conditions. Low water content is one of the features that magnify the material's strength as mentioned in 2.6.1 but that requires special attention when preparing a mix. To that extent initial procedures aimed at optimising this process and to allow for the desired workability and resulting properties.

Fehling et al. (2014) discusses the advantages of using high-speed, intensive mixers that can vary the mixing energy. Such equipment can assist towards an

increased flowability while mixing. For all the experimental work throughout this campaign the S5R was mixed within the integrated mixer of a worm pump. Further details on the grouting equipment are discussed in section 3.6.1. Subsequently, fresh grout was examined and cylindrical, cubic or beam members were casted and tested to investigate the compressive and tensile properties of the material as those highly-depend on the achieved mixture and curing conditions. The dry powder (see Figure 3.2a) was mixed in a variable speed pan mixer with 7.8% ( $w/v$ ), meaning that 1000 kg of dry powder 78L of water were required. The procedure that was followed is described below:

The amount of dry UHSG powder to be mixed was inserted into the mixer along with 80% of the total required water. The proportion of water and powder which is poured into the mixer tank is important when engine-powered mixers are used. Engine power must be taken into consideration as the workability of the material is less pronounced initially. It is recommended that smaller amounts of material are poured in the tank until the cementitious medium comes to a workable condition. It was found that this process allows for full exploitation of the superplasticiser of the material and the mixture becomes soluble without blocking the mixer. Once the desired consistency was achieved the remaining water was added and the mixture was compounded for an additional five to seven minutes. The quality of each mixed batch was verified in two stages. Primarily, during the mix a flow test was performed aiming for a 300 mm flow. Subsequently, once the process was finalised, the grout compressive and tensile strength was determined from cubic and prismatic samples.

Engineering practice during the installation of a GC dictates casting grout cubes from the fresh mixture. Curing conditions of the material can also be of importance for HSGs. Once casted the exposed side of the cube is covered with a lid and the cubes are cured in water until tested, in a temperature of 20( $\pm$ 2) °C as

per standard codes such as BSI 12390-3 (2009). This approach aims to imitate the actual conditions experienced from the grout. However, although it succeeds doing so, it is considered rather unconventional by the author as it does not follow any codified method and no surface of the material is exposed to water during the curing period. Bespoke approaches are often used in the field rather than a codified method with respect to curing conditions.

To this extent the S5R cubes were cured using different protocols to examine if those have any substantial impact on the material properties. Initially following standard code (BS EN 12390-2, 2009) the cubes were casted and left in the moulds for a minimum of 24 hours (Figure 3.2b). No vibration was used once the grout was in the mould in contrary to typical concrete mixes for all cases. However, during casting, the moulds were filled with successive material layers, to allow for air to be released. Nevertheless, it was still noted that for the majority of the cubes “air pockets” were present at the exposed surface once the grout has hardened. However, the top surface air bubbles are considered to be superficial and did not have any impact on the grout properties.

Following casting, the moulds were removed, and the cubes were cured in a water tank at a temperature of approximately 20 °C until tested (Figure 3.2c). Similarly, to the above process several cubes were cured varying the initial dry period. In the two remaining protocols that were followed, cubes were left in a dry environment for 3 and 7 days before being transferred to a water tank. Results from compression tests did not reveal any pronounced differences on the strength development of those cubes. Hence for this work the properties that are used for the S5R refer to the tests that followed the corresponding codified approach in BSI 12390-3 (2009).

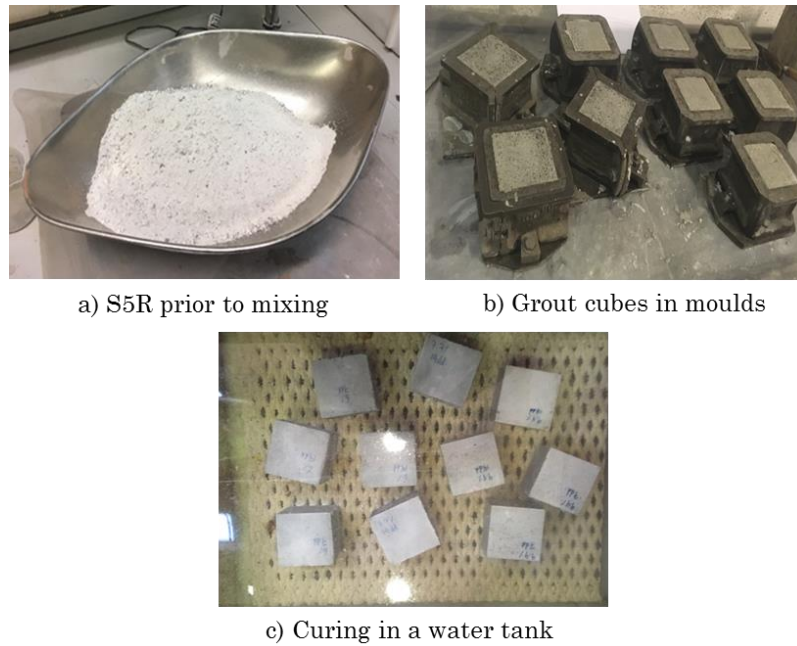


Figure 3.2: The process for compressive strength determination of grout cubes: a) Weighing Ducorit® S5R prior to mixing, b) Grout casted in cubic moulds, c) Curing of grout cubes in water-filled tank

In Figure 3.3 two halve cross-sections of a typical cured and split cylindrical grout member are shown. The even distribution of the aggregates along the height and width of the section can assure that excellent workability and mixing was achieved, and no segregation or internal air voids were present. This also confirmed that the air pockets were present only at the surface of the samples.



Figure 3.3: Cylindrical S5R sections

### 3.5 Material testing

The properties of the steel members were defined through tensile coupon tests while the grout characterisation was achieved through a series of extensive compressive, splitting and flexural tests. The material properties were subsequently used as input in the numerical models in order to conduct the validation study.

#### 3.5.1 Steel coupon tensile tests

Following completion of the tests, rectangular sections were extracted from the steel members across the longitudinal axis. Subsequently, coupons were machined using a water jet. The engineering stress-strain behaviour was defined by means of tensile tests at room temperature in accordance with BS 6892-1 (2009). The curvature of the coupons was not pronounced, nevertheless a small load was introduced while gripping. The set-up and the different stages of the tensile test are shown in Appendix A1. A two stage Ramberg-Osgood material model was fitted to the data which is subsequently used for the validation study (Mirambell and Real, 2000). The obtained results are tabulated in Table 3.2, including the Young's modulus, yield strength ( $f_y$ ), ultimate strength ( $f_u$ ), the corresponding strains at yield ( $\epsilon_y$ ) and fracture ( $\epsilon_u$ ), along with the two exponents  $m$ ,  $n$ . A typical stress-strain curve obtained from the coupon tests is depicted in Figure 3.4. The first and second exponent values proposed in Gardner and Yun (2018) fit well the test data, hence they were adopted herein.

Table 3.2: Material properties of steel parts (Average values)

$f_y$ [MPa]	$f_u$ [MPa]	$E$ [MPa]	$\epsilon_y$	$\epsilon_u$	$m$	$n$
374.2	545.1	205,961	0.026	0.32	7.6	4

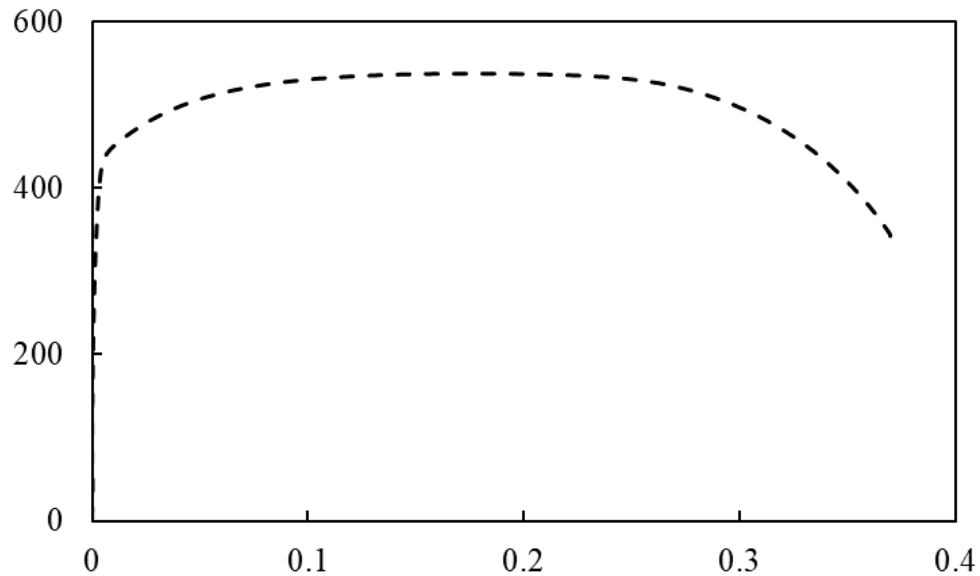


Figure 3.4: Example of stress strain curve from steel coupon test

### 3.5.2 Grout mechanical testing

The material properties of the grout were defined following an extensive series of tests. Beams, grout cubes and cylinders were casted following the sequences discussed in section 3.4.1 to define the compressive and tensile properties of the S5R. Cubic (100x100x100), prismatic (100x100x600) and cylindrical (100x300) samples were casted. A total of 65 cubes were tested in compression following BS EN 12390-3 (2009), 18 prismatic samples (BS EN 12390-5, 2009) and 12 cylinders were tested for splitting strength (BS EN 12390-6, 2009). The density of the specimens was measured in accordance with BS EN 12390-7 (2009). In Table 3.3 the acquired average values describing the grout properties from the author tests along with the manufacturer's nominal specifications are tabulated. Table 3.3 lists the properties of the material per specimen which were acquired at 28+ days according to BS EN 12390-6 (2009). The tabulated tensile strength reported in Table 3.3 was defined through splitting strength following BS EN 12390-6 (2009) and according to the offshore guidelines DNV OS-C502 (2012).

Table 3.3: Ducorit® S5R mechanical properties

Description-Symbol	Units	S5R	GC-1	GC-2
Compressive strength, $f_c$	[MPa]	130	115.5	135.25
Density, $\rho$	[kg/m <sup>3</sup> ]	2382	2339.5	2375.5
Tensile strength, $f_t$	[MPa]	7	5.1	5.9

A typical strength-development curve of the UHPC material is shown in Figure 3.5. In Figure 3.6 the test frames that were used for the compressive and tensile tests along with the dominant failure modes that were recorded during the tests are summarised and illustrated. Typical failure modes of the cylindrical and cubic samples are shown in Figure 3.6d-f for varying curing-age specimen. Most cubes tested on or after the 28<sup>th</sup> day exhibited an explosive failure which is a common feature for UHPGs.

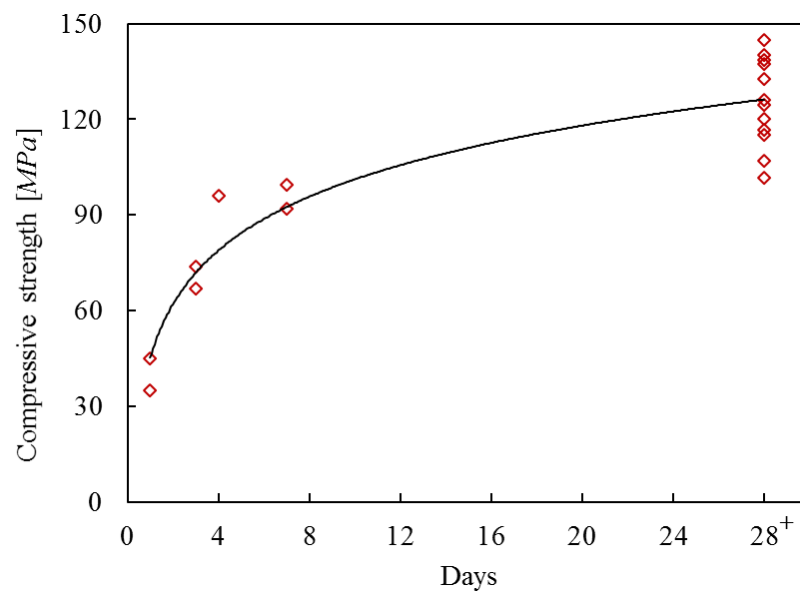


Figure 3.5: Strength-development curve of S5R UHSG after 28 days

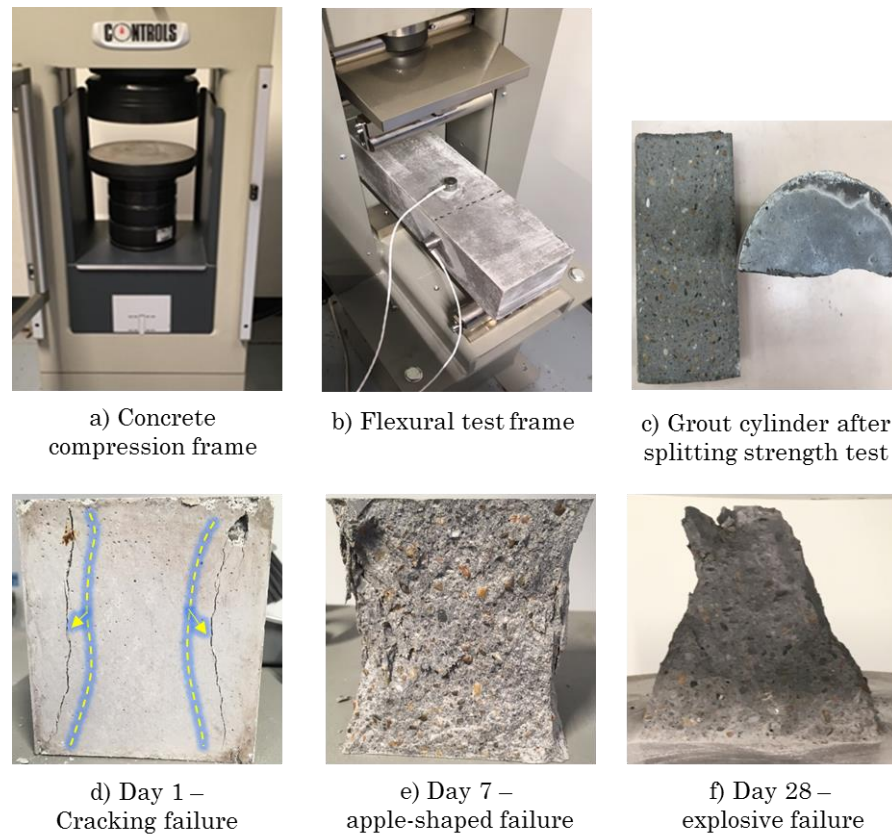


Figure 3.6: (a, b) Test frames for compression and flexural tests along with (c) cylinder (d-f) and grout cube failure modes after 1, 7 and 28 days

### 3.6 Grouting procedure

Grouting in laboratory conditions requires diligence, owing to issues associated with downscaling of the annuli thickness and the specialised equipment that is required for pumping a typical offshore HSG. Additionally, when aiming to achieve grouting in a realistic manner such that depicts offshore conditions, difficulties can arise due to pile size and arrangement.

In real applications of GCs, grouting on monopiles takes place from bottom to top. Several holes – typically six to eight, are located around the circumference and used as inlet for the infill material. The grout is then pumped, displacing the water in the annuli formed by the TP and foundation pile. If the GC is located well below the mean sea level, then a pre-calculated overflow of the grout is

performed to overcome any potential segregation that could potentially lead to a material with varying strength along the connection. The reason for that is the mixing of sea water with the HSG is unavoidable despite the coherence of the material. This is a common practice particularly for jacket substructures where the GCs are always submerged, and the control of the grouting process is minimal. In the present study due to health and safety laboratory regulations, an overflow was not possible, hence several trial tests aimed at achieving a perfect material composition prior to grouting the connections.

### 3.6.1 Trial grouting tests

To avoid any flaws in the pumping process grouting trials were performed on a test assembly. The assembly was designed to replicate the GC geometry of the specimens as per section 3.3 and is shown in Figure 3.7. The sleeve was fabricated as a two-part bolted sleeve to enable opening after grouting is complete. Eventually, the sleeve acted as a “cast” for the grout so that visual inspection of the grout around the shear keys could take place

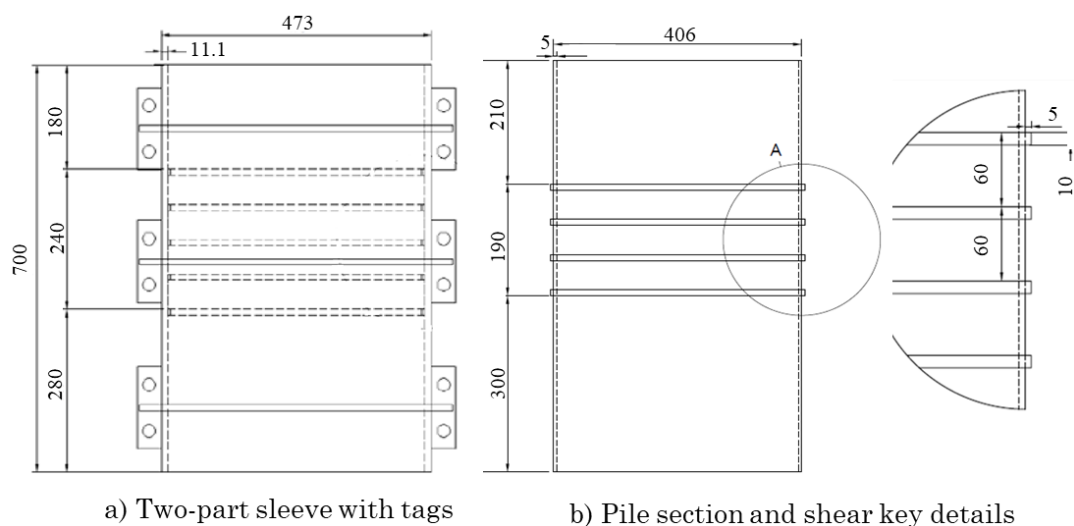


Figure 3.7: Pile and sleeve geometry of GC mock-up used in trial tests (dimensions in *mm*)

The objective of the trial was to develop a realistic grouting procedure while avoiding uneven distribution of the grout and air entrapment without requiring any overflow. Voids during grouting were reported in previous works by Wilke (2013) where their impact was not documented. Similar defects were found in the specimen grouted by Bechtel (2017), where uneven distribution of the grout was reported at the top of the GC and below shear keys. It was stated that inhomogeneous mixture resulted in a reduced fatigue capacity which is in agreement with Chen et al. (2018) who argues that grouting conditions have an impact on the performance of the GC.

The steel tubes were rolled from flat sheets with a 5 *mm* nominal wall thickness. Although the wall thickness was not exactly the same as with the one in the tests the grout thickness was maintained to serve the purpose of the trial. As shown in Figure 3.8a external stiffeners had to be welded around the sleeve in order to maintain a perfect curvature as the rolling process can cause a certain level of distortion to the steel sheet. The grout inlet was a drilled 50 *mm* diameter hole (Figure 3.8b) at the bottom of the section. In both sections circumferential shear keys were welded (Figure 3.8c) in the exact locations as the ones intended for the specimens. The resulting annuli between the pile and sleeve was 22.4 *mm*. The dimensions of the two parts are illustrated in Figure 3.7.

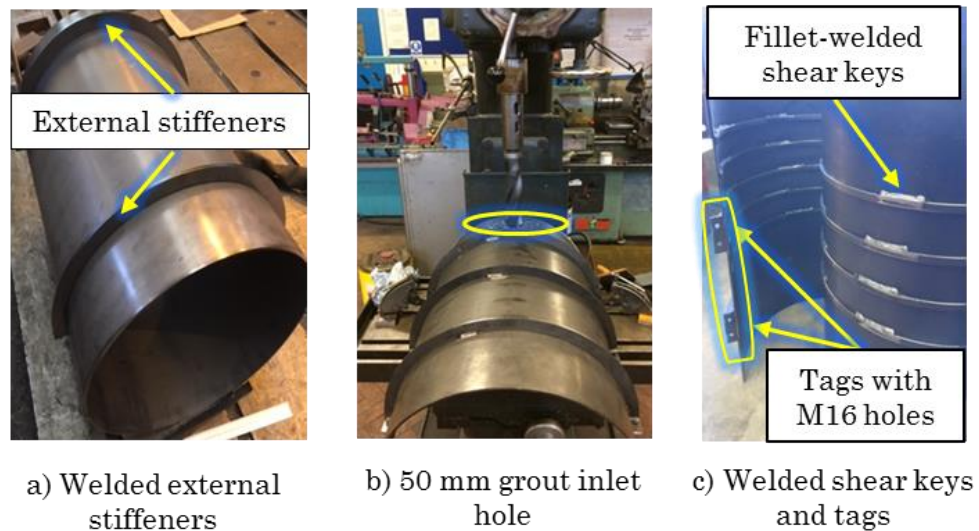
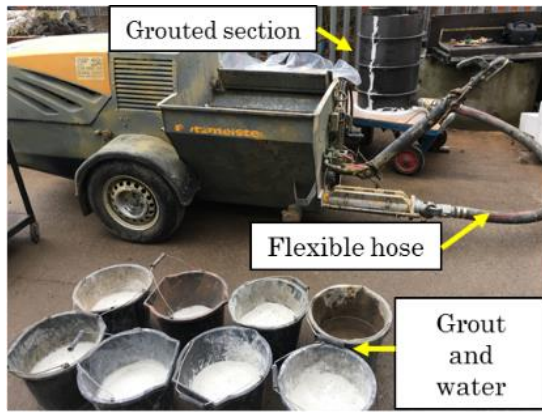
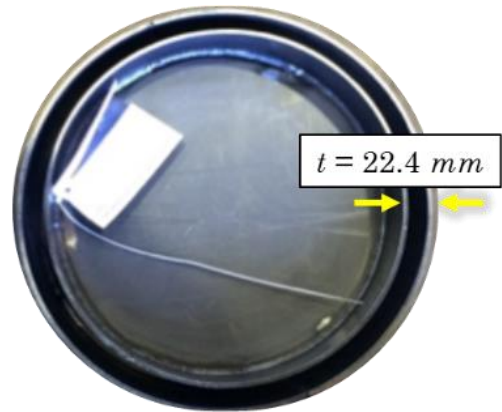


Figure 3.8: Fabrication process of steel parts for trial grouting

The setup for the mock-up grouting and the annuli of the connection are shown in Figure 3.9a and Figure 3.9b respectively. Along with the internal distribution of the grout and particularly the enclosure of the shear keys, the pumping pressure was another variable that required calibration so as to avoid blockages in the rotor/stator. The trial grouting tests were performed using different pump pressures to conclude to the optimum settings. Pumping of the S5R was achieved through a flexible hose which was connected to the sleeve inlet with a camlock-type fitting. To accommodate the pumping a Putzmeister SP11 LMR worm pump (Figure 3.10) with an integrated mixer was used. The pump can handle grouts with aggregates and can accommodate pumping at varying pressure settings and a maximum operating pressure of 15 bars. The S5R grout was mixed in the swivel mixer following the process described in 3.3.1.



a) Grouting mock-up test arrangement



b) Top view of the GC annuli



c) Dismantled sleeve after grouting during trials



d) Hardened grout within the annuli

Figure 3.9: Mock-up grouting layout and investigations

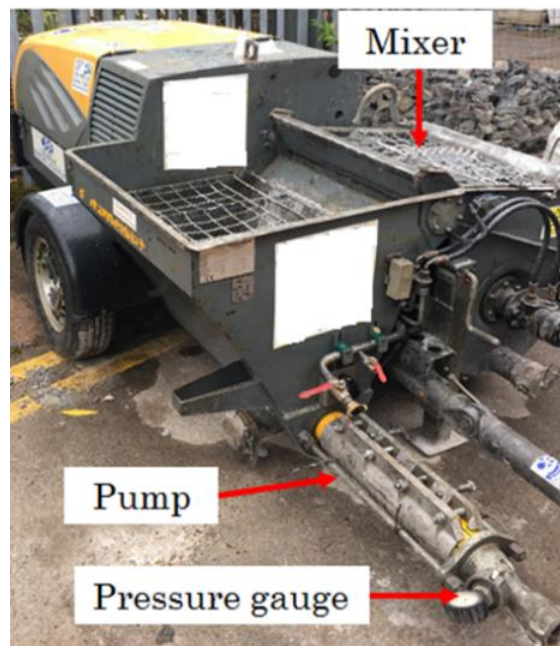


Figure 3.10: Putzmeister SP11 LMR

To ensure that there are no leaks due to the bolted connection on the split-halves, a water-tight sealant was applied longitudinally across the sleeve. Four wooden guide spacings were inserted within the gap to ensure that the thickness of the grout is uniform along the circumference and were removed after positioning was completed. For all the tests that were performed, once the grout reached the top of the section, pumping was stopped, and the grout was removed (Figure 3.9c) prior to hardening so for the test to be repeated using different settings.

Dry and water filled tests were carried out and to ensure that no mixing or segregation of the material takes place. Both methods were found to have the same outcome due to the excellent composition that was achieved. Once the desired grouting approach was finalised the material was left to harden, and the sleeve was removed after 24 hours as shown in Figure 3.9d. Visual inspection revealed excellent and even distribution of the material along the height of the section despite the large shear keys that were used. Furthermore, no signs of bleeding, or segregation was detected around the welded beads. Finally, layers of grout were removed, and no visible defects were detected. Following, the multiple trials the following remarks ought to be considered when performing small-annuli connection grouting:

- If larger lengths than the one used are grouted, it is recommended to use at least two or multiple grout inlets as the material is not evenly distributed while filling the gap. This is of importance for larger annuli as it can result in an uneven distribution.
- When worm pumps such as the Putzmeister SP11 or S5 are used for laboratory grouting, high pressure pumping should be avoided. Instead, pumping should be performed with a steady flow rate and a relatively low pressure. This is primarily to avoid excessive heat friction in the rotor – stator assembly of the pump which can lead to blockages which will

obstruct the grouting process. Also, high temperature gradients along the length can lead to cracks during the hardening process.

### 3.6.2 Pressure grouting of specimens

Grouting took place in an upright position as shown in Figure 3.11 to replicate the procedure followed during the trial tests and depict offshore installations. For ease of positioning the arrangement was upside down; the sleeve was positioned on the floor. To avoid any movement and securely support the steel tube, ratchet-straps were used to attach it on a frame (Figure 3.11a). Thereinafter, the pile was positioned inside the sleeve using an overhead crane. For the duration of the annular grouting and hardening the pile was supported by the crane to ensure that the tubes are concentric. Additionally, internal and external spacings were employed to ensure that no alignment tolerances occur and equal grout thickness along the circumference is achieved (Figure 3.11b).

The flexible hose was connected to the inlet via a two-inch BSP and a gate-valve to control the grout flow once the annuli was filled. The arrangement of the inlet fitting that was used is depicted in Figure 3.11c. At the bottom of the sleeve a custom rubber-Styrofoam seal (Figure 3.11d) was used to ensure that the grouted length is identical in both tests and the connection length yields an overlap length ( $F_0$ ) equal to 1.5.

Once grouting was completed, the GCs were left in an upright position for a minimum of 72 hours. Thereinafter, the connections were removed and left to cure horizontally until testing was performed. Both tests were conducted at least 60 days after grouting and additional mechanical testing of the grout samples was carried out on the day of each test. The compressive test results of all the grout cubes are included in Table 3.3.

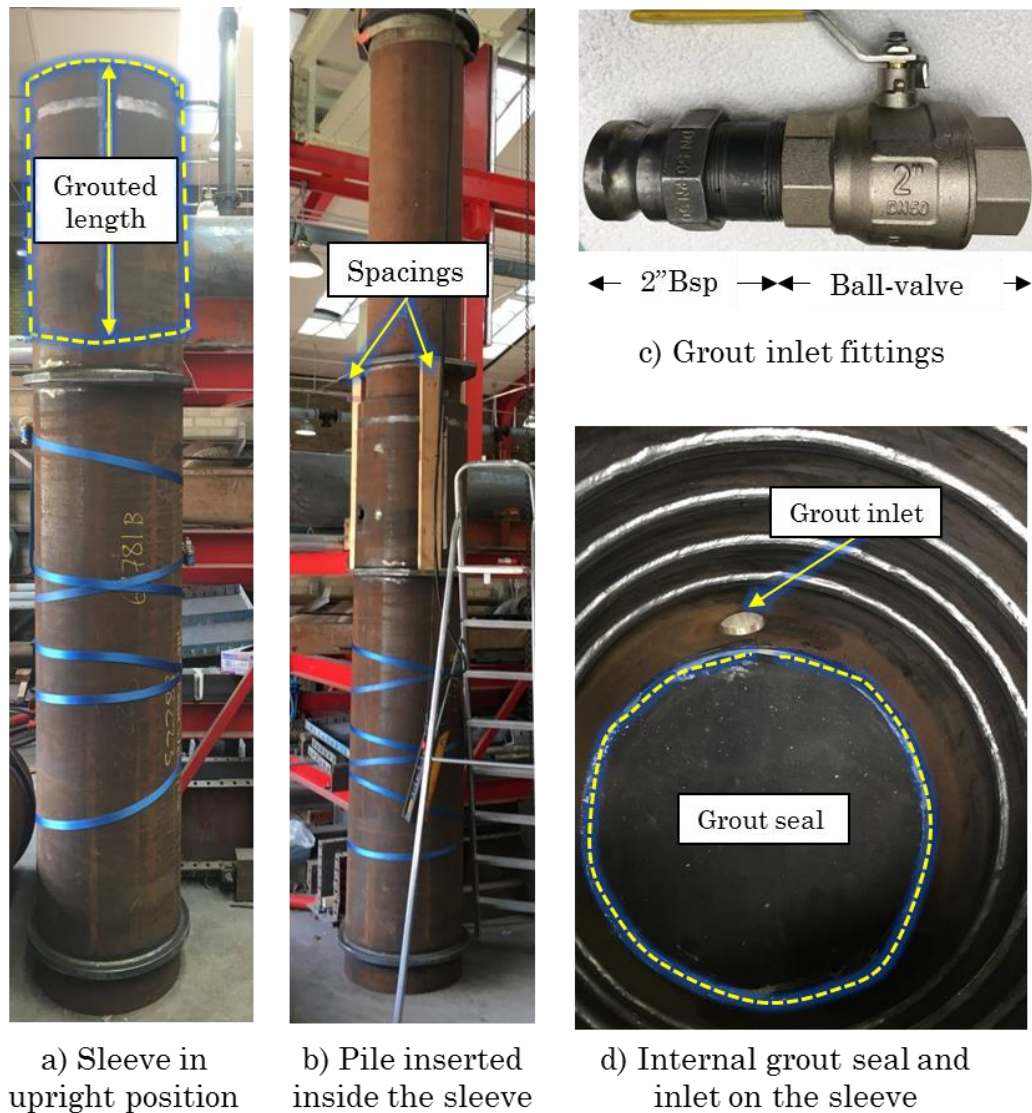
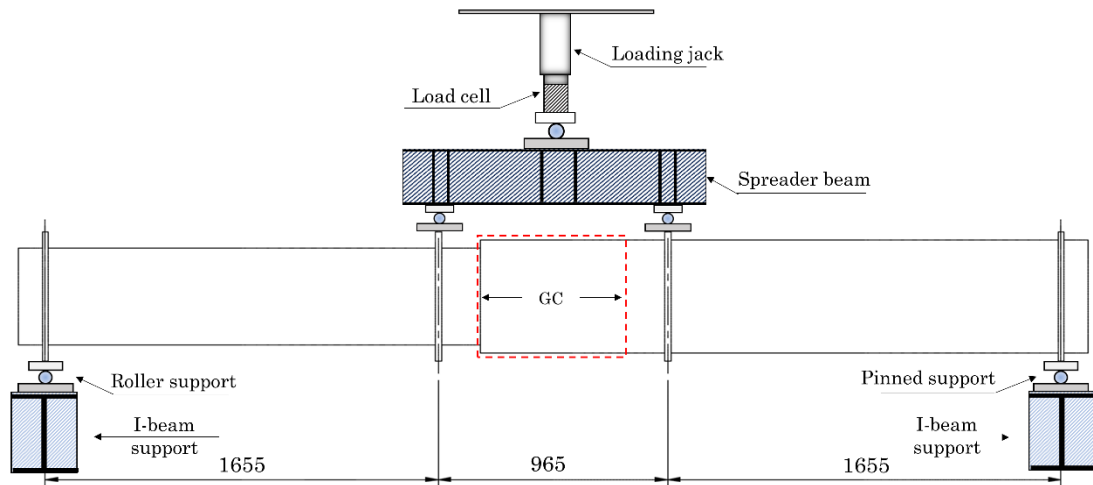


Figure 3.11: Set-up for laboratory bottom-to-top grouting

### 3.7 Ultimate strength-test layout

Two test rigs were manufactured and assembled to facilitate testing under the same four-point configuration during the fatigue and ultimate tests. The static test rig is depicted in Figure 3.12 along with a schematic layout of the ultimate bending test. Details of the test configuration are shown in Figure 3.13. I-beams with welded stiffeners across their length have been used to support the specimens and steel rollers were used for boundary conditions. The total span of the specimen was 4500 mm with an overhang of approximately 100 mm on each

side after the roller support. The load was applied through a 1000 kN hydraulic jack and was transferred on the connection using a spreader beam.



a) Static test rig



b) Static rig with positioned GC

Figure 3.12: Schematic layout (top) and set-up of the ultimate bending test (bottom)  
(dimensions in *mm*)

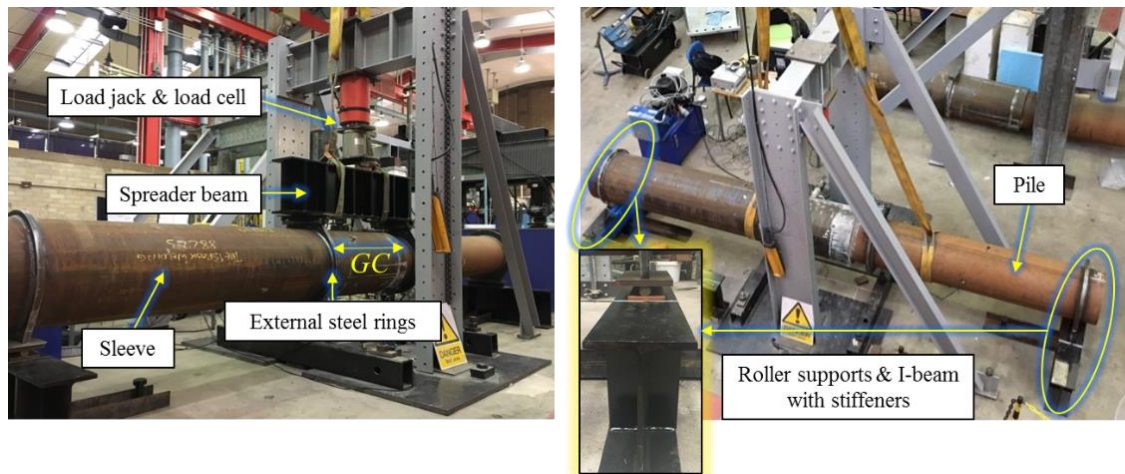


Figure 3.13: Details of the specimen set-up for the four-point ultimate strength bending tests

### 3.7.1 Fatigue test rig

A second test rig and support system was required for the fatigue test to enable for reversed loads to be realised. An overview of the assembled test frame is illustrated in Figure 3.15. The height-adjustable frame consisted of long U-channel sections, parallel flange sections (PFC) and diagonal braces. The columns were connected using M16 bolts along the length and an I-beam with welded stiffeners and end-plates was employed to connect them and attach the dynamic actuator as illustrated in Figure 3.15a. The PFC sections were equipped with clearance holes and were anchored to the strong floor with M33 steel threaded studs (Figure 3.15b). A total of six anchor points were utilised on the strong floor.

Additional diagonal braces were bolted to the frame and a threaded stud was extended from the columns to the strong wall (Figure 3.15d) to ensure that movement of the test-rig in all directions is fully-restrained. For the purpose of the test a hydraulic actuator with a capacity of 250  $kN$  was used. The actuator was fitted with a fatigue rated load-cell and a swivel end. The swivel end was used to minimise any backlash during the transition from tensile to compressive loads

and accommodate a high frequency test.

As this test was carried out using a different test rig assembly a certain eccentricity had to be introduced due to the fixed location of the strong floor anchor points. Even so it allows for direct comparison with tests from the literature. The support system is depicted in Figure 3.14 and was formed by parallel box sections (200x200x1500). Clearance holes were drilled at fixed intervals aligned with the strong floor anchor points (1.2 m) and M33 threaded rods were employed for fixation. Owing to the intended high-number of cycles and test frequency, nyloc or double nuts were fitted to tighten the threads and delay loosening during the test. Nevertheless, due to the reversed loads and frequency of the test had to be stopped at pre-determined time intervals to ensure that no bolts are loose and that there is no damage due to wear on the supports.

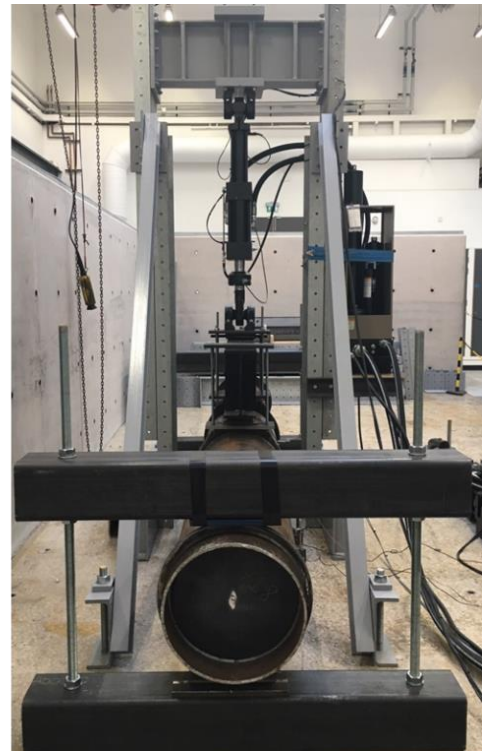
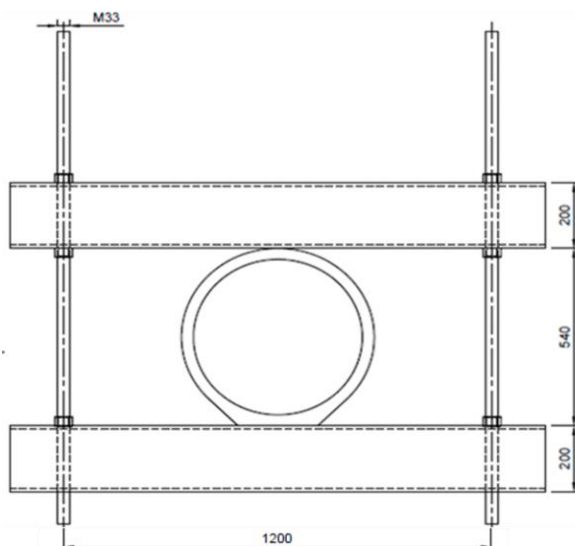


Figure 3.14: Support system during the fatigue test (dimensions in *mm*)

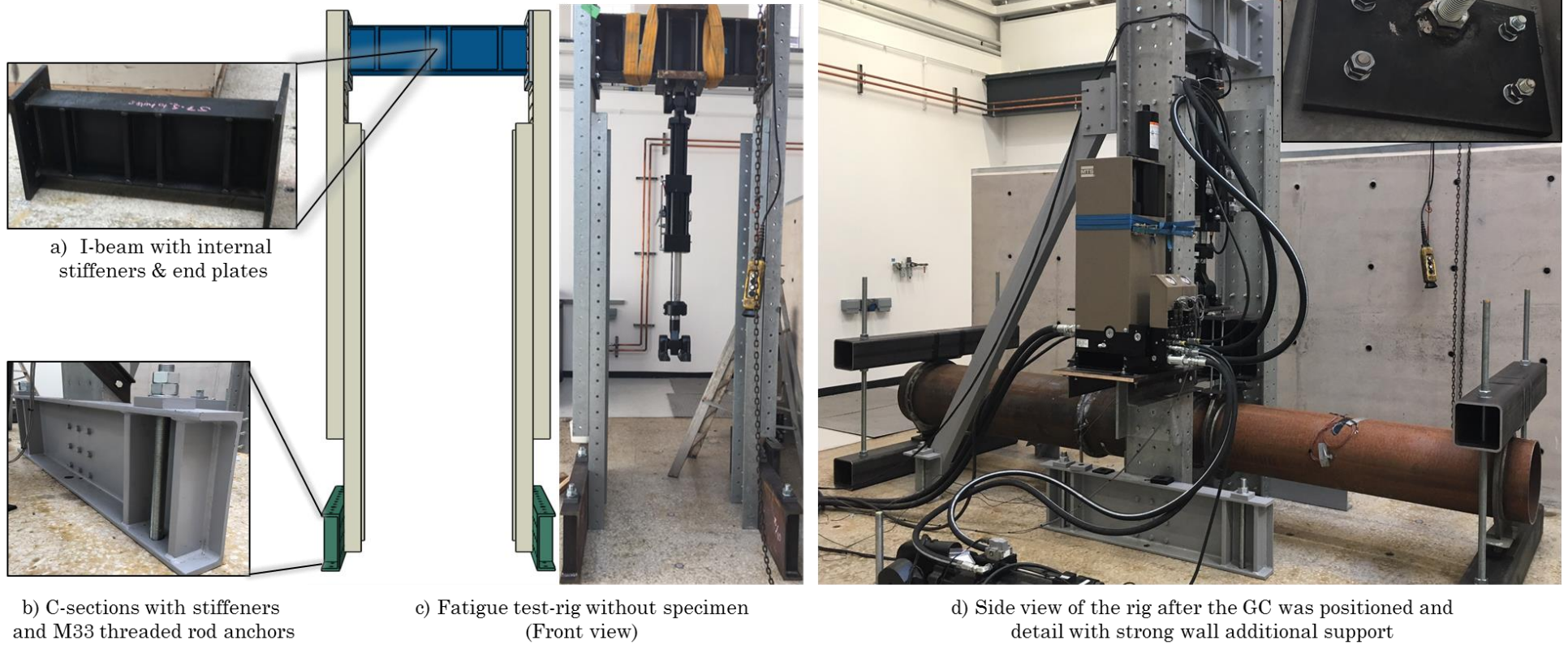


Figure 3.15: Fatigue test set-up

### 3.8 Instrumentation

The instrumentation on the GCs involved Linear Variable Displacement Transducers (LVDTs), strain gauges, load cells and four AE sensors (Figure 3.16). The load cell was directly located below the loading jack and a total of five LVDTs were used to measure displacements during the tests over the connection's length. Those were located at the load application points and one at the midspan between them. To measure the interface opening two transducers measure the deflections of the pile and sleeve. An overview of the installed LVDTs along the specimens is given in the schematic layouts of Figure 3.16a. Further details on the AE instrumentation and the monitoring aspect of the tests will be extensively covered in Chapter 4.

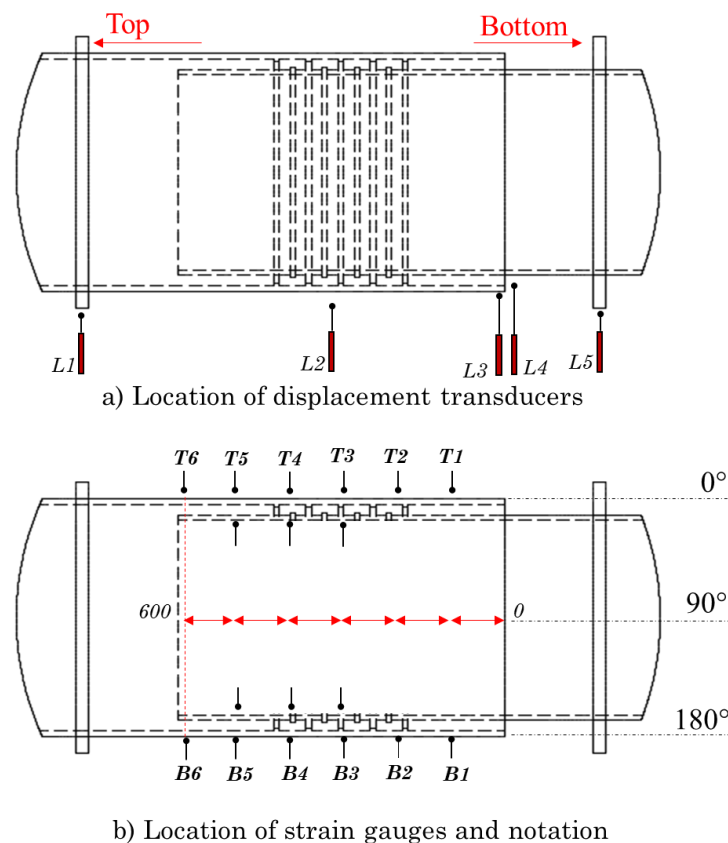


Figure 3.16: Instrumentation plan on the GC specimen

Along with deflections, the strains of the steel tubes were monitored during the bending tests by attaching strain gauges along the length of the piles at equally-spaced locations as shown in Figure 3.16b. Internal strain gauges were mounted on the pile prior to grouting due to access restrictions (Figure 3.17a). Measurements from all instruments were recorded at fixed time increments of 1 sec for the strength tests and 150 *microseconds* during the fatigue tests. The location notation which will be used throughout for the tests is summarised in Figure 3.18.

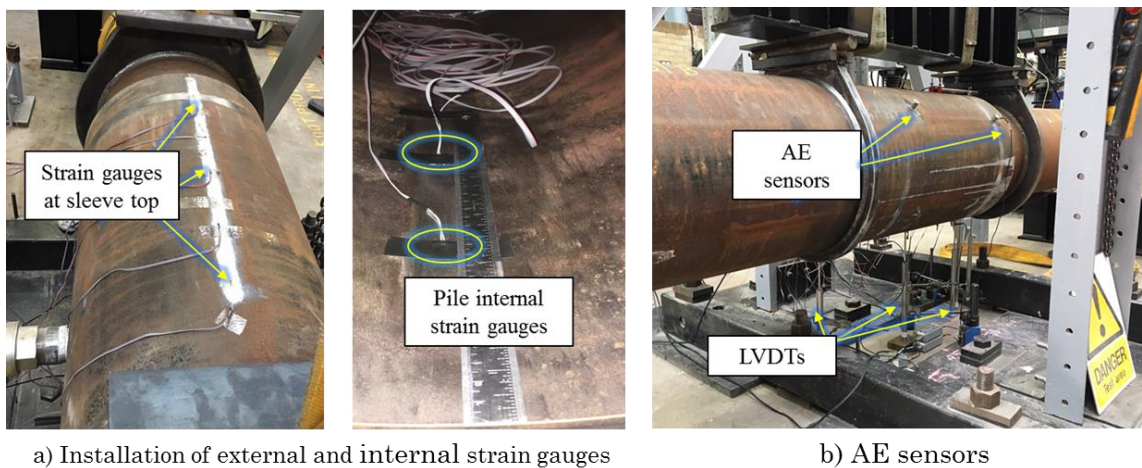


Figure 3.17: Strain gauges LVDTs and AE sensors on GC

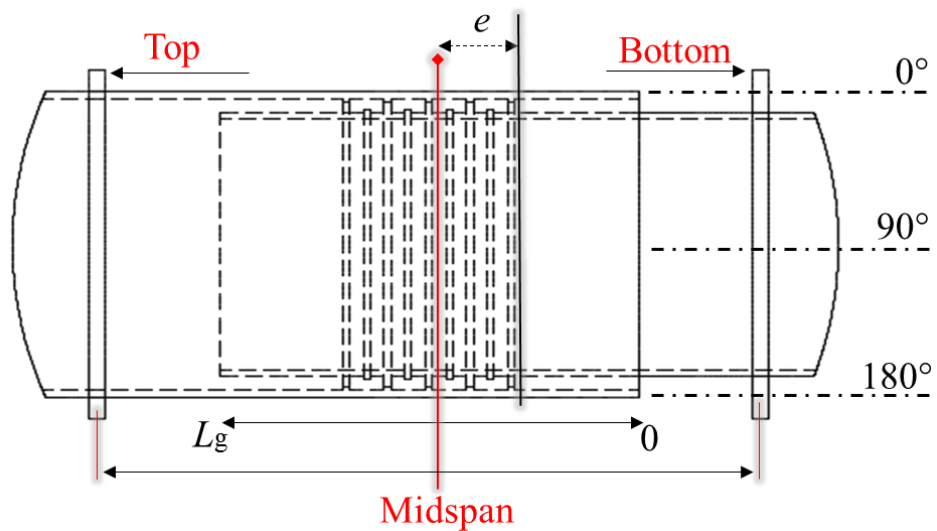


Figure 3.18: GC notation and orientation used for the experiments

## 3.9 Test protocols

All tests were performed under load control for consistency. For the static tests fixed increments of 50 *kN* were applied while the GC was in the elastic stage which led to a load ratio of approximately 1.5 *mm/min*, whereas the load rate was reduced once failure was approaching. The specimens were unloaded once failure has occurred.

### 3.9.1 Fatigue programme

The fatigue stage was performed applying reversed cyclic loads considering the fact that very limited tests with representative load protocols have been conducted to date. At the time of the tests there has been no published research work focusing on reversed bending loads. Furthermore, rather than subjecting the specimen to millions of cycles a shorter duration was elected to imitate storm events and subsequently investigate if there is any influence on the remaining bending capacity.

Selecting the appropriate load range for a fatigue test can be done by means of a nominal contact pressure ( $P_{nom}$ ) as dictated by DNV ST-0126 (2016) or by selecting a load level directly from the ultimate bending capacity ( $M_u$ ) defined by a monotonic bending test. The DNV ST-0126 (2016) approach requires limiting  $P_{nom}$  to 1.5 *MPa* at the bottom of the GC so as to determine  $M_d$ . Initially the effective spring stiffness is determined as per equation 2.3 and the subsequently equation 2.2 is used to determine  $M_d$ . In Table 3.5 the resulting ratios from both methods are tabulated for the final stage of the fatigue test which was designed to be the most detrimental to the integrity of the specimen.

Table 3.4: Fatigue bending load range during the final load stage

$P_{nom}$ [MPa]	$M_d$ [kNm]	$M_u$ [kNm]	$M_a/M_d$		$M_a/M_u$	
			Upper	Lower	Upper	Lower
1.5	~120.50	468.82	0.69	0.55	0.18	0.14

The load stages which comprised the fatigue test are shown in Table 3.5. The cyclic stress ratio for all stages was 0.8 achieving almost fully reversed loading conditions. The lower bound of the stress cycle was chosen to be slightly-smaller, thus resulting in a ratio of  $R = -0.8$  in order to account for the dead load of the turbine. Such a provision is also recommended for tubular GCs in bending by DNV ST-0126 (2016).

Table 3.5: Fatigue test load stages

Stage	Lower bound	Upper bound	$R$	Cycles
1	-16	20	-0.8	50000
2	-32	40	-0.8	50000
3	-48	60	-0.8	50000
4	-64	80	-0.8	100000
5	-80	100	-0.8	500000

All five stages were performed with a frequency of 2 Hz. Although, in real environments the load is applied on OWTs at much smaller frequencies (~0.3 Hz) Schaumann et al. (2016) noted that for tests being conducted in dry laboratory condition the loading frequency does not have an influence on the performance of the GC. Similarly, Chen et al. (2017) selected a frequency of 4 Hz while Bechtel (2017) conducted tests on axially-loaded GCs at frequency levels between 1 and 2 Hz. In the presented tests the frequency was kept constant for the whole duration as the effect of varying frequencies is not known when it comes to AE

monitoring which was part of the acquisition.

### 3.10 Ultimate bending results

The results from the initial static test (GC-1) are presented in the form of load-displacement curves along with the failure modes and strains that were exhibited. In the following sections if no reference is made to the location of the measured deflection, it will always refer to the midspan of the grouted length. In Figure 3.19 the resulting load-deflection curve for GC-1 is depicted.

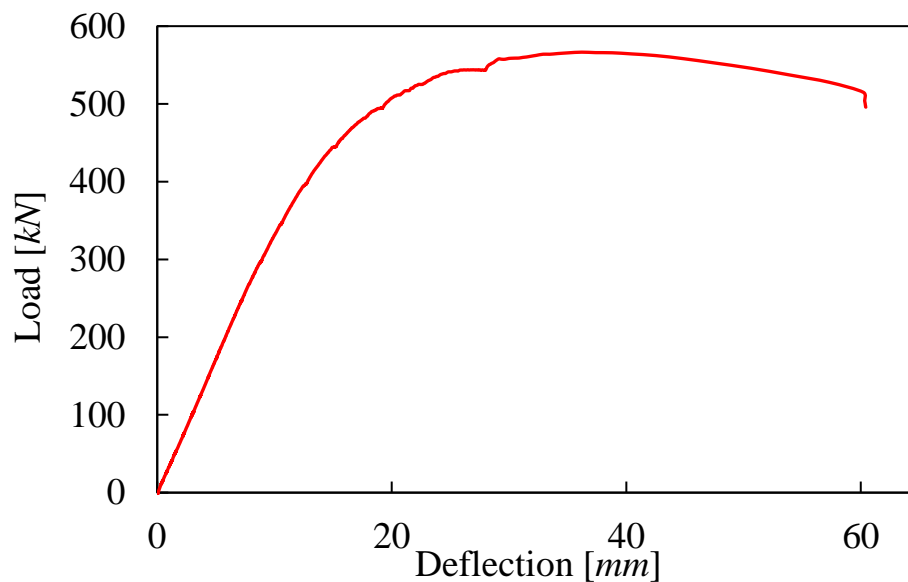


Figure 3.19: GC-1 load-deflection curve

The specimen exhibited a typical ductile-type behaviour comprising an elastic stage up to approximately 300 kN and an elasto-plastic stage until the ultimate load. The load starts to decrease once the grout struts have failed and a sudden drop occurs when pile buckling has fully developed. The joint sustained a maximum load of 566.55 kN which led to a midspan deflection of 36.20 mm. The test was stopped once the pile at the compressive side of the GC bottom buckled locally, outside the grouted region and a distinct load-drop followed.

Despite the simplicity of the geometry and concept of a GC the mechanisms that develop within a tubular joint with shear keys are quite complex owing to the multiple failures that occur. The failure modes that accompanied GC-1, were damage within the grout core in the form of diagonal cracks and crushing of the grout, interface gaps and ultimately local buckling of the steel pile. Figure 3.20 depicts the local buckling and the gap that developed at the interfaces. Such a mechanism could potentially be classified as progressive considering the successive strut failure. Following the failure of the first strut a distinct gap appeared to have developed at the pile-grout interface at the visible bottom side of the connection. Similar failure patterns and sequence have been reported by Lotsberg (2013) and Bechtel (2018).

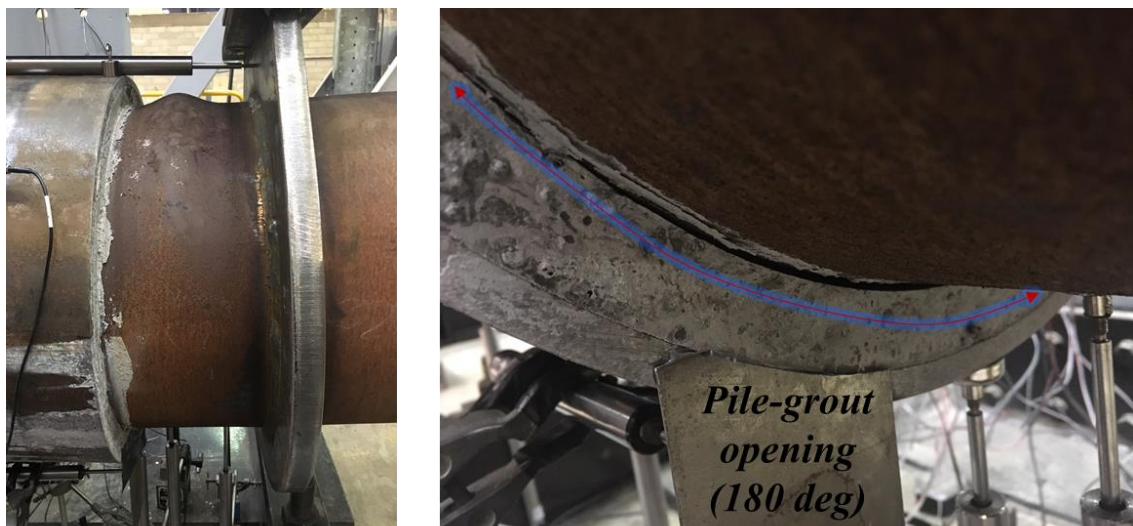


Figure 3.20: (left) Pile local buckling at GC bottom (location:  $0^\circ$ ) and (right) interface opening (location:  $180^\circ$ )

The development of the longitudinal strains are given in Figure 3.21. They are shown across the length of the connection on the bottom following the notation of Figure 3.16b. The increase of strain along the length is indicative of the load-transfer mechanism that took place from the sleeve to the pile. Owing to the radial stiffness of the steel sections and the equally spaced shear keys, a relatively

smooth transition is found.

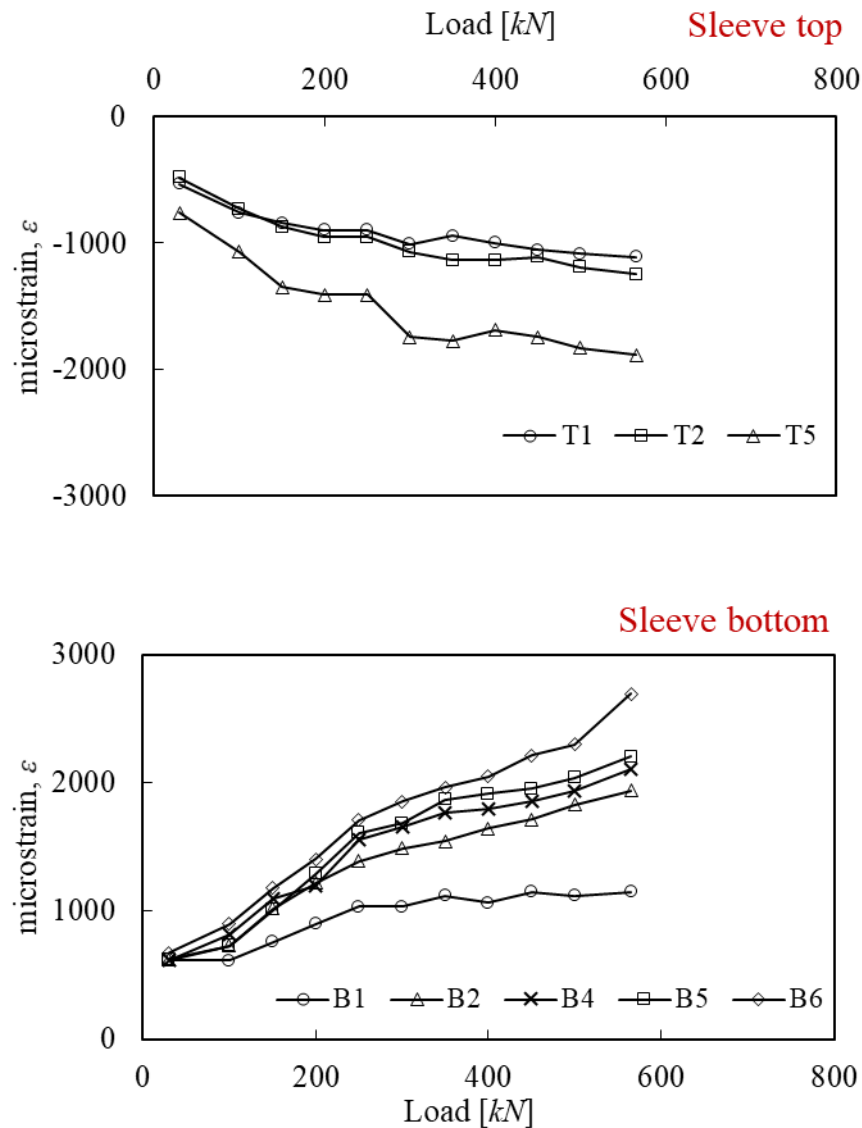


Figure 3.21: Longitudinal strains for GC-1 at sleeve top (top) and bottom (bottom)

To allow for visual inspections of the grout to be carried out, and to evaluate the condition of the enclosed grout, a section from the sleeve was removed following the test. Primarily, the visible grout was investigated for grouting related defects, such as bleeding or voids, but no obvious deficiencies were found, denoting that grout has been homogeneously distributed within the annuli. As expected the moment-transfer between the sleeve and the pile was mainly accommodated by the shear keys in the vicinity of the grouted region as implied by the location of

the cracks. Diagonal cracks occurred between successive shear keys indicating the successive strut failure that was mentioned earlier. The failure modes for GC-1 are summarised in Figure 3.22 and Figure 3.20.

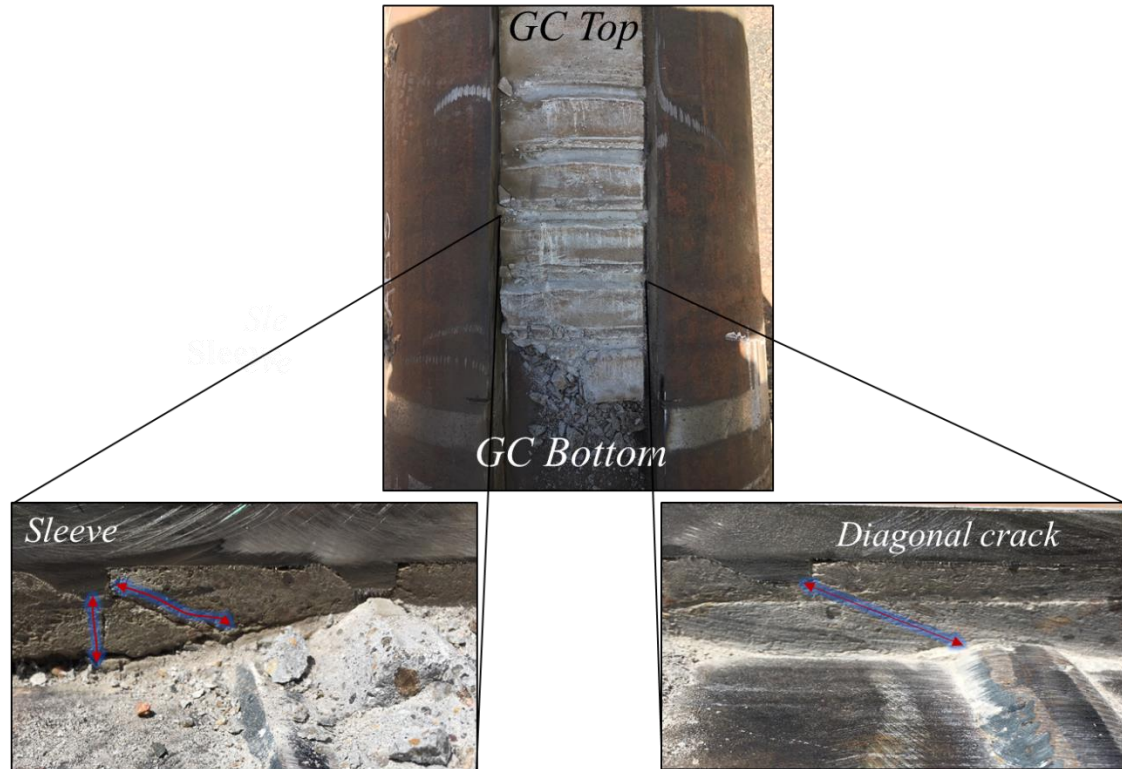


Figure 3.22: Grout cracking patterns following inspection of GC-1

### 3.11 Fatigue bending results

Herein, the global behaviour of GC-2 during the loading cycles of the fatigue test is presented by means of displacements and specimen stiffness ( $k_{gc}$ ). During the cyclic test measurements of load and deflection were directly taken from the actuator's embedded load-cell and transducers and were exported to a dedicated software, MTS elite-suite™ and are the ones used in this section. Displacements will typically refer to the ones taking place in the vertical direction unless otherwise stated. The remaining LVDTs were located as per Figure 3.16a.

In Figure 3.23-Figure 3.26 the load-displacement curves reveal an overview of the

global behaviour of the GC during load levels (1-5) of the cyclic protocol. The negative load values on each curve refer to the tensile part of the loading cycle whereas the positive corresponds to the compressive part. The figures aim at highlighting the transition between the load levels. Each curve does not include all the cycles that were performed during the level for illustration purposes.

The GC depicts a linear behaviour, which is more pronounced up to a level 3. A slight hysteresis can be noticed during the final cycles, however no global deterioration was observed. By completion of the cycles no obvious radial cracks or irreversible interface gaps have developed on the visible bottom side of the joint. The small deviation between the two curves of the final level is attributed to the test frame rather than loss of stiffness of the GC. Owing to the scale, size of the connection and the reversed applied loads, it was required to readjust its position at evenly timed intervals. Thus, it was concluded that the GC has survived the total number of cycles with no obvious degradation.

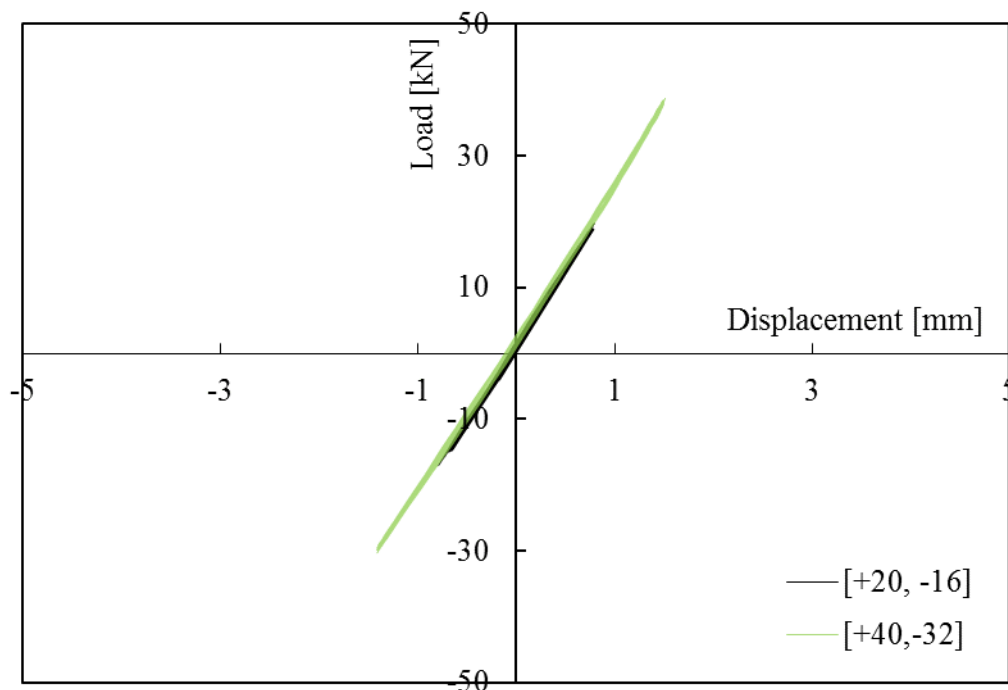


Figure 3.23: Load versus displacement curve during stages 1 and 2

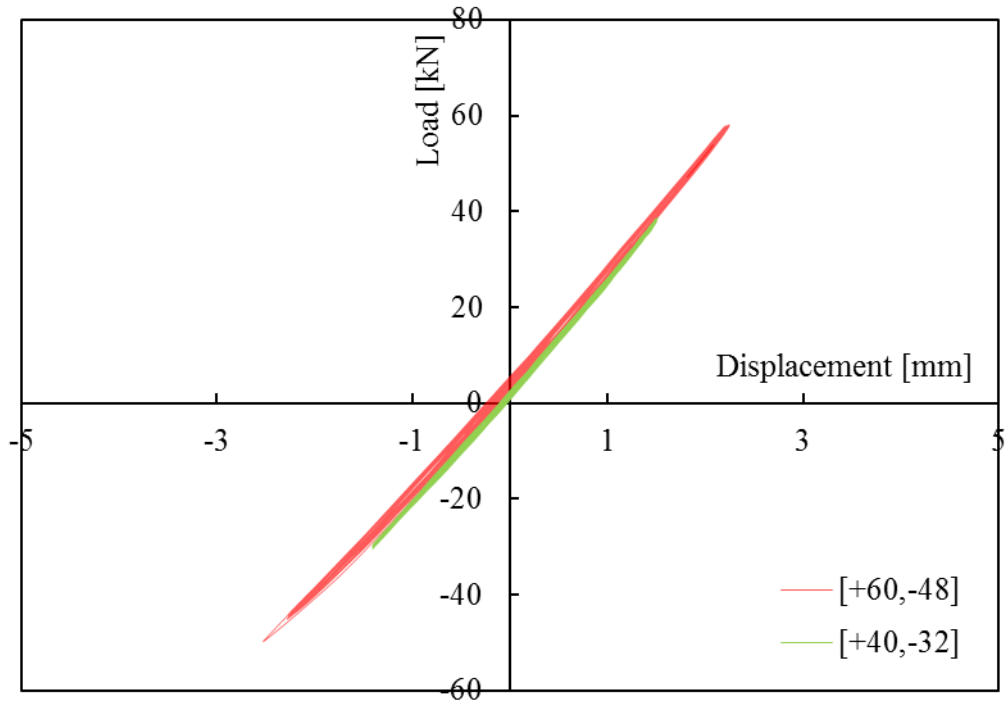


Figure 3.24: Load versus displacement curve during stages 2 and 3

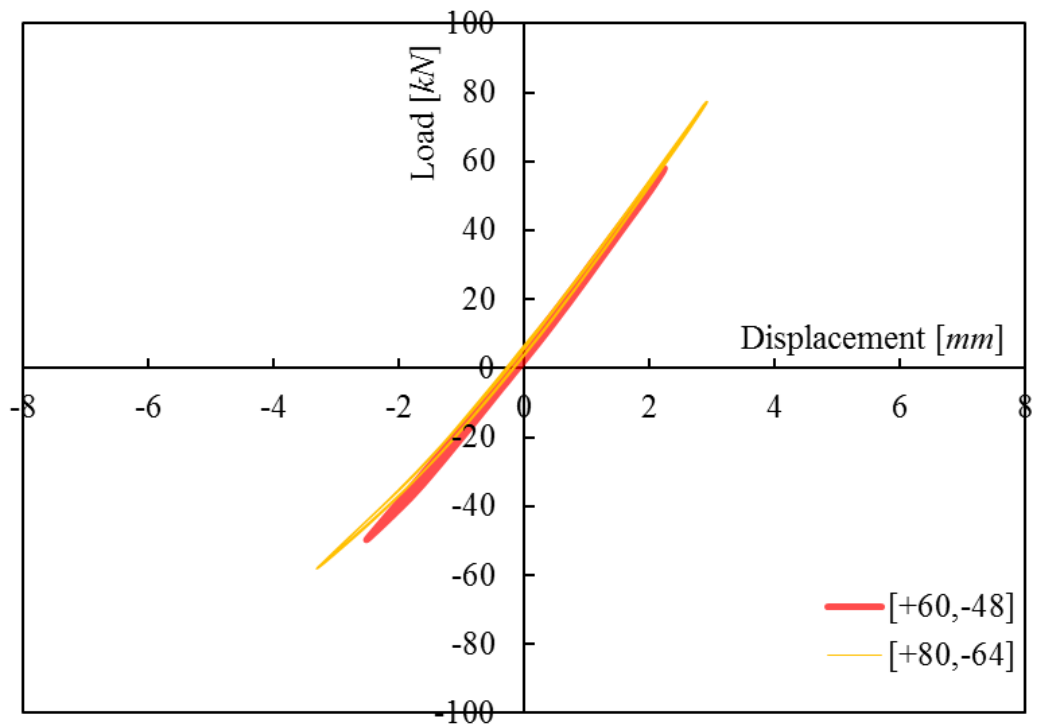


Figure 3.25: Load versus displacement curve during stages 3 and 4

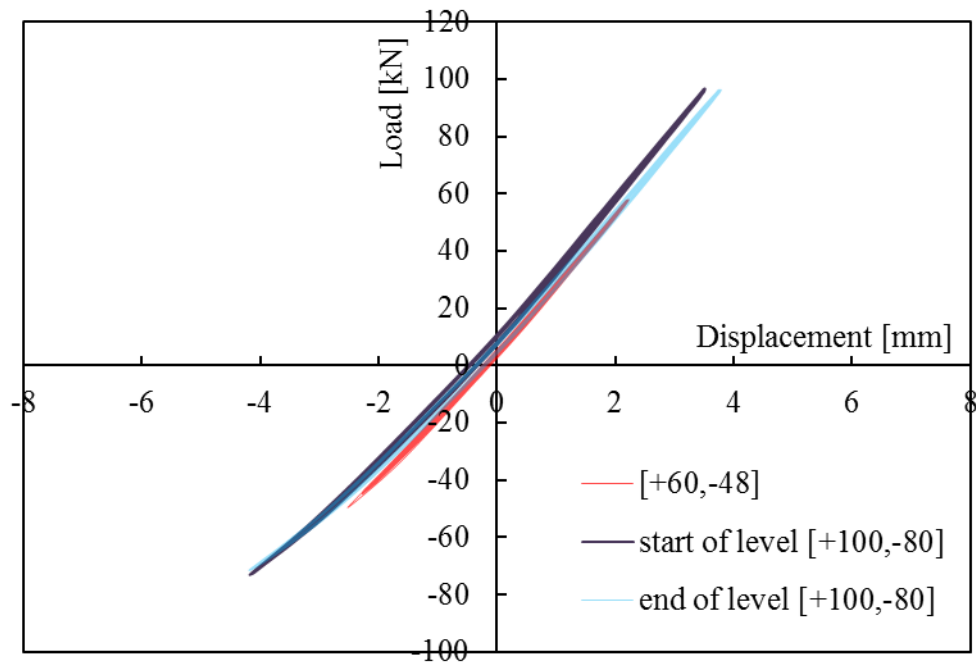


Figure 3.26: Initial and final cycles of stage 5 and comparison with stage 3

In order to provide a better understanding of the specimen's performance during all the cycles of each level, the stiffness of the GC ( $K_{gc}$ ) was calculated following the equation below:

$$K_{gc} = \frac{\Delta F_{(max-min)}}{\Delta u_{(max-min)}} \quad 3.1$$

In Figure 3.27-Figure 3.29 the equivalent stiffness is illustrated. It is confirmed that no damaged occurred on the GC surviving the applied cycles as no distinct drops in stiffness can be found. Any slight deviations during the load levels are a result of bolts becoming loose or repositioning of the specimen. No obvious major radial cracks were present after the completion of level 5 on the visible end of the GC, apart from a series of hairline cracks. However, some audible cracks did occur during the final two levels. Additionally, no permanent gaps on the pile-grout interface nor any axial slippages could be detected.

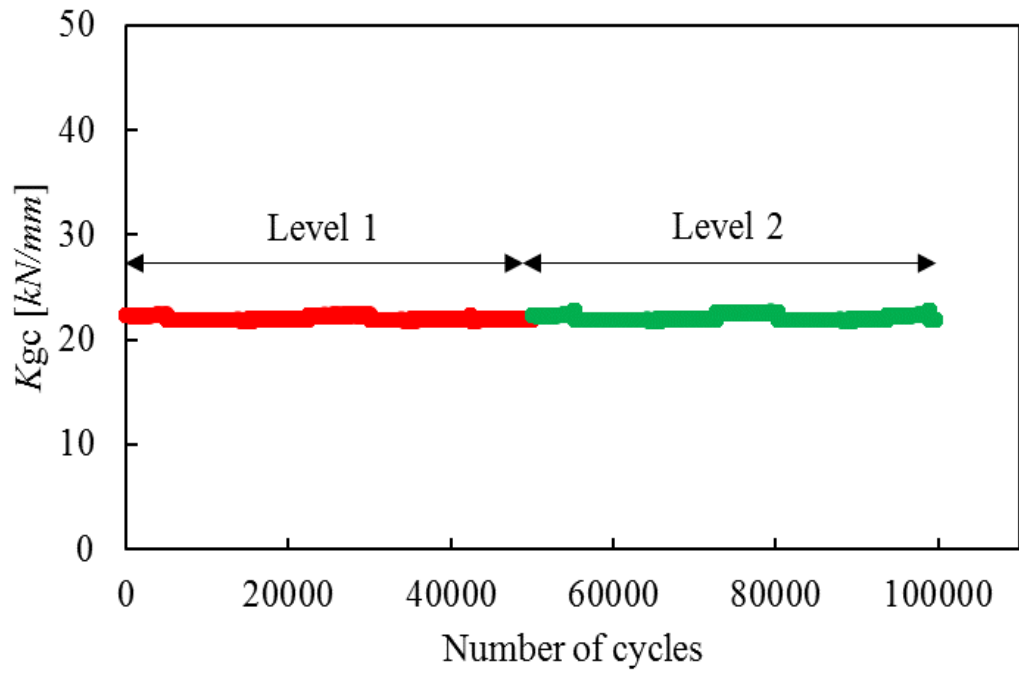


Figure 3.27: Specimen stiffness for Levels 1 and 2

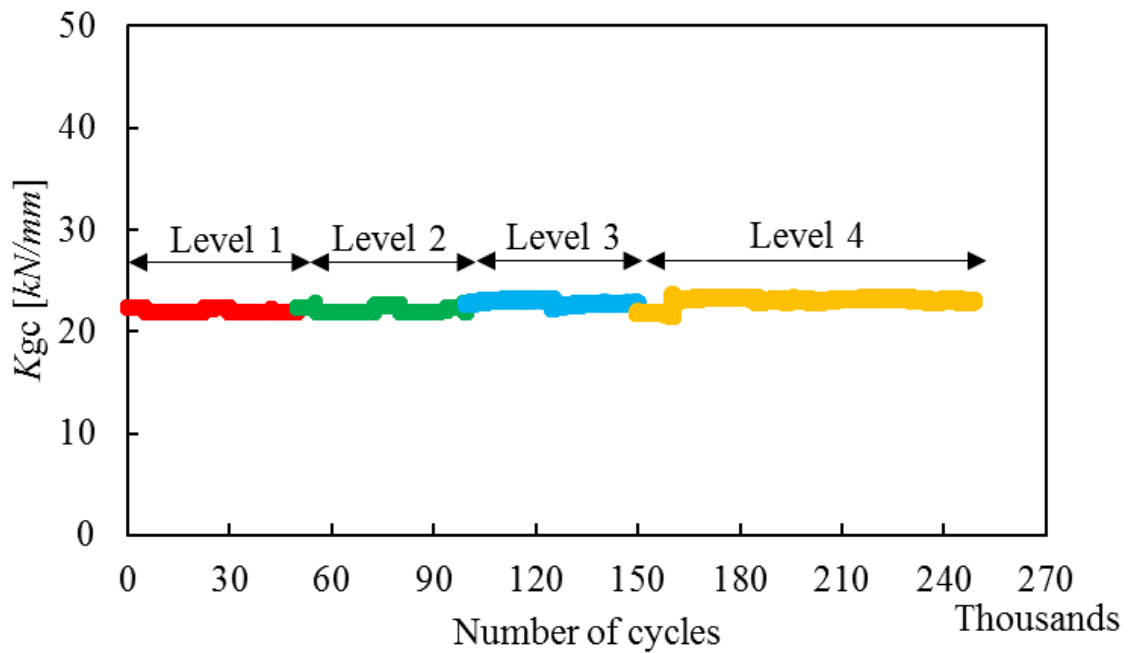


Figure 3.28: Specimen stiffness at different load levels

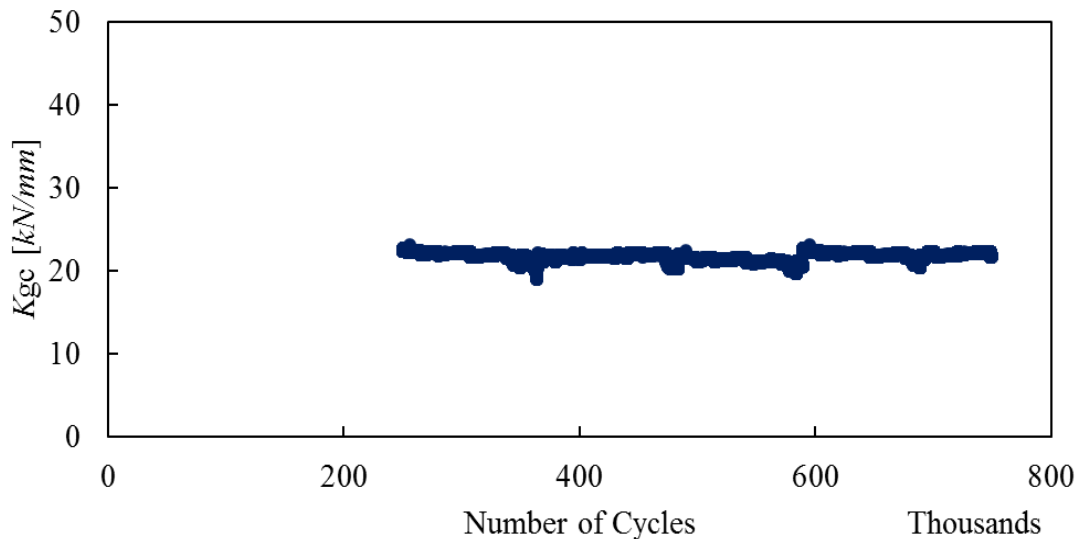


Figure 3.29: GC stiffness during load level 5

### 3.12 Residual bending capacity

Following completion of the fatigue test and due to GC-2 surviving the applied cycles, the joint was transferred to the static test rig to be subjected to a strength test, in order to assess if the loading protocol had an influence on the remaining bending capacity.

The specimens exhibited almost identical behaviour and ultimate bending strengths as shown in the load-deflection curves of Figure 3.30. Similarities on the behaviour were even more pronounced when it comes to the progressive failure patterns that were described in section 3.10. Failure of the shear key struts was progressive and was accompanied by distinct drops corresponding to the four pairs of effective shear keys which are denoted in Figure 3.30 by green arrows. Characteristic failures of the diagonal struts that develop between pile and sleeve shear keys initiated at approximately  $396.8 \text{ kN}$  corresponding to a  $12.6 \text{ mm}$  deflection. The second and third strut failed at  $442.5 \text{ kN}$  ( $15.0 \text{ mm}$  deflection),  $499.7 \text{ kN}$  ( $18.6 \text{ mm}$  deflection) respectively and the fourth at  $543.2 \text{ kN}$  ( $28.1 \text{ mm}$  deflection). The progressive strut failure is superseded by the gradual interface opening between pile and sleeve until a similar pile buckle occurred outside the

GC region. The ultimate moment along with the maximum load and deflection each GC sustained are given in Table 3.6.

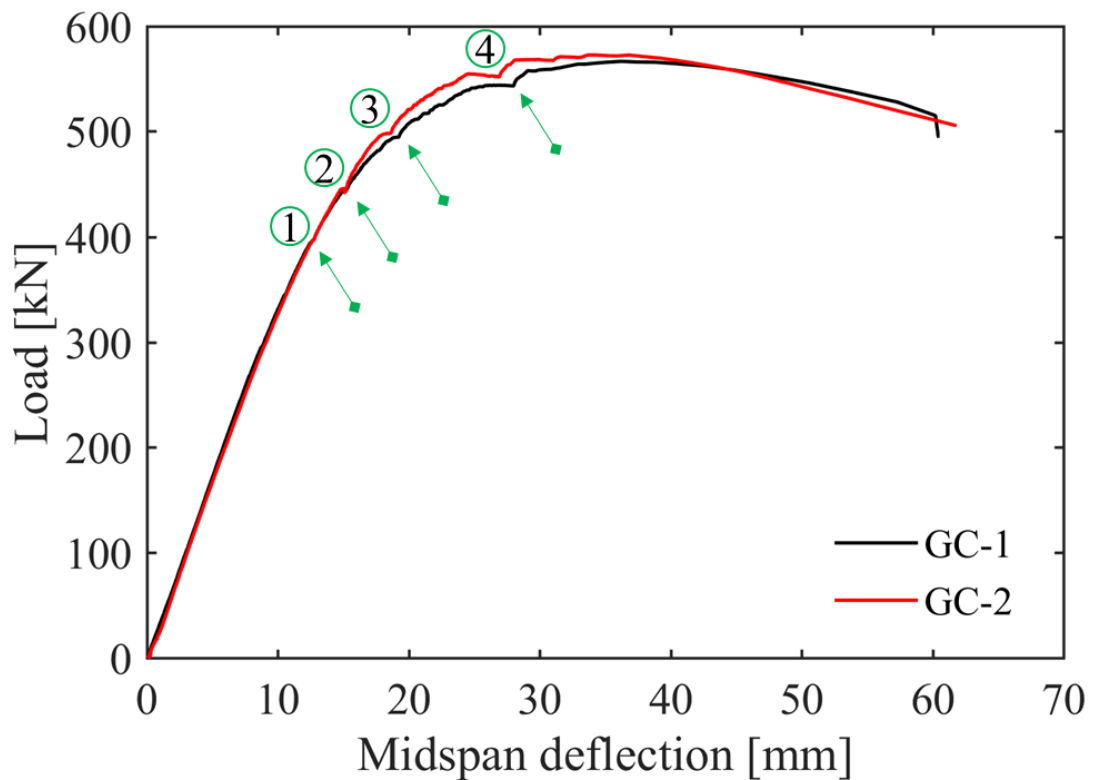


Figure 3.30: Load-midspan deflection curves for GC specimens

Table 3.6: Ultimate load and moment corresponding midspan deflection for each GC

Specimen ID	$F_u$ [kN]	$\delta_u$ [mm]	$M_u$ [kNm]
GC-1	566.55	36.20	468.82
GC-2	572.60	34.17	473.82

As with the first specimen, in order to assess the internal grout a section was removed from the sleeve and the findings are summarised thereafter. Initially, a slight misalignment of the shear keys (see Figure 3.31) of a few millimetres was found which was a result from the upright grouting position. However, considering the results and the numerical simulations which are presented in Chapter 6 the ultimate load was not influenced. Such misalignments do take

place in offshore environments and are often considered in the design process. Typically, misalignments up to 5% of the nominal distance between shear keys are accounted by the material factors (DNV ST-0126, 2016). Similar provisions are taken for position misalignments leading to uneven grout thickness along the circumference. Both cases are examined in section 6.8 by means of numerical models.



Figure 3.31: Shear key misalignment following visual inspection for GC-2

Considering both specimens, some hairline cracks were found in longitudinal directions on the outer surface of the grout as indicated in Figure 3.32. The crack patterns that were found for the second specimen confirm the findings and failure mechanisms reported in the first test (see Figure 3.34b-d). The excellent grout distribution was also confirmed as shown in Figure 3.34a. Failure of the grout around the shear keys is shown in Figure 3.35, where crushed grout wedges at the tip of shear keys were found for GC-2. De-bonding occurred at the bottom of the connection as per Figure 3.33. Considering the data from AE and the high-speed camera the opening was accelerated following the progressive failure of the individual diagonal struts and the interface opened significantly along the length. For GCs subjected to considerable bending moments this justifies the use of shear keys in the middle third of the GC, otherwise this would result in a pair of shear keys being ineffective. Following the interface gap buckling of the pile occurred outside of the connection for both specimens (Figure 3.33).

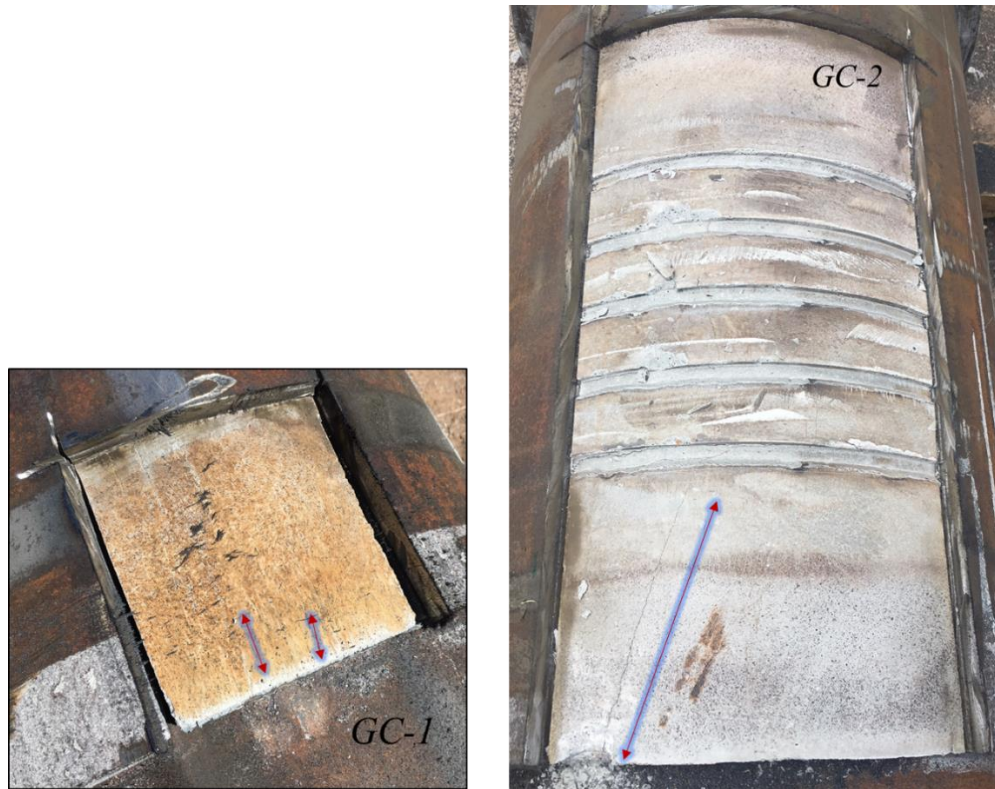


Figure 3.32: Hairline cracks on the outer grout surface of GC-1 (left) and GC-2 (right)

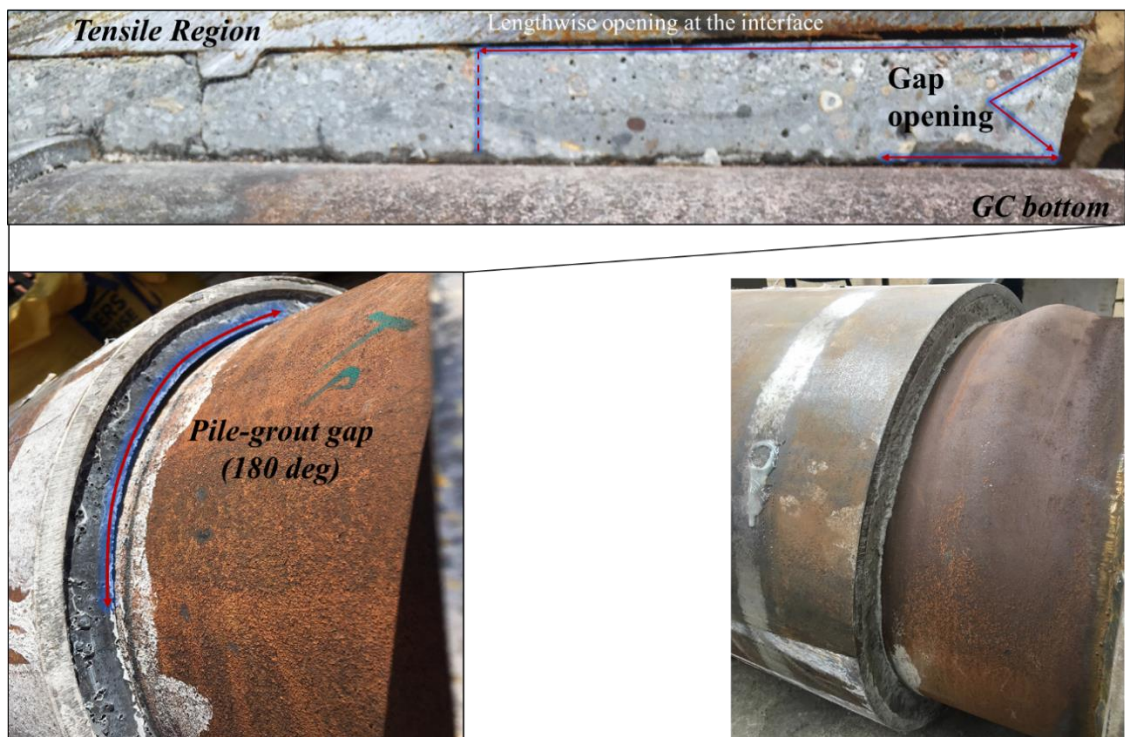


Figure 3.33: Interface opening along the length of the connection in cut view (top) and side view (bottom-left) and pile buckling (bottom-right)

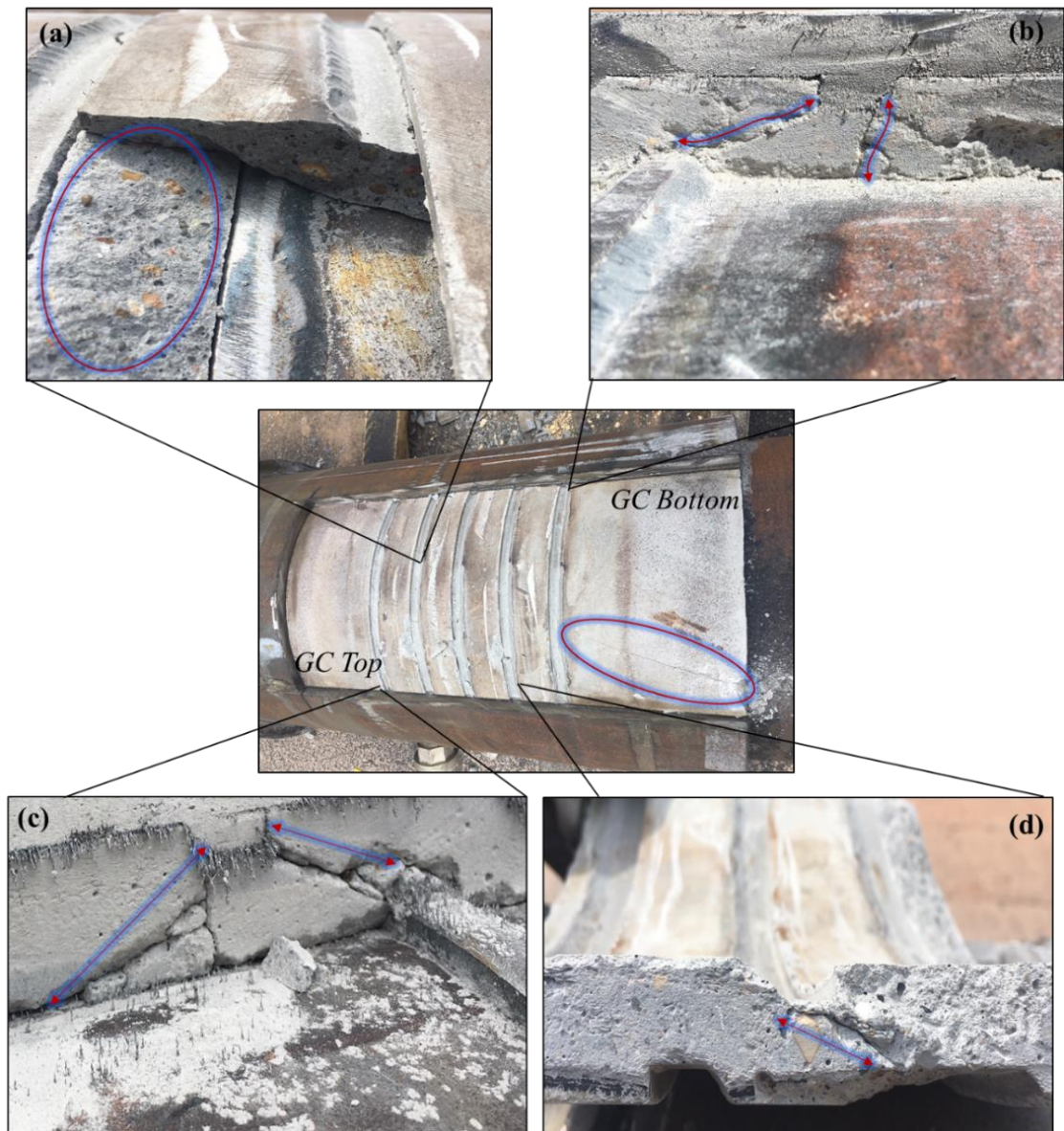


Figure 3.34: Visual inspection of GC-2 core. a) Evenly distributed aggregates at the middle of the grouted length, b-d) Grout crack patterns and failure surfaces between two opposing shear keys at bottom and top locations

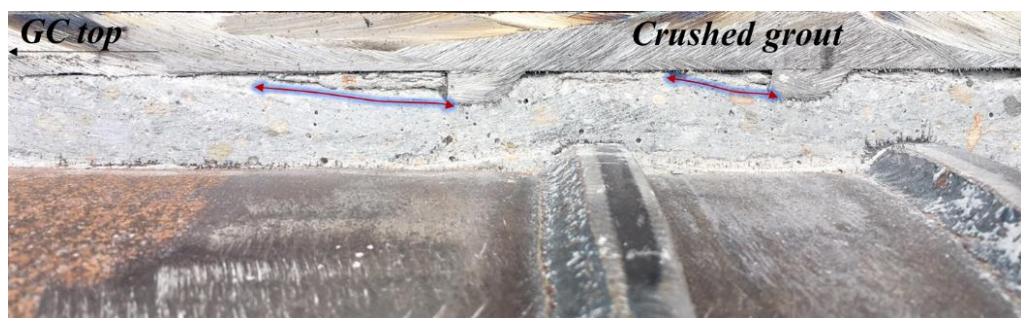


Figure 3.35: Crushed grout in front of shear key tip (GC-2)

# 4 ACOUSTIC EMISSION MONITORING

## 4.1 Overview

Chapter 4 introduces the monitoring aspect of the experiments and the SHM approach which was employed during testing. The results will be presented in the form of a pilot case-study to illustrate the capabilities of acoustic monitoring for OWTs. Initially, some theoretical aspects on the working principles of AE along with relevant literature on specialised topics are presented, followed by the analysis of the experimental tests. The post-filtering and processing rationale and methods that were employed are also presented in detail. More specifically, sections 4.2 and 4.3 introduce the notation and fundamental principles on which the subsequent analysis is based. In section 4.4 a description of the sensors, instrumentation and Data Acquisition System (DAQ) is given. In 4.5 the most important KPIs, as identified within the context of these tests are presented and discussed. The statistical analysis which was conducted is laid out in detail in sections 4.6 and 4.7 and finally, the  $b$  and  $Ib$ -value analyses are presented in section 4.8.

## 4.2 Acoustic Emission principles

AE is one of the established techniques which belong to the family of SHM that is being employed for inspection purposes on a variety of operating civil engineering structures (Behnia et al., 2014). The working principle of AE is based on elastic waves which are emitted from a structure or component when it is exposed to an external excitation. This local emission can only be detected by a sensor when it is being formed or developed. The emitted signals are detected through piezoelectric sensors which are directly attached on the structure of interest. For this purpose, epoxy-based adhesives are commonly selected to mount the sensors. Subsequently, the sensors convert the detected transient elastic waves to weak electric signals, which are then enhanced to a pre-defined gain by means of amplifiers. The electric signals are continually logged and visualised through dedicated AE software (Assimakopoulou and Philippidis, 2010). A schematic of the AE DAQ which was used during the tests is shown in Figure 4.1.

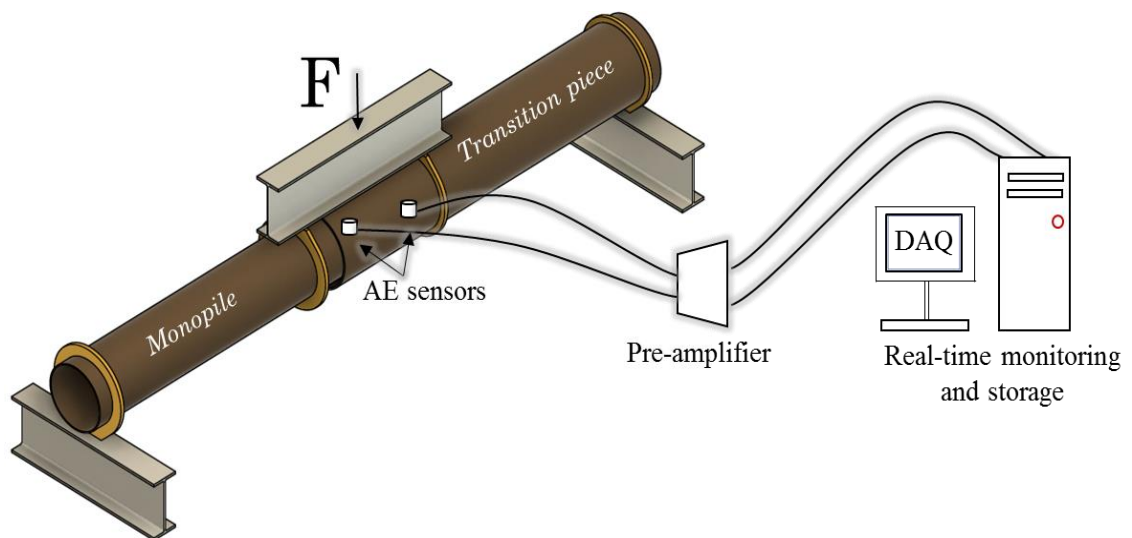


Figure 4.1: Schematic layout of AE instrumentation and acquisition system

Applying AE and acquiring acoustic measurements is a fairly simple procedure owing to technological developments and does not involve significant cost,

however collecting useful and reliable data requires particular care. Careful consideration and sound engineering practice is necessary when it comes to sensor location, type and post-processing techniques. Processing of AE data can be carried out using two approaches; Signal and parameter-based processing. Signal processing can often prove to be impractical or even impossible depending on the application, as the AE signals need to be processed and studied individually (Behnia et al., 2014). This can be more pronounced for field measurements owing to noisy backgrounds resulting in excessive amount of logged data. Noise-related signals are also present during laboratory tests, however due to the controlled environment it is easier to filter out unwanted signals prior to testing or during the post-processing step (Shiotani et al., 2001; Ziehl and Pollock, 2012; Aggelis et al., 2015).

Alternatively, characteristic signal features or parameters which are extracted from the AE waveforms in real time can be used to perform a parametric analysis (Aggelis et al., 2015). Such features can be extracted from time series and contain useful information on the shape of the AE waveform which allow for quantification of the signals (Aggelis et al. 2015; Li et al., 2017). Some of the main AE parameters are the peak amplitude (A), duration (DUR) and rise time (RT). A short description of the notation used is given in section 4.3 to assist the reader with the subsequent analysis.

For this study a parametric approach is elected and different post-processing techniques are investigated for the analysis of the data. Initially, signal features are examined as potential KPIs for damage assessment and secondly, a statistical analysis of AE descriptors is performed. Reference to KPIs is made to those parameters that were found to be correlated with damage evolution within the GCs and a change in value indicates any form of degradation within the structure. A parametric correlation with the structural data is also performed to

enable the identification of the failure mechanisms that took place.

### 4.3 Acoustic emission notation

In AE nomenclature the recorded occurrences are often referred to as AE events or hits. As expected, the number of hits can provide an initial indication of the activity that took place. Such indicative measures are useful for structures like tanks and vessels (Aggelis et al., 2015). However, this is not sufficient for other types of civil engineering structures such as OWTs or bridges for which identification of damage mechanisms the assessment of several other characteristics is required. The key descriptive features of an AE signal are illustrated in Figure 4.2, whereas the main signal parameters which are often employed in parametric analysis to quantify the signals along with frequency features are the following: AE Energy, Peak Amplitude ( $A$ ) in  $V$ , Rise time  $RT$  in  $\mu s$ , Counts, RA (Rise time to amplitude ratio) in  $\mu s/dB$ , Duration in  $\mu s$  and Average frequency (AF) in  $kHz$ .

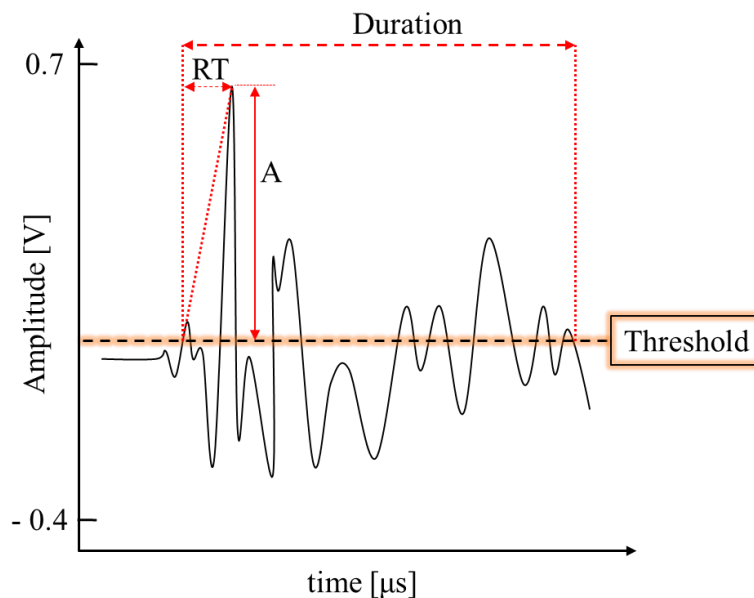


Figure 4.2: AE signal parameters

When it comes to the energy of the AE signals there are several parameters that

typical AE software calculate and extract. For the employed DAQ from Physical Acoustics Corporation (PAC), USA, AE Energy is an artificial quantity with no direct physical meaning whereas the absolute energy measured in  $aJ$  is the actual energy contained under the envelope formed by the signal. By peak amplitude we refer to the voltage value which corresponds to the peak of the signal. Duration is the time expressed in  $\mu s$  between the first and last intersections of the signal with the threshold line. Rise time is the time between the first intersection of the threshold until the peak amplitude is reached and finally, Counts are the total number of intersections of the signal with the threshold limit.

#### 4.4 Sensors and instrumentation system

The instrumentation that was used during the tests involved a four-channel acquisition panel from PAC and a dedicated software for live monitoring and visualisation, AEwin™ (PhysicalAcoustics, 2018). A total of four AE resonant transducers – type PAC50a, were mounted on the steel sleeve at different locations along the connection as shown in Figure 4.3. As crack and damage degradation was the main focus of the study rather than source location, two sensors on the tensile and compressive sides were considered sufficient. The operating range of the sensors was from 150 to 700 kHz. The sleeve on both GCs was prepared by mechanically cleaning the surfaces prior to attaching the sensors. Thereafter, a rapid setting two-component epoxy was applied to attach them on top and bottom locations of the GC.

The threshold was set at 45 and 50 dB for GC-1 and GC-2, respectively, to eliminate any background interference from the laboratory environment. GC-2 threshold was set higher than that of the first test to reduce the number of logged waveforms. Considering background noise, the gain was set to 40 dB using pre-amplifiers (see Figure 4.3) along with a signal filter from 100 to 1000 kHz and a

sampling rate of 5 MSamples/s.

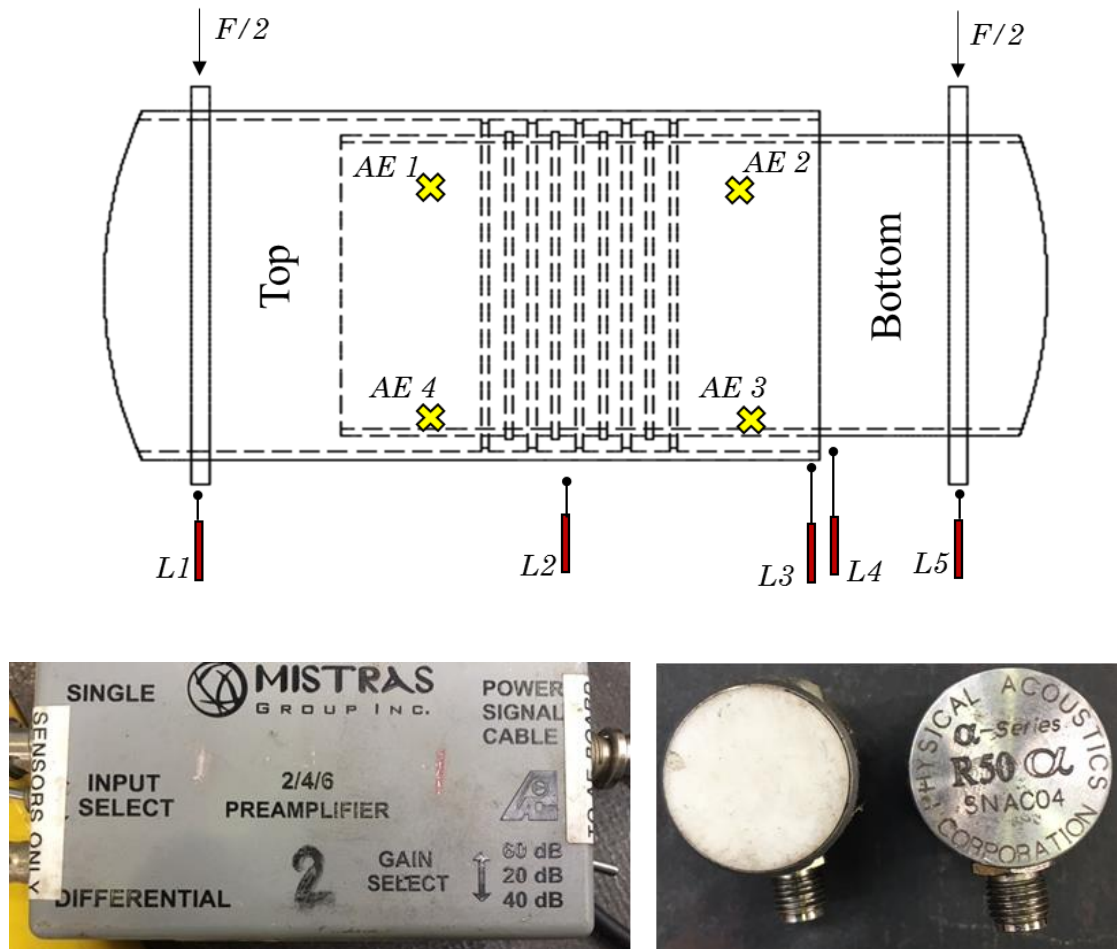


Figure 4.3: AE sensor location along the grouted length (top) and pre-amplifier used to set signal gain along with R50a sensors (bottom)

For calibration purposes and to ensure that the spurious hits due to refraction or scattering are not recorded, the Hsu-Nielsen source method was conducted at various locations prior to testing. The main acquisition settings which were used during the tests are tabulated in Table 4.1.

Table 4.1: Acquisition parameters

Parameter	Unit	Value
Pre-amplification	<i>dB</i>	40
Threshold	<i>dB</i>	45, 50
Analogue filter	<i>kHz</i>	100-1000
Sampling rate	<i>MSamples/s</i>	5
Pre-trigger	$\mu s$	256
Length	<i>k</i>	10000

## 4.5 Key Performance Indicators (KPIs)

The peak amplitude ( $A$ ) of an AE wave is a critical waveform parameter linked with the intensity of the signal which is widely used to evaluate the AE intensity or quantify damage. The amplitude of each AE signal corresponds to an energy content strongly-dependent on the event generating damage, the distance between the event and the sensor as well as the attenuation of the wave (Shiotani et al., 2007). However, previous research by Muralidhara et al. (2010) has highlighted that the magnitude of an elastic wave can vary in energy content. To demonstrate that argument an example is shown in Figure 4.4, where amplitudes of the same magnitude appear to be with varying energy contents. Therefore, it is easily appreciated that isolated peak amplitudes of events must be treated with care as those are not a clear indication of damage within a structure, hence signal energy is more representative and useful as a KPI.

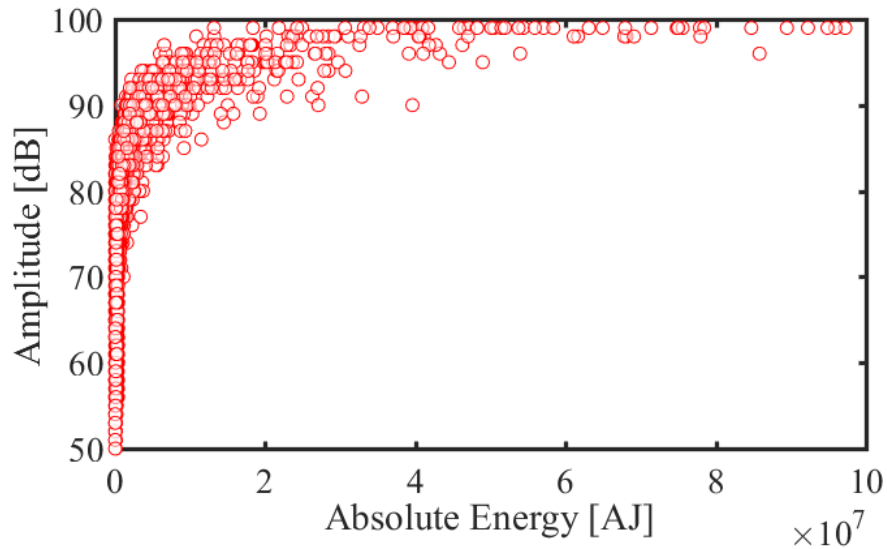


Figure 4.4: Amplitude against absolute energy - AE4 sensor specimen GC1

#### 4.5.1 Acoustic Emission events and energy

For post-filtering purposes from the logged data, those with zero AE or PAC energy were neglected as those represent spurious events rather than real emissions. Sensor AE3 – located at the bottom side of the GC and the tensile vicinity, acquired the largest amount of data, which can be linked to the proximity of the sensor with the damage source.

The recorded AE activity for both GC specimens under examination increased while the applied load was incrementally applied as expected. This is demonstrated in Figure 4.5, where the number of AE events for GC-1 are plotted per unit time. It is worth highlighting that during the first stages a large number of hits were recorded which can be attributed to the S5R content and aggregate size (up to ~5 mm) which possibly provoked additional AE activity. This was adjusted in the second test by increasing the threshold as discussed in section 4.4.

At first small populations of events were monitored which can be attributed to the grout's brittle nature and content. Those can be associated with formation of cracks within the core at a microscopic level and friction generated between the

grout-steel interfaces. The recorded hits increased rapidly once the applied load reached half of the connection's capacity. Failure mechanisms that excited the growth of AE signals are related to transition from micro to macrocracking and grout crushing. Once closer to failure a distinct gap developed between the pile and grout and finally pile local buckling occurred.

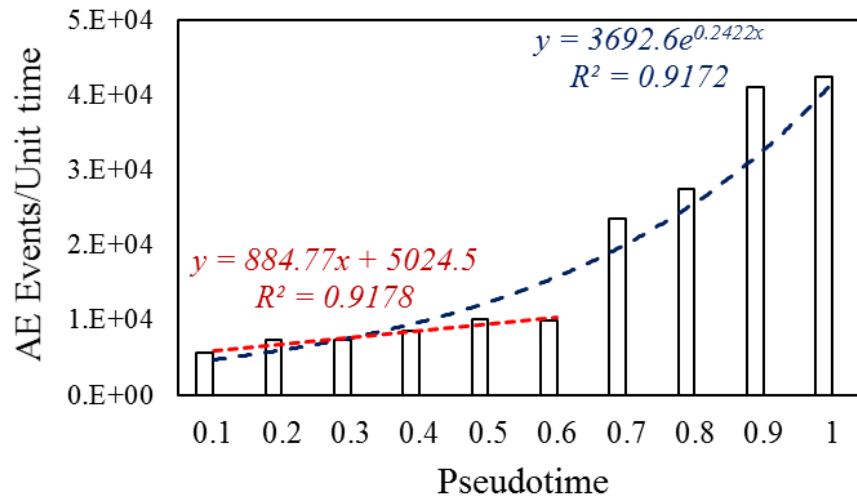


Figure 4.5: AE events per unit time (GC-1)

Although the number of events or counts is a useful indicator, it does not provide information on the intensity of the individual signals hence conclusive deductions cannot be made (Bagherifaez et al., 2014). In addition, due to the size of the specimens, the test set-up which involved roller supports, spurious hits could have been recorded, in particular those with large durations. To that extent alternative AE parameters can be used to assess the condition of the GCs. Those are the duration of the signal, the cumulative energy, the root mean square (RMS) of voltages and finally the cumulative signal strength (CSS).

The scatter diagram in Figure 4.6a provides some further insight on the integrity of the grout annulus and the damage growth. The individual data points represent the duration of each event for the entire time series. It is evident that during the formation of first microcracks emitted low-duration and a limited of events. Once the severity of damage increased a significant number of events was

recorded. These results suggest that duration is highly-sensitive to damage and contains useful information on the different stages that took place. Figure 4.6b demonstrates that for both GCs an increase in amplitude reflects on higher counts. A smaller population of events is presented for GC-2 due to the slightly different settings used in the acquisition set-up in order to reduce the recorded emissions, however the trends for both specimens are of the same patterns.

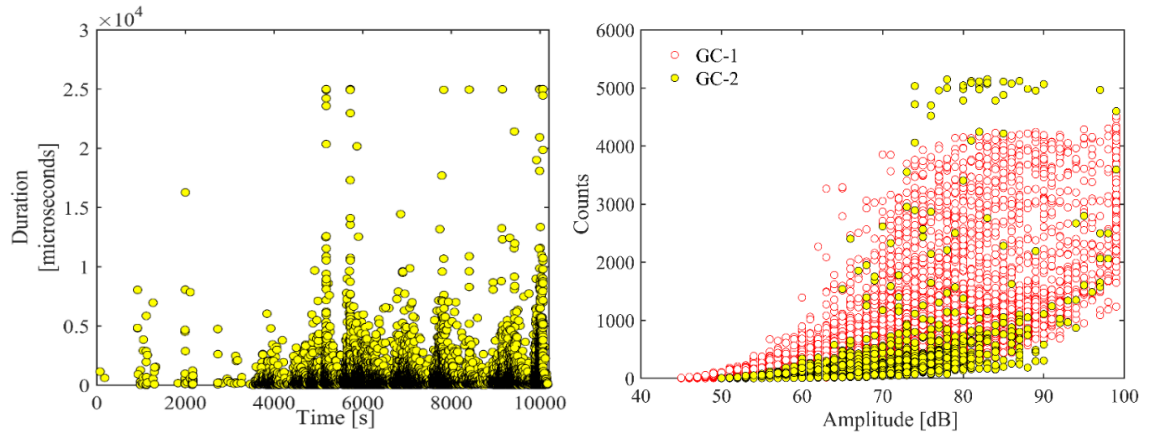


Figure 4.6: Duration of AE signals against time for GC-2 (left), Cross plot of amplitude against counts (right)

If we now turn to the energy of the AE signals as illustrated in Figure 4.7 the gradient change is evident once higher-energy content waveforms were received. The cumulative energy from two sensors which are attached in opposing regions of the grouted length is compared. AE2 recorded slightly lower activity, however increased rates were captured simultaneously. The magnitude variation can be associated with the proximity of the sensors to regions where more intensive cracking occurred between opposing shear keys. Additionally, AE3 was closely located to the bottom of the connection where de-bonding at the interface between pile and grout occurred.

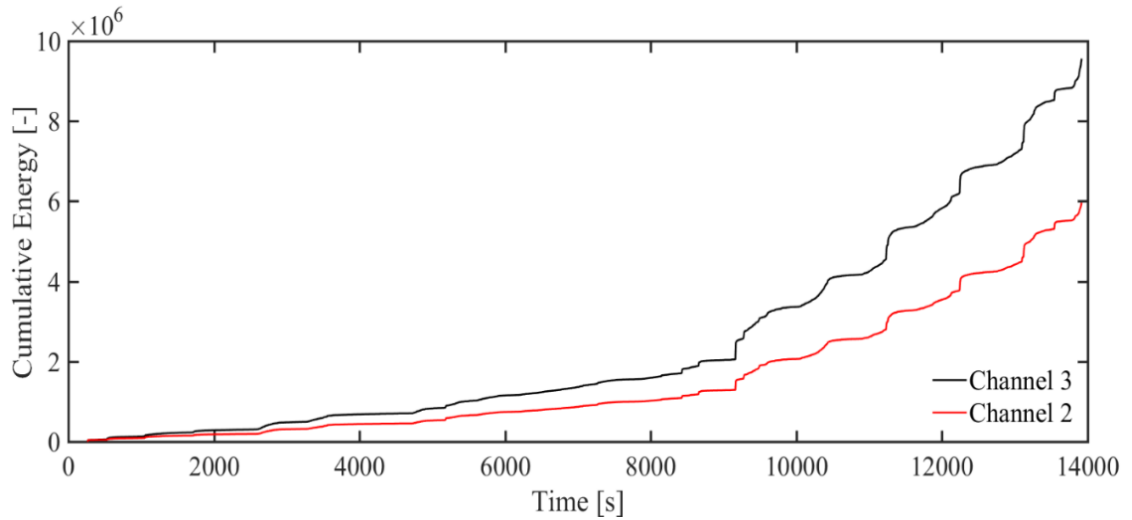


Figure 4.7: Cumulative energy from GC-1 at the tensile (AE3) and compressive side (AE2)

Larger growth rates correspond to larger AE populations which are commonly associated with damage. Consequently, steep peaks can be related to macrocracking events especially at earlier stages. An exponential trend of growth for the cumulative energy was also found for GC-2 (Figure 4.8), which is in agreement with findings from earlier studies (Aggelis et al., 2011). The cumulative energy is found to increase with increasing load levels as failure approaches. Identical growth rates were found for both GCs.

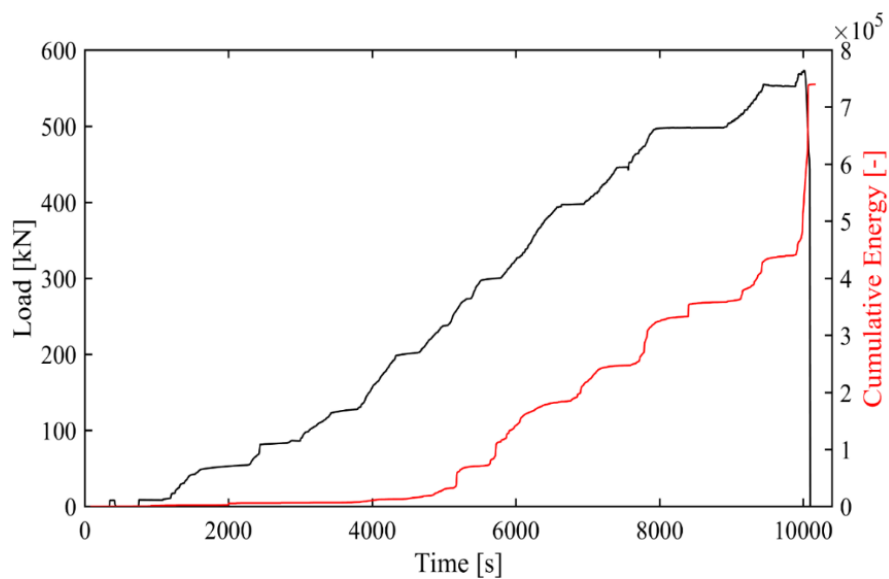


Figure 4.8: Load against cumulative energy (AE3) for GC2

## 4.5.2 Root Mean Square (RMS) analysis

An additional waveform parameter that was investigated is the RMS of captured voltages. Results from previous studies indicate an interesting correlation between RMS and ultimate loads. It is highlighted that when failure is approaching, a considerable increase in RMS can be noted (ElBatanouny et al., 2014; Aggelis et al., 2015). This is due to the fact that RMS is directly related with the signal energy.

RMS values at specific instances of the tests are used instead of the complete time series and its data point represents one hit. The first stage corresponds to the elastic stage of the test and load levels below 100 *kN*. The second stage contains values recorded at 200-250 *kN* and finally the third, after 400 *kN* were reached (Figure 4.9). In Figure 4.10, the RMS is plotted against the peak amplitude for GC-1 (top) and GC-2 (bottom) during three different stages of the flexural test. The three levels were selected considering the findings from the cumulative energy and duration distribution of the events. It is easily identified that increasing values of RMS occur once failure is approaching. Similar trends were noted for the duration and energy results as shown in section 4.5.1. However, RMS values increased significantly from stages 1 and 2 to the final stage when failure was approaching. This suggests that RMS could be implemented in industrial applications as a KPI in monitoring tools in order to assess the condition of the grout and prevent catastrophic events. The maximum values of RMS for both specimens during the three stages are tabulated in Table 4.2.

Table 4.2: RMS values for GCs during bending tests

Specimen ID	RMS [V]		
	Stage 1	Stage 2	Stage 3
GC-1	0.022	0.0442	0.2654
GC-2	0.0118	0.046	0.2134

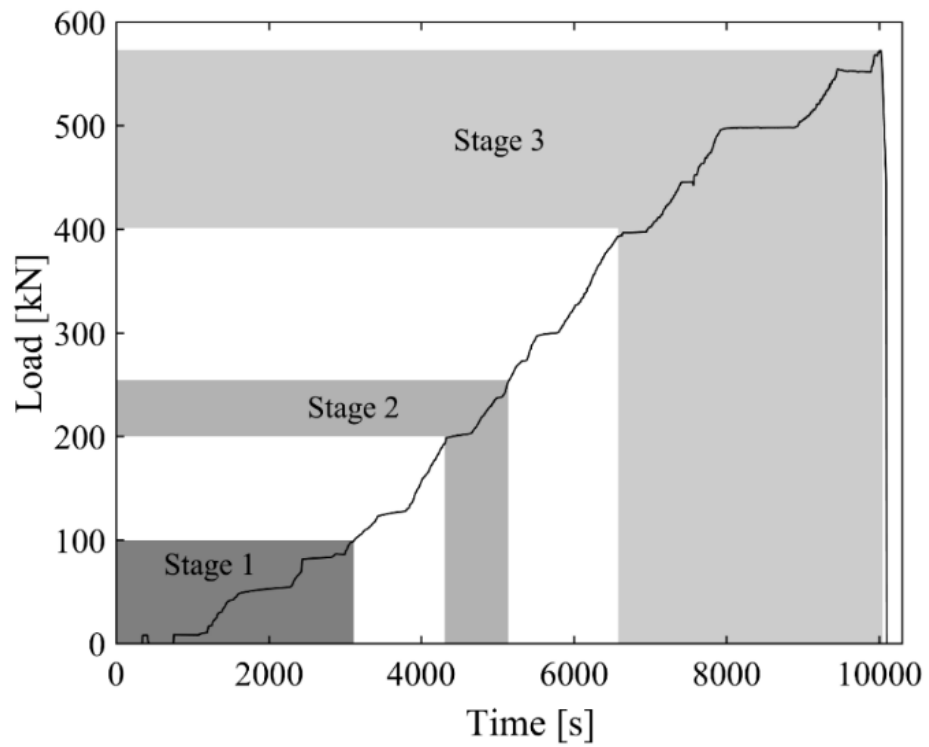


Figure 4.9: Phases used for RMS analysis

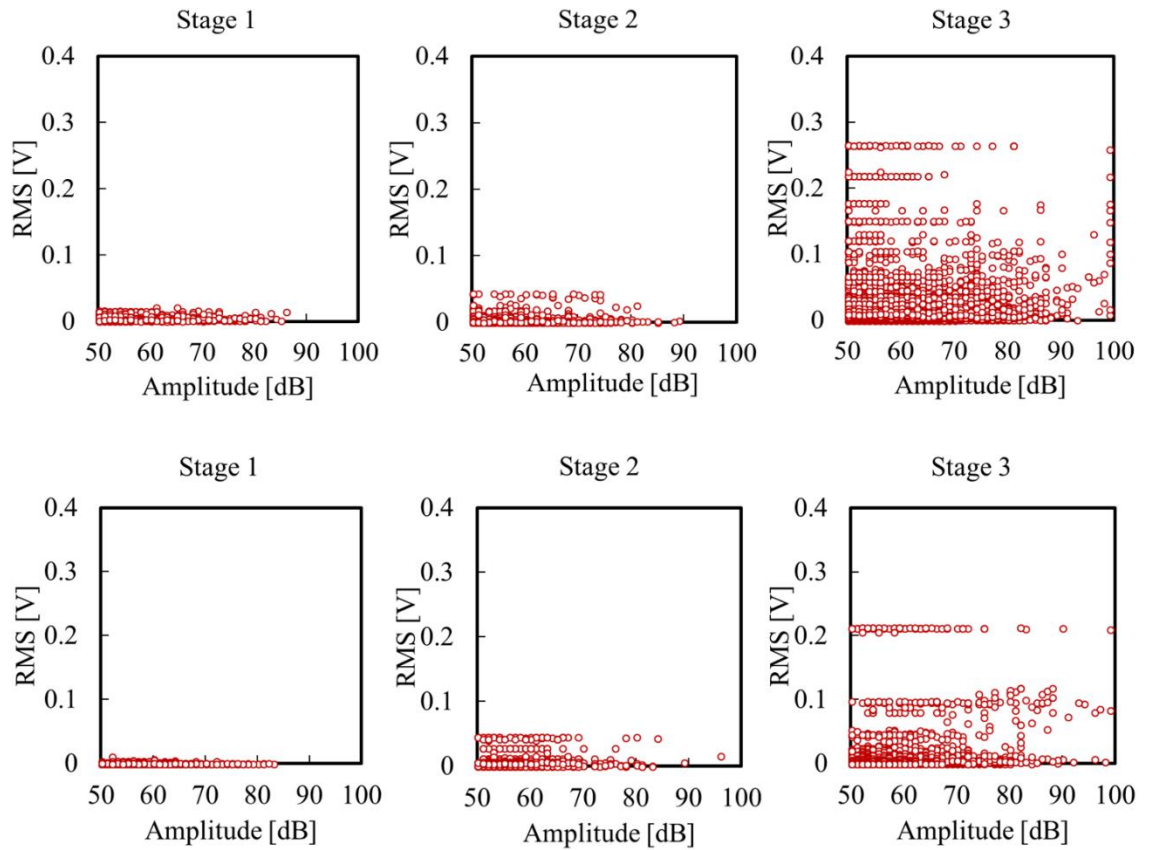


Figure 4.10: RMS for GC-1 (top) and GC-2 (bottom) at different stages during test

An overview of the RMS correlation with the increasing load for both specimens is depicted in Figure 4.11. The sensitivity of RMS to load and subsequent failure can prove very useful for in-situ assessment of OWTs.

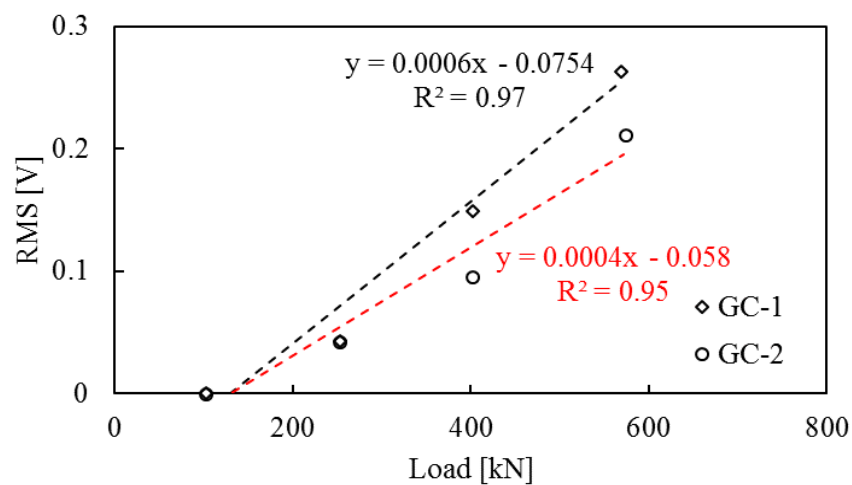


Figure 4.11: Correlation of AE RMS with load

## 4.6 b-value analysis

For the examination of the peak amplitudes an alternative statistical approach was adopted so as to study the whole time series of amplitudes rather than isolated events. A tool which uses the cumulative distribution of the recorded amplitudes is the *b*-value analysis. The *b*-value method derives from earth sciences and is specifically used in earthquake engineering, where it is employed to investigate seismic events (Gutenberg and Richter, 1956). It is based on an empirical mathematical formula which reads:

$$\log_{10}N = a - bM_L \quad 4.1$$

where *N* is the frequency of events within the selected magnitude range, *a*, *b* are constants and *M<sub>L</sub>* is the magnitude of the earthquake.

In recent years, the applicability of *b*-value has been examined on AE signals and promising results were found in several studies (Colombo et al., 2003; Carpinteri et al., 2006; Carpinteri et al., 2008; Sagar and Rao, 2014). Particularly, when it comes to fracture of brittle material such as concrete or rock, *b*-value analysis has been found to be an excellent tool for the evaluation of damage content (Rao and Lakshmi, 2005). For use with AE data sets Equation 4.1 needs to be modified to include the peak amplitude in *dB* divided by a factor (Colombo et al., 2003) so as to allow comparisons with the seismic *b*-value as follows:

$$\log_{10}N = a - b\left(\frac{A_{dB}}{20}\right) \quad 4.2$$

An interesting characteristic of the computed *b*-values for brittle media, especially when failure is approaching, is that significantly lower values occur, indicating macrocrack formation (Frohlich and Davis, 1993; Kurz et al., 2006; Farhidzadeh et al., 2012; Sagar and Rao, 2014). The relationship between increasing stresses and *b*-values appears to be inversely proportional (Rao and

Lakshmi, 2005). Typical  $b$ -values range from 2.5 in early stages, to values below 1 closer to failure (Colombo et al., 2003).

## 4.7 $Ib$ -value analysis

The study of the slope of the linear fit of the cumulative frequency distribution of amplitudes against the magnitude provides a good indication of imminent fracture. However, the relationship is not always linear. For this reason, Shiotani et al. (1994) suggested an improved  $b$ -value which involves statistical measures of the data set, namely the mean amplitude and standard deviation of the distribution. For the computation of the improved  $b$ -value the following equation is used:

$$Ib = \left( \frac{\log N(\mu - \alpha_1\sigma) - \log N(\mu - \alpha_2\sigma)}{(\alpha_1 + \alpha_2)\sigma} \right) \quad 4.3$$

where  $\mu$  is the mean amplitude,  $\sigma$  the standard deviation and  $\alpha_1, \alpha_2$  are user-defined constants. From a sensitivity analysis for both constants a value of 1 was selected. Following this, PAC also developed a dedicated software for  $Ib$ -value calculation which allows the use of the peak amplitude or the energy as input:

$$Ib = \left( \frac{\log N_1 - \log N_2}{a_1 - a_2} \right) \quad 4.4$$

where  $a_1 = \mu - \alpha_1\sigma$ ,  $a_2 = \mu + \alpha_2\sigma$  while  $\alpha_1$  and  $\alpha_2$  ranges from 0.5 to 5.

## 4.8 $b$ and $Ib$ -value results

As already discussed in section 3.1 alternative tools ought to be utilized to extract further insights from the peak amplitudes to allow for the evaluation of the GC integrity. Hence, the  $b$  and  $Ib$ -value analysis were performed as per Sections 4.6 and 4.7 respectively. The computations were performed using complete time

series unless stated otherwise.

Initially, the peak amplitudes were divided in small-ranged bins from the set-threshold to 100 dB with a magnitude of 5 dB. Groups of events were formed and a sliding function of 50 events was used in order to trace all the important events. In order to calibrate the optimum number of events within each group several trials were performed to ensure that the results are independent of the selected group size. This was initially noted by Colombo et al. (2003). A comparison for both approaches using a varying event number is presented in Figure 4.12, where 500 seconds of the GC-1 test are used for demonstration purposes. As the sliding function and the number of events of each group were found not to affect the results, groups formed by 150 events were chosen for the following analysis.

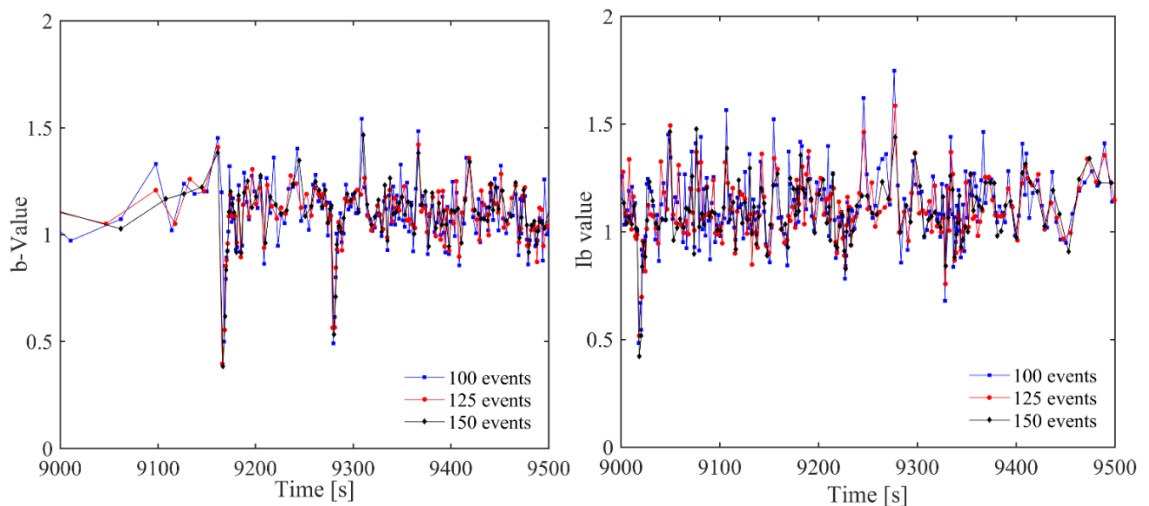


Figure 4.12: Effect of event number on  $b$  (left) and  $Ib$ -value (right)

In Figure 4.13 the results from the  $b$ -value and  $Ib$ -value analysis are presented simultaneously for the whole duration of the static test. Taking into consideration the results, it is evident that for the current test similar trends are shown for both methods. Similar trends for the two approaches were also reported in Sagar and Rao (2014). The resulting time series of the two computations contain a large number of data points as the only filtering that was performed was the removal of AE data with no PAC energy. The average  $b$  value is close to 1 as expected.

However, when such analysis is performed the main areas of interest are those where peaks or drops of the gradient which can be associated with events of high-importance are noted. In previous studies peaks have been associated with microcrack formation and drops with the transition to macrocrack growth and crushing of cementitious material. Thus, it is easily appreciated that after the first 4000 s some peaks and drops are emerging. The  $Ib$ -value extremes are slightly more pronounced for the whole time series. Also, the notion that the gradient of the slope reduces dramatically once failure is upcoming can be confirmed if one considers the patterns after 8000 s. The density of events increased significantly while distinct drops well-below the average value of 1 are present from both methods. As the trends of the two methods appeared to produce similar results for the remaining sections only  $Ib$ -value will be considered.

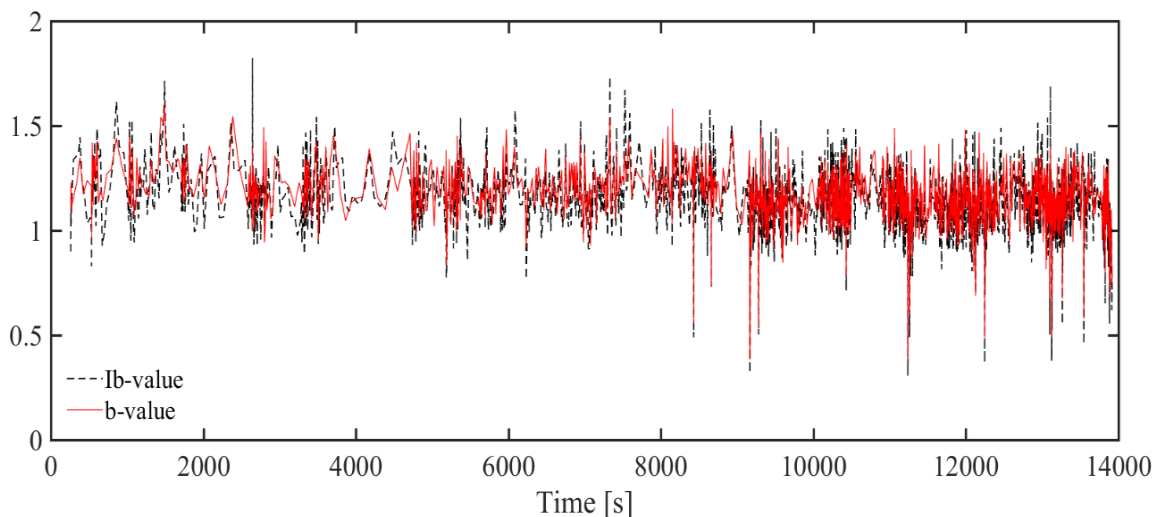


Figure 4.13: Comparison between  $b$  and  $Ib$ -value

In Figure 4.14 an envelope of the local maximum and minimum  $Ib$ -values is plotted against the load level. The load level corresponds to the load at the time of interest normalised against the ultimate load sustained by the GC. The extreme values of  $Ib$  enable the identification of different damage states within the connection in a quantitative way. During phase I, values up to 1.824 were found, while in phase 2 the  $Ib$ -value dropped from 1.671 to 0.306 and a number of drops

are captured. During the last phase of the test, distinct drops resulting in low values were also recorded until final failure of the specimen. In Colombo et al (2003) similar trends and magnitudes were shown. The authors correlated values higher than 1.7 with microcracking, while larger cracks can be associated with lower values.

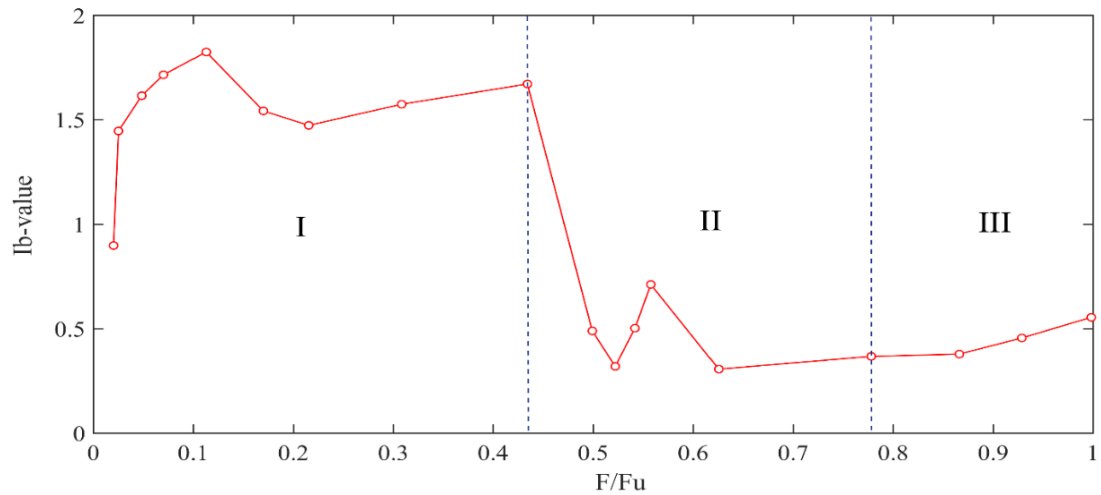


Figure 4.14: Peaks and drops of  $Ib$ -value for GC-1

To correlate these sudden drops with other AE parameters the rate of CSS has been selected. The CSS exhibited an exponential trend while the applied load on the GC increased as a function of time (Figure 4.15). Identical trends were reported with the cumulative energy of the waveforms confirming that CSS is interconnected with energy as discussed in section 3.1.

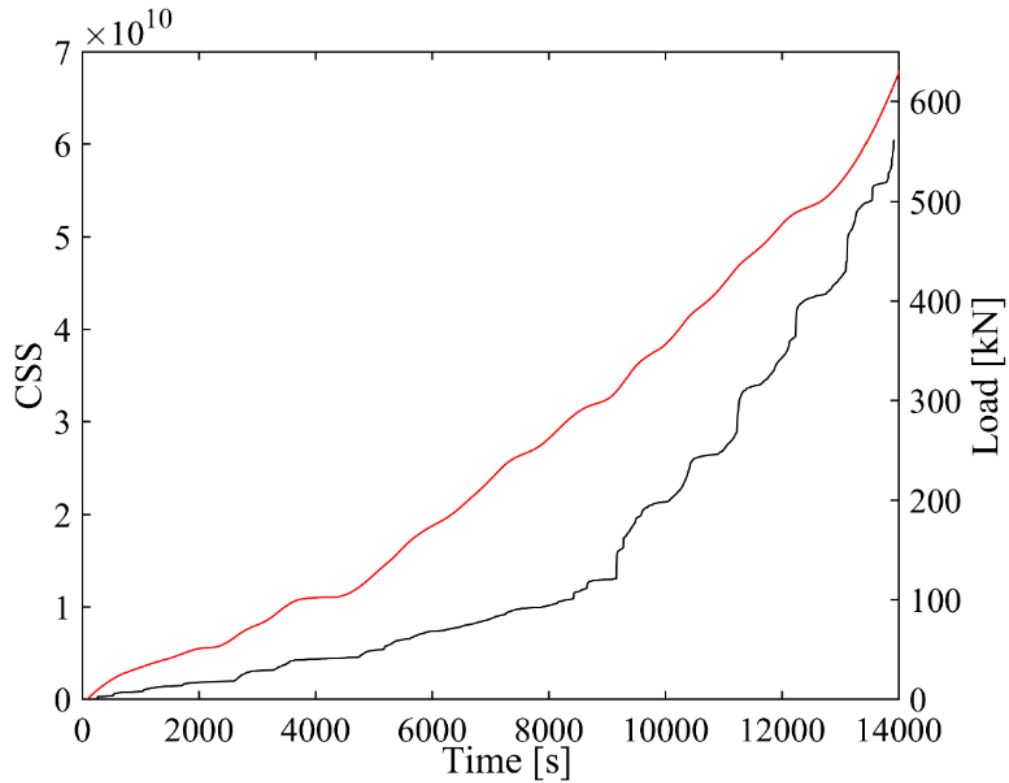


Figure 4.15: Cumulative signal strength against applied load for GC-1

In Figure 4.16 the final stages of the test where the majority of damage occurred are shown by comparing the growth rate of CSS with the  $Ib$ -value. The results indicate an excellent agreement between the two parameters. The pronounced  $Ib$  drops which are highlighted in red are in excellent agreement with CSS peaks indicating significant events.

The trends of  $Ib$ -value have been also compared with the RA ratio values. RA value has also been used to investigate fracture of brittle material and more often in concrete and has been closely associated with crack-type classification. RA is computed as follows:

$$RA = \left( \frac{\text{Rise time}}{\text{Amplitude}} \right) \quad 4.5$$

As depicted in Figure 4.17 the macrocrack formation which is suggested from the  $Ib$ -value drops well below unity, is coinciding with the peaks in RA values. To

sum up, RA ratio, CSS, RMS are important KPIs along with the statistical analysis of the amplitude distribution.

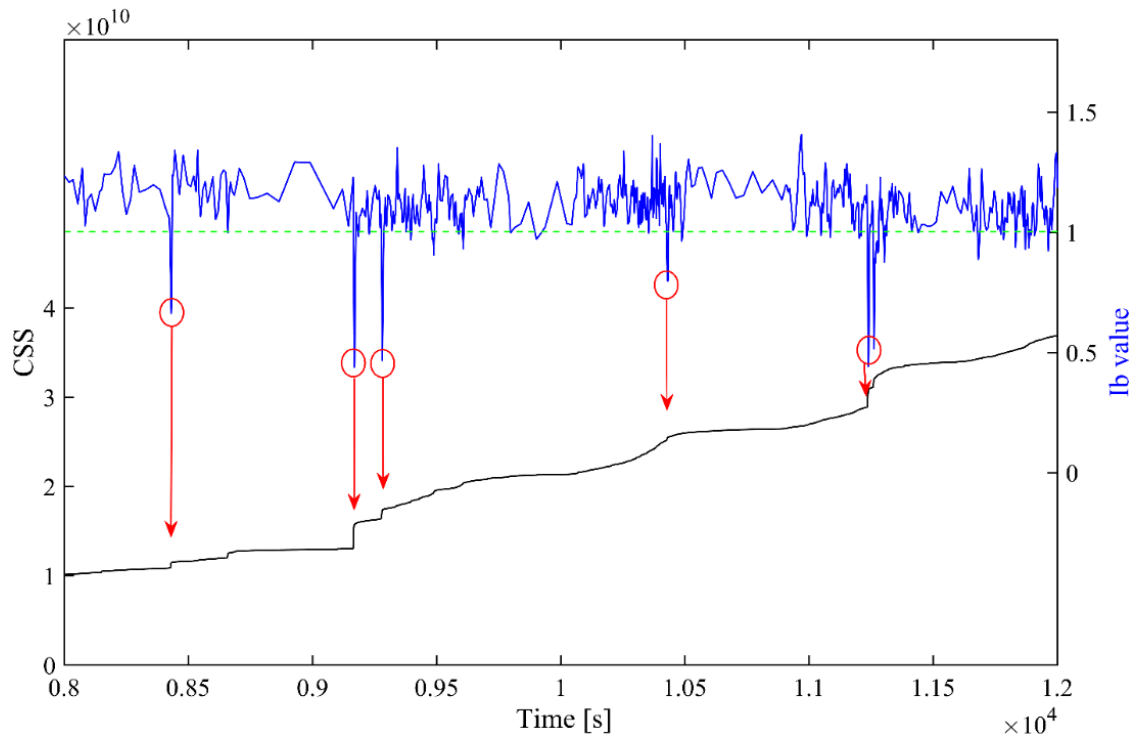


Figure 4.16: CSS and *Ib*-value correlation

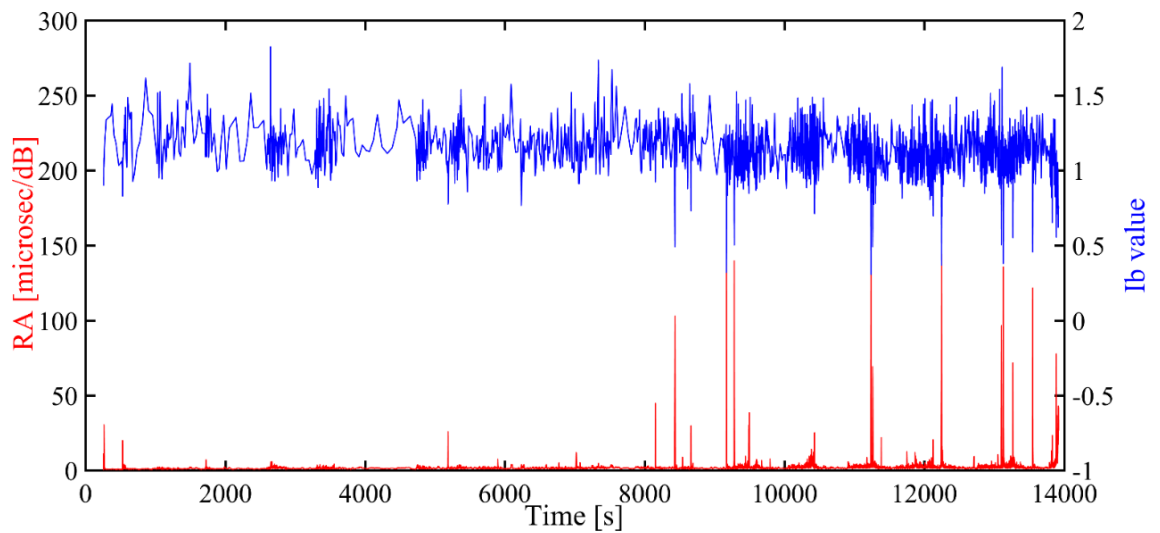


Figure 4.17: Correlation of *Ib*-value and RA

# 5 NUMERICAL MODELLING

## 5.1 Overview

This chapter presents the numerical scheme and formulations that were used to develop and validate the FE models against experimental data sets. Initially, in sections 5.2-5.4 some theoretical considerations on FE modelling are presented. Those are directly related with the presented approaches and linked with previous studies on GCs using FEA. Material modelling is discussed in 5.5 whereas model validations under different loading conditions are given in detail in sections 5.6, 5.7 and 5.8. For this purpose, the author's experimental tests, which were presented in Chapter 3, along with tests from the literature were employed for validation purposes. Finally, a comparison of the simulated model results with analytical predictions from the offshore design code DNV ST-0126 (2016) is performed to enhance the validity and confidence in the numerical models.

Research papers relevant to this chapter's scope have been published by the author and are explicitly referenced in text where applicable:

**Tziavos, N.I.**, Hemida, H., Metje N. and Baniotopoulos, C. (2019). Non-linear

finite element analysis of grouted connections on monopile wind turbines, *Ocean Engineering*, 171, pp. 633-645.

**Tziavos, N.I.**, Hemida, H., Metje N. and Baniotopoulos, C. (2018). Grouted Connections for offshore wind turbines: A numerical study. *In Energy and Geotechnics, vol 18, Springer, The first Vietnam Symposium on advances in offshore engineering.*

## 5.2 Numerical schemes and computations

In this thesis the general-purpose FE software Abaqus (Abaqus, 2013) is employed throughout and the majority of the simulations have been performed using the high-performance computational cluster BlueBEAR (Birmingham Environment for Academic Research). The cluster was employed to reduce the computational effort that was necessary for the numerical models. For example, a typical GC model with ~120,000 solid elements would require a running time from 20 to 24 hours in a conventional laptop, whereas the time required in the cluster was reduced up to three times.

Research on FE modelling of GCs has mainly emphasised on static analyses. To that end, two alternatives exist for static problems, *i*) the implicit and *ii*) the explicit procedure. Both pathways provide incremental solutions. However, their fundamental difference is that in implicit approaches equilibrium needs to be achieved in every iteration.

The implicit approach is the conventional way to tackle a static problem, as it results to an unconditionally stable solution. However, for challenging problems involving contact formulations, materials with complex behaviour such as concrete or a combination of those, convergence problems are common. In practice for an FE simulation this translates to a solution that is not reaching the ultimate load limit. A non-converging solution is induced from non-linearities demanding a large number of iterations. Even though a solution can be achieved sometimes, either by using viscoplastic regularisation or increasing the maximum number of iterations, it often results to be computationally expensive.

On the contrary, calculations with explicit methods are conditionally stable and no iterations are required as the solution is transferred directly from the previous increment (Abaqus, 2013). The stability of the computations is relying on time

increments ( $\Delta t$ ) and is ensured by maintaining it smaller than the minimum time increment ( $\Delta t_{\min}$ ). The definition of the stable time increment is given in 5.1.

$$\Delta t = \min\left(\frac{L^e}{c_d}\right) \quad 5.1$$

where  $L^e$  is the selected element length and  $c_d$  is the dilatational wave speed as per 5.2,

$$c_d = \sqrt{\frac{\lambda + 2\mu}{\rho}} \quad 5.2$$

where  $\rho$  is the density of the material and  $\lambda, \mu$  are Lamé constants. Considering equations 5.1 and 5.2 it is shown that the element size is dictating the computational expense of the numerical simulation.

Nevertheless, this means that engineering judgment and care must be given to the development of the model and the results of such an analysis as it can lead to non-physical outcomes. Abaqus/Explicit is a dynamic solver, but it can also be used to perform quasi-static simulations. To do so the inertia effects ought to be reduced to a minimum. Abaqus (2013) suggests that when the following condition is satisfied it is a good indication of a quasi-static solution being achieved:

$$\text{Kinetic Energy} < 2\text{-}5\% \text{ Internal Energy}$$

In Figure 5.1 such an example of the abovementioned condition being met is presented. The kinetic and internal energy are obtained from a quasi-static simulation of a GC model.

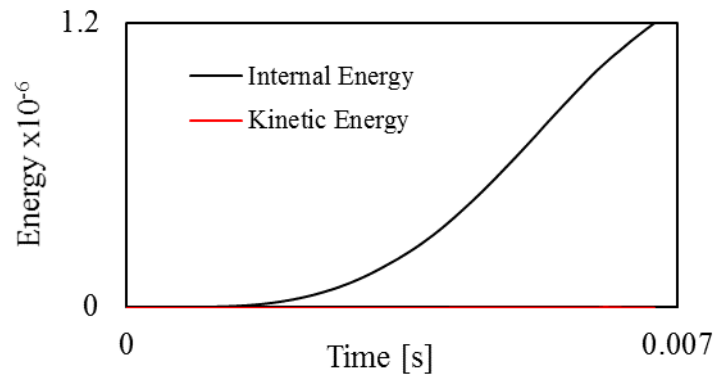


Figure 5.1: Example of energy output from quasi-static simulation for a GC model solved with Abaqus/Explicit

When it comes to GCs the non-linear brittle behaviour of the grout along with the steel-grout bond, dominate the analysis and determine whether the computations are completed or not. Preliminary simulations revealed that in order to achieve convergence with sufficiently accurate results, significant computational cost is involved. For example, on an axially-loaded connection once the slip strength is reached and the non-linear behaviour initiates the solution typically aborts. Convergence is not guaranteed even if a very small time increment is used or a very dense mesh.

Therefore, the presented three-dimensional FE models were solved by means of a quasi-static explicit analysis including the nonlinear behaviours. The explicit approach alleviates the contact challenges as the enforcement of contact formulations does not affect the simulation and there is no limitation in the contact regions.

For larger models or for those that finer discretisation was employed, to further reduce the computational cost, semi-automatic mass scaling with a fixed time increment in every step was applied. The time increment in each model was selected aiming to maintain negligible kinetic and artificial strain energy. Mass-scaling in structural problems has been effectively employed in previous studies for several applications and particularly when concrete or brittle materials are

involved (see, e.g., Pavlovic et al., 2013; Liu et al., 2016; Tziavos et al., 2018).

### 5.3 Element selection

An extensive library of elements with varying nodes, formulations and integration points are available in Abaqus or Abaqus/Explicit. Compared to an implicit approach, one of the drawbacks of an explicit method is the element type availability. In this work, for all the components of a GC assembly, three-dimensional continuum (solid) elements have been employed and herein discussed. Solid elements offer an accurate representation of the actual geometry and their use is suitable for interfacial problems. Tetrahedral (e.g., C3D10M) or hexagonal (C3D8R) elements can be employed for discretisation purposes. When it comes to modelling the grout core of a connection, although tri- and tet-elements can yield solutions of similar accuracy, those can prove computationally more expensive than hexagonal elements due to refined meshes that are required and overly stiff response.

The constitutive modelling of the grout's behaviour is of particular interest and therefore it is recommended that it should only be modelled with solid elements, particularly when local stresses are of interest. Herein the grout is modelled exclusively with solid C3D8R elements. This type of element has been found to accurately model the response of cementitious material sufficiently as shown in several studies (see, e.g., Pavlovic and Veljkovic, 2017). For consistency purposes, the same element type was also used for the steel parts of the FE models as the expense in computational resources was not compromised. Shell elements can be used alternatively, however a shell to solid coupling is required.

A common issue arising is hourglassing (Abaqus, 2013). The phenomenon is caused due to strains not being detected on the single integration point as shown in Figure 5.2.

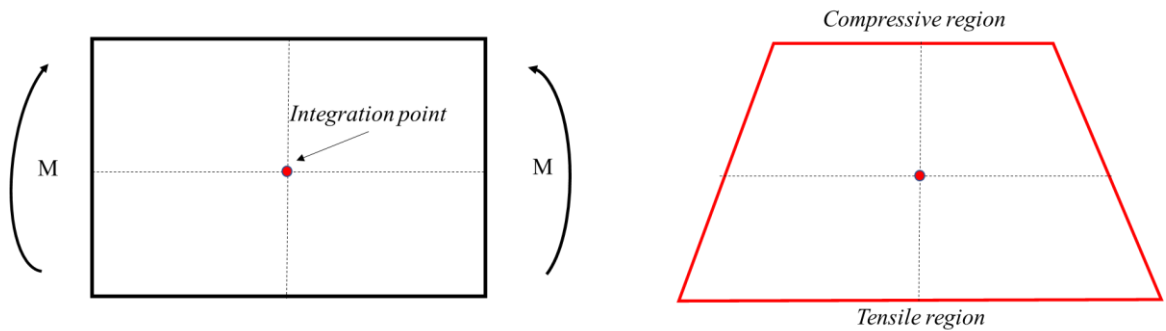


Figure 5.2: Zero energy mode on an element with reduced integration in bending

Hourglassing in other words refers to elements that have no energy or zero energy mode as it is commonly referred to due to the undetected strain at the point of integration. It can be detected as a sequence of distorted elements. An example is given in Figure 5.3, where the phenomenon can be identified. To avoid such issues enhanced hourglass control was employed. A

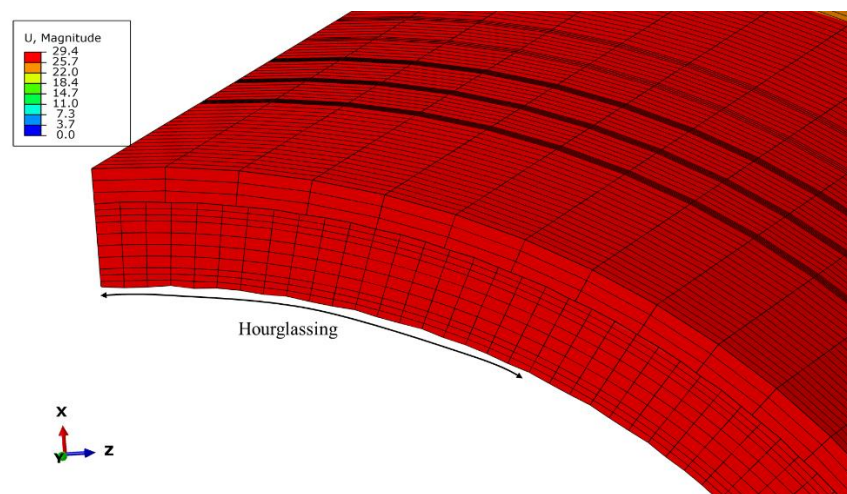


Figure 5.3: Hourglassing mode example on a GC model. The pile has been removed for illustration purposes

## 5.4 Contact considerations

FE models involving contact problems are challenging in many ways and require diligence due to severe non-linearities arising. Those often do not help towards convergence especially in implicit approaches which require repetitive iterations.

A surface to surface discretisation is advantageous for contact problems in terms of penetrations occurring with master-slave formulations. Although this discretisation is less reliant on master and slave allocation it is still suggested that slave surfaces are finely meshed. On the contrary increasing the mesh of the master surface will not necessarily improve the accuracy of the solution.

Contact properties can be assigned in normal and tangential directions. The normal behaviour is the one that defines the pressure-overclosure relationship and typically a hard contact formulation is employed to allow for compressive stresses to be transferred at the interfaces and enable gap opening at sleeve-grout interfaces (Tziavos et al., 2018). For the tangential behaviour a friction model can be employed using an appropriate friction coefficient ( $\mu$ ). The surfaces in contact transfer contact pressure until it becomes zero, when clearance is initiated. Such an enforcement method is used by default in implicit methods. Convergence issues can also emerge when transitioning from no clearance condition to clearance condition. Hence, explicit approaches are favourable for contact-problems as the solution does not require equilibrium in every iteration.

Another aspect of the contact formulation is sliding between the interfaces when surface to surface contact is enforced. Sliding can be finite or small with a kinematic or penalty contact constraint (Abaqus, 2013). Small sliding induces less convergence difficulties and the computational cost can be reduced; However, it may result in non-realistic results and solutions. For GCs the author suggests avoiding the use of small sliding as it is usually intended for very small movements between parts or components when compared to the selected element size. Additionally, within a GC, a small relative movement is a necessity to initialise the connection's structural behaviour as described in section 2.7. Considering the constraint formulations, the kinematic uses a predictor-corrector approach whereas the penalty method introduces a small penalty stiffness which

enables a small elastic slip (Abaqus, 2013).

### 5.4.1 Cohesive modelling

Numerical studies conducted to date (Löhning et al., 2013; Wang et al. 2017; Tziavos et al., 2018) mainly employ friction models to simulate the bond between the grout and steel tubulars. However, when modelling GCs and particularly for ultimate strength purposes, the bond behaviour between the grout, pile and sleeve is critical to ensure that the FE models yield appropriate results with the desired level of accuracy.

Abaqus (2013) offers the capability to simulate the behaviour of bonded parts with cohesive elements or a cohesive surface behaviour. Both methods are similar in principal and a traction-separation law dictates their behaviour, however they are defined differently. For example, separation in cohesive surfaces refers to the distance between the open interfaces, whereas for cohesive elements separation is defined as nominal strain of the cohesive layer.

One fundamental difference between these models is that cohesive elements are only enabled for bonded assemblies prior to starting the simulation whereas cohesive behaviour can be achieved anytime. Moreover, cohesive layers of elements are suitable in cases where a finite thickness interfacial behaviour can be defined (Abaqus, 2013). Thus, it needs to be clarified that when cohesive behaviour is defined interaction properties are assigned rather than a material property. Considering previous numerical studies and the aforementioned, a surface-based cohesive interaction will be subsequently investigated for modelling of GCs, thus some basic theoretical formulations will be presented in the following section.

## 5.4.2 Surface-based cohesive behaviour

For the definition of cohesive surface-based behaviour a traction-separation model can be employed as described in Figure 5.4. The definition of this interaction property strongly depends on the stiffness matrix  $\mathbf{K}$  and a coupled or uncoupled behaviour can be chosen following the expression in 5.3.

$$\begin{pmatrix} t_n \\ t_s \\ t_t \end{pmatrix} = \begin{bmatrix} K_{nn} & K_{ns} & K_{nt} \\ K_{ns} & K_{ss} & K_{st} \\ K_{nt} & K_{st} & K_{tt} \end{bmatrix} \begin{pmatrix} \delta_n \\ \delta_s \\ \delta_t \end{pmatrix} \quad 5.3$$

The uncoupled term refers to the tangential and normal components. That indicates that any separation in the normal direction will not induce shear forces in the remaining tangential directions and vice versa. It is the simplest case of cohesive-based behaviour and only the diagonal elements of the stiffness matrix require values. If no stiffness value is defined in normal and tangential directions Abaqus uses default penalty contact constraints.

The stiffness matrix defines the behaviour of the interface until a predefined separation triggers damage. In practice the initial slope defines the elastic behaviour as defined in Figure 5.4. Subsequently, damage evolves following a user defined evolution law. The failure mechanism of the bond is defined by those two stages: initiation and evolution.  $t_n^o, t_s^o, t_t^o$  refer to maximum stresses for the normal and tangential components whereas  $\delta_n^o, \delta_s^o, \delta_t^o$  refer to the corresponding separations and  $\delta_m^{max}$  refers to the maximum recorded separation.

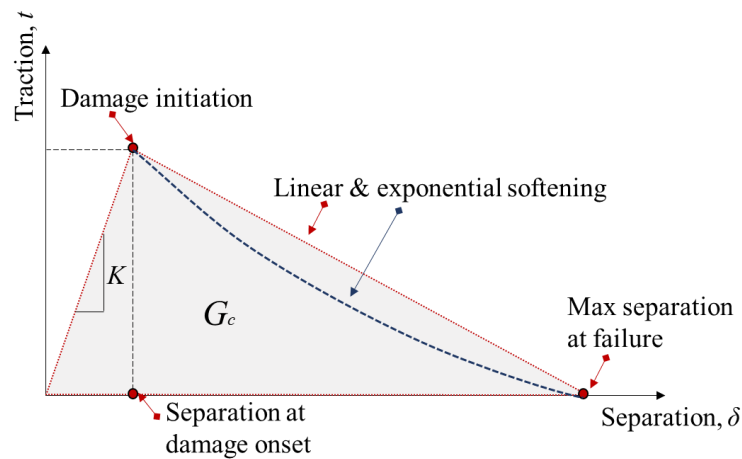


Figure 5.4: Traction separation constitutive model and damage evolution

Damage initiation sets the conditions for bond degradation to initiate and it can be assigned to the model either as contact stress or separation with an appropriate criterion. Those can be classified as: 1) the maximum stress, 2) quadratic stress, 3) maximum separation and 4) quadratic separation criteria. Each one of them is met once a value equal to unity is reached or exceeded. Stress criteria are based on the notion that a stress level is reached whereas for separation an amount of slip at the interface is achieved.

Following initiation, damage evolution can be either displacement based, or energy based. Displacement formulations are considering the relative separation of the interfaces and can use a linear or exponential softening function as illustrated in Figure 5.4. The separation is computed based on the separation at failure ( $\delta_m^f$ ) subtracting the reference separation once damage initiates ( $\delta_m^o$ ). Energy based damage evolution is directly related with fracture energy ( $G_c$ ) and the energy being released due to the degradation of the bond and it can be expressed as a power law criterion. For more details on the aforementioned modelling approaches reference is made in Abaqus (2013).

In this work an uncoupled traction-separation behaviour will be used and compared with FE models employing a Coulomb friction model. Damage

initiation is defined using the maximum stress criterion and evolution with an exponential softening function by means of maximum separation. Those are summarised in the following functions:

$$D = 1 - \left\{ \frac{\delta_m^o}{\delta_m^{\max}} \right\} \left\{ 1 - \frac{1 - \exp\left(-a \left( \frac{\delta_m^{\max} - \delta_m^o}{\delta_m^f - \delta_m^o} \right)\right)}{1 - \exp(-a)} \right\} \quad 5.4$$

$$\max \left\{ \frac{\langle \delta_n \rangle}{\delta_n^0}, \frac{\delta_s}{\delta_s^0}, \frac{\delta_t}{\delta_t^0} \right\} = 1 \quad 5.5$$

## 5.5 Material modelling

Constitutive material models also affect the computational demand which is required for a FE model. This is pronounced when aiming to model the HSG comprehensively, including cracking and crushing behaviour (Tziavos et al. 2018). Considering GCs previous research often neglects the local behaviour of the grout in order to address issues related with convergence and cost. In the following sections material modelling of steel and grout are addressed in detail.

### 5.5.1 Steel modelling

The steel parts for all the different FE models were described with the von Mises yield criterion and isotropic hardening. Data originating from the corresponding mechanical tests are employed for this validation study from the author's tests and Wilke (2013).

The true stress,  $\sigma_{\text{true}}$ , and strain,  $\epsilon_{\text{true}}$ , curve was obtained from the nominal engineering stress,  $\sigma_{\text{eng}}$ , and strain,  $\epsilon_{\text{eng}}$ , whereas the Young's modulus ( $E$ ) and Poisson's ratio ( $\nu$ ) was set to 210 GPa and 0.3, respectively. A density of 7850 kg/m<sup>3</sup> has been used for steel.

## 5.5.2 Grout modelling

The tensile and compressive behaviour of HSGs exhibits common characteristics with normal concrete. Thus, HSG modelling is primarily based on concrete constitutive material models. The stress-strain behaviour of UHPC in compression is best described in two stages as illustrated in the schematic of Figure 5.5. For the ascending branch, the distinct feature is the linear behaviour almost up to  $0.8 - 0.9f_{cm}$ . Once the nominal compressive strength is reached, the post-failure branch is best described by a steep drop owing to the internal microstructure and content, which causes the abrupt brittle nature. However, normally this part of the curve reveals much more scatter than the ascending branch, due to the explosive failure which takes place as discussed in 0. This is indicated by the two different descending branches of Figure 5.5. Fehling et al. (2014) highlights that this variation can be even more pronounced with the addition of steel fibres.

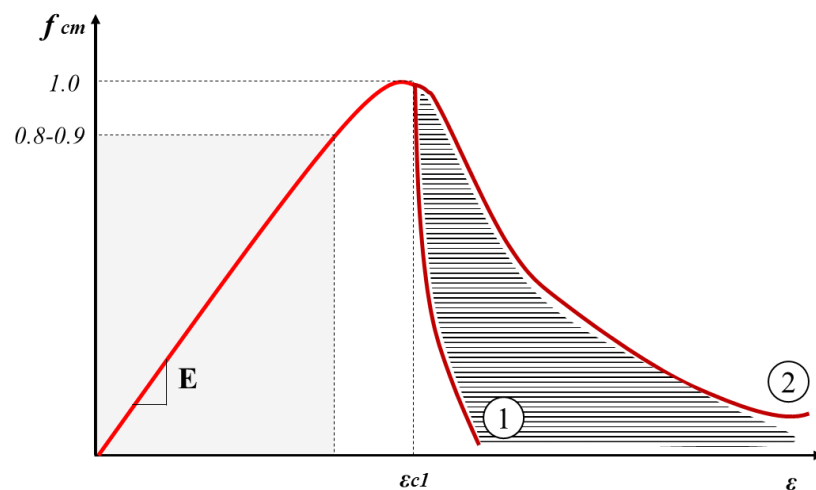


Figure 5.5: Typical  $\sigma$ - $\epsilon$  curve of UHPC in compression (Concept adopted by Fehling et al., 2014)

The experiments that are subsequently used for the validation study, involve the same type of material, with similar microstructure, fine aggregates ( $d_a < 5 \text{ mm}$ ) and a nominal compressive strength of approximately  $130 \text{ MPa}$ . Thus, the material behaviour is kept consistent throughout this thesis. Nevertheless, Fehling et al. (2005) notes that no variation in the mechanical properties of the UHPG is to be expected when the aggregate dimensions differ.

The CDP model (Lubliner et al., 1989; Lee and Fenves 1998) is chosen, which allows the definition of the grout behaviour in compression and tension and can effectively trace crushing and cracking. Taking the above into consideration, the ascending branch of the stress-strain curve was assumed to be linear until the peak strength is reached. Based on the numerical simulations that were performed, this approximation that results in a two-stage compressive behaviour, yields the most accurate results.

When it comes to the determination of the peak strain ( $\varepsilon_{c1}$ ), this is often assumed to be equal to 0.0022, however this approach is limited to lower strength concrete, with a maximum compressive strength of  $80 \text{ MPa}$  (CEB-FIP, 1990). Therefore, a modification to the peak strain was employed based on the formulation proposed by Tomaszewicz (1984) which better reflects the material's behaviour and reads:

$$\varepsilon_{c1} = \frac{0.7f_{cm}^{0.31}}{1000} \quad 5.6$$

An exponential post-peak branch was chosen following the expression in model-code CEB-FIP (1990), whereas damage in compression was defined by variable ( $d_c$ ), according to the following expression which gives values from 0 to 1:

$$d_c = 1 - \left( \frac{\sigma_c}{f_{cm}} \right) \quad 5.7$$

where  $\sigma_c$  is the stress corresponding to the inelastic strain. The normalised engineering and true stress-strain curve is shown in Figure 5.6. Despite the brittle behaviour once failure is approaching when it comes to modelling a less steep approach is recommended as convergence issues often arise.

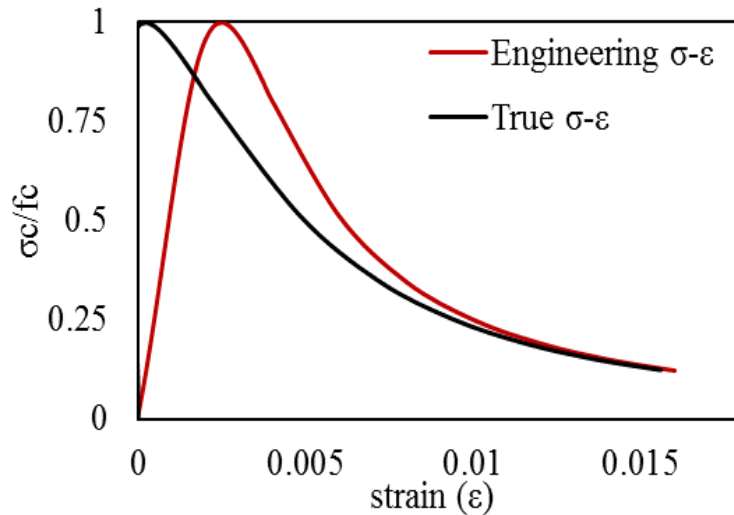


Figure 5.6: Grout engineering and true  $\sigma$ - $\epsilon$  curve

For the definition of the tensile behaviour a fracture energy approach (Hillerborg et al., 1976) was adopted. Alternative formulations, such as the strain formulation were found to cause numerical instabilities, which is in agreement with findings from several numerical studies involving cementitious material (Abdelatif et al., 2016). To define the fracture energy the relationship from CEB-FIP (1990) was followed:

$$G_F = G_{F0} - \left( \frac{f_{cm}}{f_{cm0}} \right)^{0.7} \quad 5.8$$

where  $G_{F0}$  is the base value for the fracture energy as a function of the aggregate size and  $f_{cm0}=10 \text{ MPa}$ . For the determination of  $G_{F0}$  values for aggregate sizes down to 8 mm are available, which in this case was selected as this size lies closer to the aggregate size of the modelled grout. Part of the fracture energy approach is to define the tensile softening of the grout. Three approaches can be used: i) a

linear, *ii*) a multi-linear and *iii*) an exponential softening model. The exponential model as defined by Cornelissen et al (1986), was found to yield better agreement so it used herein. Damage in tension was defined in a similar manner as damage in compression. The softening and damage definition is shown in Figure 5.7.

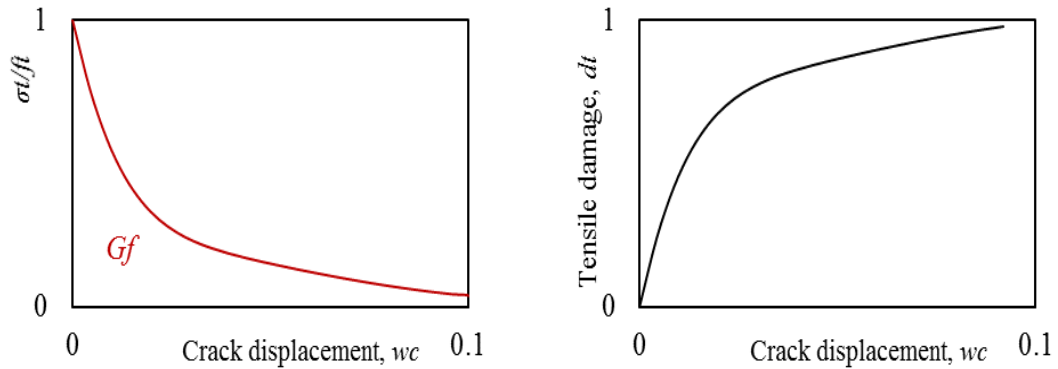


Figure 5.7 Exponential tensile softening (left) and damage (right)

Apart from compressive and tensile behaviour, the CDP model requires a series of properties to be defined as tabulated in Table 5.1. The parameter that had an impact on the global response of the model was found to be dilation angle ( $\theta$ ) values, hence the parameter must be carefully selected considering the grout material used and should always be calibrated against experimental data. In this study, it was selected following a sensitivity study and examining its effect on the global model response when compared to the test results. A wide range of values are found in the literature (see, e.g., Andersen and Petersen, 2004; Moon et al., 2012).

Table 5.1 HSG and CDP parameter identification

Description/Symbol	Value/Unit	CDP	Value/Unit
Modulus of Elasticity, $E$	50000 [MPa]	Dilation angle, $\theta$	38°
Poisson's ratio, $\nu$	0.19	Eccentricity	0.1
Density, $\rho$	2380 [kg/m <sup>3</sup> ]	$\frac{\text{Compressive yield stress}}{\text{Uniaxial yield stress}}$	1.162
Tensile strength, $f_t$	7 [MPa]	Viscosity	0
Fracture Energy, $G_F$	150.8 [Nm/m <sup>2</sup> ]	$K_c$	0.666

## 5.6 Finite Element model validation

The developed FE models and the experimental tests that were selected so as to validate the global and local behaviour of a GC under different loading configurations. For this purpose, bending tests that were conducted by the author, Wilke (2013) and Lochte-Holtgreven (2014), along with the axial tests presented in Wilke (2013) were employed. The rationale is that the main actions on monopiles are bending moments which have an effect on the axial capacity of the GC. Additionally, those tests provoke typical failure modes that can be found on monopile OWTs. For each model, boundary conditions, constraints, mesh discretisation and finally contact formulations are discussed in the corresponding sections, whereas material modelling is kept consistent throughout following the abovementioned approach.

## 5.7 Axially-loaded connections

Initially, in order to benchmark the whole modelling approach and calibrate the CDP contact parameters, a small scale GC (Figure 5.8) was developed and modelled based on the tests presented by Wilke (2013). The full geometry of the

pile, sleeve and grout were modelled using solid elements (C3D8R) imitating the experiment. The geometrical parameters of the 3-D model are tabulated in Table 5.2 and the final assembly is shown in Figure 5.8. A zoomed view of the structured mesh that was applied is also shown in Figure 5.8. As shown a refinement in the shear key region and close to the interface was applied. Although the orientation of the model is reversed which is unconventional for monopile GCs, it imitates the test set-up, which was elected for practicality reasons.

Table 5.2: Geometrical parameters of GC model in compression

Description/Symbol	Value [mm]
Sleeve outer diameter, thickness – $D_s, t_s$	114.3, 6.75
Pile outer diameter, thickness – $D_p, t_p$	57.80, 9.75
Grouted length, thickness – $L_g, t_g$	90, 21.5
Shear key height, spacing – $h, s$	1.25, 22.5

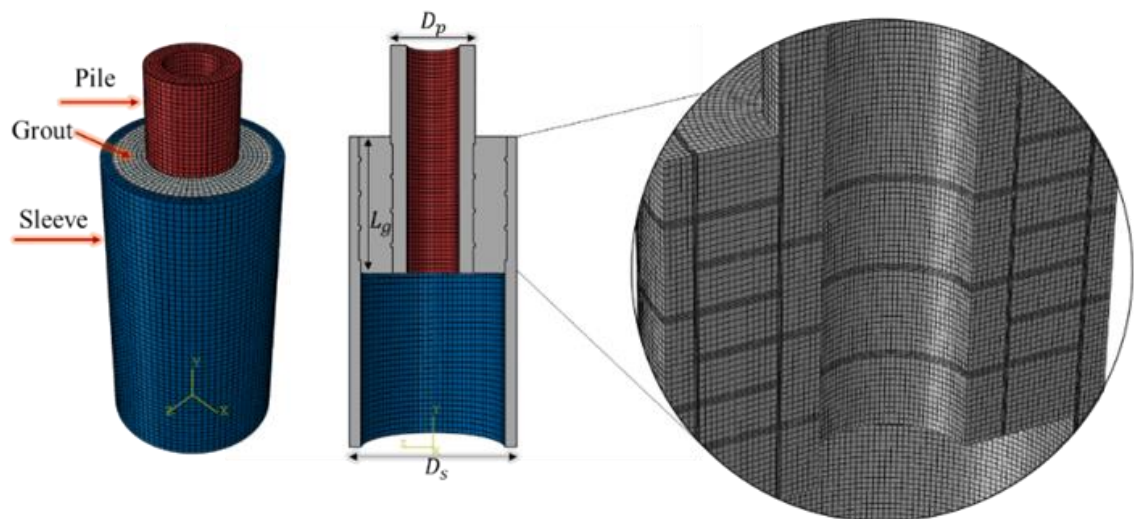


Figure 5.8: Small scale FE model (left) and component identification (right) (Tziavos et al., 2018)

### 5.7.1 Boundary conditions

To imitate the boundary conditions of the axial compression test, a fixed boundary condition was applied at the sleeve's bottom-surface nodes. The load was similarly applied at the nodes of the pile's top surface as a forced displacement boundary condition. For simplification the boundary conditions were applied on reference points. The sleeve and pile nodes and their degrees of freedom were tied to two reference points by means of a rigid body constraint.

At the grout-pile and sleeve-grout interfaces a surface-to-surface contact was enforced using contact pairs. The normal behaviour was modelled with a hard contact and friction model with a penalty constraint was applied tangentially. To define the friction coefficient of a sensitivity analysis was carried out, from which a value of  $\mu=0.4$  was adopted. In the existing literature, different values have been used by researchers (Qureshi et al., 2011; Wilke, 2013; Abdelatif et al., 2015) ranging from 0.3 to 0.7 for the friction coefficient. Owing to the size of the model no mass scaling was required to accelerate the computations.

### 5.7.2 Model validation

In Figure 5.9 the force-displacement curve from the numerical model is compared against the test results. In the right-hand axis of the figure the bond strength development during the test is illustrated. Overall very good agreement is achieved between the experiment and numerical model. The ultimate load ( $F_u$ ) sustained by the GC is very well captured along with the overall response of the joint. In GCs under axial loads previous studies (see, e.g., Lamport, 1988; Wilke, 2013; Wang et al., 2017) have highlighted the a distinct two-stage response is to be expected when shear keys are used.

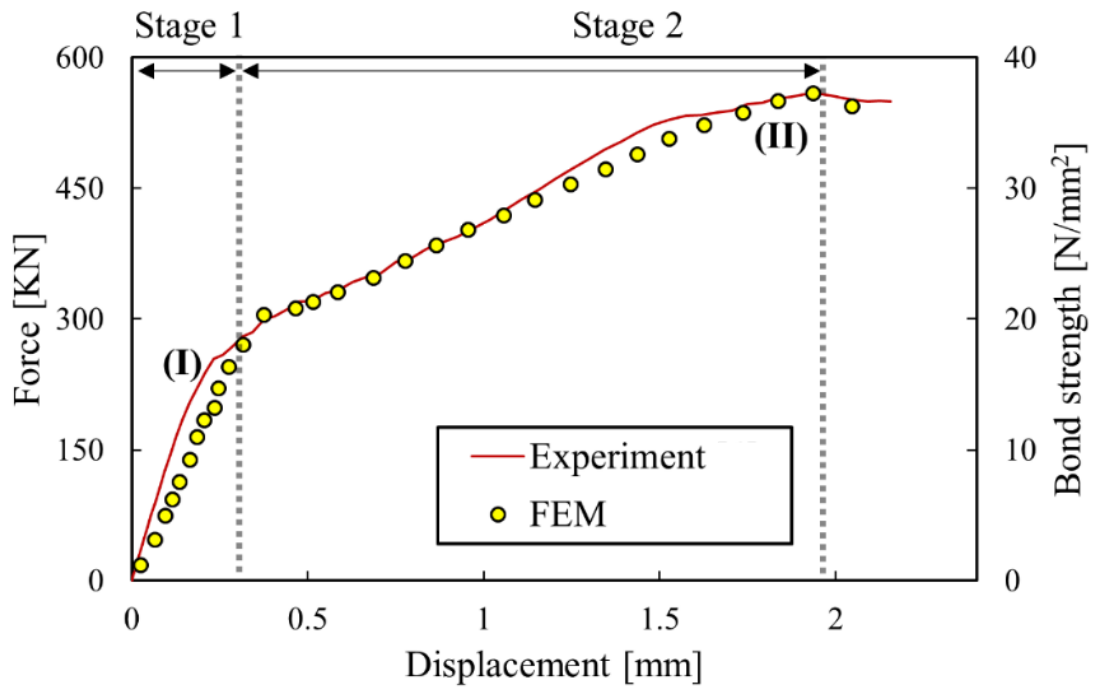


Figure 5.9: Comparison between numerical simulation and experimental results  
(Tziavos et al., 2018)

This two-staged behaviour is defined by two distinct points on the load-deflection curve; *i*) the slip strength ( $F_{su}$ ) and *ii*) the bond strength ( $F_{bu}$ ). The maximum slip strength is defined by the point at which the load-deflection curve transitions from a strongly linear-elastic behaviour, whereas bond strength, is determined by the ratio of the ultimate load over the interface surface area between grout and steel. Considering Figure 5.9, in the FE model the slip strength is exceeded approximately at  $\sim 0.5F_u$  (see Point I) where the GC remains in the elastic stage, whereas from that point and onwards the diagonal compression struts that indicate the load-transfer at the shear-keyed region start failing resulting in a rapid loss of stiffness. At point II the bond strength of the joint is reached and is followed by a decrease in force while displacement increases, and the connection cannot withstand any more load. The results are summarised and compared in Table 5.3.

Table 5.3: FEM vs experiment of axially-loaded GC

	$F_u$ [kN]	$F_{bu}$ [N/mm <sup>2</sup> ]	$F_{su}$ [kN]	$F_u$ (FE/Exp)	$F_{su}$ (FE/Exp)
*Experiment	551.0	33.6	303.05	1.01	0.9
FE	558.2	32.7	273.5		

\* Avg. of 5 specimens

In Figure 5.10 the crack development is visualized using the grout plastic strains. The analysis was shown to accurately capture the diagonal compression struts that developed between the opposing shear keys during the different stages and those are in agreement with cracks found after the test.

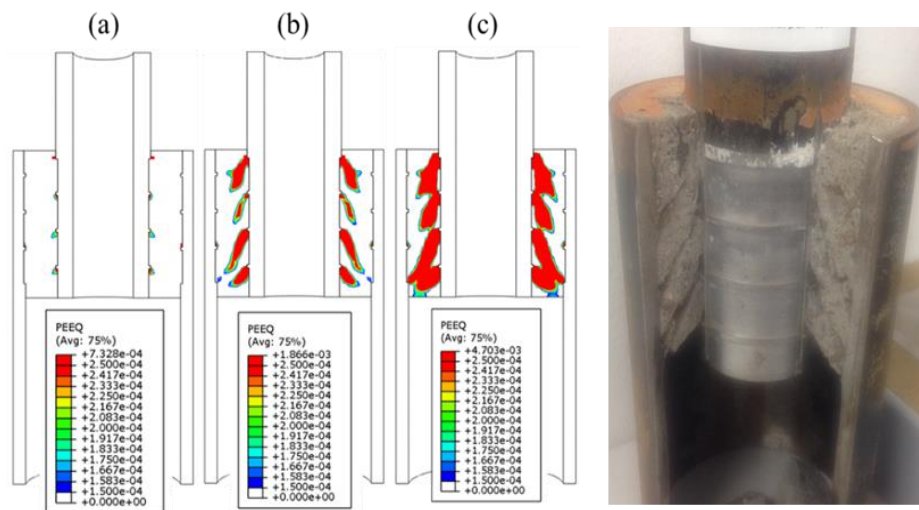


Figure 5.10: Cracking within the grout core by means of plastic strains from initiation to fully-developed compression struts. Crack patterns (right) from experimental test (Photo property of GROWup research project)

Cracking within the core initiated at the tip of the pile shear keys (Figure 5.10a) until reaching the opposing shear keys of the sleeve progressively (Figure 5.10b, Figure 5.10c). This mechanism is triggered once small displacements take place as described in section 2.7 which in reality takes place when the applied load overcomes the adhesion between the grout and steel piles. The cracks at the final

pair of shear key tend to form a common failure surface when the maximum bond strength was reached.

### 5.7.3 Dilation angle and friction coefficient

Dilation angle  $\theta$  is used to define the flow potential and there is a range of values that could potentially be used depending on the behaviour of the specific material in question. In Abaqus the range for  $\theta$  is from  $0^\circ$  to  $56^\circ$ . In order to use an appropriate value for  $\theta$ , several simulations were performed in order to achieve good agreement against the experiment. In Figure 5.11 force-displacement curves for a range of values of  $\theta$  are shown. A value of  $\theta=38^\circ$  was found to be the most suitable for the current set of experiments. Subsequently  $\mu$  was calibrated using a sensitivity analysis (Figure 5.11) yielding a 0.4 value.

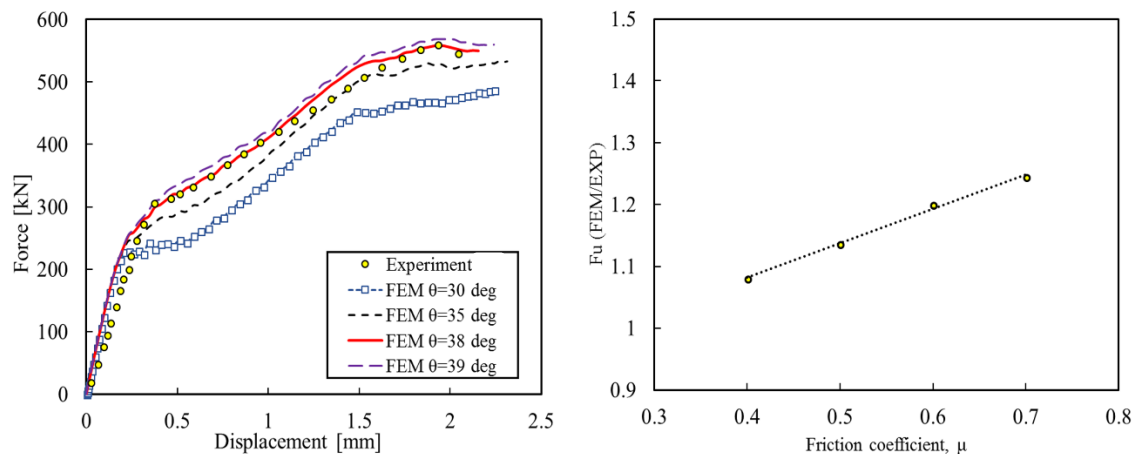


Figure 5.11: Effect of Dilation angle (left) and friction coefficient (right) (Tziavos et al., 2018)

## 5.8 Grouted connections in bending

The subsequent sections deal with numerical models of GCs under bending loads and their validation study. The current limits for monopiles allow for the design of GCs with varying radial stiffness. In practice this mainly depends on the

conditions at the offshore location which then dictate the requirements for the design of the substructures. To that extent the following validation study includes GCs of different diameter to thickness ratio aiming to study a range of GC with different stiffness and geometrical parameters. Those involve the presented experiments and the tests by Wilke (2013) and Lochte-Holtgreven (2014). Considering the current literature this is the only numerical study that thoroughly investigates the performance and robustness of the FE models against different geometries and scales. A summary of the main model parameters that dictate the geometries under investigation is given in Table 5.4. The selected slenderness ratios, overlap lengths and shear keys allow for a validation study that covers the monopile geometric ranges as those are dictated by DNV ST-0126 (2016), thus resulting in a comprehensive validation study. For all subsequent analysis the notation depicted in Figure 5.12 will be followed. Bottom of the GC will always refer to the direction pointing towards the mudline, whereas top of the GC is towards the tower as it would be in reality.

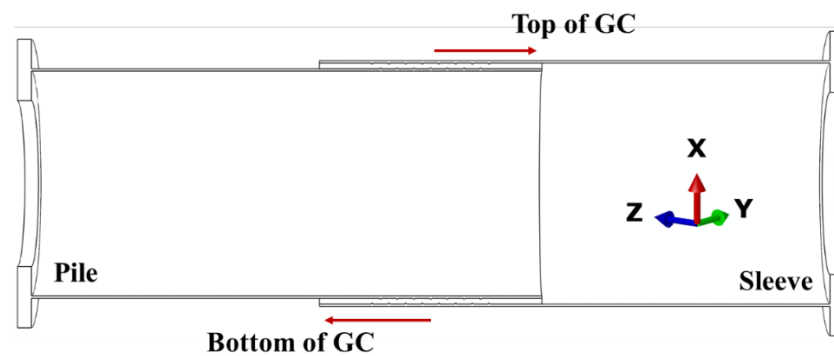


Figure 5.12: GC notation for FE models

Table 5.4: Summary of GC tests in bending used within the validation study

Source	$D_s/t_s$	$D_p/t_p$	$D_g/t_g$	$F_o$	$h/s$
Wilke, 2013 (SKGC1)	107.0	100.0	42.0	1.3	0.05
Wilke, 2013 (PGC)	107.0	100.0	42.0	1.3	n/a

Lochte-Holtgreven, (SKGC2)	2014	107.0	100.0	42.0	1.0	0.05
Tziavos, 2018		42.6	50.7	20.1	1.5	0.083

### 5.8.1 Experiments at Leibniz University of Hannover

Initially, the tests which were carried out at University of Hannover are jointly presented within this section and do represent the upper range of pile and sleeve slenderness ratios. It is worth noting that some parameters lie outside the limits, however in monopiles this is often the case in engineering practice. For example, the tests were performed on connections with  $F_o=1.3$ . In Figure 5.13, the full assembly of the FE models is schematically presented along with a close-up of the GC and its middle region. The PGC and SKGC1 show a plain pipe GC and one with shear keys.

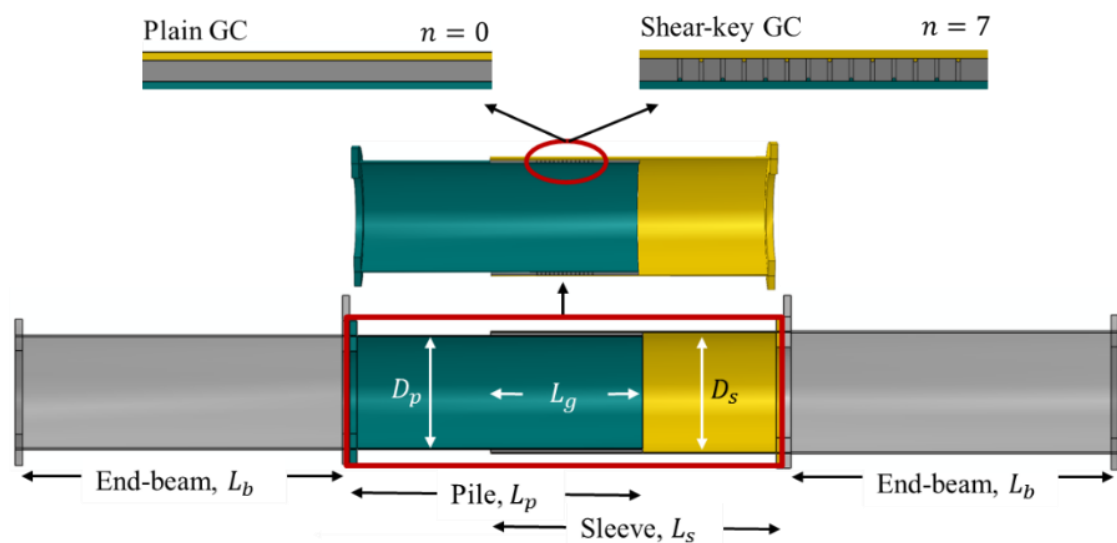


Figure 5.13 Model geometry and close up on (top left) PGC and (top right) SKGC1

The models consist of four hollow tubular beams with circular flanges at each end. The two end-beams are connected by bolted connections to the pile and sleeve which are subsequently attached by the grout cast. The model geometries are identical to the experiments carried out by Wilke (2013) and Lochte-

Holtgreven (2014). and differ between them in terms of overlap lengths and shear key numbers. Important geometrical parameters are listed in Table 5.5. In the FE model for simplification reasons the bolted connections are replaced by appropriate constraints which were found to not have any effect on the results. Additional parts of the test frame were also not included in the numerical models, and their role was simulated using appropriate constraints and boundary conditions reflecting the exact set-up.

Table 5.5: FE model geometry based on Wilke, 2013 and Lochte-Holtgreven, 2014

Parameter	Wilke (2013)	Lochte-Holtgreven (2014)
$h/s$	0.05	0.05
$w/h$	2	2
$n$	0, 7	5
$L_p, L_s$	1955	1955
$L_g$	1040	800
$D_p, t_p$	800, 8	800, 8
$D_s, t_s$	856, 8	856, 8
$D_g, t_g$	840, 20	840, 20
$F_o$	1.3	1.0
$L_b, t_b$	1950, 14	1950, 14

Each individual part was finely discretised using C3D8R elements taking into account regions of higher interest. For example, to reduce the total number of elements, a coarser mesh was used for the end-beams when compared to the pile, sleeve and grout discretisation. Nevertheless, for the models that include shear keys an increased number of elements is inevitable as a higher density mesh on the grout is required. Along the thickness of the steel parts a minimum of three-elements is maintained to avoid locking, whereas a finer discretisation was used

for the grout. The shear key geometry was modelled as perfectly circular without considering irregularities due to welding so as to achieve a higher quality structured mesh. Twelve seeds along the circumference of the shear keys were required for their as shown in Figure 5.14. Due to the small size of shear keys that were used in these tests a large number of elements was needed for refinement purposes and to achieve the curvature of a perfectly circular shear key. However, considering the explicit scheme used and that the solution time is strictly related to the element size in such computations, this led to models with shear keys being computationally demanding compared to the plain-pipe GCs. The PGC, SKGC1,2 were all equipped with the same constraints, interaction and material properties for consistency purposes. A detailed illustration of the selected constraints and applied boundary conditions used in the FE models is shown in Figure 5.15 using the SKGC1 model as an example.

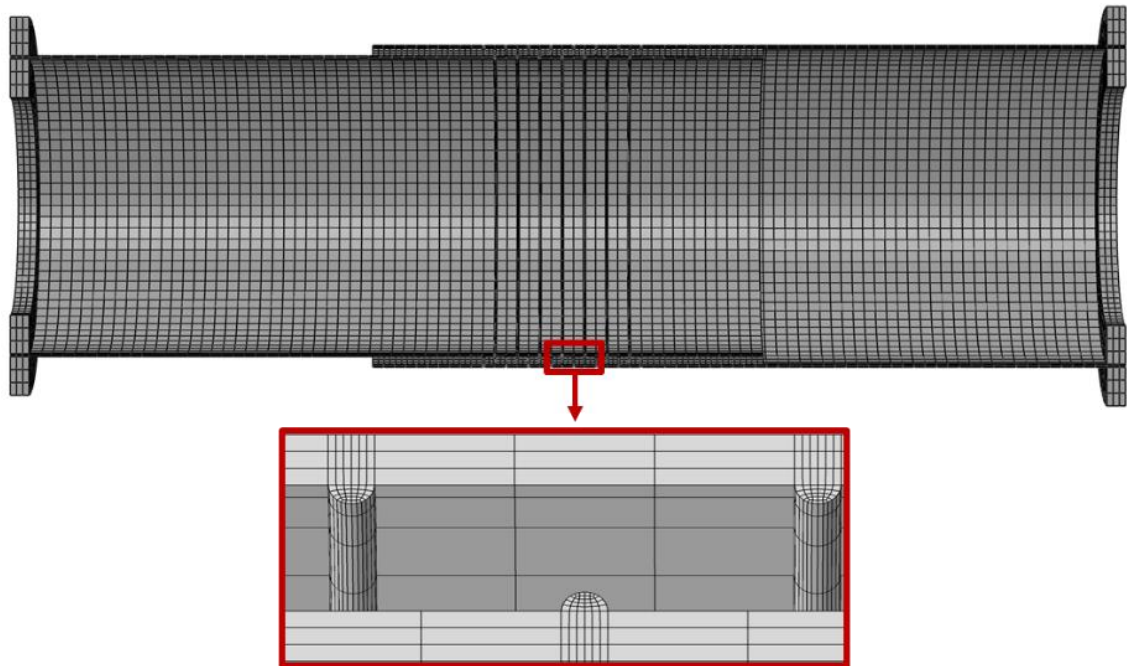


Figure 5.14 Meshed GC and zoomed shear key detail

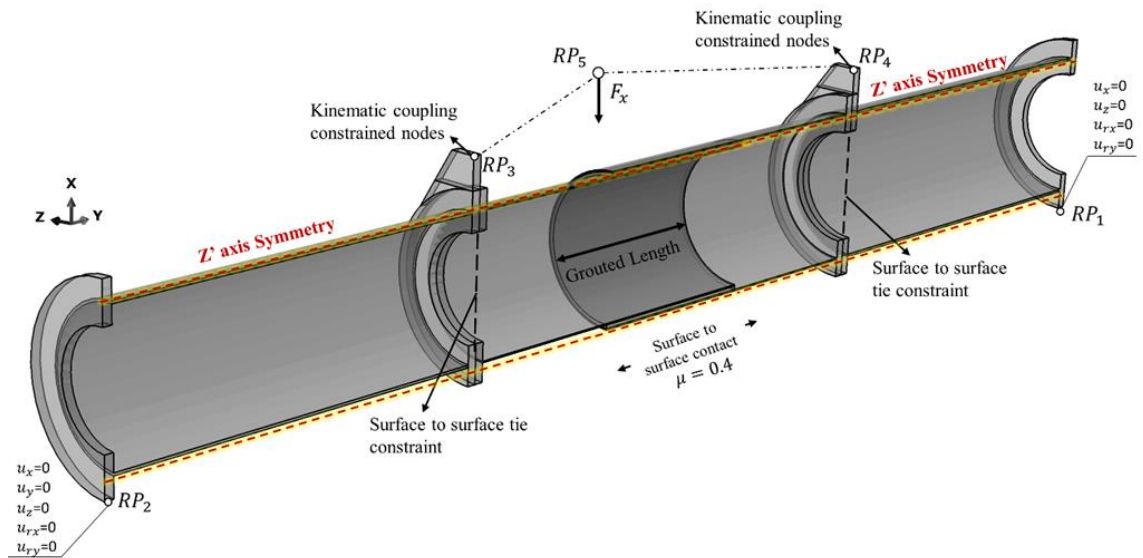


Figure 5.15 Boundary conditions and constraints applied in the FE model

## 5.8.2 Global behaviour and failure modes

For validation, the FE models were examined against the experiments in terms of global behaviour by using typical load-deflection expressions, stress development on the steel parts across the overlap length of the joint and interface separation between steel and grout. For the PGC and SKGC1 models a comparison of the overall response is made in Figure 5.16a and Figure 5.16b and the developed gaps are depicted in Figure 5.16c and Figure 5.16d. Overall the results from the numerical models are in excellent agreement with the experiments and the ability of the FE model to replicate the response of the GC numerically is demonstrated convincingly.

For the examined GCs the load was applied until pile yielding occurs to the bottom of the GC (see Figure 5.17b) due to the slender cross-section employed. At this point, a distinct gap in the opposing top and bottom ends of the connection has already developed as shown in Figure 5.17a and as reported in the test results. Despite both models exhibited a similar behaviour the interface de-bonding, for SKGC1 the gap was significantly reduced. Finally, when

comparing the peak displacement of the two specimens a 6% higher deflection was observed for the PGC which is identical with the experiments (see Table 5.6).

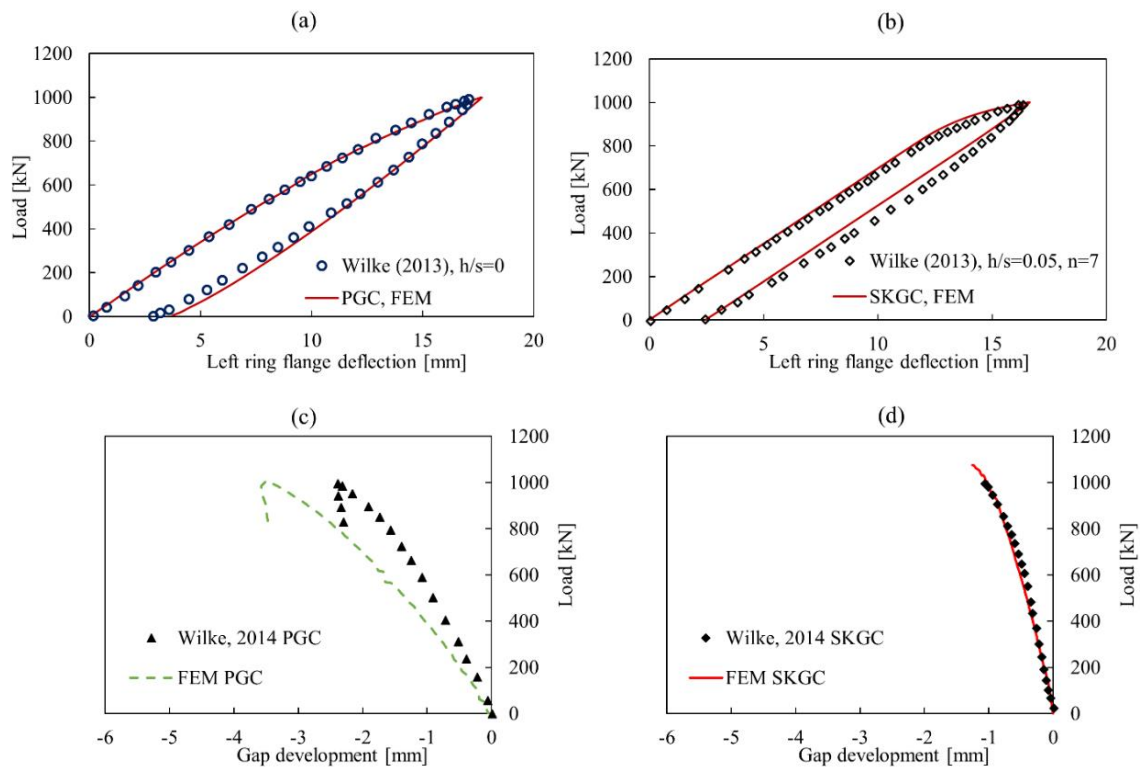


Figure 5.16: Force-displacement and force-gap between FE models and experiments

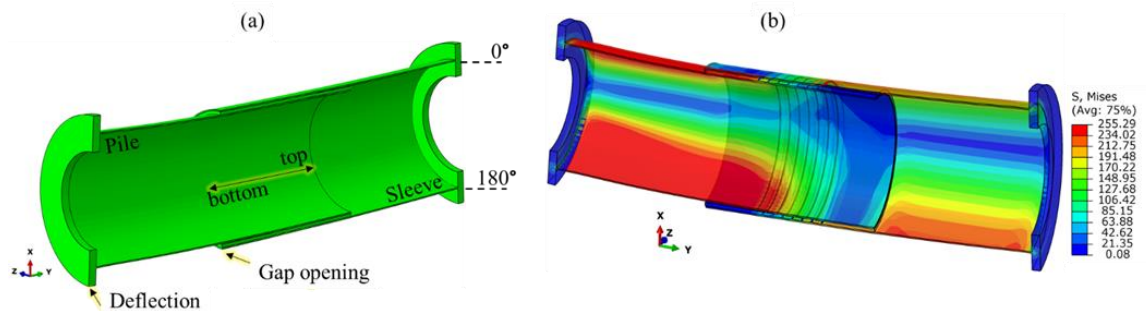


Figure 5.17: a) Gap formation owing to force-transfer mechanism and b) stresses on GC under bending

To enhance the validity of the FE models, the longitudinal stresses ( $\sigma_{22}$ ) are also illustrated in Figure 5.18 and Figure 5.19. Good agreement is achieved overall and only the stresses at the top of the PGC sleeve are slightly underestimated.

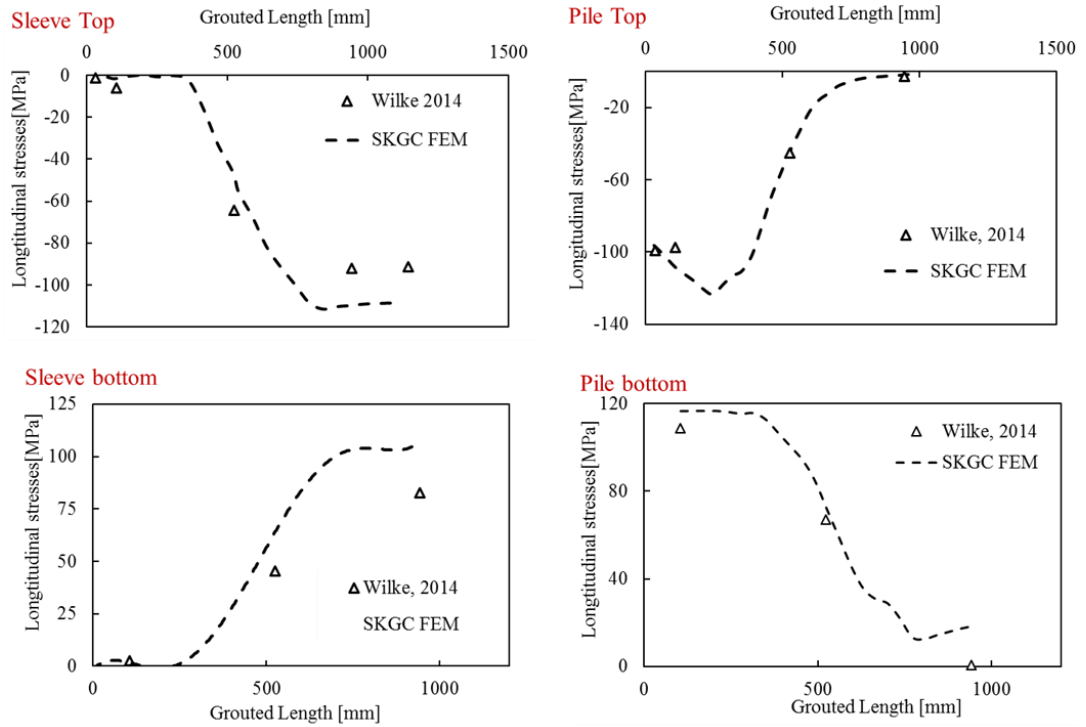


Figure 5.18: Longitudinal stresses at load level  $F=435\text{ kN}$  for SKGC

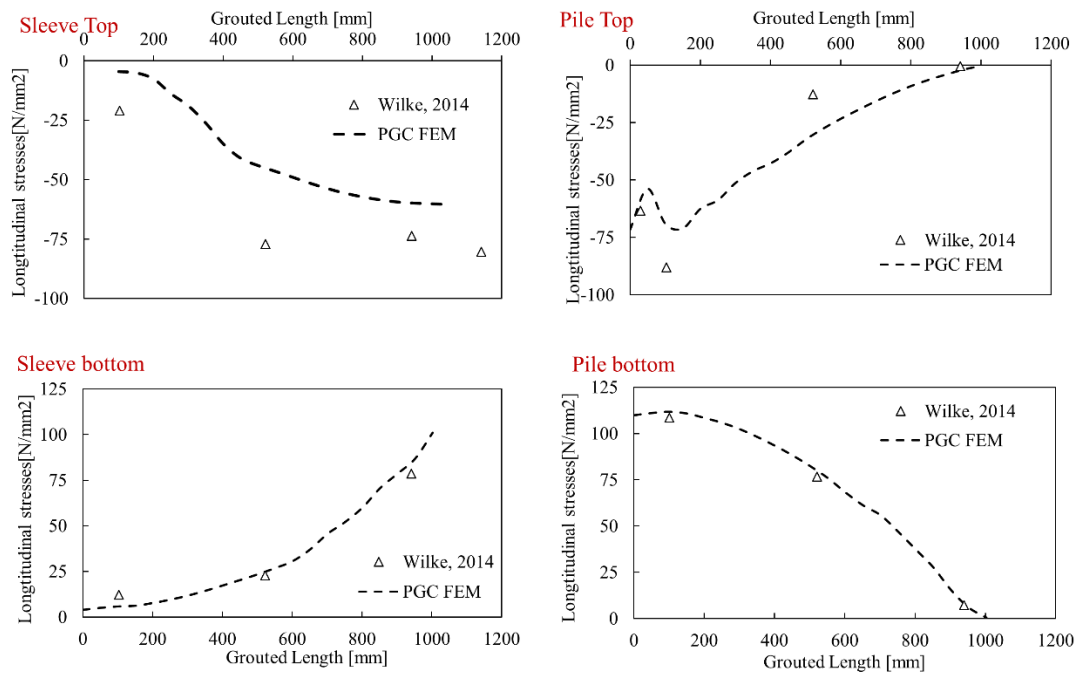


Figure 5.19: Longitudinal stresses at  $F=435\text{ kN}$  for PGC

Concerning SKGC2, a comparison of the FE model against the test conducted by

Lochte-Holtgreven, 2014 is presented in Figure 5.20. Owing to the lack of an ultimate load test the model was validated within the elastic stage following the experimental load protocol. The grout stress state for SKGC2 is shown in Figure 5.21, where it is shown that the maximum stress is located in the internal side of the grout cast at the first shear key location at the top of the GC.

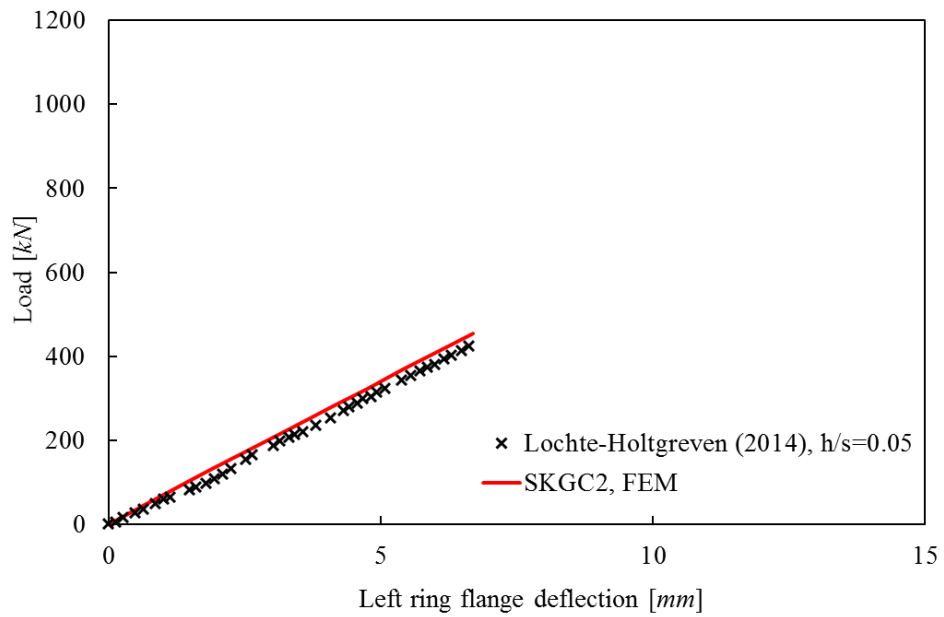


Figure 5.20: Force-displacement for GC with  $F_0=1$

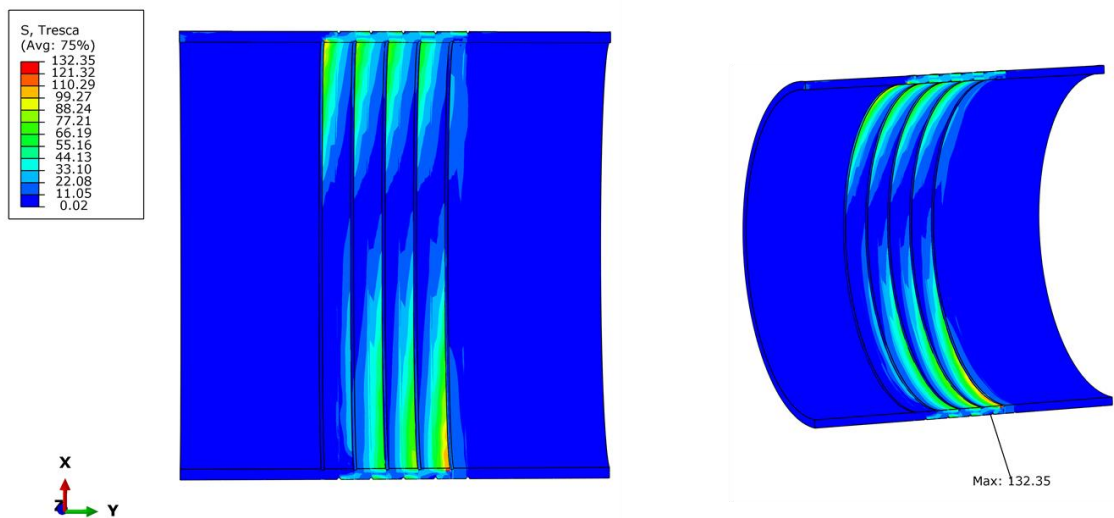


Figure 5.21: Tresca stresses on the pile-grout interface

### 5.8.3 Experiments at University of Birmingham

The FE models imitate the four-point bending configuration of the tests conducted by the author and at the same time the symmetry of the tubular GC is exploited to reduce the total number of elements required. The parts forming the assembly were discretised using a total of 176,190 C3D8R elements. External parts such as spreader beams, columns or supports which were part of the test set-up were replaced by appropriate boundary conditions and constraints resulting in a simply-supported beam similarly to the models in section 5.8.1. The boundary conditions and constraints which were used to define the FE model are summarised in Figure 5.22.

The boundary conditions were employed on reference points (RP<sub>1-4</sub>) located on the external surfaces of the rings. RP<sub>1,4</sub> correspond to the pile whereas RP<sub>2,3</sub> to the sleeve. The subsequent nodes were tied to them with rigid body constraints. The load was applied at points RP<sub>3</sub> and RP<sub>4</sub> in the form of displacement boundary condition. Similarly, the simply-supported boundary conditions were employed at points RP<sub>1</sub>, RP<sub>2</sub>. Overall a consistent set of boundary conditions and constraints was maintained for all the tests regardless of the origin of the experiment.

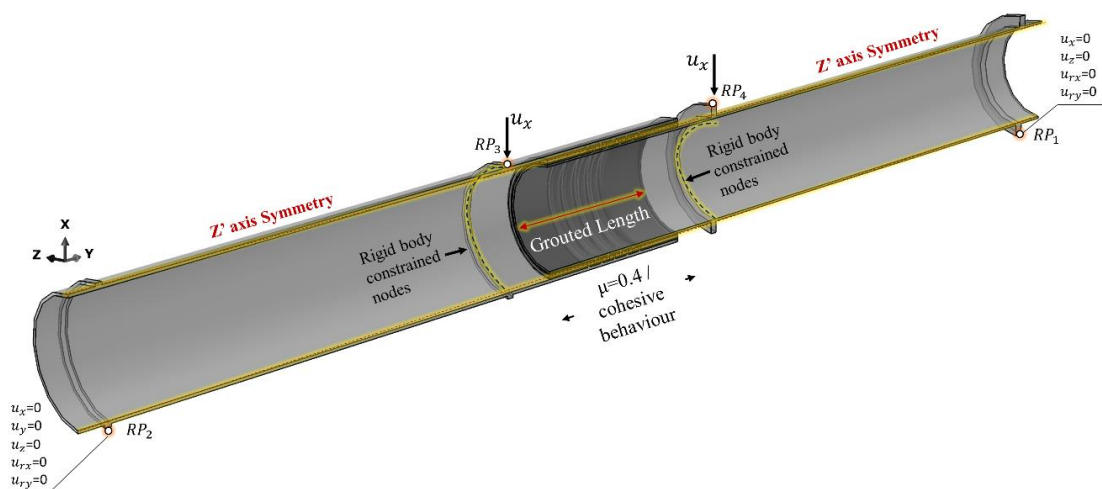


Figure 5.22: Four-point test configuration and boundary conditions

### 5.8.4 Global behaviour and failure modes

The global behaviour is initially compared with the recorded response from the experimental tests (Figure 5.23). Overall very good agreement was found considering the ultimate load and failure modes that were reported from the experiments, however the overall response is slightly overestimated by the numerical model.

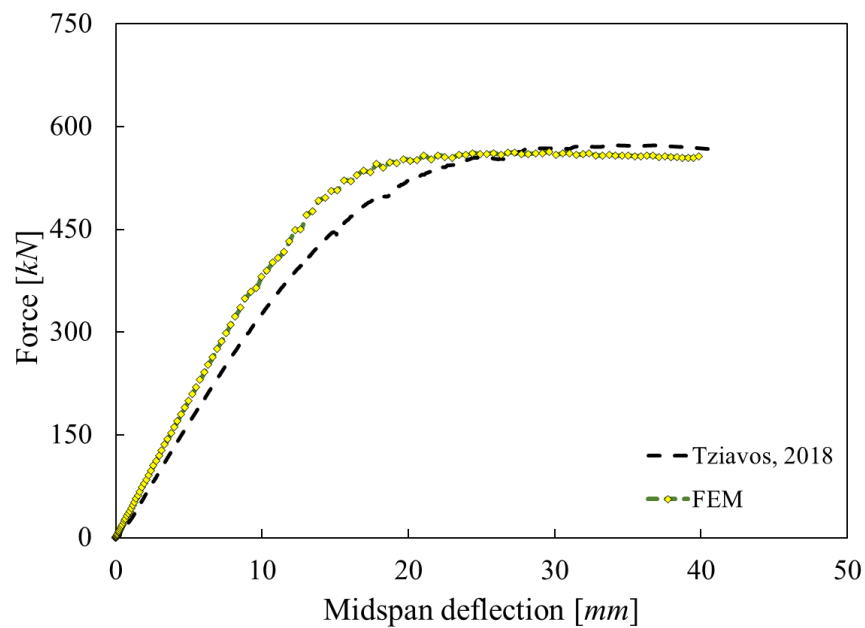


Figure 5.23: FE results against UoB tests

The failure mode comparison is summarised in Figure 5.24 and Figure 5.25. The gap at the interface occurring between the pile and grout at the tensile region of the GC was accurately traced (Figure 5.24a). Gapping developed significantly along the length of the connection almost reaching the first shear key at the sleeve region. Buckling of the pile occurred at the bottom of the connection (Figure 5.24b) once the diagonal struts failed successively as thoroughly discussed in sections 3.10 and 3.12. The local behaviour of the grout in the shear-keyed region was also captured in great detail. Cracks initiated at the tip of opposing shear keys as shown in Figure 5.25 and developed circumferentially.

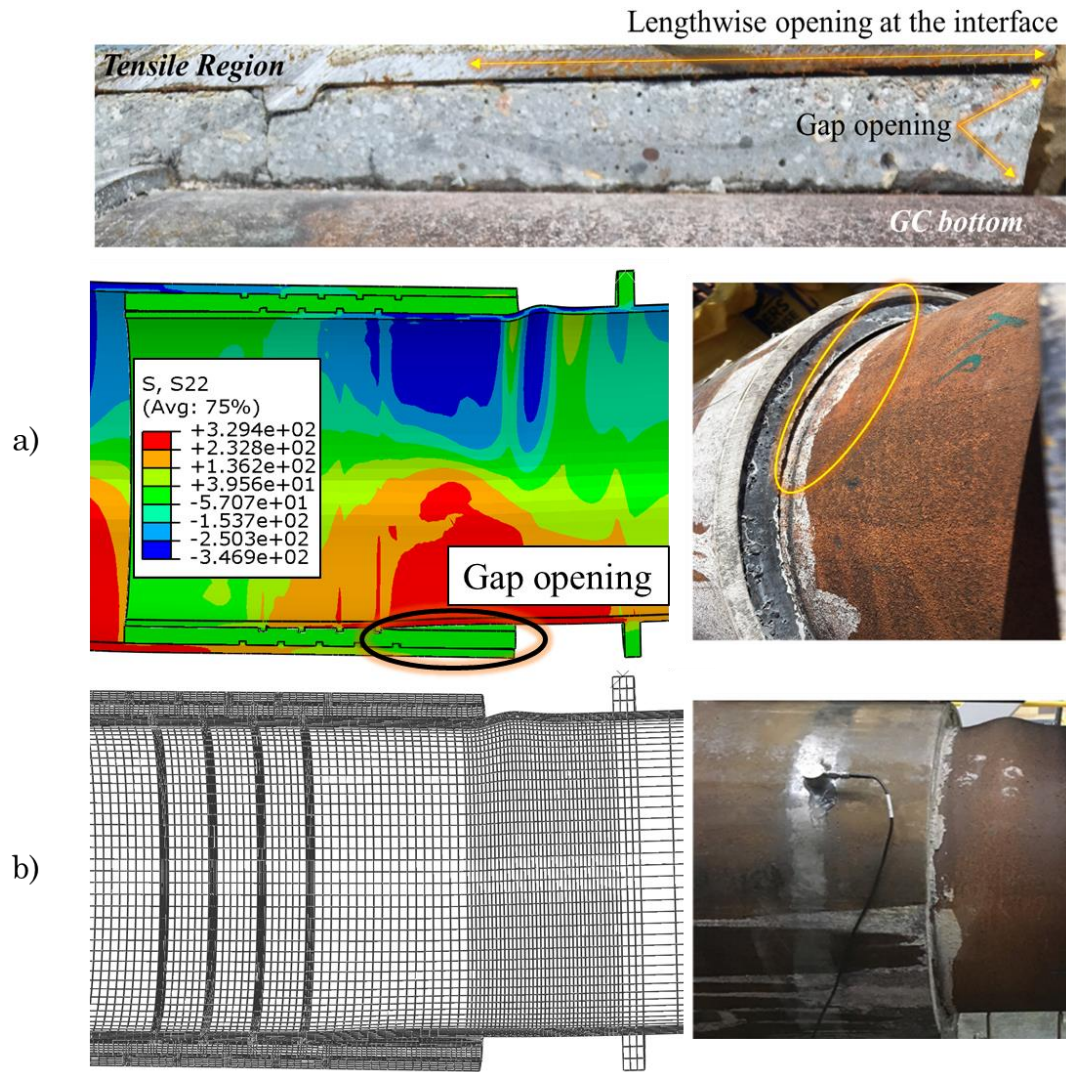


Figure 5.24: FE model failure modes

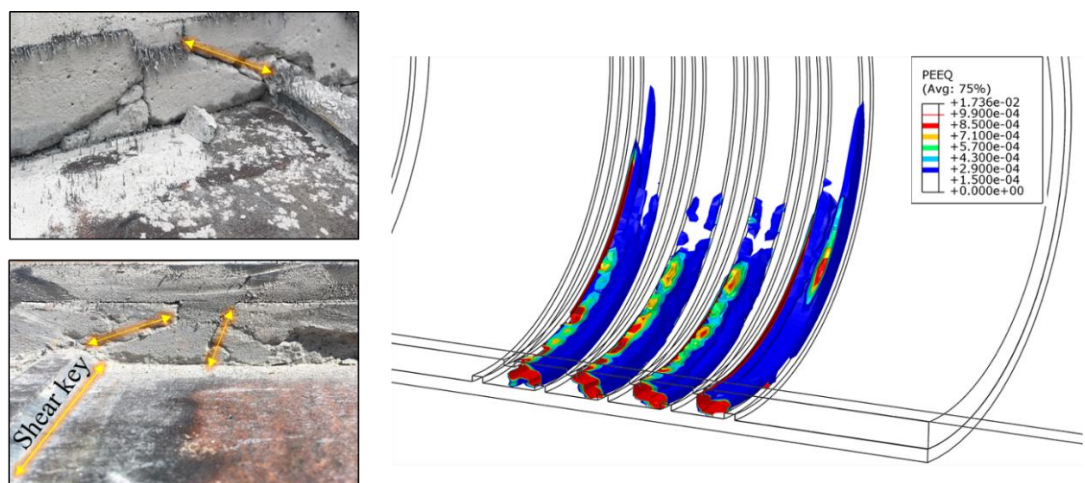


Figure 5.25: Strut cracking in the grout core and corresponding plastic strains from FE model

The longitudinal stresses that developed along the steel piles for different applied loads are depicted in Figure 5.26. The start of the grouted length that is depicted as zero in the horizontal axis is located at the bottom of the GC.

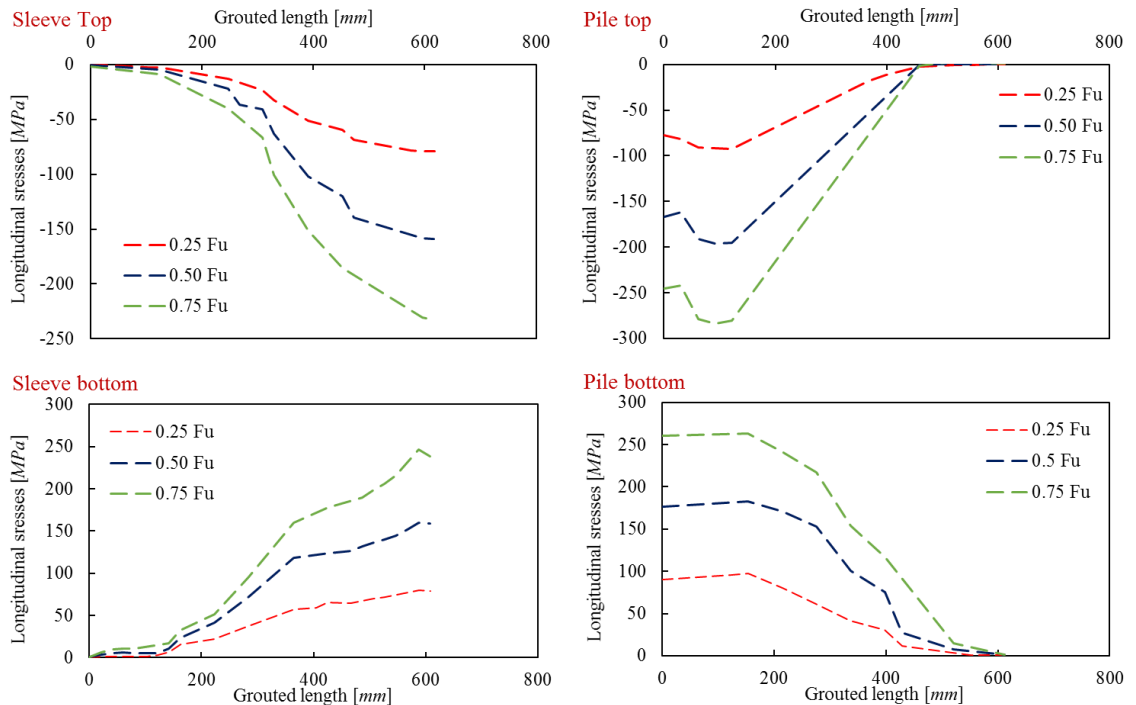


Figure 5.26: Longitudinal stresses at different load levels

### 5.8.5 Grout confinement and composite action

For experiments carried out by the author an investigation on alternative techniques for modelling the GC composite behaviour was conducted so as to model the interface behaviour of the model. As already discussed within this thesis (see sections 2.11 and 5.5) analytical models including confinement effects are not commonly employed for offshore UHPGs. This was also the case within this research project. As shown the overall behaviour was well captured using a high dilatancy and a simplified expression of the compressive behaviour with no confinement effects. Furthermore, in the literature concerning GCs, the tangential behaviour is being exclusively treated with friction models. In order to develop a FE model that captures the complex bond behaviour and improves the overall

behaviour as described in 5.8.4 a cohesive-based behaviour of the surfaces was examined in combination with the unconfined material model.

In an earlier study by Moon et al. (2007) it was noted that employing such an interaction property at the interfaces along with a non-confined material model, is a better approximation of the stress state such composite structures experience. The authors modelled the confinement effect and overall composite action of a tubular composite beam under bending loads by using cohesive-GAP elements and noted the benefits of the approach.

Therefore, a comparison between the two methods was carried out. Initially, a friction coefficient  $\mu=0.4$  in the tangential component and a hard formulation in the normal direction was used to define the contact scheme as in the aforementioned validation models. The results were compared against a cohesive-based behaviour model. In Abaqus when the explicit method is followed the cohesive modelling is only available within a general contact formulation, hence the Coulomb friction model was also applied with a general contact scheme. The definition of it has already been discussed, however the cohesive behaviour requires a new series of parameters to be identified (see section 5.4) and those are discussed herein.

An uncoupled traction-separation was chosen with an elastic diagonal stiffness matrix  $K$  defining the normal ( $K_{nn}$ ) and tangential direction ( $K_{ss}$ ,  $K_{tt}$ ) components. The stiffness values for the interface behaviour in the tangential direction are those which affect the model behaviour the most (Lee et al., 2011; Mollazadeh and Wang (2014)). Hence, for the presented models the normal component value was assumed to be equal to the tangential component values. They were chosen by conducting a sensitivity analysis for a range from 1 to 500  $N/mm^3$  due to lack of dedicated experimental data. A similar approach was followed by Mollazadeh and Wang (2014). The sensitivity analysis revealed that

values from 25 and higher yielded similar results, hence a value of  $25 \text{ N/mm}^3$  was selected. Damage initiation was defined by means of maximum nominal stress while normal and shear components were selected to represent the experimental tests. A displacement-based damage evolution was used along with an exponential softening behaviour as per section 5.4.2. The comparison of the contact schemes is illustrated in Figure 5.27. Overall, both models capture the ultimate loads accurately, however the cohesive-behaviour model is in better agreement with the overall response of the GC. This is due to the bond-slip behaviour being controlled by the interface gaps that were found in the tests. In practice the traction-separation law that controls the behaviour of the interface, is elastic until damage initiation. This corresponds well with the progressive and abrupt failure of the struts between shear keys as reported in the experiments.

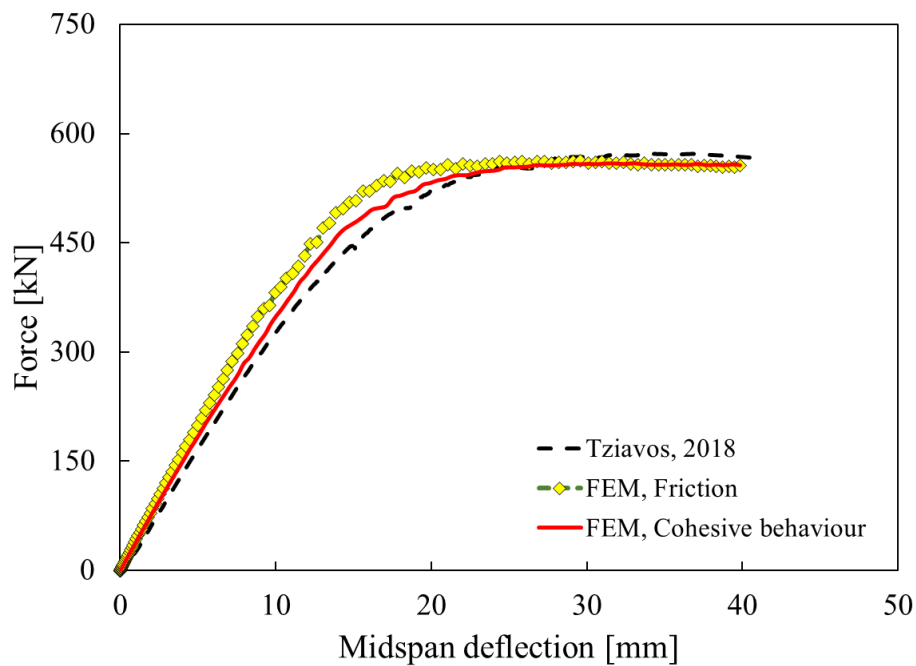


Figure 5.27: Comparison between Coulomb-friction model and Cohesive behaviour

Table 5.6 summarises the performance of the FE models against the selected experiments. For the tests conducted by the author the cohesive models are used. All in all, the numerical models were accurately validated against a series of

geometries and types of GCs and are considered a reliable representation of physical models. Thus, in the subsequent chapter, they are taken forward to conduct a parametric analysis.

Table 5.6: Summary of FE model results against test results

Model	$F_{Exp.}$ [kN]	$F_{FE}$ [kN]	$F_{FE}/F_{Exp}$	$\Delta_{Exp.}$ [mm]	$\Delta_{FE}$ [mm]	$\Delta_{FE}/\Delta_{Exp}$
<sup>1</sup> Tziavos, 2018	569.5	558.2	0.98	35.1	39.8	1.08
<sup>2</sup> Wilke, 2013	999.6	1000	1.0	17.0	17.6	1.03
<sup>3</sup> Wilke, 2013	992.9	1001	1.0	16.3	16.6	1.02
Lochte-Holtgreven, 2014	442.4	454.2	0.99	6.6	6.69	0.95

<sup>1</sup>Average of two specimens, <sup>2</sup>Plain-pipe GC, <sup>3</sup>Shear key GC

# 6 PARAMETRIC ANALYSIS

## 6.1 Overview

The validated FE models which were presented in sections 5.8.1 and 5.8.3 were taken forward to conduct a detailed parametric investigation. The presented analysis has two main aims: *i)* to illustrate the robustness of the developed FE models by accurately capturing different grout failure modes depending on the variation of pile and sleeve geometry and *ii)* to assess the effect of each individual parameter on the global behaviour of a GC. Therefore, the focal interest is set on shear keys. Local grout patterns as a function of spacing between neighbouring shear keys are illustrated in section 6.3. The influence of the shear key ratio and the shear key number are investigated on GCs with varying  $F_0$  in sections 6.4 and 6.5 to allow for the assessment of the length's influence. The influence of diameter to thickness ratio for grout and steel is presented in sections 6.6 and 6.7 respectively, whereas installation tolerances are examined and discussed in 6.8.

Research papers relevant to this chapter's scope have been published by the author and are explicitly referenced in text where applicable:

**Tziavos, N.I.**, Hemida, H., Metje N. and Baniotopoulos, C. (2019). Non-linear finite element analysis of grouted connections on monopile wind turbines, *Ocean Engineering*, 171, pp. 633-645.

## 6.2 Parametric study notation

The results extracted from this parametric investigation are classified into two main categories: *i*) the global and *ii*) local behaviour of the models. For global behaviour reference will be made to the overall performance of the GC as this is highlighted through typical load-displacement curves or gaps at the interfaces. On the contrary, local behaviour will mainly focus on the grout core and the cracking or crushing patterns that become visible within the material once failure mechanisms initiate. The distinction from global to local behaviour is made to prove the robustness of the model to predict changing failure modes of the grout based on the geometrical characteristics of the GC and highlight the reliability of the numerical approach.

The main cross-sectional properties of the parametric FE models under investigation are given in Table 6.1. The table includes dimensions of the parameter of interest when compared to the base-validated models, hence those that are not tabulated are kept unchanged. Plain-pipe along with shear-keyed GCs are amongst the simulated models aiming to achieve a comparison between the two types and highlight the differences between the load-transfer mechanisms that occur. In order to maintain consistency along the parametric models, constraints, material models and boundary conditions were kept constant and identical as those used in the corresponding validation model of Chapter 5. The parametric FE models comply with the following notation:

$$F_{o,i} - n_i - s_i - D_{t,i}$$

where,  $F_{o,i}$  corresponds to GC overlap length with  $i$  ranging from 1 to 1.5 and  $n, s$  denoting the height and spacing between shear keys respectively.  $D_{t,i}$  corresponds to the cross-sectional properties of the part with subscript  $i$  denoting  $s, p, g$  for sleeve, pile and grout. For example, the model  $F_{o13n5s60Dt_s40}$

corresponds to a GC with an  $F_o = 1.3$ , five shear keys distributed at evenly spaced intervals of 60 mm and a  $D/t$  ratio of the sleeve equal to 40. Two groups of FE models were investigated and the notation is marked accordingly. All subsequent simulations involved GCs where shear key number refers to the effective number of shear keys of the sleeve following the expression  $n_{\text{eff}} = n + 1$ . This was elected so as to comply with the current practice as dictated by DNV ST-0126 (2016).

### 6.3 Local behaviour of grout

In Lamport (1988) the first experimental tests aiming to study the behaviour of the grout based on the effect shear key parameters such as spacing and height. Typically, cracks within the annular grout evolve diagonally with varying inclination owing to spacing between a pair of shear keys. Once spacing increases at the tip of each shear key cracking develops in the form of a cylindrical failure surface. Such changes in failure modes of the grout depending on the spacing of the shear keys were initially noted by Lamport (1988).

For this purpose, models with varying shear key spacing were simulated to verify that the selected FE approach can trace all possible failure modes within the grout cast. Such an objective is of importance as it would prove this modelling approach can be used in real-case scenarios which trigger such changes in the failure mode. Such examples include but are not limited to pile inclinations and misalignments, shear key misalignments during the installation and grouting phase and finally uneven grout thickness along the circumference. All these scenarios are also addressed and discussed in the following sections of this chapter.

Varying spacing of  $s=30, 60$  and  $120$  mm was investigated on GCs with a fixed overlap length of 1.3. The effect of spacing was isolated by keeping a constant

shear key height at  $h=3 \text{ mm}$  resulting in the following height to spacing ratios: 0.1, 0.05, 0.025. The grout compressive strength was maintained at  $130 \text{ MPa}$  as in all validated models.

To assist visualisation, cracks are demonstrated by means of plastic strains similarly to section 5.8.4. Cracking initiated at the tip of shear keys for all the arrangements. In Figure 6.3 iso-surfaces and contour plots of plastic strains within the grout in the tensile region of the connection are illustrated. The shear keys within the GC correspond to a ratio ( $h/s=0.05$ ) that has been employed in the tests by Wilke (2013), Lochte-Holtgreven (2013) and Wang et al. (2017).

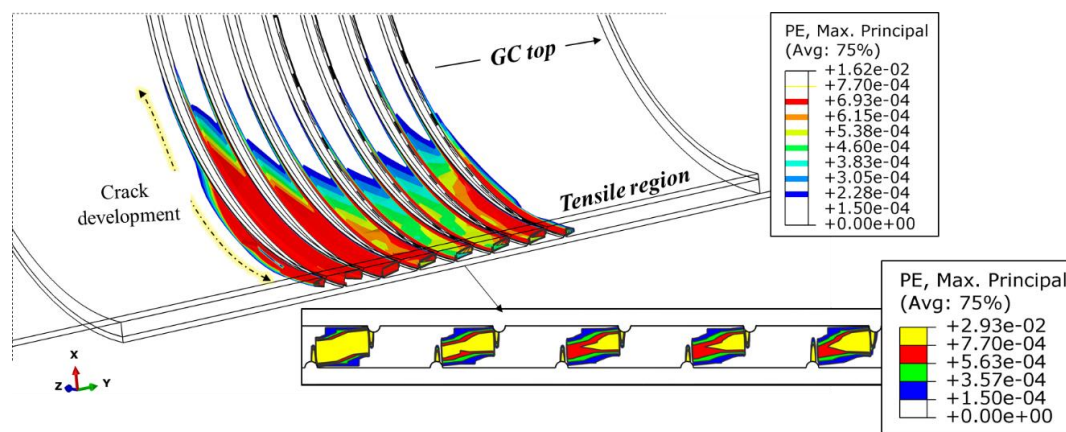


Figure 6.1: Iso-surface and contour plots depicting grout plastic strains on a GC with a spacing of  $s=60 \text{ mm}$

For  $s=60 \text{ mm}$  cracks developed simultaneously between shear key pairs of the pile and sleeve until they merge to form a diagonal strut which enables the load-transfer mechanism (Figure 6.4a). Once the load increases additional wedged cracks formed in front of the shear key. The inclination of the strut between two shear keys for this configuration was found to be  $34^\circ$  (Figure 6.4a).

Once the spacing of the shear keys was reduced to  $s=30 \text{ mm}$ , the struts forming between the shear keys were formed with a steeper inclination (Figure 6.2). The struts failed with an inclination of  $53^\circ$  as illustrated in Figure 6.4b. This cracking

behaviour compares well with the findings reported on previous experimental studies involving GCs with opposing shear keys (Anders and Lohaus, 2008). For the calculation of the angle of the diagonal cracks within the matrix ideal distances and geometries were used.

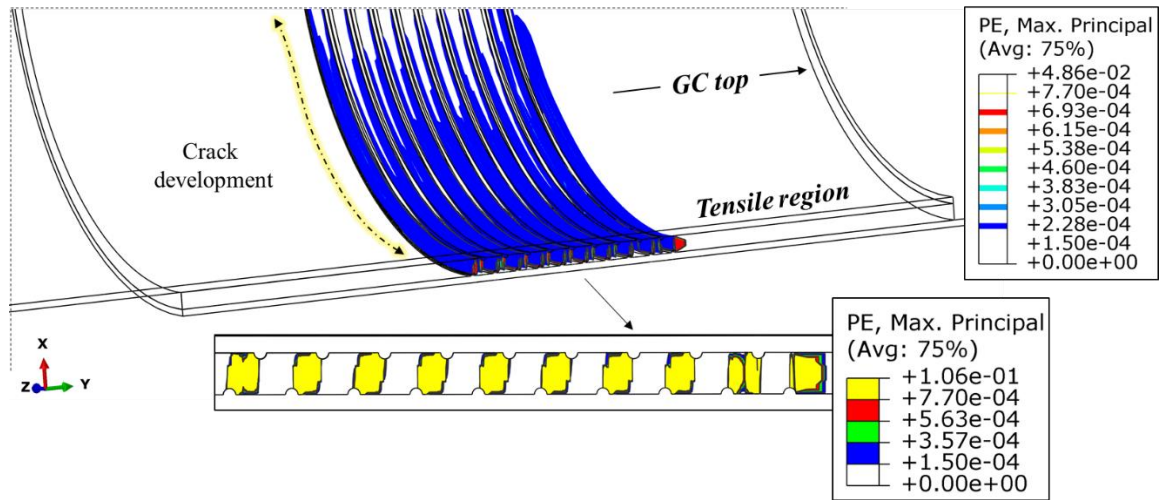


Figure 6.2: Iso-surface contour plots depicting grout plastic strains on a GC with a spacing of  $s=30 \text{ mm}$

Finally, the plastic strains for  $s=120 \text{ mm}$  are presented in Figure 6.3 and Figure 6.4c. The increasing distance leads to a very low shear connector ratio aiming to provoke the change in failure mode. Initially, due to the arrangement, the cracks initiated in front of the pile shear keys in contrast to the previous models. The crack developed until reaching the sleeve and the formation of a cylindrically-shaped failure surface originated circumferentially across the connection. The same mechanism was reported for all shear keys of the GC.

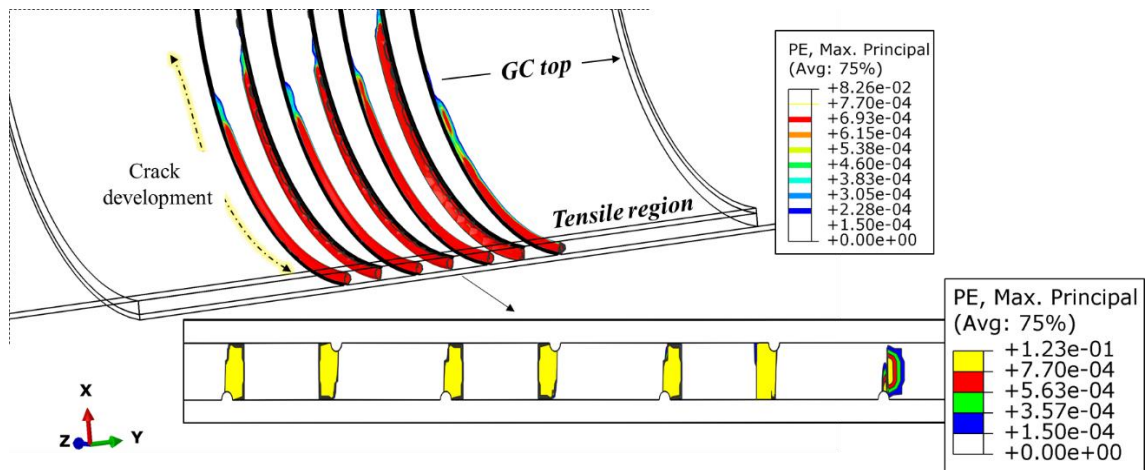


Figure 6.3: Iso-surface contour plots depicting grout plastic strains on a GC with a spacing of  $s=120\text{ mm}$

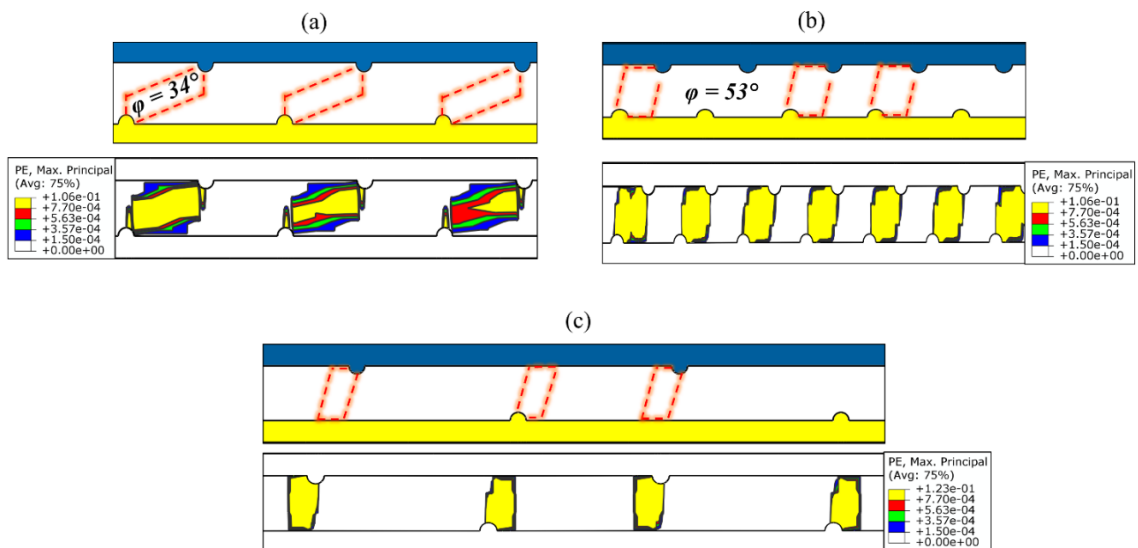


Figure 6.4: Grout failure modes for varying shear key spacing. a)  $s=60\text{ mm}$ , b)  $s=30\text{ mm}$ , c)  $s=120\text{ mm}$

## 6.4 Influence of shear key number and overlap length

Experimental campaigns conducted to date, often involve connections with  $F_0 < 1.5$  although this lies outside the recommended limits by DNV ST-0126 (2016) and previous versions. Initially, to demonstrate the benefit in bending stiffness with increasing grouted lengths, a typical force-displacement curve of selected models is shown in Figure 6.5. Models with shear keys are also included to

demonstrate the superior performance exhibited when compared to plain connections.

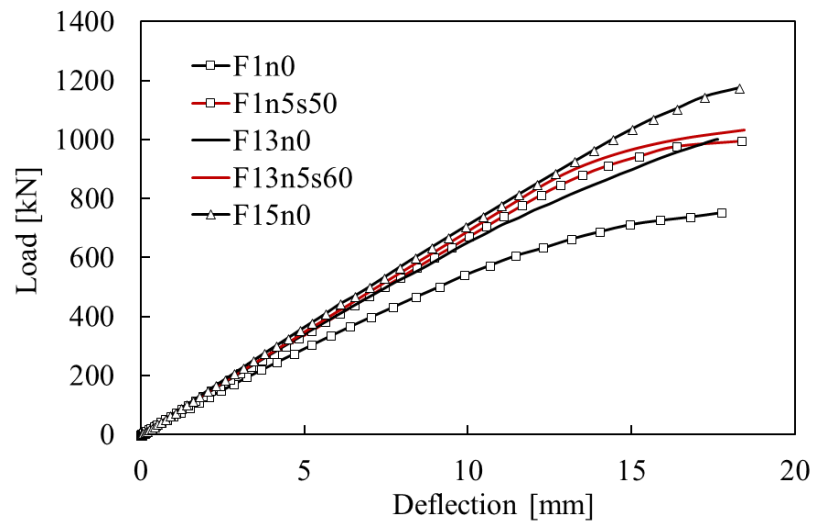


Figure 6.5: Force–displacement curve illustrating the effect of  $F_o$

A series of numerical models with varying shear keys were developed to monitor their effect on the connection. In agreement with the validation study, the interface gap occurring for an increasing number of shear keys at the opposing sides of the grout is also minimised (Figure 6.6), illustrating the considerable effect shear keys and grouted length have on the overall performance.

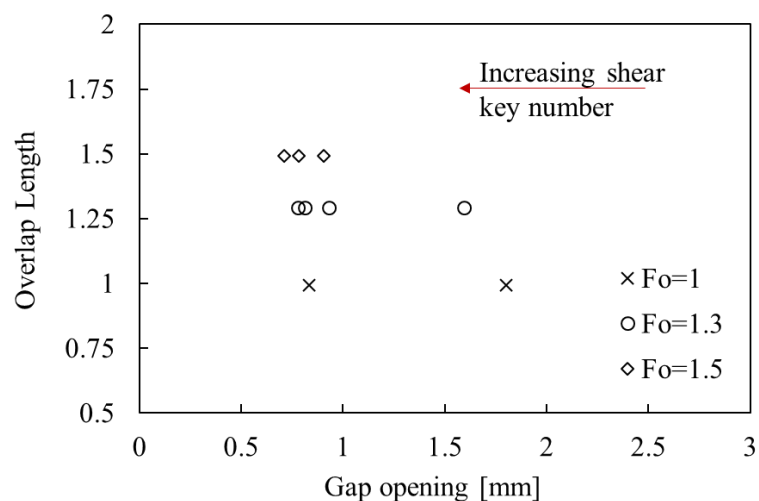


Figure 6.6: Maximum interface opening at the bottom of the GC

In Figure 6.7 the global response of representative models dictates that an increasing number of shear keys is beneficial. This is particularly pronounced for the lowest overlap length. From the parametric analysis it was observed that the influence of the shear key number is reduced for  $F_o=1.5$ .

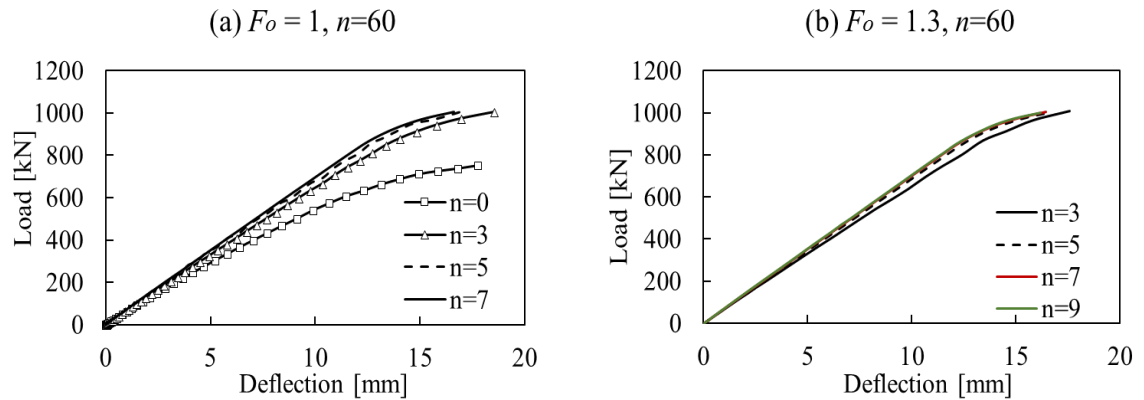


Figure 6.7: Force-deflection curves for: a)  $F_o=1$ , b)  $F_o=1.3$

The gap that develops in the steel grout interfaces due to bending in the connection is of considerable interest, as it leads to water ingress. This results in reduced friction between steel and grout which can effectively disrupt the performance of the joint (Schaumann et al., 2016). According to recent studies (Schaumann et al., 2017), GCs tested in dry environment have superior performance when compared to GCs in wet conditions.

To investigate the interface behaviour of the numerical models the maximum gap opening at the bottom of the connection was determined for the maximum applied load. Thereinafter, the results are compared with the analytical model proposed in Lotsberg (2013). In Figure 6.8, the opening that developed on GCs with  $h/s=0.05$  is compared with the prediction from the analytical model. For most of the investigated geometries very good agreement was found. The biggest discrepancies between the numerical and analytical solution appeared for the models with the lowest number of shear keys. It is apparent that an increased number of shear keys minimises the gap in the interface for all the examined

grouted lengths.

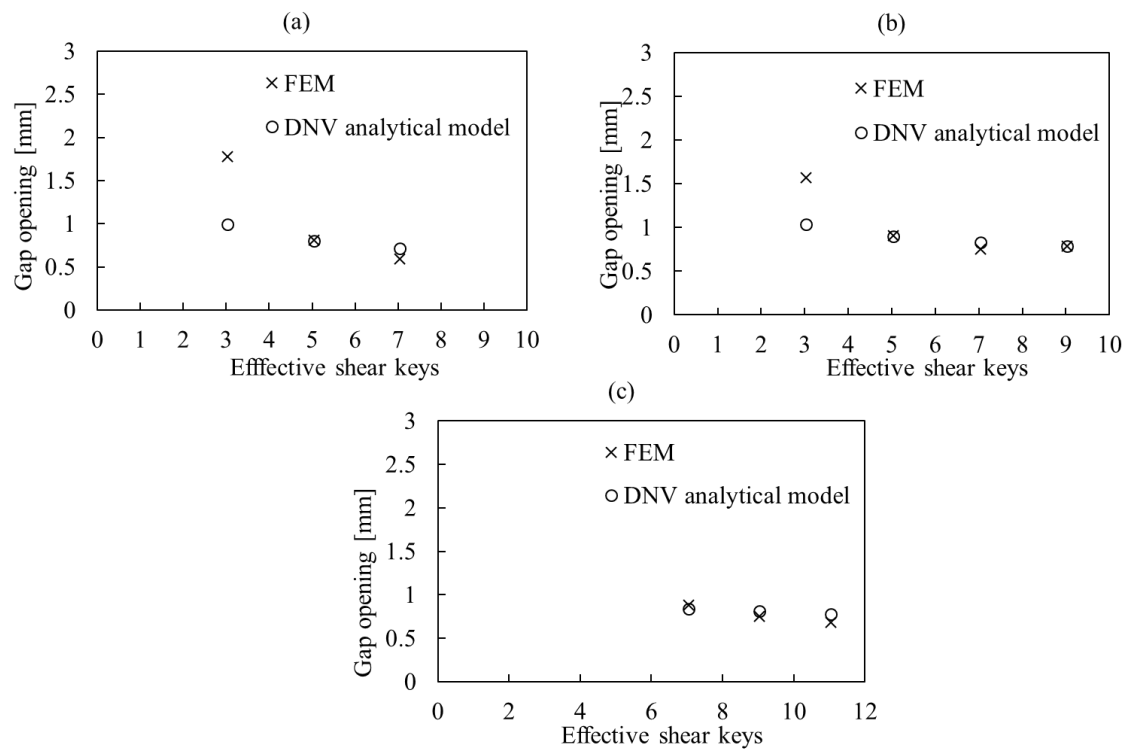


Figure 6.8: Maximum developed gap at the top of GC at Mmax for a)  $F_o=1$ , b)  $F_o=1.3$ , c)  $F_o=1.5$

The use of shear keys alters the force transfer mechanism compared to a plain connection. The loads are mainly transferred through the shear key region which subsequently reduces the stresses at the top and bottom of the connection. This is illustrated in Figure 6.9a and Figure 6.9b where the pressure along the circumference of the sleeve is given for models with varying shear keys and overlap lengths. The stresses shown, are exerted on the inner sleeve surface, at the top of the GC. Three neighbouring circular paths on the sleeve were used to extract the stresses from the sleeve nodes. The data points shown in Figure 6.9 depict the average values of the stresses from the three nodes on each location of the circumference.

An indicative fourth order polynomial trendline is fitted to the data-sets to highlight the distribution of stresses along the circumference of the sleeve. An

increase in the number of shear keys was also shown to be beneficial as the contact pressure reduces away from the shear keys. Connections with a higher number of shear keys exhibit lower stresses, particularly in the region between  $0^\circ$  and  $90^\circ$  where contact pressure peaks.

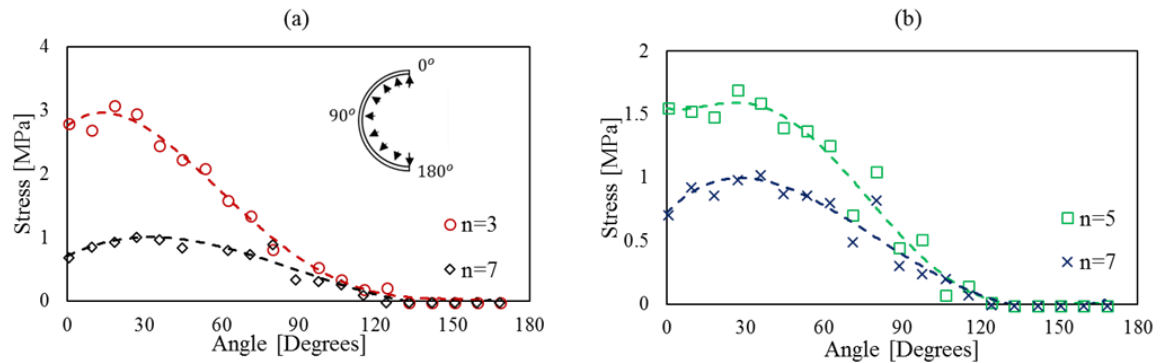


Figure 6.9: Contact pressure at maximum opening around the sleeve circumference for  
a)  $F_o=1$ , and b)  $F_o=1.3$

The stresses on the sleeve reduce to zero when approaching  $180^\circ$  as opening has occurred at the tensile side of the shell. The findings are in agreement with Schaumann et al. (2010) and Wilke (2013), as the shear-key region is now transferring a higher proportion of the applied loads when compared to a plain GC. Consequently, this translates to lower stresses at the top and bottom of the grout. The alteration in load-transfer can also be realised if one considers the intensity of plastic strains in the shear key vicinity. In Figure 6.10 the direction of plastic strains on a grout core are shown. The increased population of arrows in the tensile shear-keyed region depicts the damage occurrence taking place in this area.

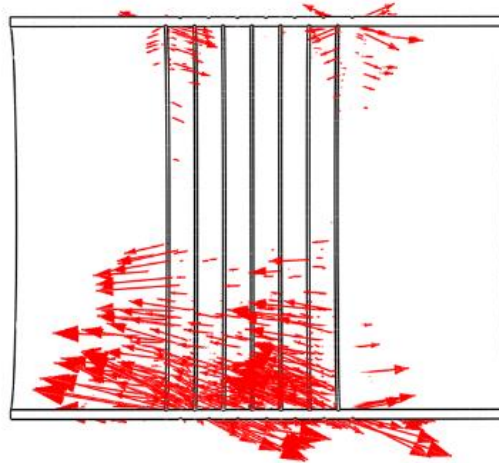


Figure 6.10: Grout plastic stain vectors at maximum load level

## 6.5 Effect of shear key spacing

The upper limit suggested in design guidelines (DNV ST-0126, 2014) for GCs with shear connectors is set to  $h/s < 0.1$ . Previous studies involving connections under bending have mostly employed lower shear key ratios from 0.02 to 0.05 (Lamport, 1988; Anders and Lohaus, 2008; Wilke, 2013). Similar ratios can be found in the literature for axially loaded GCs. In order to study the influence of higher ratios, nine models with a ratio of 0.06 were numerically solved. To achieve this ratio the spacing between two consecutive shear keys was reduced to 50 mm maintaining the same height and width for the shear keys.

In Figure 6.11a, b the maximum displacement over a normalised length (shown in red in Figure 6.11) is presented for models of different overlap lengths. For all the analysed models with various  $F_0$  a consistent pattern is noticed. Although a stiffer response is depicted for an increased overlap length and shear key number as discussed in section 4.2, increasing the shear key ratio did not improve the performance of the connection. The lower growth in displacement for GCs with  $h/s = 0.05$ , resulted in a better bond action between the grout and steel. Likewise, with the results in section 4.1, for  $h/s = 0.06$  the influence of the parameter is

noticeable for lower  $F_o$ , but significantly declines for  $F_o=1.5$  (Figure 6.11b).

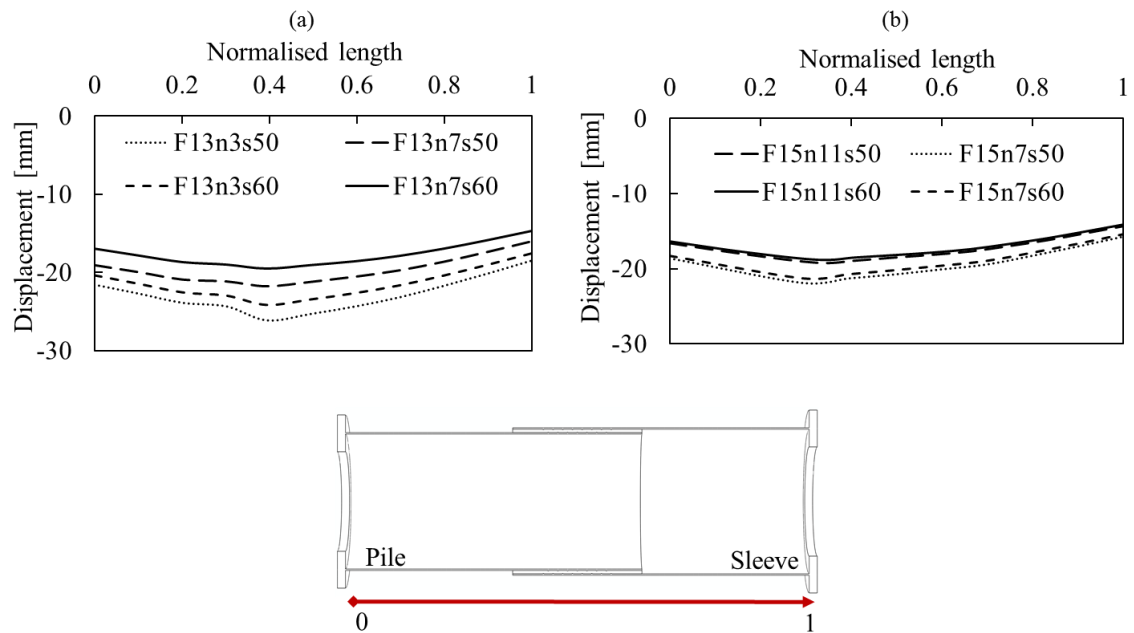


Figure 6.11: Displacement growth over normalised length for: a)  $F_o=1.3$ , b)  $F_o=1.5$

In addition, as depicted in Figure 6.12 the relative displacement which was found between the pile and sleeve for the parametric models is significantly higher for models with a shorter shear key region. Another deduction from Figure 6.12 is the fact that gaps on the interface can take place a lot sooner than ultimate loads are reached. Particularly for models with smaller shear key regions (see, e.g.,  $F_o1n3s50$  and  $F_o15n3s60$ ) significant gaps occurred rapidly at  $F \sim 0.6F_{\max}$ .

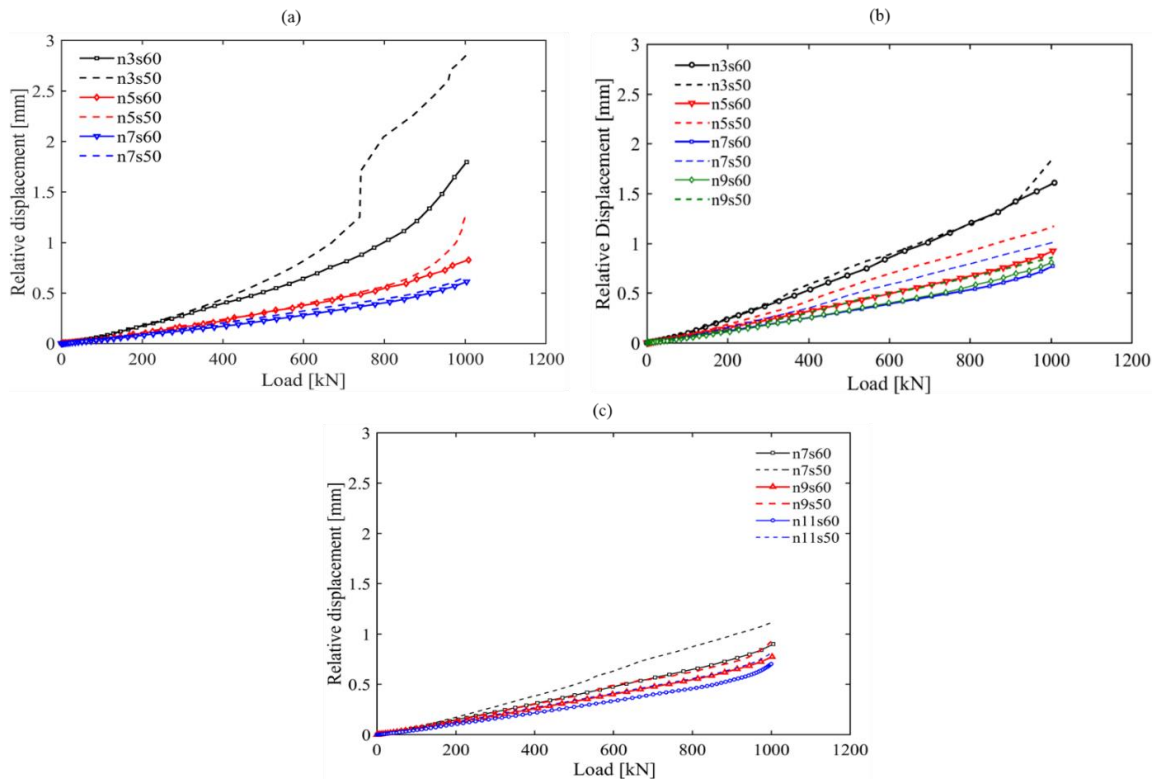


Figure 6.12: Force – Relative displacement for a)  $F_o=1$ , b)  $F_o=1.3$ , c)  $F_o=1.5$

Finally, in Figure 6.13 an overview of the interface gap calculated from the parametric models is presented as a function of the shear key region of each GC. The developed gaps form a plateau when the shear key regions are close to half the grouted length. However, it is evident that connections with shear keys in the middle third of the grouted length or less would benefit from a higher number of shear keys. An increasing number of shear keys is significantly reducing the de-bonding of the connection particularly for low overlap lengths.

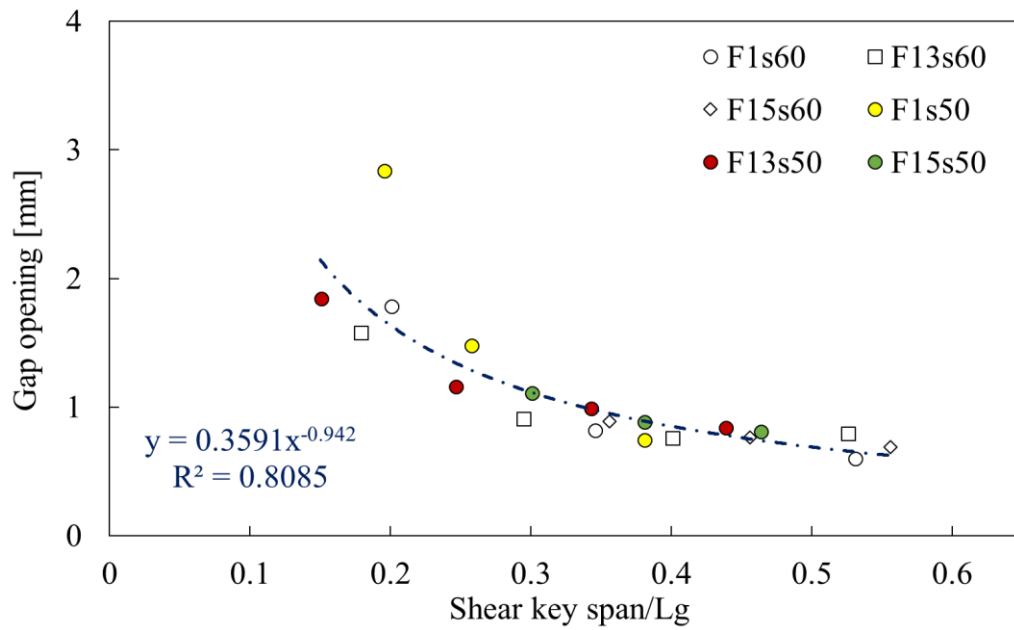


Figure 6.13: Maximum gap opening against shear key span from parametric models

Table 6.1: Geometrical characteristics of FE models for parametric analysis

Name	$F_o$	$n$	Dimensions [mm]				
			$L_{p,s}$	$t_{s,p}$	$h$	$s$	$L_g$
$F_o 1n0s0$	1	-	1835	8	n/a	n/a	800
$F_o 1n3s60$	1	3	1835	8	3	60	800
$F_o 1n3s50$	1	3	1835	8	3	50	800
$F_o 1n5s60$	1	5	1835	8	3	60	800
$F_o 1n5s50$	1	5	1835	8	3	50	800
$F_o 1n7s60$	1	7	1835	8	3	60	800
$F_o 1n7s50$	1	7	1835	8	3	50	800
$F_o 13n0s0$	1.3	-	1955	8	n/a	n/a	1040

$F_{\circ}13n3s60$	1.3	3	1955	8	3	60	1040
$F_{\circ}13n3s50$	1.3	3	1955	8	3	50	1040
$F_{\circ}13n3s120$	1.3	3	1955	8	3	120	1040
$F_{\circ}13n9s30$	1.3	9	1955	8	3	30	1040
$F_{\circ}13n5s60$	1.3	5	1955	8	3	60	1040
$F_{\circ}13n5s50$	1.3	5	1955	8	3	50	1040
$F_{\circ}13n7s60$	1.3	7	1955	8	3	60	1040
$F_{\circ}13n7s50$	1.3	7	1955	8	3	50	1040
$F_{\circ}13n9s60$	1.3	9	1955	8	3	60	1040
$F_{\circ}13n9s50$	1.3	9	1955	8	3	50	1040
$F_{\circ}15n0s0$	1.5	-	2035	8	n/a	n/a	1200
$F_{\circ}15n7s60$	1.5	7	2035	8	3	60	1200
$F_{\circ}15n7s50$	1.5	7	2035	8	3	50	1200
$F_{\circ}15n9s60$	1.5	9	2035	8	3	60	1200
$F_{\circ}15n9s50$	1.5	9	2035	8	3	50	1200
$F_{\circ}15n11s60$	1.5	11	2035	8	3	60	1200
$F_{\circ}15n11s50$	1.5	11	2035	8	3	50	1200

---

## 6.6 Cross-section effect on bending strength

The cross-sectional characteristics of the pile and sleeve as dictated by the diameter to thickness ratio have an influence on the capacity of tubular GCs. To that end, GCs with varying ratios compared to the validated model presented in section 5.8.3 were investigated. To achieve different ratios, the thickness of the pile or sleeve was modified aiming to maintain a grout core with a constant thickness. To isolate the influence of each steel tube, their effect was studied individually. For each case four alternate cross-sections were investigated resulting in ratios of 40, 50, 60 and 70 with a constant grout compressive strength of 130 MPa. The developed FE models are tabulated in Table 6.2. The results are summarised in the form of load-displacement curves in Figure 6.14 and Figure 6.15, where displacement refers to the deflection recorded at the midspan of the model. Similarly, as in the experimental study midspan is half the distance between the loading points.

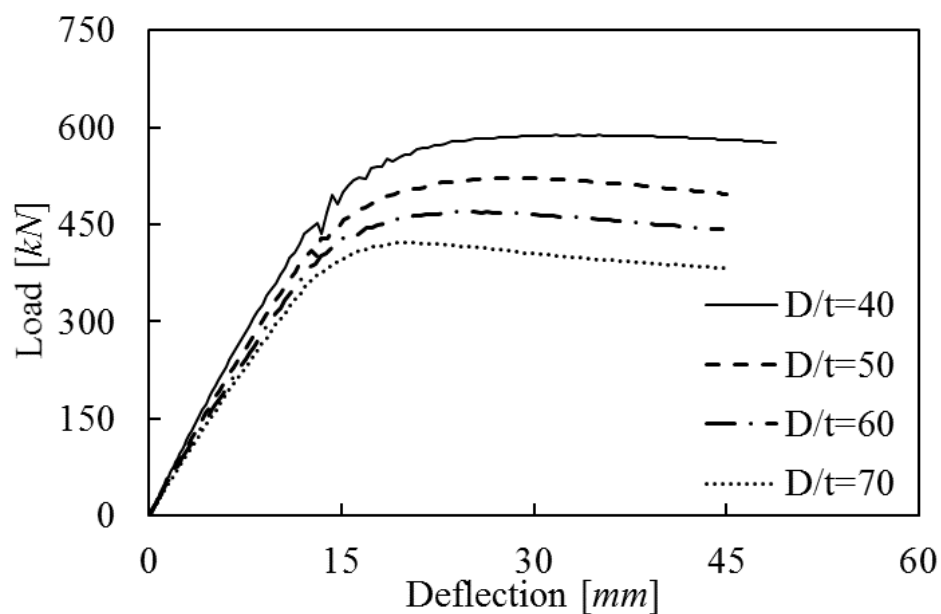


Figure 6.14: Effect of pile  $D/t$  to the overall response

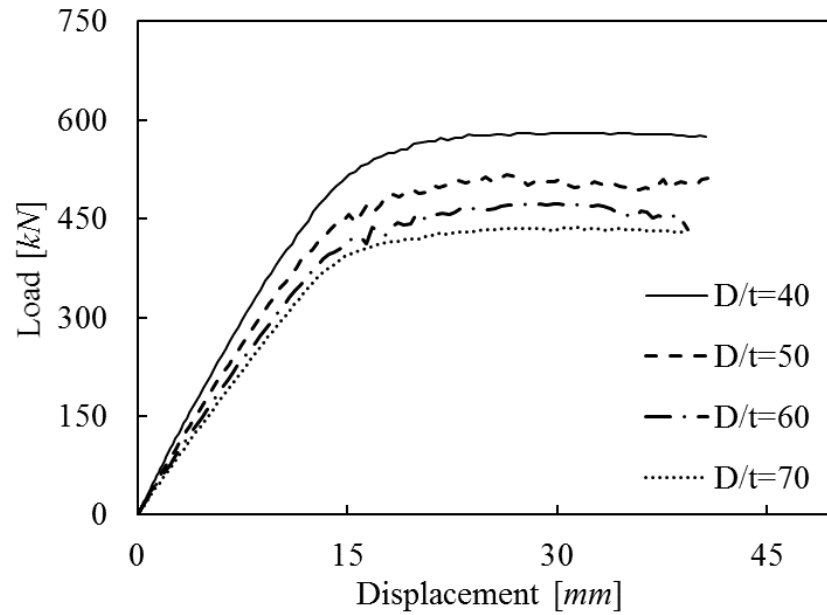


Figure 6.15: Effect of sleeve  $D/t$  to the overall response

The ultimate capacity was enhanced significantly for both configurations once the ratio increases. For example,  $F_{0.15n4s60Dt_s70}$  sustained approximately 400 kN when compared to the  $F_{0.15n4s60Dt_s40}$  which failed at a load of 589 kN denoting an increase of about 50%. This variation was anticipated due to the increasing thickness which results in stockier cross-sections. The effect of steel ratios ( $D/t$ ) is summarised for each group of simulations in Figure 6.16 and Figure 6.17. The normalised  $F_u$  over the average experimental  $F_u$  is plotted against the slenderness ratio (RS) of each GC which is defined as follows:

$$\mathbf{RS} = \frac{(D/t)_s}{(D/t)_p} \quad 6.1$$

Similar linear trends were found for both pile and sleeve confirming the expected enhanced performance with lower ratios.

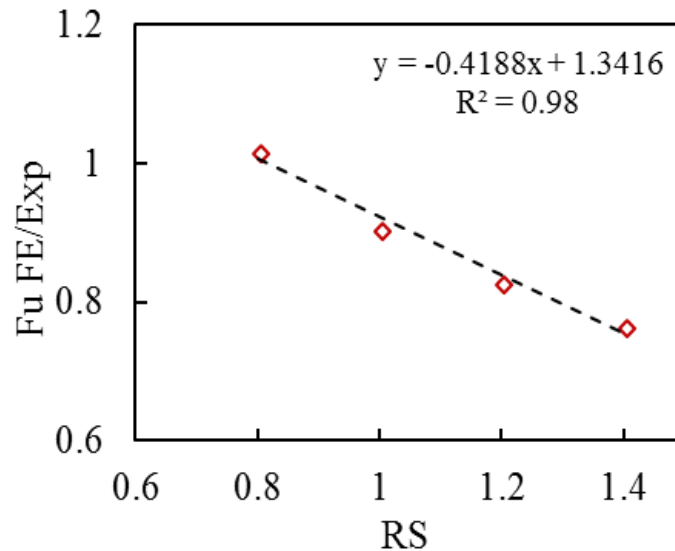


Figure 6.16: Sleeve contribution to ultimate load

The cross-sectional parameters on GCs is commonly linked with the radial stiffness  $k$  as calculated by equation 2.5. Radial stiffness is limited to a value of 0.02 in the DNV ST-0126 (2016) guidelines. Considering the gain in ultimate bending capacity for only slightly higher values up to 0.022 it is suggested that ratios larger than 0.02 can be employed. Such findings are in agreement with a recent experimental study by Bechtel (2017) where GCs with  $k$  up to 0.03 were tested.

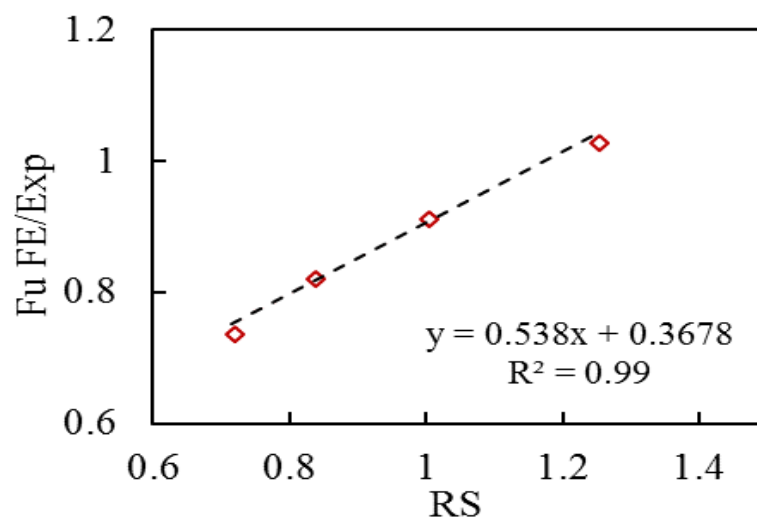


Figure 6.17: Pile contribution to ultimate load

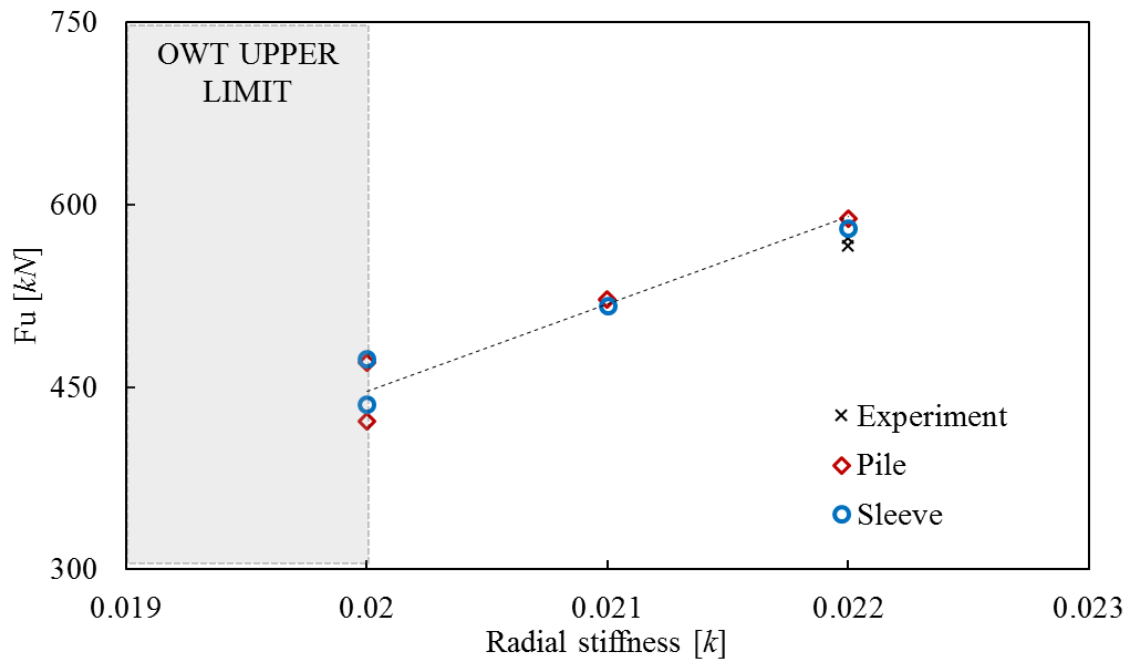


Figure 6.18: Influence of radial stiffness

Table 6.2: FE parametric models for  $D/t$  effect

Name	$F_o$	$n$	Dimensions [mm]				
			$L_{p,s}$	$t_{s,p}$	$t_g$	$D_g$	$L_g$
$F_{o15n4s60Dt_s40}$	1.5	4	2555	11.86/8	22.4	406	610
$F_{o15n4s60Dt_s50}$	1.5	4	2555	9.39/8	22.4	406	610
$F_{o15n4s60Dt_s60}$	1.5	4	2555	7.77/8	22.4	406	610
$F_{o15n4s60Dt_s70}$	1.5	4	2555	6.62/8	22.4	406	610
$F_{o15n4s60Dt_p40}$	1.5	4	2555	11.1/10.15	22.4	406	610
$F_{o15n4s60Dt_p50}$	1.5	4	2555	11.1/8.12	22.4	406	610
$F_{o15n4s60Dt_p60}$	1.5	4	2555	11.1/6.76	22.4	406	610
$F_{o15n4s60Dt_p70}$	1.5	4	2555	11.1/5.8	22.4	406	610

---

$F_{o15n4s60Dt_{gs}15}$	1.5	4	2555	9.75/8.12	31.21	468.42	610
$F_{o15n4s60Dt_{gs}20}$	1.5	4	2555	9.39/8.12	22.4	450.8	610
$F_{o15n4s60Dt_{gs}25}$	1.5	4	2555	9.06/8.12	14.5	435	610
$F_{o15n4s60Dt_{gs}30}$	1.5	4	2555	9.19/8.12	17.65	441.3	610
$F_{o15n4s60Dt_{gp}15}$	1.5	4	2555	11.1/8	30.05	450.8	610
$F_{o15n4s60Dt_{gp}20}$	1.5	4	2555	11.1/8	22.4	450.8	610
$F_{o15n4s60Dt_{gp}25}$	1.5	4	2555	11.1/8	18.02	450.8	610
$F_{o15n4s60Dt_{gp}30}$	1.5	4	2555	11.1/8	15.02	450.8	610

---

## 6.7 Influence of grout thickness

The objective of the analysis of the following FE models is to examine the effect of the grout thickness on downscaled GCs. For this purpose, four grout cores with varying thickness were examined, leading to  $D/t$  ratios equal to 15, 20, 25, 30. The selected ratios are within standard code guidelines (Norsok N-004, 2013). Although GCs with such geometries are within monopile range, in real structures such ratios are more commonly found on GCs employed by jacket substructures and represent the lower limit for monopile substructures.

The thickness of the annuli is directly linked to the cross-sectional properties of the sleeve and pile forming the GC. To investigate the effect of grout thickness independently and to isolate the influence from pile and sleeve eight models were developed. Initially, the first group comprised of four FE models where the grout thickness was altered along with the pile maintaining a constant sleeve cross section. In a similar manner the remaining models formed the second

group, where the grout core was adjusted based on a constant pile cross-section. This distinction allowed for direct evaluation of the grout core. Additionally, the notion that thicker grout cores lead to more pronounced cracking was also examined. The global response of the models is shown in Figure 6.19 and Figure 6.20 in the form of load-displacement curves.

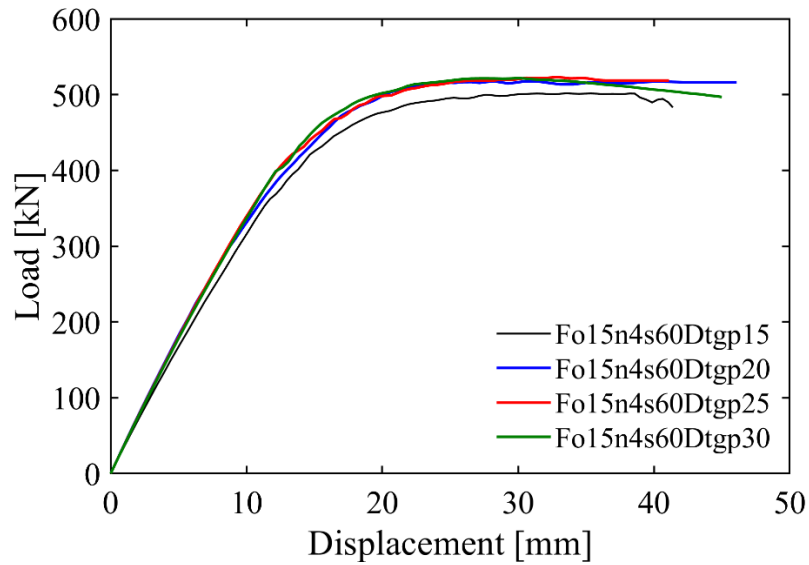


Figure 6.19: Load-displacement curves for varying grout cores (effect of pile - constant sleeve)

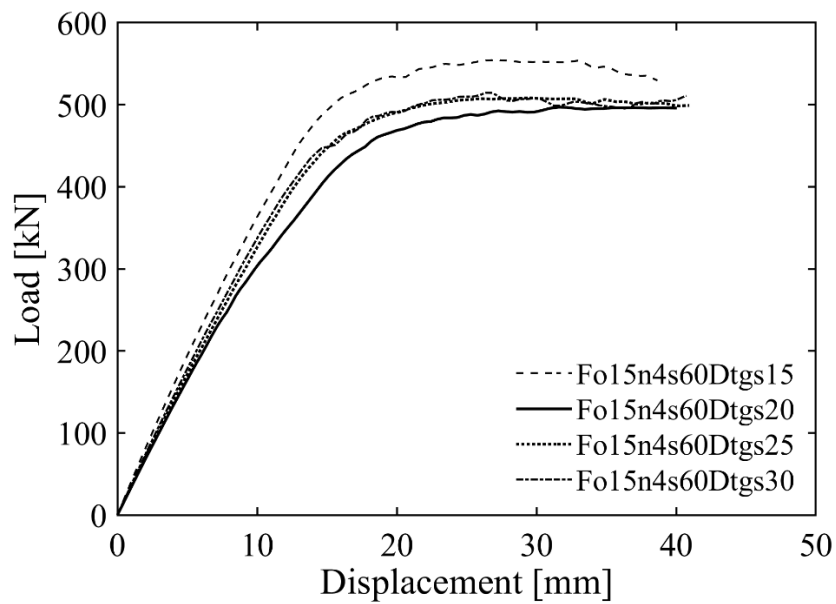


Figure 6.20: Load-displacement curves for varying grout cores (constant pile)

## 6.8 Installation tolerances

During the installation phase of an OWT substructure, three types of tolerances can occur on the GC. In DNV ST-0126 (2016) those are categorised in horizontal, vertical and inclined tolerances leading to an uneven thickness on the connection, shear key location misalignment and inclinations. The horizontal and vertical tolerances are illustrated in Figure 6.21 and are discussed in the subsequent sections.

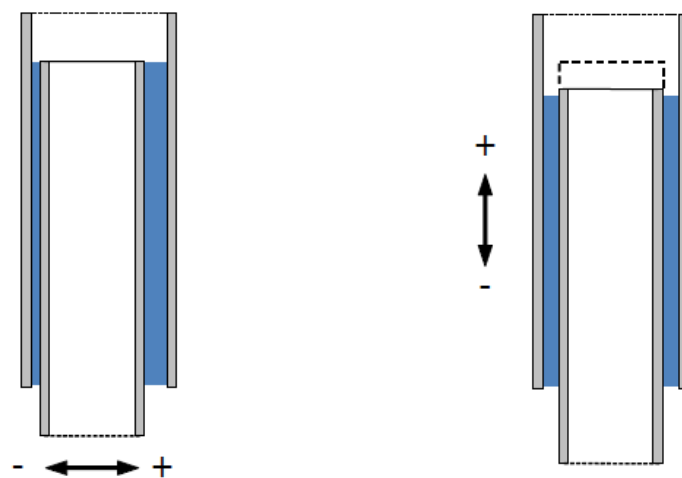


Figure 6.21: Horizontal and vertical tolerances during GC installation (DNV ST-0126, 2016)

### 6.8.1 Influence of horizontal tolerance

GCs on monopiles offer higher accuracy if it comes to concentric installation when compared to driven piles on jacket structures (DNV ST-0126, 2016). However, such installation issues resulting to grout thickness variations can occur offshore and are examined herein. Three dedicated FE models were developed with eccentric sleeve in relation to the pile resulting in uneven annular grout. For this purpose, the ratio of smallest to largest thickness in the annuli is denoted as horizontal tolerance. Considering Figure 6.22 it was found that there is no significance influence on the ultimate load each GC can withstand. A similar

conclusion was made by Lamport (1988) following some experimental tests on O&G connections. However, such an argument is ought to be further examined for thicker connections on larger scale models or tests where further damage is expected within the core.

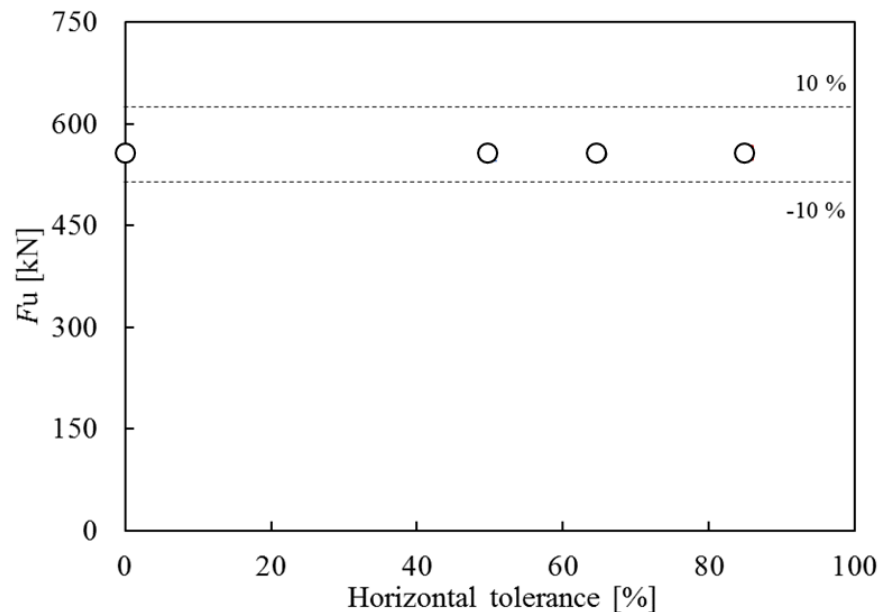


Figure 6.22: Influence of uneven thickness on ultimate load

## 6.8.2 Influence of vertical tolerance

The outcome from mis-positioning the TP is unintended locations for pile and sleeve shear keys. Due to shear keys being installed and aimed as pairs, such misalignments can lead to different inclinations of the struts or even keys being inactive during the load-transfer mechanism. For this purpose, a model with sleeve and pile shear keys at the exact same locations was simulated. Despite the fact that there was difference on the ultimate strength compared to the model with no misalignments, it was found that struts do not develop diagonally. In Figure 6.23 cracks on the tensile region of the connection are shown in the form of iso-surfaces. The cracks initiate from the sleeve shear keys forming failure surfaces until reaching the opposing shear key of the pile. As a result, the first

shear key is shown to be inactive which is crucial for OWT GCs due to significant costs involved with welding.

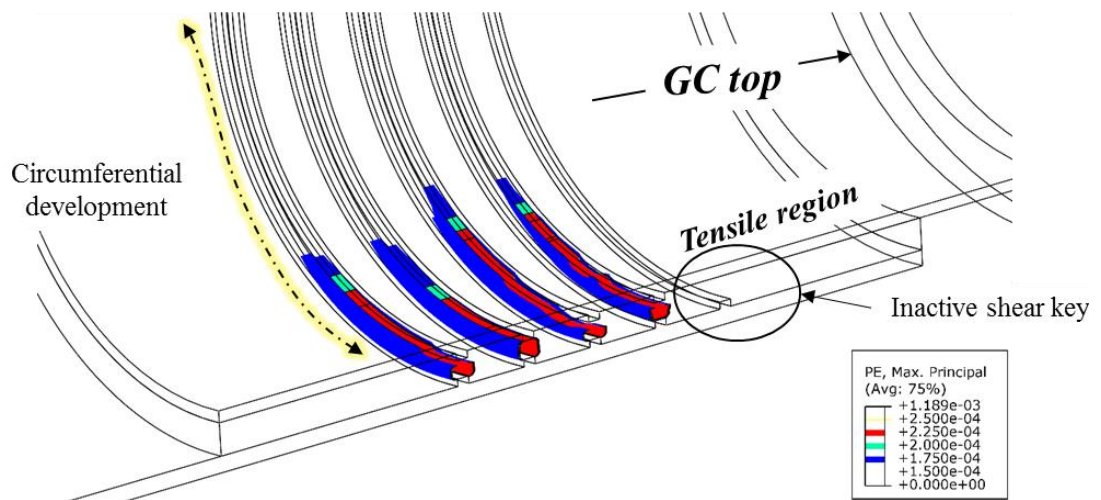


Figure 6.23: Iso-surface plot on GC model with misaligned pile and sleeve shear keys

## 6.9 Summary

Shear key parameters such as spacing and height, installation tolerances, geometrical parameters of the steel sections and finally grout thickness were investigated and discussed through the extensive parametric study that was presented within this chapter. It was found that stockier pile and sleeve result in favourable bending strength for even higher values of radial stiffness than the ones allowed for in standard guidelines. It is suggested that the limit of radial stiffness is conservative however, it is proposed to be further examined by FE models and experimental tests.

# 7 CONCLUSIONS AND RECOMMENDATIONS

## 7.1 Overview

Within this final chapter a short summary is initially given in section 7.2. Principal findings and conclusions of this study are discussed in section 7.3. The discussion also highlights the novel contributions and scientific gaps. In section 7.4 the potential impact of this work to the industry is discussed and finally, considering the experience gathered, recommendations for future research are provided in section 7.5.

## 7.2 Summary

The presented research study was set out to investigate the performance of steel-grout-steel composite connections, commonly referred to as GCs, on OWTs by means of experimental and numerical methods. The motivation for this research work were the inspections that took place on several monopiles at the onset of the current decade. Findings reported that the performance of GCs is different

than the intended leading to unexpected failures of different nature, putting the integrity of the substructure and subsequently the monopile in doubt. Typical failures were in the form of TP settlements, cracking of the grout core, water pooling at the top visible side of the GC and gaps at the interfaces. After thorough and careful consideration and review of the global literature, the main aim was set towards enhancing and improving our existing knowledge entailing the design and monitoring of GCs in OWTs. Hence, a detailed experimental campaign was designed to enable the realisation of this research and subsequent objectives that were put forward.

### 7.3 Conclusions

The key findings of this work are presented thereafter and categorised based on the field of application. Hence, this section is subdivided to cover the three main pillars of this project: experimental testing, numerical modelling and acoustic monitoring.

#### **Experimental testing**

For substructures used on monopile OWTs bending loads are of critical importance and recently this is also becoming relevant to modern jackets. However, to date the effect of bending on the connection is not fully understood owing to the majority of the tests being carried out under axial loads and employing small scale specimens. More specifically, the monopiles are subjected to harsh environmental conditions in the offshore regime which are best described as fully-reversed (tension-compression cycles). Taking that into consideration, a test campaign to investigate the residual bending capacity of a GC under fully-reversed bending loads was designed. The tests also enhance the global data pool of experiments, while it is worth mentioning that square shear keys were employed instead of semi-circular beads. Square shear keys were

avoided in previous experimental campaigns due to concerns that sharp edges can provoke cracking. However, this was not found to be the case for the presented tests, due to the welds around the square shear key resulting in a smoother profile. This would apply to laboratory tests where shear key heights are particularly small due to down scaling.

The ultimate bending capacity of the GC was not influenced by the preceding cyclic loads. Although the specimen was subjected to fully reversed loads there was no obvious deterioration of the grout condition or the global stiffness of the GC. There was no indication for irreversible gaps occurring at the interface for the applied load level during the cycles and the specimen survived the cycles it was subjected. It is suggested that the selected low  $D/t$  ratio and the scaling might have resulted in an overly stiff connection which did not lead to steel ovalisation or debonding. Nevertheless, as scaling of GCs is not fully comprehended to date, further tests on varying scales are recommended later on to bridge this gap.

Aiming to investigate the static and fatigue performance of GCs with high shear key ratios, identical specimens with  $h/s \sim 0.083$  were designed. The static tests revealed the majority of the loads are transferred between the steel piles and through the grout. This mechanism takes place within the shear key region of the GC. Hence, it was confirmed that the shear keys contribute immensely to the load transfer. Considering the analysed data and visual inspections, the complex failure modes of the GCs during the strength tests, were identified. The progressive failure of the compressive struts, which resulted in failure surfaces of cylindrical shape within two successive shear keys, along with crushed grout at the shear key tip, initiated the interface gaps at the pile and sleeve interfaces with the grout. The particularly high ratio of shear key connectors that was selected in combination with the square profile, which are the largest welded beads reported in the literature, was not found to reduce the ultimate capacity.

Additionally, there was no alteration to the inclination of the struts between two successive shear keys and as inspections of the grout revealed those developed within the expected inclination limits. Therefore, the author suggests the differentiation of the height and spacing parameters as their combined effect is not replicated when those are studied individually.

### **Numerical modelling**

The design of GCs by means of FEA is often based on assumptions with a tendency towards simplified material and contact models that result in reduced computational cost. Such approaches have been favoured due to modelling uncertainties and limited experimental data sets as highlighted in Chapter 2 and 5. Nevertheless, the significant role of the connections in future OW development along with the total cost of experimental campaigns necessitate the development and utilisation of additional methods towards reliable and efficient design guidance.

In the presented models, material non-linearity, improved contact formulations and full-solid elements were employed to achieve high accuracy of the computations as discussed in Chapter 5. The presented computational scheme overcame aspects that increase the cost of computations without compromising accuracy which can result in a design process of improved efficiency. To that end a detailed framework for the development of comprehensive three-dimensional numerical models was presented. An explicit method with semi-automatic mass scaling was adopted resulting in a quasi-static solution. The suggested numerical scheme accomplished results of excellent accuracy and the robustness of the FE models was assessed against a range of experimental data with varying geometrical features.

A high level of refinement of the meshed parts is highly recommended for shear

keys and the corresponding grout region in order to capture the local stresses occurring in this vicinity. The notion that the grout can accommodate the load-transfer process on the connection even after cracking was also confirmed, however cracking initiation occurred at low load levels when the connection is subjected to bending. This was also confirmed by AE data analysis presented in Chapter 4.

An approach to improve modelling of the bond-slip behaviour of GCs was suggested. For the examined tests and models, it was concluded that the confinement of the grout is better described by a cohesive-based behaviour of the interfaces in conjunction with an unconfined material model for the grout. The approach was tested against stockier cross-sections and replicated the tests conducted by the author more accurately. A linear load-slip behaviour was found suitable for the examined configuration. The CDP material model allowed for the nonlinear behaviour UHPG material and modelled accurately the cracking of the grout core under bending and axial loads. A key material parameter which was found to affect the global response of GCs is the dilation angle, which in lack of dedicated material tests is recommended to be assessed using a sensitivity analysis.

The parametric FE study was carried out to assess the influence of geometrical factors on the global and local behaviour of the models. Cross-sectional properties ( $D/t$ ), overlap lengths ( $F_o$ ) and shear key parameters were studied on GCs subjected to bending. Plain GCs exhibited reduced bending capacity when compared to shear keys resulting in pronounced de-bonding of the pile-grout interface. On the other hand, the mechanical interlock provided by the shear keys led to reduced contact stresses at the opposing ends of the connection.

Local cracking of the grout core occurred for all the parametric models in the region between shear keys. Primary diagonal cracking within neighbouring

shear keys was the failure mode of FE models with  $h/s=0.05$  and  $0.06$ . The change in failure modes was very well predicted for models with reduced and increased spacing between shear keys. Cylindrical failure surfaces were captured for GCs with increased spacing between shear keys. Interface opening was also found to be limited when increasing the number of shear keys. The ability of the numerical model to predict all failure modes corresponding to different geometrical features will serve as a solid foundation for future design efforts based on FEA.

Contrary to the impact of increasing shear key numbers, the higher shear key ratio did not yield superior performance owing to the change of grout failure. The relative displacement between the pile and sleeve calculated in all the numerical models revealed that shear key regions on the steel tubes occupied by shear keys is of equal importance to the height and spacing. Finally, based on the presented FE models, overlap lengths equal to unity should be avoided as the stress intensities are increased. It was also shown that the grouted length of the connection is of significant importance to the performance of the connection.

### **AE monitoring**

Monitoring of GCs is a necessity nowadays and could be of great benefit for the current and future substructures. It can provide information on the integrity of the connections throughout their lifetime and as a result, enhance their reliability. Consequently, reliable GCs can also benefit the design process in the offshore sector.

Within this context and during the destructive bending tests on GCs a SHM method – AE, was applied using acoustic sensors to monitor the condition of the joint until failure. Owing to the scale of the tests, structure composition and that to the author's knowledge no similar experiments are reported in the literature, the primary aim was to investigate the applicability of AE for damage detection,

initiation and development and assessment. Within this context the results are presented in the form of a pilot study and the approach is benchmarked for laboratory-scaled GCs. It was demonstrated that AE has excellent potential for operating OWTs and can be a useful tool when it comes to inspection tasks. Monitoring tools employing AE can be developed assisting towards preventive maintenance. Additionally, there is potential which still remains unexplored for AE data to be used for the determination of the remaining useful life of the substructure.

It was shown that the employed post-processing techniques allow the identification of different damage patterns. More specifically, damage detection and development in the form of cracks was traced with high accuracy during the tests. To do so a parametric analysis of the AE signal features was performed, showing promising results while reducing the post-processing computations. It was confirmed that increasing damage is proportional to AE activity. Therefore, several AE parameters were individually examined to single out those that are more sensitive to failure and could be employed for damage assessment. As a result, a series of KPIs (e.g., RMS, RA, duration, CSS) were identified and isolated so as to examine their correlation with damage taking place within the GC. Moreover, the total event number and the duration of signals during the tests proved useful for identification of damage evolution.

Changes in RMS value were particularly pronounced with increasing damage and is one of the KPIs that can be implemented in monitoring tools to act as a prognosis tool for hindering failures mainly associated with the integrity of the grout. RMS values revealed stable magnitude levels while the GC remained in the elastic stage whereas increased values were recorded during the tests once 60 to 70% of the capacity was reached. RMS cross plots revealed similar trends for both GCs increasing the confidence in this KPI. When it comes to RA ratios along

it was shown that in conjunction with other indicators, they were effectively used to isolate cracking events. CSS rate was one of the parameters that were used in conjunction and thus both were classified as KPIs.

The peak amplitudes of the AE waveforms were examined by means of  $b$ -value and  $Ib$ -value analysis. The analytical approach was examined as a tool for assessment of the GC condition. It was also used in parallel with KPIs to correlate cracking events within the specimens. It was found that cracking events with high energy release were satisfactorily captured and associated with drops in both  $b$  and  $Ib$ -value. The frequency distribution of the AE signal amplitudes can reveal information on imminent critical events that could potentially be critical for the integrity of the GC. Correlation of steep drops with failure modes of the specimen was possible when compared with CSS, RA and visual inspections. The hypothesis that both  $b$  and  $Ib$ -value drop closer to events of significance, such as cracking is valid and verified by the presented analysis.

Although the presented pilot study was verified for a limited number of specimens it is believed that the examined KPIs are excellent indicators for monitoring purposes. Nevertheless, further tests are needed employing materials of different strengths and load configurations to enhance the applicability of AE for SHM of substructures.

One of the challenges of the presented approach was the acquisition settings and the corresponding calibration study. This is due to the size of the specimens which could potentially lead to increased scattering of AE waves. The internal structure of the grout was also of significance to the interpretation of results. It is believed that the presence of micro-voids and aggregates of varying diameters within the material led to a large number of AE which subsequently caused a higher scattering of waves.

## 7.4 Research Impact

This section summarises the potential impact and benefits from this research work to the industry and the OW sector:

- The experimental test results added to the limited existing pool of bending tests, which are of significance for the design of future monopile and jacket substructures. This is due to more vertical piles being employed even for jackets, which are prone to bending loads. Enhancing the experimental data allows for reconsiderations in the design practice of GCs.
- In addition, within the test campaign the behaviour of GCs with square shear keys with large  $h/s$  ratios on stockier pile and sleeve cross-sections was examined. The abovementioned parameters have not been previously tested, however they become more relevant considering future substructures in greater depths.
- It was shown that the design of GCs can be significantly enhanced by FE models, without compromising accuracy and time. In fact, the numerical modelling approach that was introduced produced results in very good agreement with several tests, allowing for local stress determination within the grout and shear key vicinity. It subsequently allowed for detailed parametric models.
- An alternative method for modelling the grout confinement and grout steel interaction with a cohesive-based behaviour was also examined showing promising results on the cross-sections that was evaluated.
- Finally, the monitoring framework that was presented in Chapter 4, revealed that there is significant unexplored potential for monitoring substructures with AE sensors. More specifically it was shown that KPIs such as RMS can be used as reliable metrics for evaluating the grout integrity over time in monitoring tools.

## 7.5 Recommendations for future work

Important aspects related with design and inspection or monitoring processes tasks of GCs for OWTs have been extensively covered by means of physical and numerical modelling. Experimental tests on GCs in bending along with a monitoring approach have been successfully conducted. Additionally, comprehensive and validated models were developed to perform a parametric analysis on the effect of geometrical parameters. Nevertheless, it is the author's opinion that GCs on offshore environments are an emerging and challenging field which requires further attention and interdisciplinary approaches need to be employed in order to gain further knowledge. Several aspects involved with their performance ought to be further investigated. Thus, recommendations for future research activities will be presented.

### **Experimental testing**

One of the most critical aspects in laboratory testing is the loading configuration of the test set-up. It will be of benefit to utilise test frames that can accommodate combined axial and bending loads rather than isolating their effect. To that extent the limiting experimental data pool ought to be enriched with further fatigue tests to enhance the existing knowledge and provide reliable guidelines on the design of GCs.

GCs are subject to environmental loads since their installation, which in combination with the low strength of the UHPG at early stages result in unknown performance. Thus, assessing the early age performance of plain pipe or GCs with shear keys under cyclic loads is of further interest.

Scale effects have been a matter of discussion for GCs. Thus, testing of identical specimens at different scales would provide a better understanding on the performance of large diameter GCs and quantify the effect of laboratory-based

campaigns. Finally, when it comes to UHPGs there is a lack of triaxial data from grout samples which can provide a further insight on the behaviour of the material.

### **Numerical modelling**

To date, modelling of UHPGs is performed using elastic material properties or concrete-based material models. The implementation of a grout-dedicated material model in commercial FE software could be beneficial for the design of GCs by means of FE models. As the majority of the analyses using FE models accommodates ULS design of GCs, it would be useful to accommodate a fatigue modelling approach.

Preliminary models presented in this thesis revealed that pile inclinations do not have any detrimental effect on the ultimate load sustained by the GC. However, further investigations are needed to quantify the effect of pile inclination on the results.

### **AE monitoring**

The presented analysis was based on monotonic and fatigue loads. When it comes to benchmarking the approach, this was achieved during static and fatigue tests. However, AE signals should be further investigated during fatigue tests of varying frequency. Considering the existing literature, there has been very limited research work on the effect of load frequency on AE signals.

Future studies could potentially investigate the development of automated or semi-automated tools for the exploitation of KPIs for damage assessment and monitoring of the integrity of GCs. Integrating of automatic post-processing tools could potentially reduce maintenance cost significantly.

To that extent pattern recognition algorithms could prove to be very useful in the

identification of failure modes within a connection. Such algorithms are often distinguished as supervised or unsupervised methods and can be used for fast post-processing of the AE signals. This could be particularly useful for large data sets and enable quick and reliable inspections on OWTs without requiring complete shutdown of the generators for a significant amount of time.

AE monitoring of brittle material can be used to provide a virtual map of cracks occurring with the cementitious medium. To do so in circular geometries a larger number of piezoelectric sensors is required. It is thus recommended to use more sensors on a GCs so as to optimise the selected locations.

Finally, there is room for research on the effect of alternative cementitious media on AE signals. For example, the presented tests and analysis were performed on GCs with an aggregate-based UHPG. On OWTs a variety of material can be employed with different compositions which, as revealed by the presented analysis, can have an influence on the results.

---

# REFERENCES

4Coffshore (2018). Utgrunden I wind farm. Available at:  
<https://www.4coffshore.com/windfarms/utgrunden-i-sweden-se03.html>

[Accessed at: 7 April 2016]

Abaqus (2013). ABAQUS 6.13 Documentation Collection, Dassault Systemes Simulia Corp., Providence, RI, USA.

Abdelatif, A.O., Owen, J.S. and Hussein, M.F. (2015). Modelling the prestress transfer in pre-tensioned concrete elements. *Finite Elements in Analysis and Design*, 94, pp. 47-63. <https://doi.org/10.1016/j.finel.2014.09.007>

Abdelrahman, M., ElBatanouny, M.K. and Ziehl, P.H. (2014). Acoustic emission-based damage assessment method for prestressed concrete structures: Modified index of damage. *Engineering Structures*, 60, pp. 258-264.

Aggelis, D.G. (2011). Classification of cracking mode in concrete by acoustic emission parameters. *Mechanics Research Communications*, 38(3), pp. 153-157.

Aggelis, D.G., Mpalaskas, A.C. and Matikas, T.E. (2015). Acoustic monitoring for the evaluation of concrete structures and materials. In: *Acoustic Emission and Related Non-Destructive Evaluation Techniques in the Fracture Mechanics of Concrete*, Ohtsu, M., Woodhead Publishing, pp. 269-286.

---

Aggelis, D.G., Mpalaskas, A.C., Ntalakas, D. and Matikas, T.E. (2012). Effect of wave distortion on acoustic emission characterization of cementitious materials. *Construction and Building Materials*, 35, pp. 183-190.

Anders (2008). Bearing behaviour of grouted joints. Doctoral Dissertation, Institute for Steel Construction, Leibniz Universität Hannover, Hannover, Germany.

Anders, S. and Lohaus, L. (2008). Optimized high-performance concrete in grouted connections. Tailor Made Concrete Structures-Walraven & Stoelhorst.

Andersen, A.M. (2002). Efficient connection between offshore foundation and wind turbine towers. [online] Densit a/s. Available at: <http://www.technology.stfc.ac.uk/OWEN/documents/BWEA24/Nielsen31.pdf> [Accessed at: 3 October 2016].

Andersen, M.S. and Petersen, P. (2004). Structural design of grouted connection in offshore steel monopile foundations. In Proceedings of Global Windpower Conference, Chicago, USA.

ANSYS (2013), Mechanical APDL Material Reference, "User Manual", Canonsburg, PA, USA.

API RP2A-WSD (2000). Recommended Practice for Planning, Designing and Constructing Fixed Offshore Platforms—Working Stress Design (21st edition). American Petroleum Institute, Washington, USA.

API RP2A (1977). Recommended practice for planning, designing and constructing fixed offshore platforms (9th Edition). American Petroleum Institute, Texas, USA.

API RP2A (1984). Recommended practice for planning, designing and

---

constructing fixed offshore platforms (15th Edition). American Petroleum Institute, Texas, USA.

Arany, L., Bhattacharya, S., Macdonald, J. and Hogan, S.J. (2017). Design of monopiles for offshore wind turbines in 10 steps. *Soil Dynamics and Earthquake Engineering*, 92, pp.126-152.

Aritenang, W., Elnashai, A. S. and Dowling, P.J. (1992). Analysis-based design equations for composite tubular connections. *Engineering Structures* 14(3): 195-204.

Assimakopoulou, T.T. and Philippidis, T.P. (2010). Health monitoring of composite structures based on acoustic emission measurements. In: *Fatigue Life Prediction of Composites and Composite Structures*, Vassilopoulos, A., Elsevier, pp. 466-504.

Bache, H.H. (1992). *Ny Beton - Ny Teknologi*. Aalborg Portland.

Bagherifaez, M., Behnia, A., Majeed, A.A. and Hwa Kian, C. (2014). Acoustic emission monitoring of multicell reinforced concrete box girders subjected to torsion. *The Scientific World Journal*, 2014.

Bechtel, A. (2017). *Fatigue Behaviour of Axially Loaded Grouted Connections in Jacket Structures*. Doctoral Dissertation, Institute for Steel Construction, Leibniz Universität Hannover, Hannover, Germany.

Behnia, A., Chai, H.K. and Shiotani T. (2014). Advanced structural health monitoring of concrete structures with the aid of acoustic emission. *Construction and Building Materials*, 65, pp. 282-302.

Billington, C.J. (1980). Research into composite Tubular Construction for Offshore Jacket Structures. *Journal of Constructional Steel Research*, 1(1), pp. 18-

26.

Billington, C.J. and Lewis, G.H. (1978). The strength of large diameter grouted connections. In *Offshore Technology Conference*, Houston, Texas, <http://doi:10.4043/3083-MS>

Billington, C.J. and Tebbett I (1982). Fatigue strength of grouted tubular steel connections for offshore structures. *International Association for Bridge and Structural Engineering*, pp. 625-632.

Bocher, M., Mehmanparast, A., Braithwaite, J. and Shafiee, M. (2018). New shape function solutions for fracture mechanics analysis of offshore wind turbine monopile foundations. *Ocean Engineering*, 160, pp. 264-275.

Brett, C.R., Gunn, D.A., Dashwo, B.A.J., Holyoake, S.J. and Wilkinson, P.B. (2018). Development of a technique for inspecting the foundations of offshore wind turbines. *Insight - Non-Destructive Testing and Condition Monitoring*. 60(9), pp. 19-27.

BSI 12390-2 (2009). BS EN 12390-2:2009: Making and Curing Specimens for Strength Test.

BSI 12390-3 (2009). BS EN 12390-3:2009: Testing hardened concrete. Compressive strength of test specimens.

BSI 12390-5 (2009). BS EN 12390-5:2009: Testing hardened concrete–flexural strength of test specimens.

BSI 12390-6 (2009). BS EN 12390-6:2009: Testing hardened concrete–tensile splitting strength of test specimens.

BSI 12390-7 (2009). BS EN 12390-7:2009 Testing hardened concrete–Density of hardened concrete.

BSI 19902 (2007). Petroleum and natural gas industries – Fixed steel offshore structures +A1:2013. British Standards Institution-BSI and CEN European Committee for Standardization.

BSI 6892-1 (2009). BSI 6892-1:2009: Metallic Materials-Tensile testing.

Carpinteri, A., Lacidogna, G. and Niccolini, G. (2006). Critical behaviour in concrete structures and damage localization by acoustic emission. In: *Key Engineering Materials*, Trans Tech Publications, Vol. 312, pp. 305-310.

Carpinteri, A., Lacidogna, G., Niccolini, G. and Puzzi, S. (2008). Critical defect size distributions in concrete structures detected by the acoustic emission technique. *Meccanica*, 43(3), p.349.

CEB-FIP (1990). Model code for concrete structures. Bulletin D' Information.

Chen, T., Wang, X., Yuan, G. and Liu, J. (2018). Fatigue bending test on grouted connections for monopile offshore wind turbines. *Marine Structures*, 60, pp.52-71.

Chilvers, C.A. (1984). Analysis of the structural behaviour of grouted pile/sleeve connections for offshore structures. Doctoral Dissertation, City University London, London, United Kingdom.

Colombo, I. S., Main, I. G. and Forde, M. C. (2003). Assessing damage of reinforced concrete beam using "b-value" analysis of acoustic emission signals. *Journal of materials in civil engineering*, 15(3), pp. 280-286.

Cornelissen, H., Hordijk, D. and Reinhardt, H. (1986). Experimental determination of crack softening characteristics of normal weight and lightweight concrete, *Heron*, 31(2), pp. 45–56.

Dallyn, P. (2017). Advances in foundation design and assessment for strategic

---

renewable energy. Doctoral Dissertation, Loughborough University, Loughborough, UK.

Dallyn, P., El-Hamalawi, A., Palmeri, A. and Knight, R. (2015). Experimental testing of grouted connections for offshore substructures: a critical review. *Structures*, 3: pp. 90–108. <https://doi.org/10.1016/j.istruc.2015.03.005>

Dallyn, P., El-Hamalawi, A., Palmeri, A. and Knight, R. (2017). Prediction of Wear in Grouted Connections for Offshore Wind Turbine Generators Structures, 10, pp. 117-129.

DEN (1980). Report No.ST41/80C. Report of the working party on the strength of grouted pile sleeve connections for offshore structures, Department of Energy, Wimpey Laboratories, Ltd, UK.

DEN (1984) Guidance on the design and construction of offshore installation (3rd edition), Department of Energy, UK.

Densit (2002). Foundation of Horns Rev Wind Farm – Ducorit® D4.

Densit (2018). Technical data sheet - Ducorit®. Ultra High Performance Grout. Aalborg, Denmark. Available at: <http://densit.com/media/27259/pro-ducorit-uk.pdf> [Accessed at: 05 July 2018]

DNV 0371 (2012). Capacity of cylindrical shaped grouted connections with shear keys. Summary Report No. 2012-0371, revision 4.

DNV 1053 (2010). Summary report from the JIP on the capacity of grouted connections in offshore wind turbine structures. Report No. 2010-1053, revision 5.

DNV C101-1989 (1989). Rules for classification of fixed offshore installation. Oslo. Det Norske Veritas AS.

---

DNV OC-C502 (2012). Offshore Concrete Structures. Norway. Det Norske Veritas AS.

DNV OS-J101 (2014). Design of offshore wind turbine structures – Rules and standards.

DNV ST-0126 (2016). Support structures for wind turbines, Edition April 2016. Available at: <http://rules.dnvgl.com/docs/pdf/dnvgl/ST/2016-04/DNVGL-ST-0126.pdf> [Accessed at: 22 May 2016].

Dorph, M. and Sipavicious, A. (2010). Finite Element Analysis of Compact Reinforced Composite substructure to a bucket foundation and offshore wind turbine. Master Thesis, School of Engineering, Aalborg University, Aalborg, Denmark.

ElBatanouny, M. K., Larosche, A., Mazzoleni, P., Ziehl, P. H., Matta, F. and Zappa, E. (2014). Identification of Cracking Mechanisms in Scaled FRP Reinforced Concrete Beams using Acoustic Emission. *Experimental Mechanics*, 54, pp. 69-82.

Elnashai, A.S. and Aritenang, W. (1991). Nonlinear modelling of weld-beaded composite tubular connections. *Engineering Structures*, 13(1), pp.34-42.

Elnashai, A.S. and Dowling, P.J. (1991). Strength of composite tubular connections. *Proceedings of the Institution of Civil Engineers. Part 2: Research & Theory*, 91, pp.377-398.

Farhidzadeh, A., Dehghan-Niri, E., Salamone, S., Luna, B. and Whittaker, A. (2013). Monitoring crack propagation in reinforced concrete shear walls by acoustic emission. *Journal of Structural Engineering*, 139(12), p. 04013010.

Fehling, E. Schmidt, M., Teichmann, T., Bunje, K., Bornemann, R. and

- Middendorf, B. (2005). Entwicklung, Dauerhaftigkeit und Berechnung Ultra-Hochfester Betone (UHPC). DFG research report FE 497/1-1, Structural Materials AND Engineering Series, No 1, Kassel University Press GmbH, Kassel.
- Fehling, E., Leutbecher, T., Schmidt, M. and Ismail, M. (2013). Grouted connections for offshore wind turbine structures. *Steel Construction*, 6(3), pp.216-228. <https://doi.org/10.1002/stco.201310031>
- Fehling, E., Leutbecher, T., Schmidt, M. and Ismail, M. (2013). Grouted connections for offshore wind turbine structures. *Steel Construction*, 6(3), pp.216-228. <https://doi.org/10.1002/stco.201310031>
- Fehling, E., Schmidt, M., Walraven, J., Leutbecher, T. and Fröhlich, S. (2014). Ultra-high performance concrete UHPC: Fundamentals, design, examples. First Edition Ernst & Sohn GmbH and Co. KG.
- Forsyth, P. and Tebbett, I.E., (1988). New test data on the strength of grouted connections with closely spaced weld beads. In *Offshore Technology Conference*, Houston, Texas, pp. 237-245.
- FoundOcean (2015). North Rankine platform pile grouting Available at: <https://www.offshore-technology.com/wp-content/uploads/sites/6/2017/09/pile-grouting.jpg> [Accessed at: 15 March 2016]
- Frohlich, C. and Davis, S. D. (1993). Teleseismic b values; or much ado about 1.0. *Journal of Geophysical Research: Solid Earth*, 98(B1), pp. 631-644.
- Gardner, L. and Yun, X. (2018). Description of stress-strain curves for cold-formed steels. *Construction and Building Materials*, 189, pp. 527-538.
- Gjersoe, N., Otessen Hansen, N. and Iversen, P. (2011) Long Term Behaviour of Lateral Dynamically Loaded Steel Grout Joints. In: *Proceedings of the Twenty-first*

---

*International Offshore and Polar Engineering Conference*. International Society of Offshore and Polar Engineers (ISOPE), Maui, Hawaii, USA.

Golightly, C.R. (2016). Offshore Wind Structures: Gambling with Grout – Worth The Risk? In: *EIS 4th Durability & Fatigue Advances in Wind, Wave and Tidal Energy* BAWA, Filton, UK.

Grosse, C.U. and Ohtsu, M. (2008). *Acoustic Emission Testing*. Springer Science & Business Media.

Gutenberg, B. and Richter, C. F. (1956). Earthquake magnitude, intensity, energy, and acceleration (second paper). *Bulletin of the seismological society of America*, 46(2), pp. 105-145.

Häckell, M., Friedmann, H. and Feulner, M. (2017). Detecting damage in grouted-joints of wind turbine support structures – application to a large-scale experiment. In: *11th international workshop on structural health monitoring*, Stanford, USA, 2017, pp.2467–2474. DEStech Publications, Inc.

Hahn, F., Kensche, C.W., Paynter, R.J.H., Dutton, A.G., Kildegaard, C. and Kosgaard, J. (2002). Design, fatigue test and NDE of a sectional wind turbine rotor blade. *Journal of Thermoplastic Composite Materials*, 15(3), pp.267-277.

Handelsblatt, (2016). Monopile and Jacket substructure. Available at: <https://www.handelsblatt.com/today/companies/offshore-windpower-the-monopile-monopoly/23535042.html> [Accessed at: 16 February 2017]

Harwood, R.G., Billington, C.J, Buitrago, J., Sele, A. and Sharp, J. (1996). Grouted Pile to Sleeves Connections: Design Provisions for the New ISO Standard for Offshore Structures. In: *Proceedings of the 14th international conference on offshore mechanics and arctic engineering*. OMAE, Florence, Italy, pp. 1-12.

- Higgins, P. and Foley, A. (2014). The evolution of offshore wind power in the United Kingdom. *Renewable and sustainable energy reviews*, 37, pp. 599-612.
- Hillerborg, A., Mod er, M. and Petersson, P.E. (1976). Analysis of crack formation and crack growth in concrete by means of fracture mechanics and finite elements. *Cement and concrete research*, 6(6), pp.773-781.
- Iliopoulos, A.N., Van Helerijck, D., Vlassenbroeck, J. and Aggelis, D.G. (2016). Assessment of grouted samples from monopile wind turbine foundations using combined non-destructive techniques. *Construction and Building Materials*, 122, pp. 855-862.
- Ingebritsen, T., L set,  ., Nielsen, S.G. (1990). Fatigue Design and Overall Safety of Grouted Pile Sleeve Connections. In *Offshore Technology Conference*, Houston, Texas, pp. 615-628.
- ISO 19902 (2007). Petroleum and natural gas industries – Fixed steel offshore structures (First Edition).
- ISO 19902 (2014). Petroleum and natural gas industries – Fixed steel offshore structures
- Jefferis, S.A. (2003). Grouts and grouting – Chapter 12. In Newman, J. and Choo, B.S. *Advanced concrete technology 3: processes*, Elsevier, pp. 1-47.
- Jensen, J.J., Olsen, A.S. and Mansour, A.E. (2011). Extreme wave and wind response predictions. *Ocean Engineering*, 38(17), pp. 2244-2253.
- Jiang, S.C., Wang, Z. and Zhao, X.L. (2011). Structural Performance of Prestressed Grouted Pile-to-Sleeve Connections. *Procedia Engineering*, 14, pp. 304-311. In: *Twelfth East Asia-Pacific Conference on Structural Engineering and Construction*.
- Johansen, A., Sollund, G., Lervik, A., Strande, M. and Nyb , T. (2018). Testing of

jacket pile sleeve grouted connections exposed to variable axial loads. *Marine Structures*, 58, pp.254-277.

Jonkman, J. M. and Buhl Jr, M.L. (2005). FAST user's guide. National Renewable Energy Laboratory, Golden, CO, Technical Report No. NREL/EL-500-38230.

Jungert, A. (2008). Damage Detection in wind turbine blades using two different acoustic techniques. *The NDT Database and Journal (NDT)*.

Karsan, D.I. and Krahl NW (1984). New API equation for grouted pile-to-structure connections. In *Offshore Technology Conference*, Houston, Texas, <http://dx.doi.org/10.4043/4715-MS>

Klose, M., Faber, T., Schaumann, P. and Lochte-Holtgreven, S. (2008). Grouted Connections for Offshore Wind Turbines. In: *Proceedings of the Eighteenth International Offshore and Polar Engineering Conference*, Vancouver, BC, Canada.

Klose, M., Mittelstaedt, M. and Mulve, A. (2012). Grouted Connections – Offshore Standards Driven by the Wind Industry. In: *Twenty-second International Offshore and Polar Engineering Conference*, Rhodes, Greece.

Krahl, N.W. and Karsan, D.I. (1985). Axial Strength of Grouted Pile-to-Sleeve Connections. *Journal of Structural Engineering*, 111, pp. 889-905.

Kurz, J. H., Finck, F., Grosse, C. U. and Reinhardt, H. W. (2006). Stress drop and stress redistribution in concrete quantified over time by the b-value analysis. *Structural health monitoring*, 5(1), pp. 69-81.

Lamport, W. (1988). Ultimate Strength of Grouted Pile-to-Sleeve Connections. Doctoral dissertation, The University of Texas, Austin, USA.

Lamport, W., Jirsa, J. and Yura, J. (1987). Grouted Pile-to-Sleeve Connection Tests. In: *Offshore Technology Conference*, Houston, Texas.

- Lamport, W., Jirsa, J. and Yura, J. (1991). Strength and Behavior of Grouted Pile to Sleeve Connections. *Journal of Structural Engineering*, 117(8): 2477-2498.
- Lee, J. and Fenves, G.L. (1998). Plastic-damage model for cyclic loading of concrete structures. *Journal of Engineering Mechanics*, 124(8), pp.892-900.
- Lee, J.H., Won, D.H., Jeong, Y.J., Kim, S.H. and Kang, Y.J. (2017). Interfacial shear behavior of a high-strength pile to sleeve grouted connection. *Engineering Structures*, 151, pp.704-723.
- Lee, Y-S., Choi, B-L., Lee, J.H., Kim, Y.S. and Han, S. (2014). Reliability-based design optimization of monopile transition piece for offshore wind turbine system. *Renewable Energy*. 71, pp.729-741.
- Li, D., Du, F. and Ou, J. (2017). Damage evaluation of fiber reinforced plastic-confined circular concrete-filled steel tubular columns under cyclic loading using the acoustic emission technique. *Smart Materials and Structures*, 26, pp. 1-13.
- Liu, X., Bradford, M.A., Chen, Q.J. and Ban, H. (2016). Finite element modelling of steel–concrete composite beams with high-strength friction-grip bolt shear connectors. *Finite Elements in Analysis and Design*, 108, pp.54-65. <https://doi.org/10.1016/j.finel.2015.09.004>
- Lloyd (2013). GL Technical Note–Certification of Grouted Connections for Offshore Wind Turbines. GL Renewables Certification. Hamburg, Germany.
- Lochte-Holtgreven, S. (2014). Zum Trag-und Ermüdungsverhalten biegebeanspruchter Grouted Joints in Offshore-Windenergieanlagen. Doctoral Dissertation, Institute for Steel Construction, Leibniz Universität Hannover, Hannover, Germany. (In German).
- Löhning, T. and Muurholm, U. (2013). Design of grouted connections in offshore

wind turbines. In: *IABSE Symposium Report*, 99(13), pp. 1252-1259.

Löhning, T., Voßbeck, M. and Kelm, M. (2013). Analysis of grouted connections for offshore wind turbines. *Proceedings of the Institution of Civil Engineers-Energy*, 166(4), pp.153-161. <https://doi.org/10.1680/ener.12.00009>

Lotsberg, I. (2013). Structural mechanics for design of grouted connections in monopile wind turbine structures. *Marine Structures*, 32, pp. 113–135. <https://doi.org/10.1016/j.marstruc.2013.03.001>

Lotsberg, I. and Solland, G. (2013). Assessment of Capacity of Grouted Connections in Piled Jacket Structures. In: *32nd International Conference on Ocean, Offshore and Arctic Engineering*, Nantes, France <https://doi:10.1115/OMAE2013-10850>

Lotsberg, I., Serednicki, A., Bertnes, H. and Lervik, A. (2012). Design of grouted connections for monopile offshore structures. *Stahlbau*, 81 (9), pp. 695-704. DOI: <https://doi.org/10.1002/stab.201201598>

Lotsberg, I., Serednicki, A., Cramer E et al. (2013a) Behaviour of grouted connections of monopile structures at ultimate and cyclic limit states. *The Structural Engineer*, 91(2).

Lotsberg, I., Serednicki, A., Oerlemans, R., Bertnes, H. and Lervik, A. (2013b). Capacity of cylindrical shaped grouted connections with shear keys in offshore structures. *The Structural Engineer*, 91(1), pp.42-48.

Lubliner, J., Oliver, J., Oller, S. and Onate, E. (1989). A plastic-damage model for concrete. *International Journal of solids and structures*, 25(3), pp.299-326. [https://doi.org/10.1016/0020-7683\(89\)90050-4](https://doi.org/10.1016/0020-7683(89)90050-4)

Marion, S., Johansen, A., Solland, G. and Nybø, T. (2018). Testing of jacket pile

sleeve grouted connections exposed to shear forces and bending moments. *Marine Structures*, 59, pp.401-422.

Márquez, G.F.P., Tobias, A.M., Pérez, P.M.J and Papaelias, M. (2012). Condition monitoring of wind turbines: Techniques and methods. *Renewable Energy*, 46, pp. 169-178.

Martinez-Luengo, M., Kolios, A. and Wang, L. (2016). Structural health monitoring of offshore wind turbines: A review through the Statistical Pattern Recognition Paradigm. *Renewable and Sustainable Energy Reviews*, 64, pp.91-105.

Mirambell, E. and Real, E. (2000). On the calculation of deflections in structural stainless beams: an experimental and numerical investigation. *Journal of Constructional Steel Research*, 54 (1), pp. 109-133.

Moll, J. (2018). Damage detection in grouted connections using electromechanical impedance spectroscopy. *Proceedings of the Institution of Mechanical Engineers – Part C: Journal of Mechanical Engineering Science*.

Mollazadeh, M.H. and Wang, Y.C. (2014). New insights into the mechanism of load introduction into concrete-filled steel tubular column through shear connection. *Engineering Structures*, 75, pp.139-151.

Moon, J., Roeder, C.W., Lehman, D.E. and Lee, H.E. (2012). Analytical modeling of bending of circular concrete-filled steel tubes. *Engineering Structures*, 42, pp.349-361.

Muller, N. (2017). Condition Monitoring and Fatigue. Presentation in OceaNET-Final Workshop and Meeting “Offshore Renewable Energy farm design and O&M”, Bilbao, Spain.

Muralidhara, S., Prashad, R.B.E.H. and Karihaloo, B. L. (2010). Fracture process zone size and true fracture energy of concrete using acoustic emission. *Construction and Building Materials*, Volume 24, pp. 479-486.

Nielsen, L.P. (2007). Finite element analysis of large diameter grouted connections. In *Proceedings of the 26th International Conference on Offshore Mechanics and Arctic Engineering*. San Diego, CA, USA, pp.449-457.  
<https://doi:10.1115/OMAE2007-29199>

NORSOK N-004 (2013). Design of steel structures – Standard.

Offshore Renewable Energy (2017). Offshore wind farm substructure monitoring and inspection. [online]. Available at:  
<https://ore.catapult.org.uk/app/uploads/2018/01/Offshore-wind-farm-substructure-monitoring-and-inspection-report-.pdf> [Accessed at: 26 August 2017].

Pavlović, M. and Veljković, M. (2017). FE validation of push-out tests: Using bolts as shear connectors. *Steel Construction*, 10(2), pp.135-144.

Pavlović, M., Marković, Z., Veljković, M. and Buđevac, D. (2013). Bolted shear connectors vs. headed studs behaviour in push-out tests. *Journal of Constructional Steel Research*, 88, pp.134-149.  
<https://doi.org/10.1016/j.jcsr.2013.05.003>

PhysicalAcoustics (2018). AEwin™ - Real time data acquisition and replay software. <https://www.physicalacoustics.com/by-product/aewin>

Prakhya, G., Zhang, C. and Harding, N. (2012). Grouted connections for monopiles-limits for large wind turbines. *Structural Engineer*, 90(3): 30-45.

Qureshi, J., Lam, D. and Ye, J. (2011). The influence of profiled sheeting thickness

and shear connector's position on strength and ductility of headed shear connector. *Engineering structures*, 33(5), pp.1643-1656.

Ramboll (2017). Installation of monopile transition piece with platform and appurtenances in Anholt, Denmark. Available at: [www.Ramboll.com](http://www.Ramboll.com) [Accessed at 13 December 2017].

Rao, M.V.M.S. and Lakshmi, K.J.P. (2005). Analysis of b-value and improved b-value of acoustic emissions accompanying rock fracture. *Current Science*, 89(9), pp. 1577-1582.

RenewableUK (2018). Wind Energy Statistics - RenewableUK. [online] Renewableuk.com. Available at: <https://www.renewableuk.com/page/UKWEDhome> [Accessed at: 1 September 2018].

Rolfes, R., Tsiapoki, S., and Häckell, M. (2014). Sensing solutions for assessing and monitoring wind turbines. In: *Sensor Technologies for Civil Infrastructures - Applications in Structural Health Monitoring*, Editors: M. Wang, J. Lynch and H. Sohn, Woodhead Publishing, pp. 565-604.

Sagar, R.V. and Rao, M.V.M.S. (2014). An experimental study on loading rate effect on acoustic emission based b-values related to reinforced concrete fracture. *Construction and Building Materials*, Volume 70, pp. 460-472.

Schaumann P, Raba A and Bechtel A(2014b) Fatigue Behaviour of Axial Loaded Grouted Joints in Tests. In: *Steinborn, Th. (Hrsg.): Festschrift Ludger Lohaus zur Vollendung des sechzigsten Lebensjahres, Berichte aus dem Institut für Baustoffe*, 12: 219-226.

Schaumann, P. and Wilke, F. (2006) Fatigue of Grouted Joint Connections. In: *Proceedings of the 8th German Wind Energy Conference (DEWEK)*, Bremen,

Germany.

Schaumann, P. and Wilke, F. (2007). Design of Large Diameter Hybrid Connections Grouted with High Performance Concrete. In: *The Seventeenth International Offshore and Polar Engineering Conference*, International Society of Offshore and Polar Engineers (ISOPE), Lisbon, Portugal.

Schaumann, P., Bechtel, A., Lochte-Holtgreven, S., Lohaus, L. and Griese, R. (2013). Approvals for Grouted Joints in Offshore Structures in Germany. *Bautechnik*, 90(7), pp. 402-409.

Schaumann, P., Lochte-Holtgreven, S. and Wilke, F. (2010). Bending tests on grouted joints for monopile support structures. In *Proceedings of the 10th German Wind Energy Conference (DEWEK)*, Bremen, Germany.

Schaumann, P., Raba, A. and Bechtel, A. (2014a). Experimental Fatigue Tests on Axially Loaded Grouted Joints. In: *Proceedings of the IWEC*.

Schaumann, P., Raba, A. and Bechtel, A. (2016). Impact of water on the fatigue performance of large-scale grouted connection tests. In: *35<sup>th</sup> International Conference on Ocean, Offshore and Arctic Engineering*, Busan, South Korea. <https://doi:10.1115/OMAE2016-54823>

Sele, A., Veritec, A. and Kjeóy, H. (1989) Background for the New Design Equations for Grouted Connections in the DnV Draft Rules for Fixed Offshore Structures. In: *Offshore Technology Conference*, Houston, Texas.

Shafiee, M. and Sørensen, D.J. (2018). Maintenance Optimization and Inspection Planning of Wind Energy Assets: Models, Methods and Strategies. *Reliability Engineering & System Safety*, <https://doi:10.1016/j.res.2017.10.025>

Shafiee, M., Brennan, F. and Espinosa, I.A. (2016). A parametric whole life cost

model for offshore wind farms. *The International Journal of Life Cycle Assessment*, 21(7), pp.961-975.

Shi, S., Han, Z., Liu, Z., Vallely, P., Soua, S., Kaewunruen, S. and Papaelias, M., (2018). Quantitative monitoring of brittle fatigue crack growth in railway steel using acoustic emission. *Proceedings of the Institution of Mechanical Engineers, Part F: Journal of Rail and Rapid Transit*, 232(4), pp.1211-1224.

Shiotani, T. (1994). Evaluation of progressive failure using AE sources and improved b-value on slope model tests. *Progress in Acoustic Emission VII*, 7, pp.529-534.

Shiotani, T., Aggelis, D.G. and Makishima, O. (2007). Global monitoring of concrete bridge using acoustic emission. *Journal of acoustic emission*, 25, pp. 308-315.

Shiotani, T., Ohtsu, M. and Ikeda, K. (2001). Detection and evaluation of AE waves due to rock deformation. *Construction and Building Materials*, 15(5-6), pp. 235-246.

Solland, G. and Johansen, A. (2018). Design recommendations for grouted pile sleeve connections. *Marine Structures*, 60, pp.1-14.

Sørensen, E.V. (2011). Fatigue life of High Performance Grout in Dry and Wet Environment for Wind Turbine Grouted Connections. In *Nordic Concrete Research*, 44, pp. 1-10.

The European Commission (1979). *Symposium of New Technologies for Exploration and Exploitation of Oil and Gas Resources*.

Tomaszewicz, A. (1984). *Betongens Arbejdsdiagram*. SINTEF report N<sup>o</sup> STF 65A84065, Trondheim, Norway. In: Van Gysel, A. and Taerwe, L. (1996).

Analytical formulation of the complete stress-strain curve for high strength concrete. *Materials and Structures*, 29, pp. 529-533.

Tziavos, N.I., Hemida, H., Metje N. and Baniotopoulos, C. (2016). Grouted connections on offshore wind turbines: A review. *Engineering and Computational Mechanics (ICE)*, Themed issue on offshore wind, 169(4), pp. 183-195. <https://doi.org/10.1680/jencm.16.00004>

Tziavos, N.I., Hemida, H., Metje N. and Baniotopoulos, C. (2018). Grouted Connections for offshore wind turbines: A numerical study. In: *Energy and Geotechnics*, vol. 18, The first Vietnam Symposium on advances in offshore engineering.

Tziavos, N.I., Hemida, H., Metje N. and Baniotopoulos, C. (2019). Non-linear finite element analysis of grouted connections for monopile offshore wind turbines. *Ocean Engineering*, 171, pp. 633-645.

Vasilopoulos, A. (2010). Introduction to the fatigue life prediction of composite materials and structures: past, present and future prospects. pp.1-44, Woodhead Publishing. <https://doi.org/10.1533/9781845699796.1>

Wang, Z., Zhang, Yi., Chen, F., Wang, G., Wang, L., Jiang, J. (2017). Axial bearing capacity of large-diameter grouted connections analysed by means of a simplified double shear test. *Construction and Building Materials*, 134, pp. 245-253.

Wilke, F. (2013). *Load Bearing Behaviour of Grouted Joints Subjected to Predominant Bending*. Doctoral Dissertation, Institute for Steel Construction, Leibniz Universität Hannover, Hannover, Germany.

WindEurope (2017). Offshore Wind in Europe – Key trends and statistics 2017. Available at: <https://windeurope.org/wp-content/uploads/files/about->

[wind/statistics/WindEurope-Annual-Offshore-Statistics-2017.pdf](#) [Accessed: 19 May 2018].

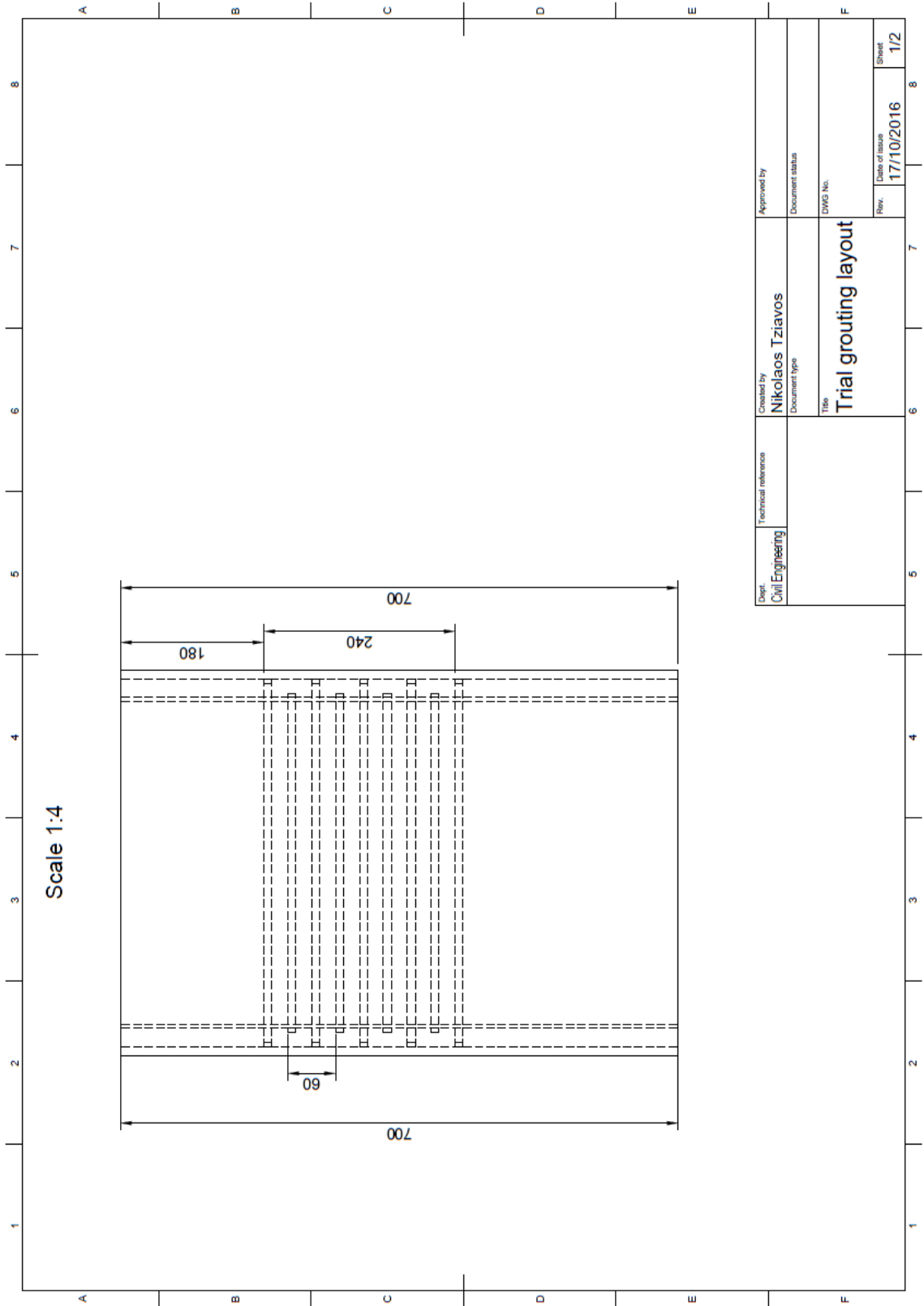
Wymore, M.L., Van Dam, J.E., Ceylan, H. and Qiao, D. (2015). A survey of health monitoring systems for wind turbines. *Renewable and Sustainable Energy Reviews*, 52, pp.976-990.

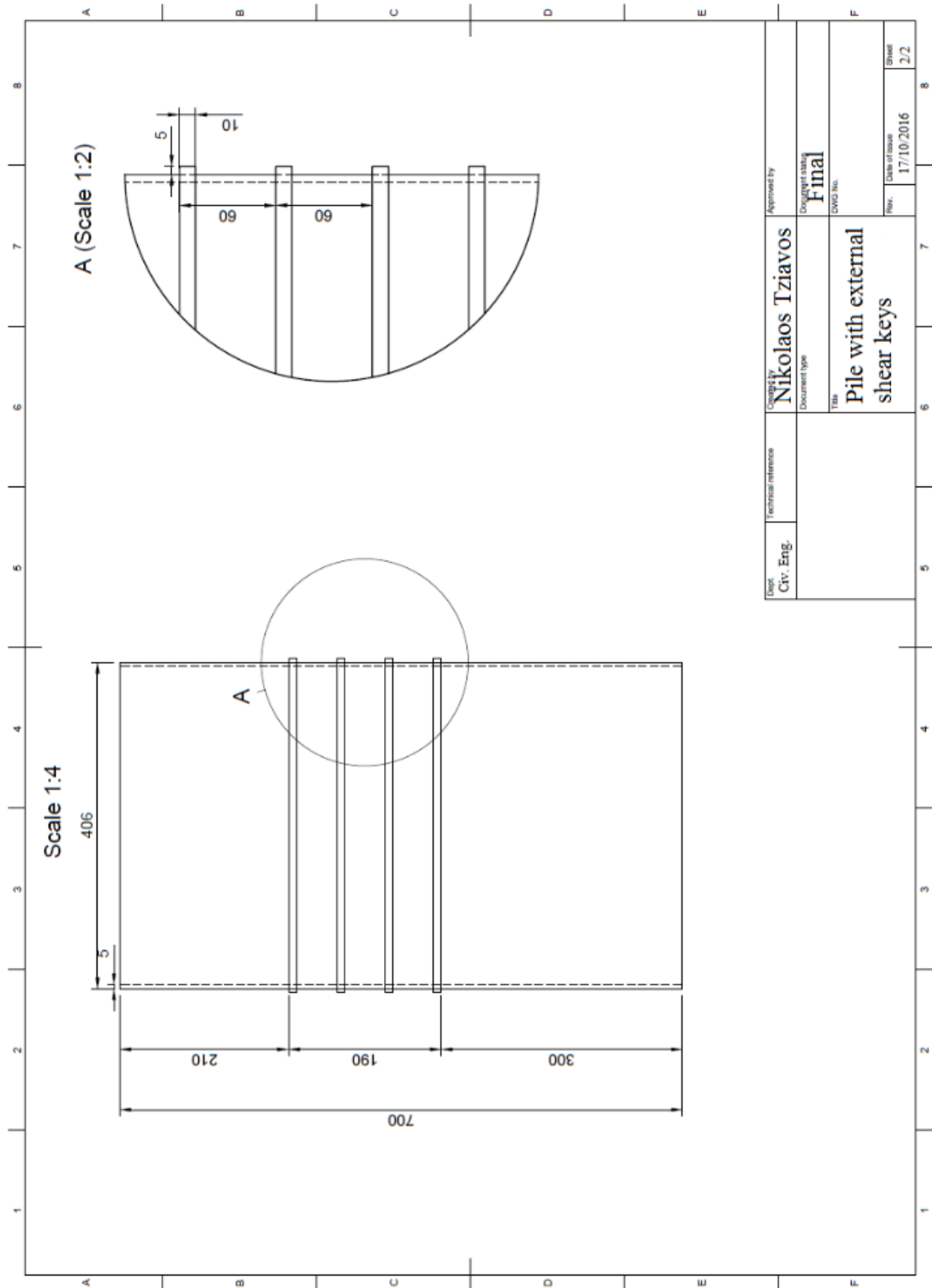
Ziehl, P. and Pollock, A. (2012). Acoustic emission for civil structures. In W. Sikorski (Ed.), *Acoustic emission*. Editor: Sirocki, W., InTech. <https://dx.doi.org/10.5772/32652>.

# APPENDICES

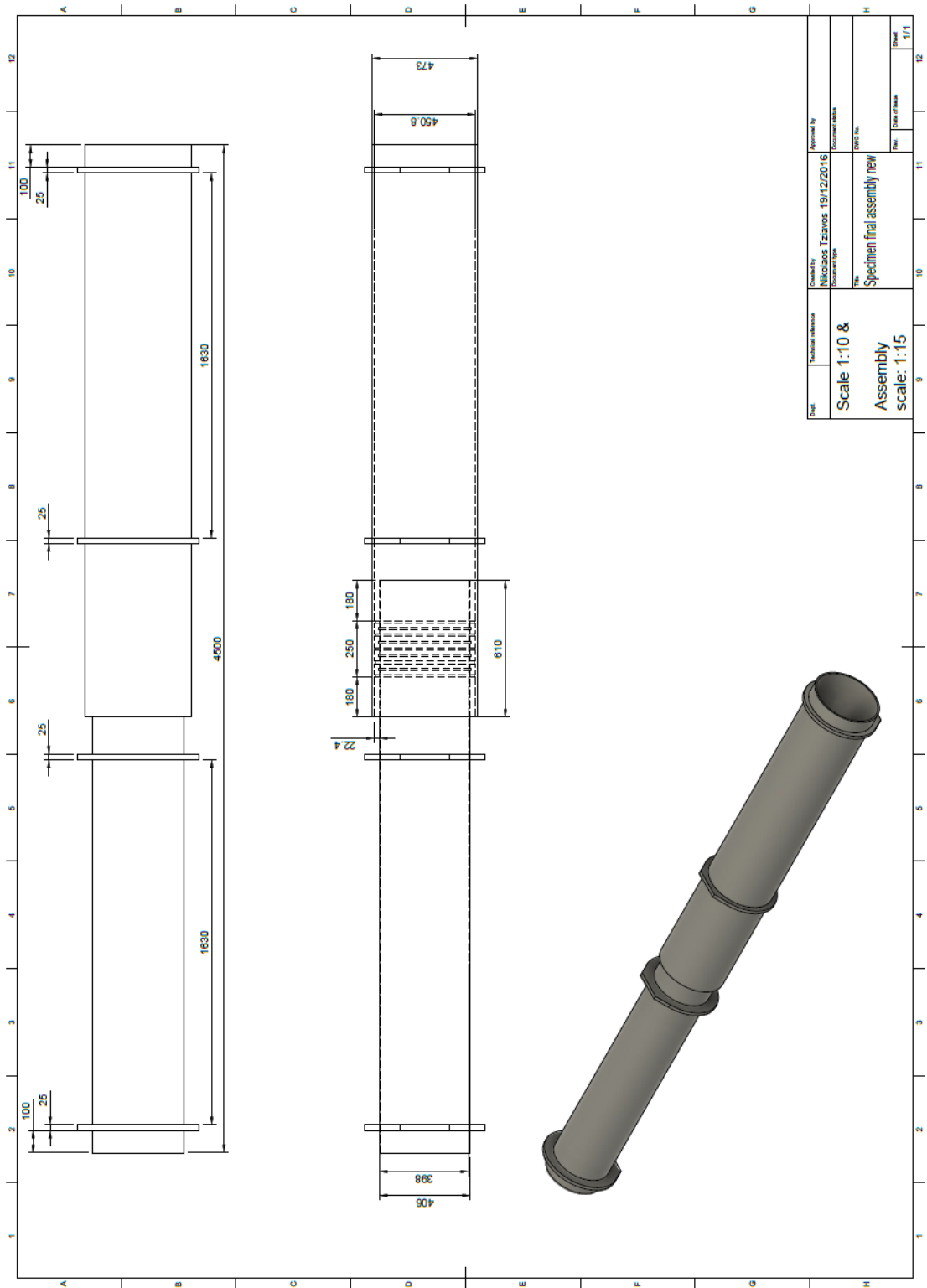
## A.1 EXPERIMENTAL DRAWINGS

Appendix A.1 includes the technical drawings that were used for the experimental campaign described in Chapter 3. The geometries of the pile and sleeve along with details on shear keys for the trial test and specimens are following. Additionally, schematics of the test rigs are accompanied with technical drawings of individual components that were used for the assembly of the frames.



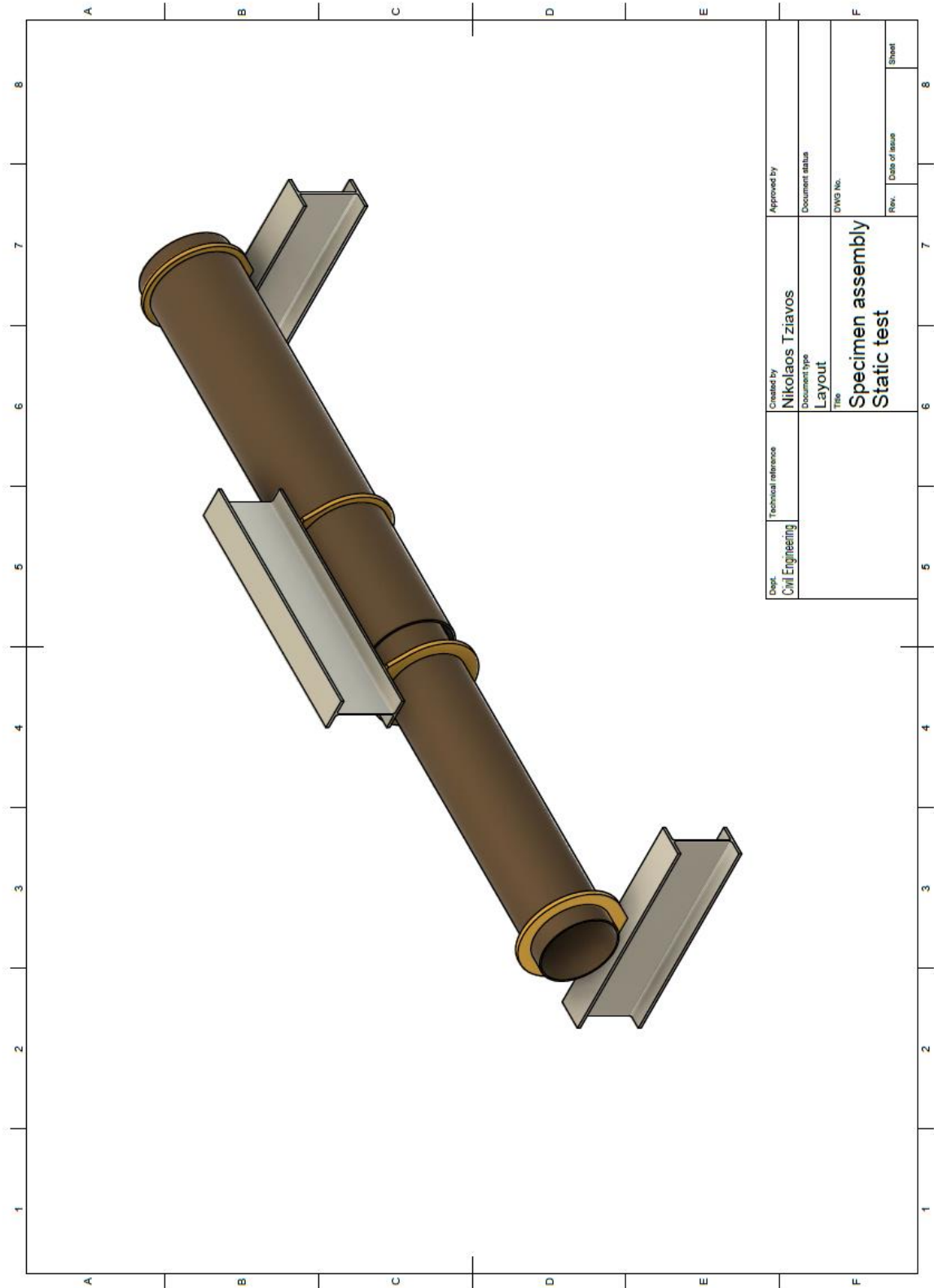


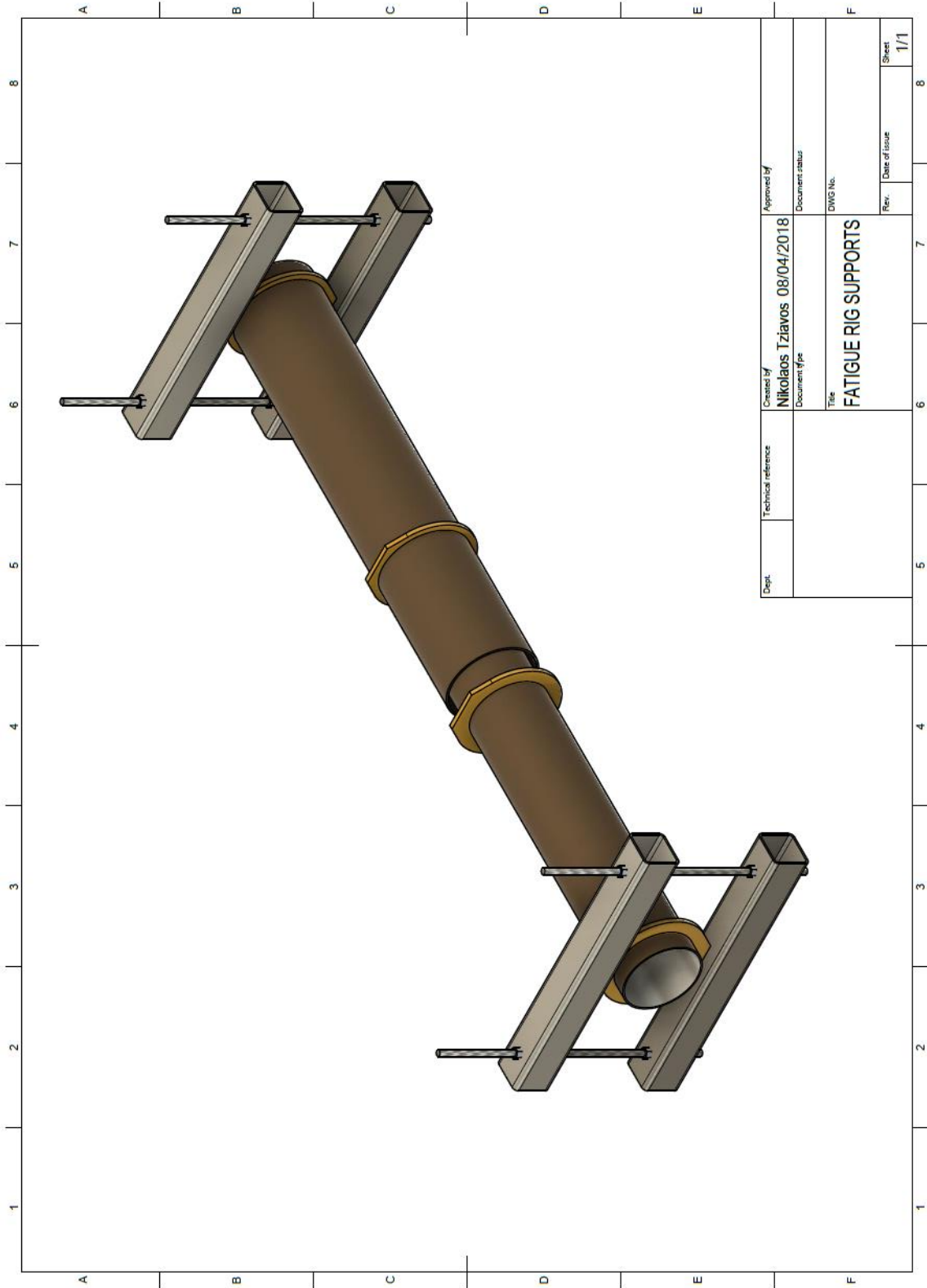
Disc: Civ. Eng.	Technical reference	Checked by <b>Nikolaos Tziavos</b>	Approved by
		Document type	Designer's status <b>Final</b>
		Title <b>Pile with external shear keys</b>	DWG No.
		Rev.	Date of issue
			17/10/2016
			Sheet
			2/2



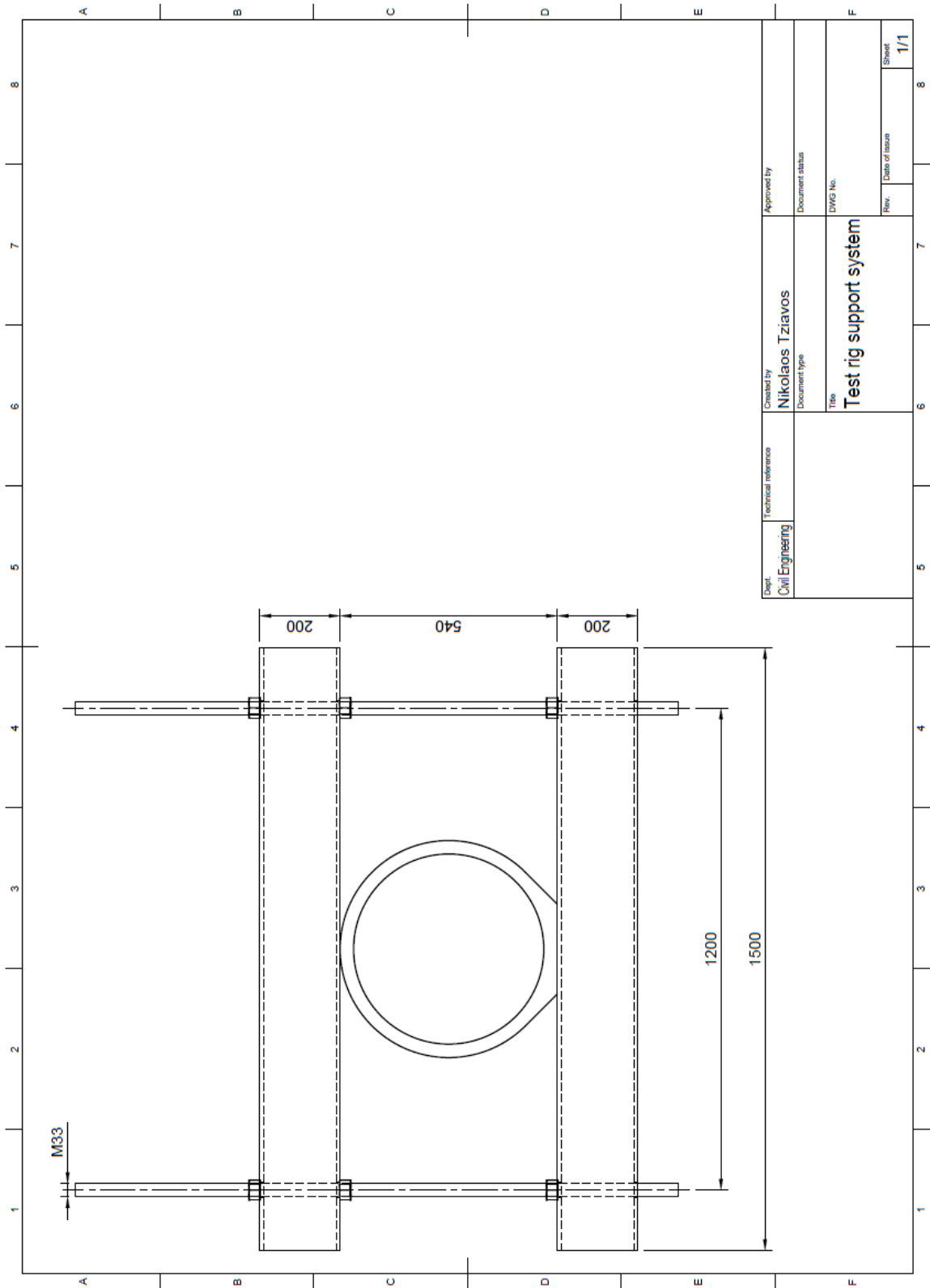




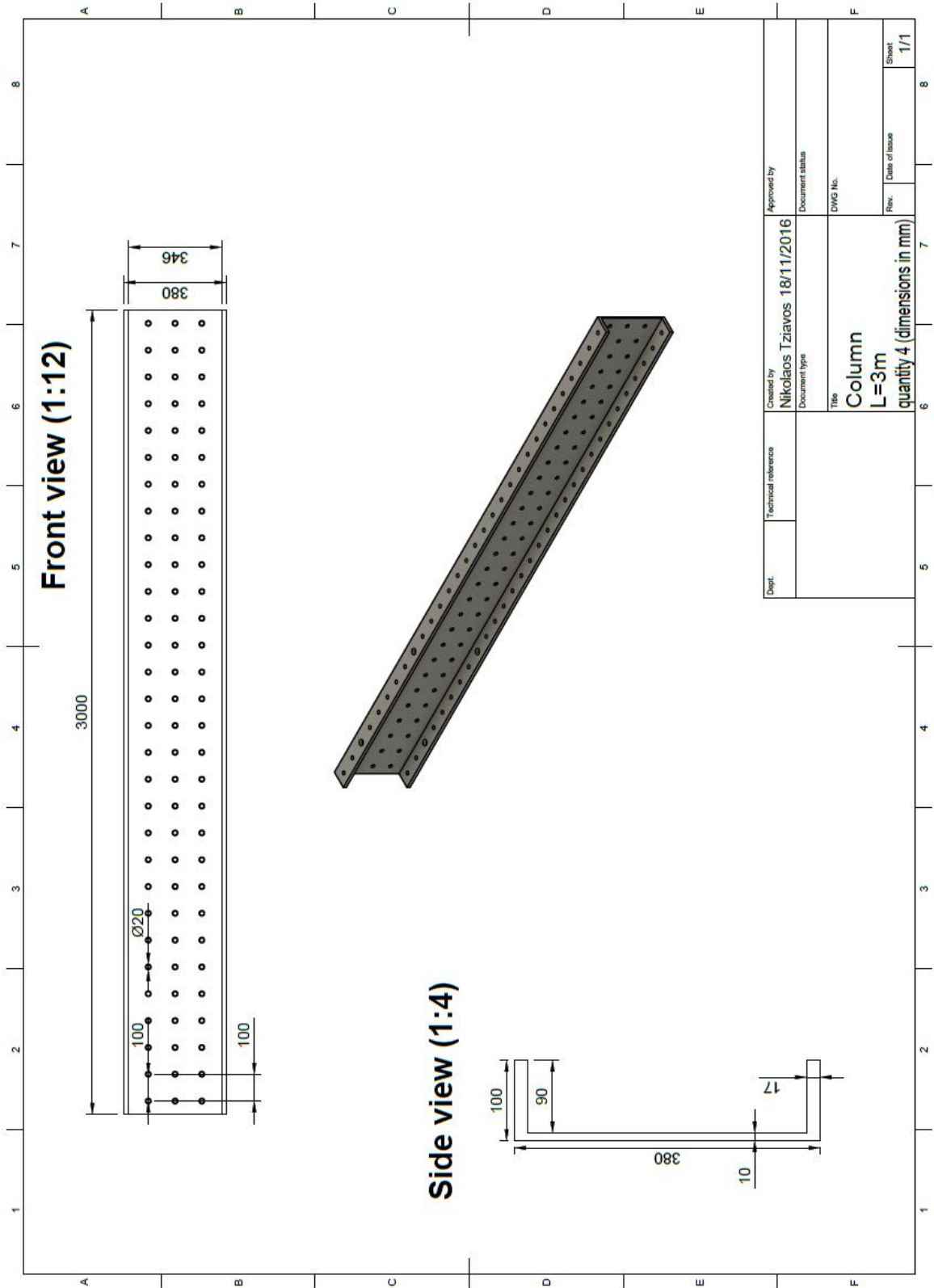


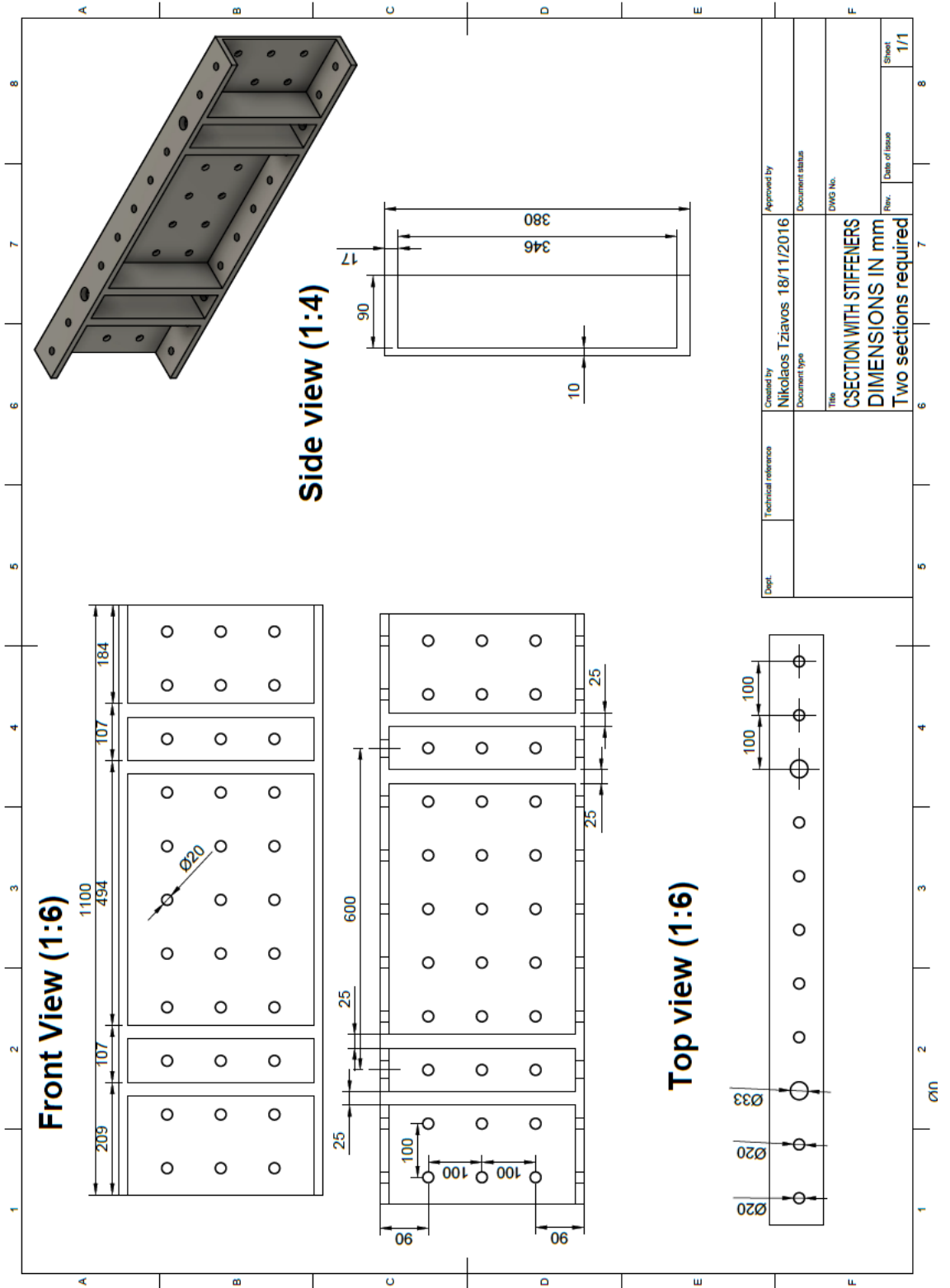


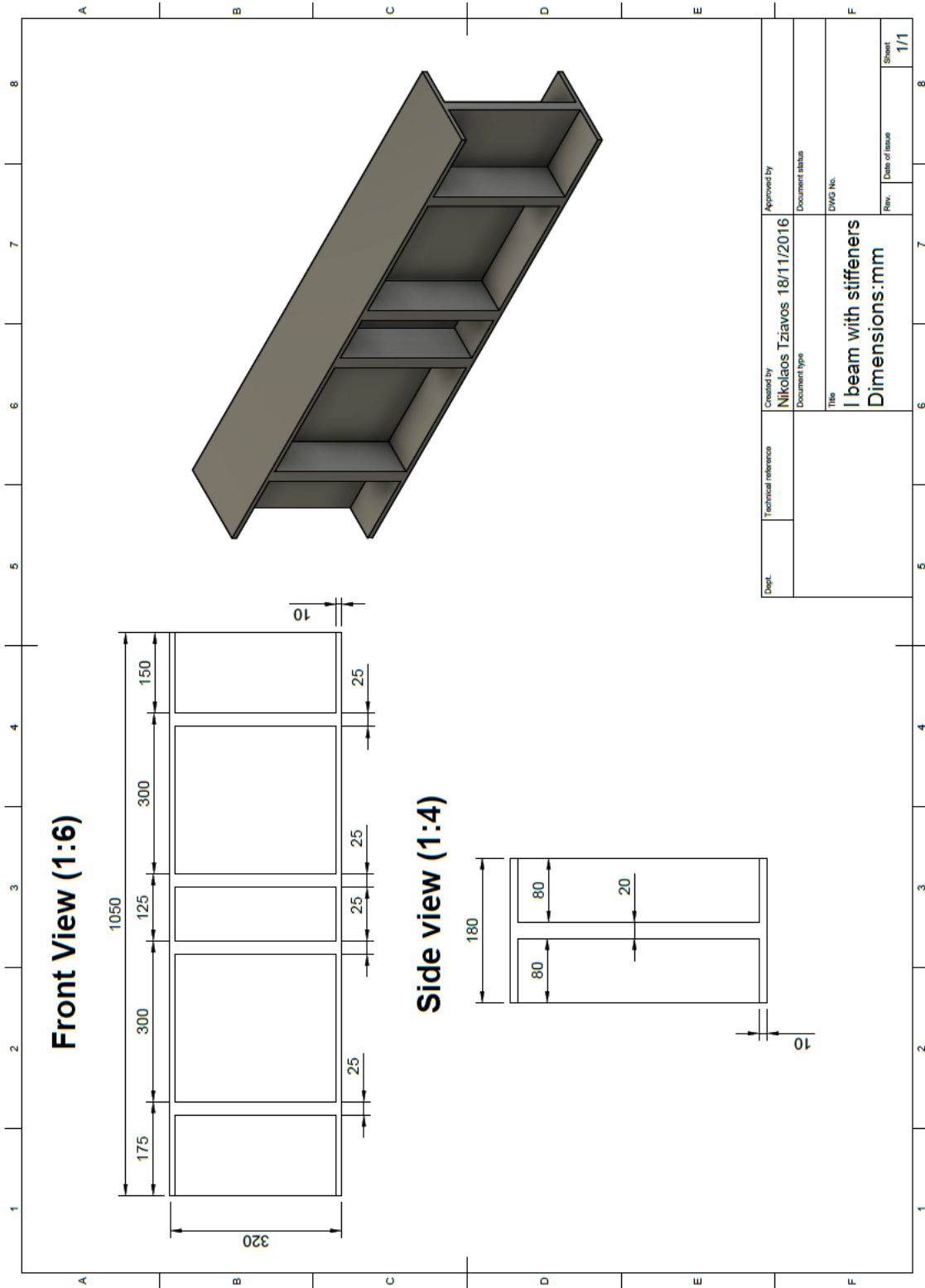
Dept.	Technical reference	Created by <b>Nikolaos Tziavos</b>	Approved by
		<b>08/04/2018</b>	Document status
		Document type	DWG No.
		Title <b>FATIGUE RIG SUPPORTS</b>	Rev.
			Date of issue
			Sheet
			<b>1/1</b>

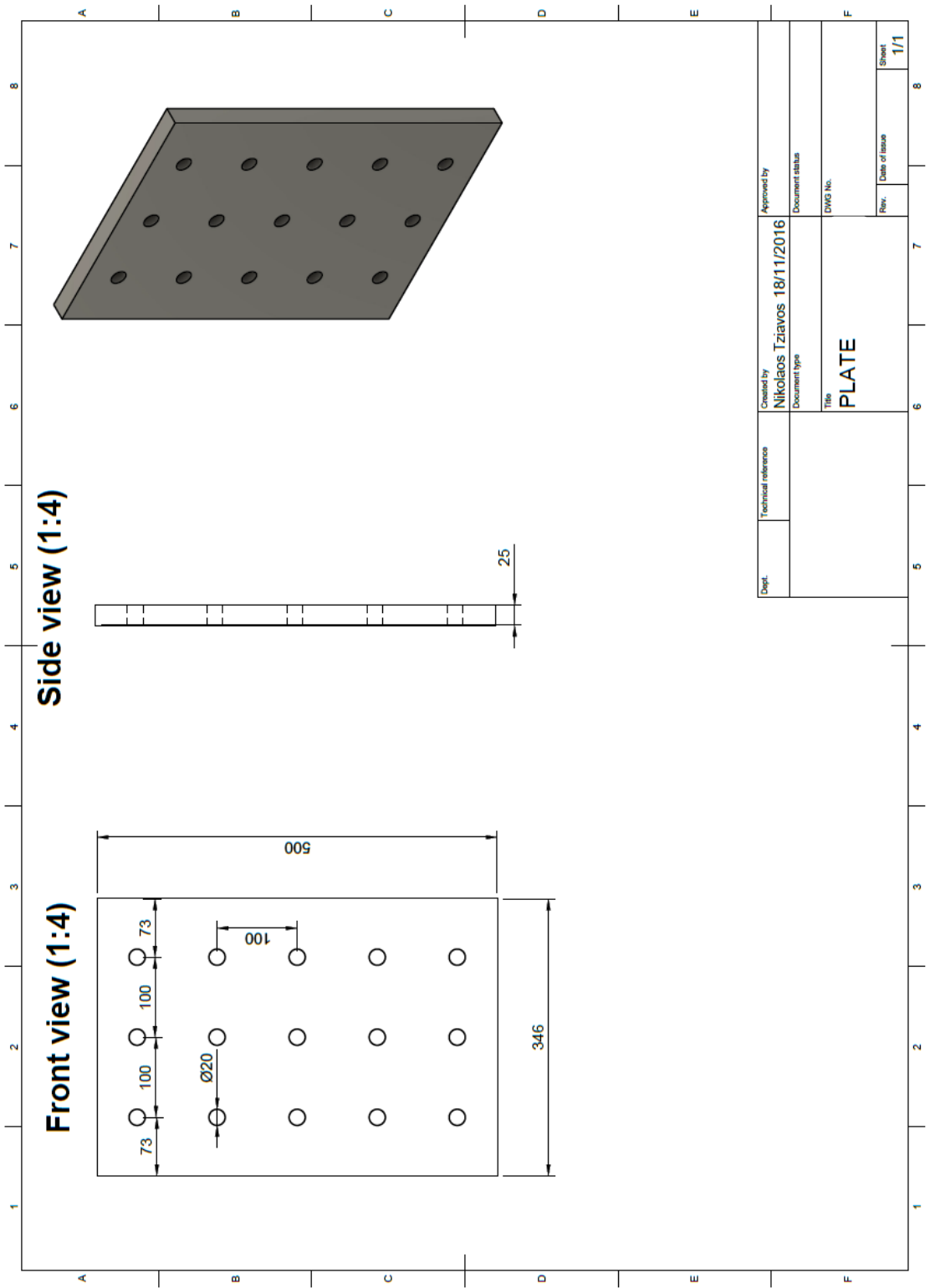


Dept. Civil Engineering	Technical reference	Created by Nikolaos Tziavos	Approved by
		Document type	Document status
		Title Test rig support system	DWG No.
		Rev.	Date of issue
		Sheet	1/1









## A.2 TENSILE COUPON TESTING

In the figure below, from left to right: Tensile coupon set-up and flat coupon prior to testing and following fracture.

